

A Thesis Submitted for the Degree of PhD at the University of Warwick

Permanent WRAP URL:

<http://wrap.warwick.ac.uk/82113>

Copyright and reuse:

This thesis is made available online and is protected by original copyright.

Please scroll down to view the document itself.

Please refer to the repository record for this item for information to help you to cite it.

Our policy information is available from the repository home page.

For more information, please contact the WRAP Team at: wrap@warwick.ac.uk

Modelling and Characterisation of Short Range Underwater Optical Wireless Communication Channels

Faezah Jasman

A thesis submitted in partial fulfilment of the requirements for the
degree of

Doctor of Philosophy

School of Engineering



بِسْمِ اللَّهِ الرَّحْمَنِ الرَّحِيمِ

“... And whoever fears Allah - He will make for him a way out.

And will provide for him from where he does not expect. And whoever relies upon

Allah - then He is sufficient for him. Indeed, Allah will accomplish His purpose.

Allah has already set for everything a [decreed] extent.”

Surah Ath-Thalaq: 2-3

To my Almighty God

Having faith in Allah, my Creator is the vital reason that keeps me going

until the completion of this journey.

TABLE OF CONTENTS

Table of Contents.....	i
List of figures	vi
List of tables	xiv
List of abbreviations	xvi
Acknowledgements	xviii
Declaration	xx
Abstract	xxi
Publications associated with this research work.....	xxiv
CHAPTER 1	1
Introduction	1
1.1 Overview	1
1.1.1 Areas of applications.....	4
1.2 Motivations and aims	5
1.3 Contributions	7
1.4 Outline of the thesis.....	9
CHAPTER 2	12
Background Research and Related Work.....	12
2.1 Introduction.....	12
2.1.1 Acoustic communication.....	13
2.1.2 Radio frequency communication.....	14
2.1.3 Optical communication.....	15
2.2 Related research	17

2.2.1	Work on channel modelling and characterisation.....	18
2.2.2	Work on system and hardware design	23
2.3	Light properties in water.....	29
2.3.1	Inherent optical properties.....	29
2.3.2	Apparent optical properties.....	33
2.4	Absorption.....	33
2.4.1	Absorption by pure seawater	34
2.4.2	Absorption by chlorophyll from phytoplankton	35
2.4.3	Absorption by coloured dissolved organic matter (CDOM).....	35
2.4.4	Absorption by organic detritus	36
2.5	Scattering.....	37
2.5.1	Molecular scattering in pure seawater	38
2.5.2	Scattering by large particles ($> \lambda$)	39
2.5.3	Turbulence scattering	39
2.5.4	Single scattering albedo, ω_o	40
2.5.5	The effect of scattering on underwater communication.....	40
2.6	Volume scattering function.....	41
2.6.1	Petzold scattering function	41
2.6.2	Analytical phase functions	42
2.7	Attenuation length	45
2.8	Channel model	45
2.8.1	Radiative Transfer Equation (RTE)	45
2.8.2	Beers-Lambert (BL) law	47
2.8.3	Limitations of BL law	48
2.9	Water types.....	48
2.10	System configurations	49
2.10.1	Line-of-sight (LOS) links.....	49
2.10.2	Non-line-of-sight (NLOS) links.....	50
2.10.3	Retro-reflector links	50
2.10.4	Reflective NLOS links.....	51
2.11	Conclusion	53

CHAPTER 3 54

Modelling of the Underwater Optical Wireless Communications Channels.....	54
3.1 Overview of Monte Carlo numerical simulation.....	54
3.2 Assumptions in simulations	57
3.3 Monte Carlo algorithm.....	57
3.3.1 Coordinate system	59
3.3.2 Spherical coordinate system.....	60
3.3.3 Initial photon position.....	61
3.4 Source modelling	62
3.4.1 Gaussian source	62
3.4.2 Lambertian source	65
3.4.3 Modelling elevated source : coordinate transformations	67
3.5 Photon propagation	68
3.5.1 Photon step size.....	68
3.5.2 Photon weight.....	69
3.5.3 Terminating photons.....	69
3.5.4 Scattering directions	70
3.5.5 Updating the direction cosines	71
3.5.6 Updating the photon propagation.....	72
3.6 Photon reception	72
3.6.1 Power loss calculation.....	73
3.7 Calculation of impulse response.....	73
3.8 Simulation setup	75
3.8.1 Simulation parameters.....	77
3.9 Simulation of diffuse sources.....	80
3.9.1 Power distribution	80
3.9.2 Frequency Response	83
3.9.3 The effect of bin sizes to the frequency response.....	83
3.9.4 The effect of number of samples on the frequency response.....	84
3.10 Conclusion	85

CHAPTER 4 87

Path Loss: Performance Analysis	87
4.1 Link budget	88
4.2 Path loss modelling.....	89
4.2.1 Diffusion length, L_D	92
4.3 Spatial distribution effects	95
4.4 Path loss performance analysis.....	98
4.4.1 Percentage of unscattered light.....	102
4.4.2 Path loss of unscattered and scattered light	105
4.5 Geometric loss.....	110
4.6 Spatial dispersion versus distance.....	113
4.6.1 Percentage of unscattered light: off-axis.....	119
4.7 Conclusion	123

CHAPTER 5 126

Temporal and Angular Dispersions: Performance Analysis....	126
5.1 Introduction.....	126
5.2 Scattering order	127
5.2.1 Scattering regimes	128
5.2.2 Scattering order histogram : Clear water	133
5.2.3 Scattering order histogram : Coastal water	134
5.2.4 Scattering order histogram : Turbid water	136
5.3 Impulse response.....	138
5.3.1 Impulse response: Analysis	140
5.3.2 On-axis	140
5.3.3 Off-axis	141
5.4 Frequency response	145
5.4.1 On-axis and off-axis.....	145
5.5 Angle of arrival (AOA) distribution	152
5.5.1 On-axis	153

5.5.2	Off-axis	153
5.6	Effect of receiver FOV.....	158
5.6.1	Effect of receiver FOV on bandwidth : On-axis.....	159
5.6.2	Effect of receiver FOV on bandwidth : Off-axis.....	164
5.7	Effect of receiver FOV on the scattering order histogram	173
5.8	Conclusion	177
CHAPTER 6		182
	Impact of Receiver Aperture and Performance Trade-Off	182
6.1	Introduction.....	182
6.2	Impact of receiver aperture size	182
6.2.1	Impact of receiver aperture size on scattering order histogram...	183
6.2.2	Impact of receiver aperture size on the received power	188
6.3	Impact of receiver FOV on the received power	191
6.4	Performance trade-off : Power and bandwidth.....	199
6.4.1	Clear water.....	199
6.4.2	Coastal water	200
6.4.3	Turbid water.....	202
6.5	Conclusion	203
CHAPTER 7		205
	Conclusions & Future Work.....	205
7.1	Conclusions	205
7.2	Future research	209
	References.....	212

LIST OF FIGURES

Figure 2.1: Absorption coefficient for wavelength from 100nm-1 mm [23].....	16
Figure 2.2: Geometry used to define inherent optical properties [22].	30
Figure 2.3: Absorption coefficient of pure water for 340-700 nm. Picture taken from [11].....	34
Figure 2.4: Absorption coefficient due to phytoplankton. Picture taken from [71].....	35
Figure 2.5: Absorption coefficient due to CDOM. Picture taken from [71].....	36
Figure 2.6: The scattering coefficient for pure water and pure seawater. Picture taken from [11].	38
Figure 2.7: The VSFs of various types of water measured by Petzold. Picture taken from [11].	42
Figure 2.8: Comparison of Petzold phase function with HG phase function for various g values. Picture taken from [71].....	44
Figure 2.9: Types of link configuration.	52
Figure 3.1: Flowchart of the MC simulation algorithm	58
Figure 3.2: Illustrations of a photon propagation path in an underwater environment.....	60
Figure 3.3: Spherical coordinate system.	60
Figure 3.4: Photon direction vector shown in Cartesian coordinate system.	61

Figure 3.5: Diagram showing the generation of Gaussian beam with a divergence.....	65
Figure 3.6: Diagram showing multiple scattering effects to the impulse response.....	74
Figure 3.7: Link Geometry.....	77
Figure 3.8: Power distribution for various beam divergences in (a) clear water, (b) coastal water and (c) turbid water.....	82
Figure 3.9: Frequency response for diffuse beam of 15° in coastal water ($c=0.4$) at 30 m for various bin sizes.....	84
Figure 3.10: Frequency response for diffuse beam of 15° in coastal water ($c=0.4$) at 30 m for various samples sizes.....	85
Figure 4.1: Normalised received power versus distance in (a) clear and coastal water and (b) turbid water.....	101
Figure 4.2: Normalised received power versus attenuation length in clear, coastal and turbid water.....	101
Figure 4.3: The percentage of the unscattered light that contributes to the total power reception.....	103
Figure 4.4: Normalised received power for (unscattered component) versus distance in (a) clear and coastal water and (b) turbid water.....	106
Figure 4.5: Normalised received power (unscattered component) versus attenuation length (AL) in clear, coastal and turbid water.....	107
Figure 4.6: Normalised received power (scattered component) versus distance in (a) clear and coastal water and in (b) turbid water.....	109
Figure 4.7: Normalised received power (scattered component) versus attenuation length (AL) in clear, coastal and turbid water.....	109

Figure 4.8: Path loss performance for diffuse beam along with theory incorporating geometrical loss in (a) clear water, (b) coastal water and (c) turbid water.....	112
Figure 4.9: Normalised received power as a function of distance for various lateral positions in clear water for (a) collimated beam, (b) 15° diffuse beam and (c) 30° diffuse beam.....	116
Figure 4.10: Normalised received power as a function of distance for various lateral positions in coastal water for (a) collimated beam, (b) 15° diffuse beam and (c) 30° diffuse beam.....	117
Figure 4.11: Normalised received power as a function of distance for various lateral positions in turbid water for (a) collimated beam, (b) 15° diffuse beam and (c) 30° diffuse beam.....	118
Figure 4.12: The percentage of the unscattered light that contributes to the total power reception for various lateral positions in clear water for (a) collimated beam (b) 15° diffuse beam and (c) 30° diffuse beam.	120
Figure 4.13: The percentage of the unscattered light that contributes to the total power reception for various lateral positions in coastal water for (a) collimated beam (b) 15° diffuse beam and (c) 30° diffuse beam.	121
Figure 4.14: The percentage of the unscattered light that contributes to the total power reception for various lateral positions in turbid water for (a) collimated beam (b) 15° diffuse beam and (c) 30° diffuse beam.	122
Figure 5.1: Scattering order histogram in clear water at 15 m for (a) collimated beam (b) 15° diffuse beam and (c) 30° diffuse beam.....	133
Figure 5.2: Scattering order histogram in clear water at 30 m for (a) collimated beam (b) 15° diffuse beam and (c) 30° diffuse beam.....	133
Figure 5.3: Scattering order histogram in clear water at 50 m for (a) collimated beam (b) 15° diffuse beam and (c) 30° diffuse beam.....	133

Figure 5.4: Scattering order histogram in clear water at 70 m for (a) collimated beam (b) 15° diffuse beam and (c) 30° diffuse beam.....	134
Figure 5.5: Scattering order histogram in coastal water at 15m for (a) collimated beam (b) 15° diffuse beam and (c) 30° diffuse beam.	134
Figure 5.6: Scattering order histogram in coastal water at 22 m for (a) collimated beam (b) 15° diffuse beam and (c) 30° diffuse beam.	135
Figure 5.7: Scattering order histogram in coastal water at 50 m for (a) collimated beam (b) 15° diffuse beam and (c) 30° diffuse beam.	135
Figure 5.8: Scattering order histogram in coastal water at 70 m for (a) collimated beam (b) 15° diffuse beam and (c) 30° diffuse beam.	135
Figure 5.9: Scattering order histogram in turbid water at 1 m for (a) collimated beam (b) 15° diffuse beam and (c) 30° diffuse beam.....	136
Figure 5.10: Scattering order histogram in turbid water at 3 m for (a) collimated beam (b) 15° diffuse beam and (c) 30° diffuse beam.	136
Figure 5.11: Scattering order histogram in turbid water at 7 m for (a) collimated beam (b) 15° diffuse beam and (c) 30° diffuse beam.	136
Figure 5.12: Scattering order histogram in turbid water at 15 m for (a) collimated beam (b) 15° diffuse beam and (c) 30° diffuse beam.	137
Figure 5.13: Channel impulse response in clear water for on-axis(left column) and off-axis(right column), with increasing distance . (a) and (b) 15 m, (c) and (d) 30 m, (e) and (f) 50 m, (g) and (h) 70 m.	142
Figure 5.14: Channel impulse response in coastal water for on-axis (left column) and off-axis (right column), with increasing distance . (a) and (b) 15 m, (c) and (d) 22 m, (e) and (f) 50 m, (g) and (h) 70 m.....	143

Figure 5.15: Channel impulse response in turbid water for on-axis (left column) and off-axis (right column), with increasing distance: (a) and (b) 1 m, (c) and (d) 3 m, (e) and (f) 7 m, (g) and (h) 15 m.	144
Figure 5.16: Frequency response in clear water ($c=0.15$) for on-axis and off-axis (4 m offset) locations using various source distributions at (a) 15m (b) 30 m (c) 50 m and (d) 70m.	148
Figure 5.17: Frequency response in coastal water ($c=0.4$) for on-axis and off-axis (4 m offset) locations using various source distributions at (a) 15 m (b) 22 m (c) 50 m and (d) 70m.	149
Figure 5.18: Frequency response in turbid water ($c=2.2$) for on-axis and off-axis (4 m offset) locations using various source distributions at (a) 1 m (b) 3 m (c) 7 m and (d) 15 m	150
Figure 5.19: AOA distribution in clear water for on-axis (left column) and off-axis(right column), with increasing distance: (a) and (b) 15 m, (c) and (d) 30 m, (e) and (f) 50 m, (g) and (h) 70 m.	155
Figure 5.20: AOA distribution in coastal water for on-axis (left column) and off-axis(right column), with increasing distance : (a) and (b) 15 m, (c) and (d) 22 m, (e) and (f) 50 m, (g) and (h) 70 m.	156
Figure 5.21: AOA distribution in turbid water for on-axis (left column) and off-axis(right column), with increasing distance : (a) and (b) 1 m, (c) and (d) 3 m, (e) and (f) 7 m, (g) and (h) 15 m.	157
Figure 5.22: Frequency response in coastal water at (a) 22 m, (b) 50 m and (c) 70 m.	161
Figure 5.23: Frequency response in turbid water at (a) 7 m and (b) 15 m.	162
Figure 5.24: Frequency response in clear water at off-axis (4 m offset) locations : (a) 22 m, (b) 50 m and (c) 70 m.	166
Figure 5.25: Frequency response in coastal water at off-axis (4 m offset) locations: (a) 15 m and (b) 22 m.	167

Figure 5.26: Frequency response in coastal water at off-axis (4 m offset) locations : (a) 50m and (b) 70 m.....	168
Figure 5.27: Frequency response in turbid water at off-axis (4 m offset) locations : (a) 1 m and (b) 3 m.....	169
Figure 5.28: Frequency response in turbid water at off-axis (4 m offset) locations : (a) 7 m and (b) 15 m.....	170
Figure 5.29: Scattering order histogram in coastal water at 15 m for (a) collimated beam (b) 15° diffuse beam and (c) 30° diffuse beam.....	174
Figure 5.30: Scattering order histogram in coastal water at 22 m for (a) collimated beam (b) 15° diffuse beam and (c) 30° diffuse beam.....	174
Figure 5.31: Scattering order histogram in coastal water at 50 m for (a) collimated beam (b) 15° diffuse beam and (c) 30° diffuse beam.....	175
Figure 5.32: Scattering order histogram in coastal water at 70 m for (a) collimated beam (b) 15° diffuse beam and (c) 30° diffuse beam.....	175
Figure 5.33: Scattering order histogram in turbid water at 1m for (a) collimated beam (b) 15° diffuse beam and (c) 30° diffuse beam.....	175
Figure 5.34: Scattering order histogram in turbid water at 3 m for (a) collimated beam (b) 15° diffuse beam and (c) 30° diffuse beam.....	176
Figure 5.35: Scattering order histogram in turbid water at 7 m for (a) collimated beam (b) 15° diffuse beam and (c) 30° diffuse beam.....	176
Figure 5.36: Scattering order histogram in turbid water at 15m for (a) collimated beam (b) 15° diffuse beam and (c) 30° diffuse beam.....	176
Figure 6.1: Scattering order histogram in clear water at 30 m for (a) collimated beam (b) 15° diffuse beam and (c) 30° diffuse beam.....	184

Figure 6.2: Scattering order histogram in clear water at 50 m for (a) collimated beam (b) 15° diffuse beam and (c) 30° diffuse beam.....	185
Figure 6.3: Scattering order histogram in clear water at 70 m for (a) collimated beam (b) 15° diffuse beam and (c) 30° diffuse beam.....	185
Figure 6.4: Scattering order histogram in coastal water at 15m for (a) collimated beam (b) 15° diffuse beam and (c) 30° diffuse beam.	185
Figure 6.5: Scattering order histogram in coastal water at 22 m for (a) collimated beam (b) 15° diffuse beam and (c) 30° diffuse beam.	186
Figure 6.6: Scattering order histogram in coastal water at 50 m for (a) collimated beam (b) 15° diffuse beam and (c) 30° diffuse beam.	186
Figure 6.7: Scattering order histogram in coastal water at 70 m for (a) collimated beam (b) 15° diffuse beam and (c) 30° diffuse beam.	186
Figure 6.8: Scattering order histogram in turbid water at 1 m for (a) collimated beam (b) 15° diffuse beam and (c) 30° diffuse beam.....	187
Figure 6.9: Scattering order histogram in turbid water at 3 m for (a) collimated beam (b) 15° diffuse beam and (c) 30° diffuse beam.....	187
Figure 6.10: Scattering order histogram in turbid water at 7 m for (a) collimated beam (b) 15° diffuse beam and (c) 30° diffuse beam.	187
Figure 6.11: Scattering order histogram in turbid water at 15 m for (a) collimated beam (b) 15° diffuse beam and (c) 30° diffuse beam.	188
Figure 6.12: Percentage of received power for various receiver aperture in (a) clear water (b)coastal water and (c) turbid water.....	190
Figure 6.13: Percentage of received power for various receiver FOV in clear water at on-axis location using (a) collimated beam, (b) 15° diffuse beam and (c) 30° diffuse beam.	193

Figure 6.14: Percentage of received power for various receiver FOVs in coastal water at on-axis location using (a) collimated beam, (b) 15° diffuse beam and (c) 30° diffuse beam.	194
Figure 6.15: Percentage of received power for various receiver FOVs in turbid water at on-axis location using (a) collimated beam, (b) 15° diffuse beam and (c) 30° diffuse beam.	195
Figure 6.16: Percentage of received power for various receiver FOVs in clear water at off-axis location using (a) collimated beam, (b) 15° diffuse beam and (c) 30° diffuse beam.	196
Figure 6.17: Percentage of received power for various receiver FOVs in coastal water at off-axis location using (a) collimated beam, (b) 15° diffuse beam and (c) 30° diffuse beam.	197
Figure 6.18: Percentage of received power for various receiver FOVs in turbid water at off-axis location using (a) collimated beam, (b) 15° diffuse beam and (c) 30° diffuse beam.	198
Figure 6.19: Trade-off between power and bandwidth as a function of FOV for diffuse beam of 15° in coastal water at (a) 22m (b) 50 m and (c) 70 m.	201
Figure 6.20: Trade-off between power and bandwidth as a function of FOV for diffuse beam of 15° in turbid water at (a) 7m and (b) 15 m.	203

LIST OF TABLES

Table 1.1: Laser and LED characteristics. Adapted from [11].	3
Table 2.1: The bandwidth supported for different ranges in typical acoustic communication system [18].	13
Table 2.2: Data rates and ranges of underwater RF communications. Table adapted from [21].	15
Table 2.3: Properties of optical, acoustic and RF technology.	16
Table 2.4: Comparisons of different communication carriers underwater [21].	17
Table 2.5: Summary of works on channel modeling and characterisation.	22
Table 2.6: Summary of experimental works in UOWC systems. It indicates the maximum data rate achieved, distance, source, modulation and turbidity level.	27
Table 2.7: Various water types with the coefficients. Table is reproduced from [22].	48
Table 3.1: Simulation parameters.	77
Table 3.2: Input and output parameters used in simulations.	78
Table 3.3: Coefficients for three types of water. Table taken from [38].	78
Table 3.4: Published simulation parameters used in MC simulation.	79
Table 4.1: Optical properties of the ocean water types with the corresponding diffusion length.	94

Table 4.2: The three regions of energy transport [117]	94
Table 4.3: The proposed transition point between minimally scattered region and multiple scattering region.....	105
Table 5.1: Classification of scattering regimes as a function of scattering order	128
Table 5.2: Select distance in various types of water.....	129
Table 5.3: Modified scattering regime description.	137
Table 5.4: Proposed transition points.....	138
Table 5.5: 3 dB bandwidth for various select distances in (a) Clear water (b) Coastal water and (c) Turbid water for three sizes of beam divergences.....	151
Table 5.6: 3 dB bandwidth for various receiver FOVs at (a) 22 m (b) 50 m and (c) 70 m for three sizes of beam divergences in coastal water.	163
Table 5.7: 3 dB bandwidth for various receiver FOVs at (a) 7 m and (b) 15 m for three sizes of beam divergences in turbid water.....	163
Table 5.8: 3 dB bandwidth for various receiver FOVs in clear water for collimated beam at off-axis locations.	166
Table 5.9: 3 dB bandwidth for various receiver FOVs in coastal water for off-axis (4 m offset) locations at (a)15 m, (b) 22 m, (c) 50 m and (d)70 m.....	171
Table 5.10: 3 dB bandwidth for various receiver FOVs in turbid water for off-axis (4 m offset) locations at (a)1 m, (b) 3 m, (c) 7 m and (d)15 m.....	172
Table 5.11: Summary of the characteristics of the scattering regime for diffuse beam (on-axis).....	181

LIST OF ABBREVIATIONS

AL	Attenuation length
AOA	Angle of arrival
AOP	Apparent optical properties
APD	Avalance photodiode
AUV	Autonomous underwater vehicles
BER	Bit error rate
BL	Beer-Lambert
BPSK	Bipolar phase shift keying
BSF	Beam spread function
CDOM	Colour dissolved organic material
DMT	Discreet multi tone
DPIM	Digital pulse interval modulation
EM	Electromagnetic
FOV	Field of view
FSO	Free space optics
HG	Henye Greenstein
IMDD	Intensity modulation direct detection
IOP	Inherent optical properties
IR	Infrared
IrDA	Infrared data association
ISI	Inter symbol interference
LD	Laser diode
LED	Light emitting diode
LOS	Line-of-sight
MC	Monte Carlo

MIMO	Multiple in multiple out
NLOS	Non line-of-sight
NRZ	Non return zero
OFDM	Orthogonal frequency division multiplexing
OW	Optical wireless
OWC	Optical wireless communication
PD	Photodetector
PMT	Photomultiplier tube
QAM	Quadrature amplitude modulation
QPSK	Quadrature phase shift keying
RF	Radio frequency
ROV	Remotely operated vehicles
RTE	Radiative transfer equation
SAA	Small angle approximation
SNR	Signal to noise ratio
TTHG	Two Term Henyey Greenstein
TTL	Transistor transistor logic
UOWC	Underwater optical wireless communications
UV	Ultra violet
UWSN	Underwater sensor wireless network
VSF	Volume scattering function

ACKNOWLEDGEMENTS



Alhamdulillah Praise and Gratitude to Allah for everything, for giving me the guidance, strength and perseverance in this PhD journey, for making the impossible, possible until the completion of this thesis.

I would like to express my deepest gratitude to Prof. Roger J. Green for his valuable time, guidance, support and kindness throughout the work and especially after his retirement. I am also indebted to Dr. Mark S. Leeson for his constructive feedback, advice and support throughout the writing up period. My sincere thanks also goes to Prof. Declan Bates and Dr. Christios Mias for the insightful discussions during the annual panel meetings which were really helpful. I would also like to take this opportunity to thank Dr. Andrew J. Philips and Dr. Daciana D. Iliescu- my viva examiners, for their very helpful comments and suggestions.

Specially for my beloved parents Jasman Rajuli and Aminah Ibrahim, and my family, thank you for the endless prayers for my success, health, happiness and for being in spirit every step of the way despite being physically an ocean away. Your love, faith and confidence in me, kept me going all these years.

To my labmates in F411, Zaiton and Zeina, thank you for the friendship, for sharing the ups and downs we faced in this journey and not to forget the sleepless nights before the deadlines. Alhamdulillah, we completed it!

Life in Warwick was made enjoyable with many nice people I met. To MCS, Warwick PH and ISOC communities, my heartfelt gratitude to all of them for sharing many colourful moments in my life. I will definitely miss the beautiful gatherings we have especially during the blessed month of Ramadhan.

Last but not the least, to all my friends, thank you for the amazing and memorable experience in Warwick. Your support and friendship means more than I can ever express. Jazakumullahu khairan katheeran!

DECLARATION

This thesis is submitted in partial fulfilment for the degree of Doctor of Philosophy under the regulations set out by the Graduate School at the University of Warwick. All work reported in the thesis has been carried out by Faezah Jasman, except where stated otherwise, between the dates of March 2012 and September 2016. No part of this thesis has been previously submitted to the University of Warwick or any other academic institution for admission to a higher degree.

Faezah Jasman

September 2016

ABSTRACT

This thesis studies the modelling and characterisation of underwater optical wireless communication links, particularly short-range diffuse links, by using numerical Monte Carlo (MC) simulation. MC simulation provides a flexible, intuitive and accurate modelling of the underwater channel, which is severely affected by absorption and scattering processes. In diffuse Underwater Optical Wireless Communication (UOWC) links, scattering is expected to have a larger impact on communication link performance due to the wider beam divergence compared to collimated beams. Thus, this thesis will investigate the characterisation of path loss, spatial, temporal and angular dispersions of diffuse links in various types of water.

Firstly, a detailed investigation on the path loss performance of diffuse beam in three types of water is presented. This includes the study on the contribution of unscattered and scattered components of light to the total received power and how they are attenuated. From the percentage of unscattered light that contributed to the total power reception, the distance at which the unscattered component drops to zero can be estimated. This distance is used to predict the transition point from minimal scattering to multiple scattering regime for

diffuse beams in coastal and turbid water. In addition to this, the spatial dispersion effect is also studied at off-axis locations.

To further understand the behaviour of scattering in diffuse links, the scattering order probability is evaluated for various beam sizes in various types of water. Currently, this kind of information cannot be obtained either analytically or experimentally. The information on the scattering order is used as the parameter to classify the links into three scattering regimes, namely minimal, intermediate and multiple scattering regimes. Further investigations into the transition regimes are conducted by investigating the impulse response and frequency response performance for temporal dispersion effects. From the impulse response and frequency response analysis, the bandwidth that can be supported by the channel can be predicted, which provides some insight into the potential and limits of the links.

In addition to temporal dispersion, the angular dispersion performance is also evaluated. It is shown through the angle of arrival (AOA) distribution that diffuse beams exhibit significant angular dispersions, implying that a large receiver field of view (FOV) is needed for optimum power performance. The information on the AOA distribution is then used to study the impact of receiver FOV on the bandwidth. Finally, the effect of aperture on the power received and scattering order histogram is evaluated.

As a conclusion, the numerical results presented in this thesis will provide an improved understanding of the effect of scattering on path loss, spatial, temporal and angular dispersions along with their relationships with each other.

PUBLICATIONS ASSOCIATED WITH THIS RESEARCH WORK

The following papers have been published/ submitted as a result of the work contained within this thesis.

Journal/Magazine Papers

Laura. J. Johnson, Faezah Jasman, R. J. Green, M. S. Leeson, "Recent advances in underwater optical wireless communications," *Underwater Technology*, 32, 167-175, Nov 2014.

Conference Paper

Faezah Jasman and R. J. Green. "Monte Carlo simulation for underwater optical wireless communications." in *2nd International Workshop on Optical Wireless Communications (IWOW)*, Newcastle, UK, 2013.

Faezah Jasman and R. J. Green. "Power distribution performance and frequency response for underwater optical wireless communications." in *20th International Workshop on Computer-Aided Modeling Analysis and Design of Communication Links and Networks (CAMAD)*, Surrey, UK, September 2015.

CHAPTER 1

Introduction

1.1 *Overview*

Optical wireless communications (OWC) or free space optics (FSO) has become a very promising technology as a complementary technology to radio frequency (RF) technology in terrestrial communication. It has demonstrated several advantages, such as a huge unlicensed bandwidth, low power and high data rate [1]. In atmospheric channel, laser beams operating at wavelengths 850 nm and 1550 nm are used to establish line-of-sight (LOS) links for various ranges of distance (from 50 m to a few kilometres range) [2]. Apart from that, a unique method using deep ultraviolet (UV) wavelengths (200 nm-300 nm) has shown significant potential in establishing a non-line-of-sight (NLOS) communication channel in scenarios where LOS links are not possible [3].

Inspired by the attractive features and performance in those environments, OWC is now seen as a potential technology for underwater applications. This is due to the fact that the current underwater technology utilising acoustic waves

is fundamentally limited by its low bandwidth (\sim kHz), large delay and severe multipath fading despite its long range performance (ie; 1-10 km) [4].

Specifically in underwater applications, wavelengths in the blue/green region are used as they experience the lowest attenuation underwater. Despite the high bandwidth ($>$ GHz) that can be provided by optical links, they are limited to several hundred metres only due to strong attenuation caused by absorption and scattering [5]. Thus, UOWC is seen as a complementary technology rather than alternative to the existing technology in underwater wireless communications.

Generally in UOWC, either laser or light emitting diode (LED) sources are used as the transmitter depending on the application. Laser-based systems are preferred for power efficient and high data rate links. Recent work by Oubei et al. demonstrated that 4.8 Gbps can be achieved at a distance of 5.4 m using QAM-OFDM [6]. Despite the high data rates achieved by laser based links, they face considerable challenges to maintain accurate pointing and tracking since laser beams are highly collimated.

In order to relax this pointing requirement, a diffuse source such as LED is used. Additionally, LED-based systems are also favoured due to their low power consumption, low operating voltage, long lifetime and low cost [7]. To increase the power of LED based system, normally array configuration is used. The comparison of laser and LED is summarised in Table 1.1.

From the literature survey conducted in Chapter 2, it can be said that most UOWC systems are still at the research stage. However, there are a few commercial products that are available on the market. Penguin Automated System Inc. developed a tele-submarine built using 70 LEDs providing 120° field-of-view (FOV) and data rates up to 100 Mbps [8]. Another product called BlueComm, also based on LEDs, was developed by Sonardyne International is capable of transmitting a maximum of 20 Mbps over a range of 200 m [9]. Ambalux Corporation also uses an array of high power LEDs with highly sensitive receivers in the design of their product. The device is capable of transmitting at 40 Mbps over a 40 m range. They used an external power supply of 36 W[10].

Table 1.1: Laser and LED characteristics. Adapted from [11].

Characteristics	Solid-state Laser	Laser diode	LED
Optical spectral width	Narrow	0.1-50nm	25-1000nm
Modulation bandwidth	~kHz to ~GHz	~kHz to ~GHz	~kHz to ~MHz
Power	High power >1 W	Low power <1 W (unless arrayed)	Low power <1 W (unless arrayed)
Beam divergence	Narrow (<10°)	Narrow (<10°)	Broad (>15°)

1.1.1 Areas of applications

The unseen underwater world is an important source to all living organisms. Thus, communication underwater is believed to be an essential medium for ocean explorations and observations. One main example of applications is in the underwater wireless sensor network (UWSN). UWSN consists of a large number of static and mobile sensor nodes. These nodes communicate and collaborate with each other to perform a specific task, such as sensing, measuring, transmitting and collecting data. The mobile nodes can also be used to locate and hover above the static nodes for data muling and to perform network maintenance functions, such as deployment, relocation, and recovery [12]. Figure 1.1 illustrates this concept.

Other than that, remotely-operated vehicles (ROVs) and autonomous underwater vehicles (AUV) are used in various fields in subsea operations, such as in real-time data transfer, surveillance, maintenance and inspection of underwater equipment. Listed below are some areas where UOWC can be applied.

- Ocean biology \Rightarrow Observing and monitoring underwater biological changes, such as the effect of human generated pollutants and global warming on marine biology.
- Environmental monitoring and sensing \Rightarrow Monitoring and collecting data (water, temperature, pH, turbidity, pressure, etc.).

- Ship hull and equipment monitoring \Rightarrow Maintenance and repair work.
- Military \Rightarrow Coordinating missions, controlling assets and transferring data.
- Disaster prevention \Rightarrow Measuring seismic activity, providing tsunami warnings and investigating seaquakes.
- Underwater mining \Rightarrow Teleoperation and determining positions accurately.

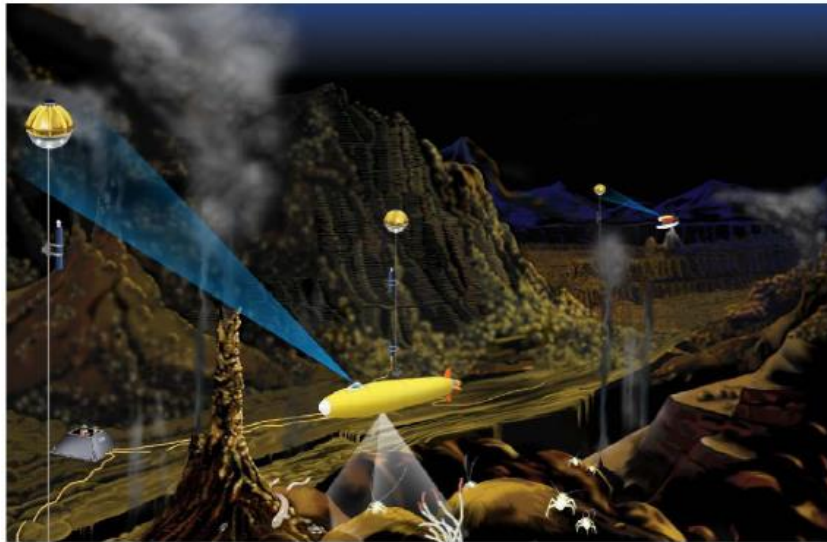


Figure 1.1: Illustrations of underwater vehicles' communication with sensor nodes.
Picture taken from [13] .

1.2 *Motivations and aims*

Motivated by the tremendous benefits that UOWC can offer, researchers in academia and industry have contributed significantly in exploring the underwater domain. Various aspects of work have focused on understanding

and developing UOWC systems, which will be detailed in Chapter 2. Despite the fact that diffuse sources such as LEDs have low efficiency compared to laser based transmitter, they are widely used in building the prototype for UOWC since they require less pointing and tracking accuracy. Furthermore, this kind of transmitter is suitable for broadcast-type links where a zone of communication can be established. In such scenarios, high bandwidth communication is achieved as long as the receiver is located within the coverage area defined by the illumination area of the light beam.

Even though a considerable amount of experimental work on diffuse systems has been reported, little has been done in characterising diffuse links comprehensively. While there are several works on channel modelling and characterisation for both collimated and diffuse links, a more detailed understanding of how diffuse links are different to collimated links is needed. For example, a method to predict the transition between minimal scattering region and multiple scattering region for collimated beam has been presented in [14] but little has been discussed regarding diffuse links. This transition region is used to predict the bandwidth performance which is useful for system designers in optimising the link. Thus, the study on parameterising the transition regime for diffuse links is expected to fill this gap. Apart from that, little is known about the angular dispersion of diffuse links in various types of water as most of the studies use small angle approximation (SAA) to model the behaviour of light underwater. Due to the wide beam divergence of diffuse beams, the angular dispersions are expected to be more significant.

Information about angular dispersions is believed to be useful for the receiver FOV design.

Thus, comprehensive and accurate channel modelling and characterisation for diffuse beams are needed to maximise their potential. As such, the primary aim of this thesis is to investigate the performance of the diffuse link in various types of water with the main emphasis being on the characterisation of path loss performance, and spatial, temporal and angular dispersion. Additionally, a method to classify the diffuse links into three scattering regimes is explored and investigated. This will serve as a general guide for system designer in predicting the power and bandwidth performance.

1.3 Contributions

As a result of this research, the following contributions have been made

1. Development of a simulation model for diffuse LOS communications links where analysis of on-axis and off-axis scenarios can be evaluated. The additional ability of the simulation model is that it is built with the purpose of investigating a zone of communication area at the receiver plane. Additionally, a different source distribution is introduced to the model to simulate diffuse beams, namely Lambertian distributions apart from Gaussian distributions.

2. An individual analysis of the path loss performance of unscattered light and scattered light is presented for diffuse beams, showing different behaviour in the attenuation rate. This results in the prediction of the distance at which the unscattered light drops to zero, as the transition point for minimal scattering regimes and multiple scattering regimes.
3. A more accurate path loss performance using MC simulation for coastal and turbid water compared to the link budget equation, which underestimates the path loss performance due to the inability to incorporate the scattering effects.
4. The analysis of scattering order probability for various beam divergences is presented and used in the characterisation of the scattering regime. As a result, the classification of the scattering regime for diffuse links is parameterised based on the link distance. From the scattering regime parameterisation, a better way of understanding link behaviour is understood. This classification will help the link designer to identify the potential and limitations of different operating schemes in order to optimise performance.
5. The evaluation and analysis of impulse response, frequency response and scattering order probability are presented showing the correlation between them. The 3 dB bandwidth supported by the underwater

channel for various link locations is calculated to establish the performance limit of such systems.

6. For the first time, the AOA for diffuse links at a wide range of distance and types of water is presented. This information will be beneficial to system designers in optimising the receiver FOV design. Several observations at off-axis locations are highlighted to show how AOA distribution is used to optimised the bandwidth performance.

1.4 Outline of the thesis

The rest of the thesis is structured as outlined below.

Chapter 2 presents an overview of the UOWC, including a discussion on the different technologies that can be used to communicate wirelessly underwater. Then, some related works and contributions by other researchers are highlighted. The subsequent section presents an introduction to the physics of light in underwater environments, which includes a discussion on absorption and scattering as the two main cause of light attenuation. In addition to that, the radiative transfer equation (RTE), which is the main equation that governs the behaviour of light underwater, is introduced, highlighting its complexity in solving it analytically. Then, the widely used channel model, Beer Lambert's law, is presented along with its limitations.

Chapter 3 focuses on the numerical modelling technique that is used in this thesis: MC (MC) simulation. Firstly, the theory and the principles of the MC method are discussed, highlighting its advantages and disadvantages compared to the experimental method and analytical method. The details of the sampling method and mathematical equations used in modelling the UOWC channel are described. A preliminary simulation is conducted to simulate different techniques used to model diffuse beams.

Chapter 4 presents a detailed analysis of path loss performance and characterisation. The path loss performances for three beams divergences sizes are presented. By simulating the path loss performance for various ranges in three types of water and comparing the performance with reference to the attenuation length, a better picture of the attenuation performance can be obtained. A detailed investigation of how unscattered light and scattered light attenuate when using a diffuse beam is also explored. This leads to the identification of the transition point between the minimally scattered region and multiply scattered region for diffuse links.

Chapter 5 investigates the effect of scattering on the temporal and angular dispersions by first exploring the scattering order probability for various beam divergences. The scattering order is used as a parameter to classify the diffuse links into three regimes. From this classification, the temporal and angular dispersions effect are evaluated. Further investigation is done on studying the

impact of reducing receiver FOV on the bandwidth and scattering order histograms.

Chapter 6 investigates the impact of receiver aperture sizes on the the scattering order histogram to evaluate the validity of using it as the parameter in classifying the scattering regime. Then, the impact of receiver aperture and FOV on the power received are also studied. Finally the chapter ends with the discussion of the performance trade-off in optimising the bandwidth performance by incorporating the effect of receiver FOV and aperture as a whole.

Finally, Chapter 7 summarises the main contributions of this thesis and highlights several extensions for future work.

CHAPTER 2

Background Research and Related Work

2.1 *Introduction*

Underwater wireless communication has attracted significant interest due to its wide-ranging applications in marine research, offshore industry, oceanography and the military. Currently, most underwater communications are based on acoustic waves and cabled systems. However, both acoustics and cabled technology have several limitations in terms of performance and maintenance. As an alternative, optical and radio waves can also be used to communicate underwater. This chapter will provide a background on UOWC. A brief introduction to acoustic and radio underwater communication is presented to highlight its advantages and disadvantages. Then, recent research developments are presented. A background on the theory of light properties underwater is also discussed in detail as this is the foundation principle of the modelling and simulation work.

2.1.1 Acoustic communication

Acoustic technology is a mature and robust technology currently used in underwater communication. Apart from being used in communication systems, acoustic technology is also used in imaging, positioning and navigation. The main advantage of acoustic technology is that it can send data at long range over several tens of kilometres with minimum attenuation. However, it suffers from multipath propagation due to reflections from the sea floor and surface and refractions resulting from varying sound speed, especially in shallow water [15]. Another disadvantage is that it is also prone to large Doppler shift resulting from relative motion between the transmitter and receiver. It also has a large propagation delay (hundreds of symbols) due to the slow speed of sound and the attenuation is higher for higher frequencies. As shown in Table 2.1, the highest bandwidth that can be provided by acoustic technology is several hundred Khz which is obviously not sufficient for video transmissions. Further discussion on the challenges of acoustic communication can be found in [16,17].

Table 2.1: The bandwidth supported for different ranges in typical acoustic communication system [18].

Range	Range (km)	Bandwidth (kHz)
Very long	1000	<1
Long	10-100	~2-5
Medium	1-10	~10
Short	0.1-1	~10-100
Very short	<0.1	>100

2.1.2 Radio frequency communication

Radio frequency (RF) waves are defined as waves with a frequency of less than 300 GHz. The propagation of RF waves in water is different from RF waves in air because of the high water electrical conductivity at high frequency. Thus, most of the commercial radio equipment in the MHz and GHz range cannot be used in an underwater environment due to this high attenuation. For example, the attenuation for 2.4 GHz radio waves in seawater is around 1685 dB/m when the average conductivity of seawater is 4 S/m [19]. Lloret has done some experimental measurements by using 2.4 GHz in the unlicensed ISM (industrial, scientific and medicine) band in an underwater environment where they managed to cover a distance of 16-17 cm at frequency 2.4 GHz using BPSK and QPSK modulations [20].

In [15], the optimum frequency range (3-100 MHz) was identified for light transmission from air into water for depths less than 5 m. Due to this, it is only suitable for very short range applications, such as control and telemetry, for example in the oil and gas industries, and oceanographic research. Table 2.2 depicts the data rates achievable with respect to the communication range. Further details on RF communication underwater can be found in [21].

Table 2.2: Data rates and ranges of underwater RF communications. Table adapted from [21].

Range	Seawater	Freshwater	Applications
< 10 m	>8 kbps	> 3 Mbps	AUV docking, diver's personal network
50 m	300 bps	150 kbps	Networks, diver conversation
200 m	25 bps	9 kbps	AUV Control, networking
> 1 km	<1 bps	<350 bps	Deep water telemetry

2.1.3 Optical communication

A special characteristic of visible light underwater is that it can travel through water with significantly lower attenuation than the rest of the electromagnetic (EM) spectrum. Figure 2.1 depicts the absorption coefficient of the EM wave from 100 nm-1 mm. As can be seen, most of the EM wave is highly absorbed by water except a small window in the visible light range. The lowest attenuation of pure seawater occurs at wavelength in the 430 nm range [22]. The red wavelengths can penetrate to approximately 15 m in the ocean while blue can penetrate only a few hundred metres in the clearest waters and much less as turbidity increases. Thus, optical waves are suitable for short range applications (<200 m) and will be a complementary technology to the acoustic technology rather than competitive. Table 2.3 provides the comparison for the main parameters for the three types of technology while Table 2.4 summarises their advantages and disadvantages.

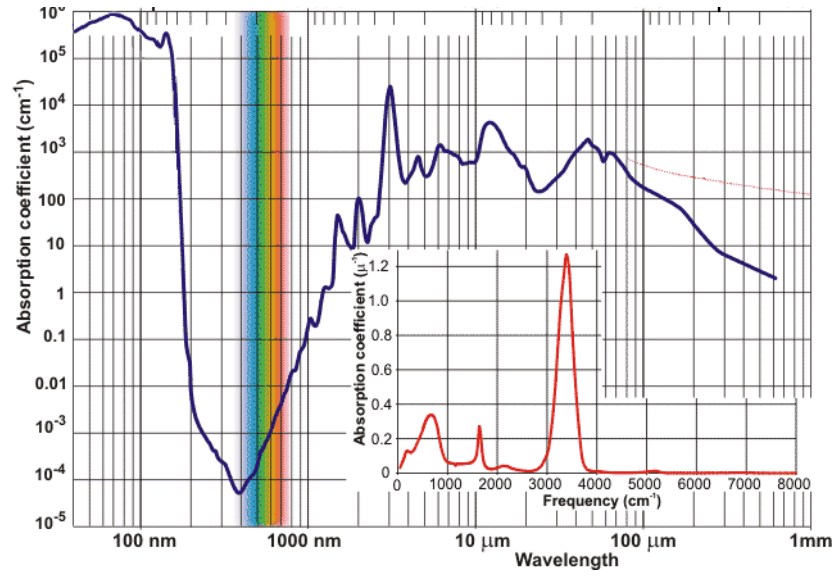


Figure 2.1: Absorption coefficient for wavelength from 100nm-1 mm [23].

Table 2.3: Properties of optical, acoustic and RF technology.

Carrier/Features	Acoustic	Radio	Optical wireless
Bandwidth	~KHz	~100Hz	~ GHz
Speed	1.5×10^3 m/s	2.24×10^8 m/s	2.24×10^8 m/s
Attenuation	Depends on frequency	High	Depends on turbidity
Range	20 km	10m	<200 m
Antenna /receiver size	0.1m	0.5m	0.1m
Power consumption	High	Low	High for laser Low for LED
Latency	High	Low	Low
Multipath	High	Low	Low

Table 2.4: Comparisons of different communication carriers underwater [21] .

Technology	Advantage	Disadvantage
Acoustic	<ul style="list-style-type: none"> • Mature technology • Range up to 20 km • Energy efficient 	<ul style="list-style-type: none"> • Limited bandwidth • High propagation delay • Impact on marine life • Multipath and fading • Poor performance in shallow water • Temporary losses of connectivity due to shadowing • High cost • Prone to failures due to corrosion
RF	<ul style="list-style-type: none"> • Immune to acoustic noise • No multipath effect • Unaffected by turbidity 	<ul style="list-style-type: none"> • Limited range through water • Antenna size is very large • Require high power • Susceptible to electromagnetic interferences
Optical	<ul style="list-style-type: none"> • Ultra-high bandwidth • Low system cost • Very secured • System size is very small and power efficient 	<ul style="list-style-type: none"> • Range is short • Need precise alignment • Susceptible to water turbidity • Susceptible to background illumination

2.2 *Related research*

Historically, research on using lasers for undersea communications started as early as the 1970s and 1980s pioneered by Karp for submarine to satellite communication using laser in the blue/green range [24, 25]. Since then, there has been extensive work done to explore optical wireless communication

underwater. This is especially motivated by the advancement of semiconductor laser and LED technology in developing high power, high bandwidth sources and high sensitivity receivers. Recently, a group of researchers reported blue and green GaN-based LED with modulation bandwidths of 225 and 463 MHz respectively [26]. Generally, research interest in UOWC can be classified into three major areas; namely channel modelling and characterisation, system design and development and modulation and networking study. The next section will present the works in the first two areas.

2.2.1 Work on channel modelling and characterisation

The modelling and characterisation of UOWC is the main step towards understanding the behaviour of the channel in order to implement the UOWC system successfully. There has been a significant amount of work conducted over the years in this area, experimentally, analytically or numerically (simulation). In terms of experimental work in characterising the underwater channel, the pioneering work has been conducted by a team in Naval Undersea Warfare Centre, USA [27, 28]. From the laboratory test conducted, the feasibility of the system operating in MHz range was demonstrated. At Naval Air Systems Command (NAVAIR), Cochenour and his team have been doing extensive experiments since 2006. Initially, they conducted an experiment based on a 3.66 m water tank for measuring temporal dispersion. From the preliminary results obtained from the experiment, they managed to prove that multiple scattering are not significant when the data rate is 1 Mbps. However

they highlighted that their observations were limited to a short distance of 3.66 m and the pointing inaccuracies were only 5° [29]. Next in [18, 30] they investigated the spatial distribution and temporal dispersion and measured the beam spread function (BSF). They proposed a theoretical model for BSF which is accurate to 12 attenuation length (AL). In 2013, further effort was taken in conducting an experiment to characterise the temporal dispersion using a high dynamic range and high sensitivity equipment. The work was then expanded to study the effect of transmitter and receiver misalignment, receiver FOV and scattering particles on temporal dispersion.

Apart from experimental work, there is also a considerable amount of work reported in modelling the UOWC using the MC method. This technique of modelling the underwater channel is preferred as it is simpler when the difficulties and high cost experimental setup can be avoided [31, 32]. This also solves the limited propagation distance issues and limited freedom in varying system parameters [33].

An early work pioneered by Jarutanawadilok used vector RTE that includes the polarisation effect in modelling the UOWC channel. In his work, MC simulation was used to quantify the effect of scattering by investigating the bit-error-rate (BER) performance [34]. Hanson and Radic also used MC simulation to measure the temporal dispersion in UOWC links apart from their experimental work [35]. They concluded that for moderate ranges a data rate of more than 1 Gbps can be achieved. In [36], the impulse response of the underwater channel

was investigated by using semi-analytic MC to improve the efficiency of the MC simulation. His simulation results were compared with the experimental data obtained in [37] where reasonable agreement was achieved.

In [38] the path loss and frequency response of UOWC were studied in various types of water. The effect of receiver aperture and receiver FOV are investigated. They demonstrated that the FOV significantly affects the path loss and bandwidth. It was concluded that for a collimated beam several GHz bandwidth can be achieved for on-axis locations. Similarly, in [39], MC method was used to investigate the performance of diffuse channel. In their model, they incorporated several system variables such as transmitter (Tx) and receiver (Rx) characteristics. They studied the delay spread of the channel and concluded that it was negligible except in turbid water. In addition to that, the path loss performance and the bandwidth performance of reflective NLOS links were also investigated in [40, 41].

A closed form double Gamma function to model the impulse response for coastal and turbid water was proposed by Tang et al. in [42]. He used MC simulation to compare the results and observed agreement between them. A further step was taken in [43, 44] in which a weighted Gamma function was proposed to model the impulse response of the UOWC multiple-in-multiple-out (MIMO) links.

In addition to the simulation works, few mathematical models have been developed in understanding UOWC. Doniec et al. proposed a signal strength model where he considered the source effects in the equation [45]. However, it is limited to clear water only. A mathematical formulation of MC model was proposed by Dalglish et al. to calculate the impulse response over a wide range of operational and environmental scenarios. They also proposed a stochastic process detector noise model that shows good agreement with the experimental validation [31, 32 and 44] .

Contrary to most of the work done to model the channel horizontally, a vertical link is considered by Johnson et al. in channel modelling where a mathematical model to calculate the variations of the attenuation coefficient due to the water depth is proposed [47]. Recently, a stochastic model was proposed in [48] that can be used to study the spatial and temporal distributions of photons. This model includes ballistic photons, single scattering and multiple scattering in their derivations where it can be treated as a generic model for UOWC. Table 2.5 summarises the work done in channel modelling and characterisation highlighting their contribution.

Table 2.5: Summary of works on channel modeling and characterisation.

Year	Author	Method	Links	Contributions (Parameter studied)
2008	Hanson [35]	MC Experiment	Collimated LOS	Impulse Response Path Loss
2008	Jarutanawadilok [34]	Vector RTE	Collimated LOS	Path Loss BER
2012	Cox [38]	MC	Collimated LOS	Path Loss Frequency Response
2012	Cochenour [14]	Experimental	Collimated LOS Diffuse NLOS	Frequency Response Beam spread Function
2013	Gabriel [39]	MC	Diffuse NLOS	Path Loss Impulse response
2013	Li [36]	Semi analytic MC	Collimated LOS	Impulse response
2013	Doniec [45]	Experimental Analytical	Diffuse NLOS	Signal Strength
2013	Tang [40]	MC	Diffuse NLOS	Impulse response
2013	Johnson [47]	Analytical Numerical Experimental	Collimated	Path Loss (vertical)
2014	Dagleish [31]	Analytical MC Experimental	Collimated	Impulse response
2014	Dong [44]	MC	Diffuse MIMO	Impulse response
2015	Zhang [48]	Statistical	General model	Path loss AOA

2.2.2 Work on system and hardware design

Apart from the research work dedicated to understanding the channel described previously, there are also several experimental works that have been conducted in developing UOWC systems with the aim of understanding the channel or designing a system prototype for specific applications. Normally, the experiments are conducted in laboratory water tanks due to the difficulty of performing experiments in the ocean [49].

The first experimental work on laser-based systems was reported in [28]. In their work, green wavelength (514-532 nm) was used to achieve a data rate of 100 MHz with a 45 m range. In [35], Hanson and Radic successfully established 1 Gbps error free transmissions at 2 m path using a 532 nm laser diode. Recently, a team of researchers from the University of Yamanashi successfully transmitted a 1.45 Gbps intensity modulation/direct detection – orthogonal frequency division multiplexing (IM/DD-OFDM) signals over a 4.8 m range [50]. A higher data rate of up to 4.8 Gbps has been demonstrated by Oubei et al. by using quadrature amplitude modulation – orthogonal frequency division multiplexing (QAM-OFDM) signals for a slightly longer range of 5.4 m [6, 51].

Generally, there are several large research groups that have contributed to the development of UOWC experimentally. The next section will briefly highlight their published works with Table 2.2 summarising some of the work done by these groups. At Woods Hole Oceanographic Institution (WHOI), several works

have been published since 2004. By using easily available technology, Schill et al. developed an optical communication transceiver using an Infrared Data Association (IrDA) physical layer for communication between a swarm of robots [19]. The infrared LED was substituted with high power green or blue LED to suit underwater applications. In 2006, Farr et al presented the design of an optical modem based on an omnidirectional source and receiver. The omnidirectional source consisted of 6 LEDs in a hemispherical orientation with FET used in the driver circuits while the receiver used PMT [13].

At the University of Genoa, Italy, a series of research on UOWC was conducted by Anguita and team. In [7] a prototype of underwater OWC systems was developed by adapting the current technology available for Underwater Wireless Sensor Network (UWSN). Transmission at a range of 1.8 m was achieved at 100 kbps . Further work was taken by this group in implementing the UOWC by building an omnidirectional transmitter using LED and designing the hardware architecture using Hardware Description Language (HDL). The system was tested for point-to-point communication but will be further developed to pave the way for omnidirectional transmitters [52]. Apart from that, they also proposed a simulation model as a theoretical model for the underwater system. The simulation model focused on two aspects, namely the light distribution and propagation in water and the communication characteristics [53].

At Massachusetts Institute of Technology (MIT), a prototype of a modem called AquaOptical has been developed for three different ranges, namely short range, long range and hybrid. From the evaluation of the modems, a maximum data rate of 1.2 Mbps is achieved in clear water [54]. Further work was carried out by Doniec et al on the design and implementation of an underwater data muling system. An underwater robot and a high bandwidth optical underwater system, which is integrated with existing acoustic communications systems, was demonstrated [55]. In [49], an integrated system of optical wireless and acoustic systems was built to perform several functions for underwater navigation and focuses on sensing, data collection and data retrieval. They have successfully demonstrated the implementation of their design. They also developed the first prototype for an underwater sensor network which has been successfully tested [12].

At North Carolina University, several researchers have conducted experiments in developing an underwater system based on LED and laser and investigated the performance of underwater links under different water conditions. Initial work was conducted by Chancey in building an UOWC system using a 1 W LED as the transmitter and a PD as the detector [56]. In [57], a system using a combination of laser and PMT as the transmitter and receiver that can achieve 1 Mbps using NRZ format was developed. A similar data rate was achieved by Simpson in , by using LED as the transmitter and PD as the receiver, which is smaller and cheaper than the previous systems [58]. Later, Simpson developed compact smart transmitters and receivers for underwater optical wireless

communications where a smart receiver was designed to have a segmented large FOV and has the ability to estimate the angle of arrival [59].

To summarise the work presented by all the researchers, Table 2.6 highlights the achievements in terms of range and data rate that are obtained from their work. From the table, it is evident that bandwidths higher than several MHz can be achieved in most of the systems designed. Several GHz is also possible by using a laser source with a shorter distance.

Table 2.6: Summary of experimental works in UOWC syatems. It indicates the maximum data rate achieved, distance, source, modulation and turbidity level.

Year	Name	Data Rate	Distance	Source/Receiver	Signal Type/ Modulation	Turbidity / types of water
1992	Snow [28]	50 Mbps	9 m	Laser/ APD & PMT	Pseudo random signal	$c = 0.6 \text{ m}^{-1}$ e-folding = 2.7 m
1995	Bales [60]	10 Mbps	20m	LED/APD	Unknown	Clear water Unknown coefficient
2000	Tivey [61]	14.4 kbps	5m	LED/PIN PD	IrDA	75% transmission
2004	Schill [19]	57.6 kbps	1.71 m	LED/PD	IrDA	Clear water Unknown coefficient
2005	Chancey [56]	10 Mbps	12 m	LED/PD	Square wave	Clear water Unknown coefficient
2006	Farr [13]	5Mbps	91 m	LED/PMT	Square wave	$c = 0.027$ e-folding = 36 m
2008	Hanson [35]	1 Gbps	2m	Laser/APD	Externally modulated Laser	e-folding = 8.3 m
2008	Pontbriand [62]	5 Mbps	200m	unknown	Digitized waveform	e-folding = 40m
2008	Cox [57]	1 Mbps	3.66 m	Laser/PMT	NRZ	Clear water Unknown coefficient
2008	Simpson [63]	5Mbps	7.7 m	LED/PMT & PD	Square wave	Clear water Unknown coefficient

2009	Brundage [64]	3 Mbps	13 m	LED/PD	TTL	Fresh water
2009	Anguita [7]	100 Kbps	1.8 m	LED/APD	DPIM	Clear water Unknown coefficient
2010	Doniec [65]	2.28 Mbps	50 m	LED/ APD	DPIM	Clear water e-folding =36
2011	Baiden [66]	40 Mbps	10 m	LED	Unknown	Clear water Unknown coefficient
2013	Cossu [67]	58 Mbps	2.5 m	LED/APD	DMT	Clear water Unknown coefficient
2015	Nakamura [50]	1.45 Gbps	4.8 m	405 nm laser/APD	IM/DD-OFDM	Clear water Unknown coefficient
2015	Oubei [51]	4.8 Gbps	5.4 m	450 nm laser diode	QAM OFDM	Clear water Unknown coefficient

*e-folding = the distance over which light intensity decreases by $1/e \sim 0.37$ [68].

2.3 *Light properties in water*

The underwater world can be seen as a complex and dynamic environment which consists of water molecules, impurities such as suspended particles, dissolved particles, organic and inorganic matter [69]. All these underwater particles interacts with light and can be described using the optical properties of seawater. This optical properties varies according to location, time of day, and organic and inorganic content, as well as temporal variations can be divided into two classes: inherent and apparent [22].

2.3.1 Inherent optical properties

The inherent optical properties (IOPs) of water are properties that depend only on the material properties of the medium itself and are independent of the ambient light field within the medium [70]. For example, IOPs are dependent upon the dissolved and suspended material in the water and the electromagnetic properties of the medium and independent of how a sample is illuminated. The main IOP includes attenuation coefficient $c(\lambda)$, absorption coefficient, $a(\lambda)$, scattering coefficient $b(\lambda)$, single scattering albedo ω_0 , index of refraction n , and volume scattering function (VSF).

Figure 2.2 shows a diagram to illustrate the method used in defining the IOPs. It consists of a small volume ΔV of water of thickness Δr where a collimated

beam with radiant power $\Phi_i(\lambda)$ is directed at it. Some of the power is absorbed $\Phi_a(\lambda)$, some is scattered $\Phi_s(\lambda)$ at an angle ψ and the remaining power is transmitted through the medium $\Phi_t(\lambda)$.

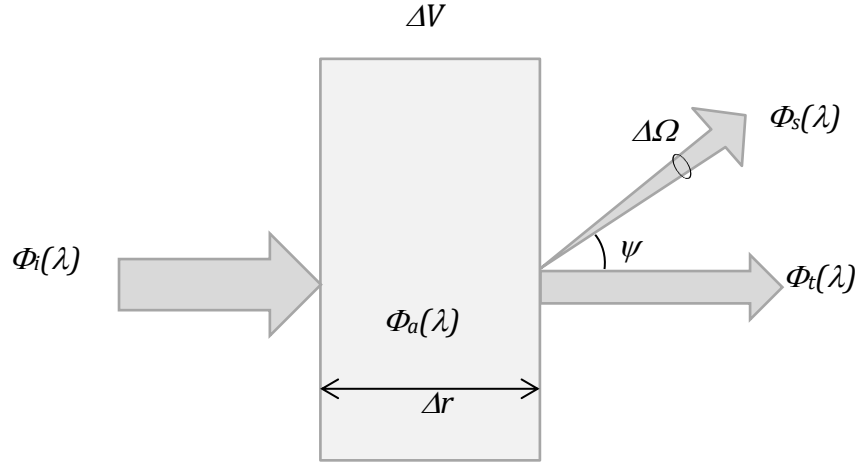


Figure 2.2: Geometry used to define inherent optical properties [22].

The spectral absorptance is defined as the ratio of the power that is absorbed to the total power incident .

$$A(\lambda) = \frac{\Phi_a(\lambda)}{\Phi_i(\lambda)} \quad (2.1)$$

Similarly the spectral scatterance $B(\lambda)$ is the ratio of the scattered power to the incident power.

$$B(\lambda) = \frac{\Phi_s(\lambda)}{\Phi_i(\lambda)} \quad (2.2)$$

The spectral absorption coefficient $a(\lambda)$ can be defined as

$$a(\lambda) = \lim_{\Delta r \rightarrow 0} \frac{A(\lambda)}{\Delta r} \quad (m^{-1}) \quad (2.3)$$

and the spectral scattering coefficient $b(\lambda)$, is

$$b(\lambda) = \lim_{\Delta r \rightarrow 0} \frac{B(\lambda)}{\Delta r} \quad (m^{-1}) \quad (2.4)$$

The spectral beam attenuation coefficient $c(\lambda)$, is defined as

$$c(\lambda) = a(\lambda) + b(\lambda) \quad (2.5)$$

The angular scatterance per unit distance and unit solid angle, $\beta(\psi, \lambda)$ is defined as

$$\beta(\psi, \lambda) = \lim_{\Delta r \rightarrow 0} \lim_{\Delta \Omega \rightarrow 0} \frac{B(\psi, \lambda)}{\Delta r \Delta \Omega} = \lim_{\Delta r \rightarrow 0} \lim_{\Delta \Omega \rightarrow 0} \frac{\Phi_s(\psi, \lambda)}{\Phi_i(\lambda) \Delta r \Delta \Omega} \quad (m^{-1} sr^{-1}) \quad (2.6)$$

Where $B(\psi, \lambda)$ is defined as the fraction of power that is scattered out of the beam through an angle ψ into a solid angle $\Delta \Omega$ centered on ψ as illustrated in Figure 2.1. Φ_s is the spectral power scattered into the given solid angle $\Delta \Omega$ and is defined as $\Phi_s(\psi, \lambda) = I_s(\psi, \lambda) \Delta \Omega$. The incident irradiance is defined as $E_i(\lambda) = \Phi_i(\lambda) / \Delta A$. Substituting $\Delta V = \Delta r \Delta A$, which is the volume of the water, gives

$$\beta(\psi, \lambda) = \lim_{\Delta V \rightarrow 0} \frac{I_s(\psi, \lambda)}{E_i(\lambda) \Delta V} \quad (2.7)$$

This equation is called the volume scattering function (VSF) and can be interpreted as the scattered intensity per unit incident irradiance per unit volume of water.

The total scattered power per unit incidence irradiance and unit volume of water can be obtained by integrating $\beta(\psi, \lambda)$ over all directions. This parameter is called the scattering coefficient.

$$b(\lambda) = \int \beta(\psi, \lambda) d\Omega = 2\pi \int_0^\pi \beta(\psi, \lambda) \sin \psi d\psi \quad (2.8)$$

The forward (b_f) and backward (b_b) scattering coefficients can be defined as

$$b_f(\lambda) = 2\pi \int_0^{\pi/2} \beta(\psi, \lambda) \sin \psi d\psi \quad (2.9)$$

$$b_b(\lambda) = 2\pi \int_{\pi/2}^\pi \beta(\psi, \lambda) \sin \psi d\psi \quad (2.10)$$

The scattering phase function $\tilde{\beta}(\psi, \lambda)$, is found by normalizing the VSF with the scattering coefficient.

$$\tilde{\beta}(\psi, \lambda) = \frac{\beta(\psi, \lambda)}{b(\lambda)} (sr^{-1}) \quad (2.11)$$

The scattering phase function can be physically understood as the probability that the photon will be scattered in the angular direction ψ .

2.3.2 Apparent optical properties

The apparent optical properties (AOPs) are properties that depend on both the geometrical structure of the light field and the inherent optical properties of the medium [22]. AOPs also depend on the distribution of light used to measure them. Examples include the system attenuation coefficient k_{sys} , radiometric quantities such as irradiance reflectance, radiance reflectance, and attenuation coefficients for upwelling and downwelling irradiance. AOPs are of particular importance when considering the penetration of radiant energy to depths in ocean waters.

2.4 Absorption

Absorption is an irreversible process during which the photon energy is lost due to interaction with water molecules and particulates. The absorption process is highly dependent on the concentration and composition of the particles in the water and the absorption coefficient $a(\lambda)$ can be expressed as the combination of the absorption coefficient of various components given as [22].

$$a(\lambda) = a_w(\lambda) + a_{chl}(\lambda) + a_{CDOM}(\lambda) + a_{det}(\lambda) \quad (2.12)$$

Where $a_w(\lambda)$ is the absorption coefficient of pure water, $a_{chl}(\lambda)$ is the absorption coefficient of chlorophyll, $a_{CDOM}(\lambda)$ is the absorption coefficient of colour dissolved organic material (CDOM) and $a_{det}(\lambda)$ is the absorption coefficient due to detritus. Previously, Figure 2.1 shows the absorption coefficient in water for 100 nm to 1 mm.

2.4.1 Absorption by pure seawater

Absorption by pure seawater can be considered as the sum of absorption of optically pure water and absorption by the salts present in seawater. Water molecules heavily absorb red spectrum and infrared (IR) by ionisation, electronic excitation, or vibrational or rotational excitation of water molecules [56]. Figure 2.3 shows the absorption coefficient of pure water where it can be seen that pure water has the lowest absorption coefficient in the region between 400 nm and 500 nm.

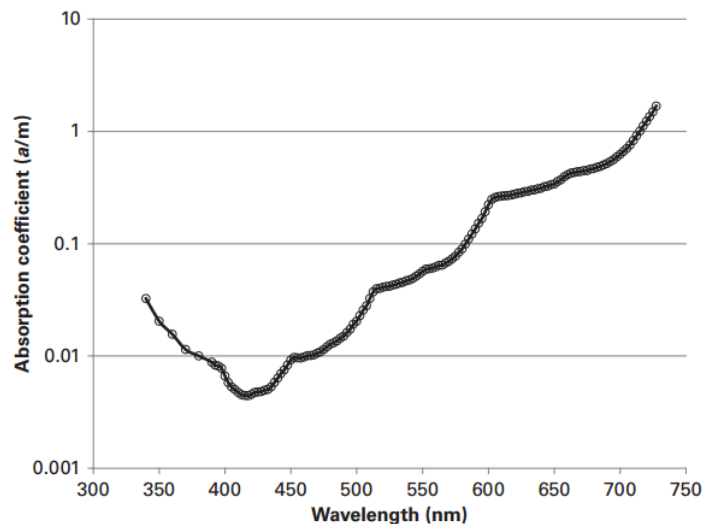


Figure 2.3: Absorption coefficient of pure water for 340-700 nm. Picture taken from [11].

2.4.2 Absorption by chlorophyll from phytoplankton

Chlorophyll in phytoplankton absorbs a lot of visible light, especially the blue and red wavelengths ($\lambda=430$ nm and 665 nm) with very little absorption in the green, as illustrated in Figure 2.4 [22]. The concentration of chlorophyll depends on the concentration of phytoplankton, which varies with geographic locations, water type and water depth.

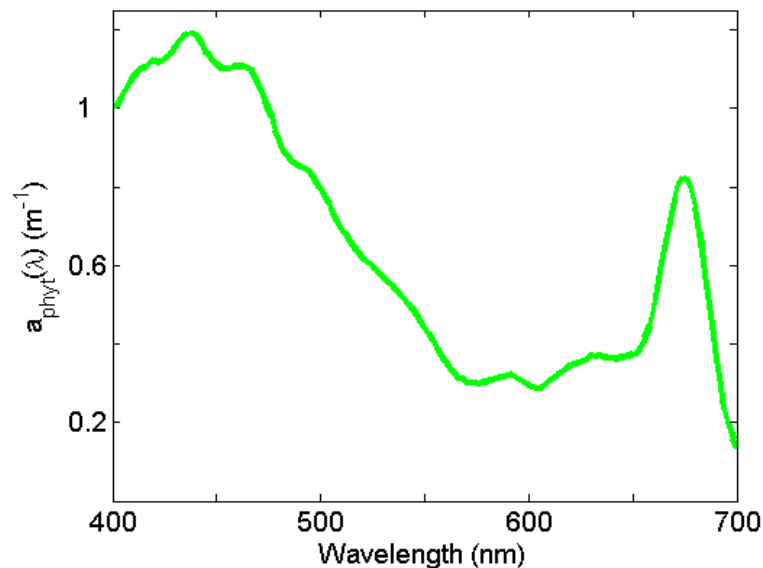


Figure 2.4: Absorption coefficient due to phytoplankton. Picture taken from [71].

2.4.3 Absorption by coloured dissolved organic matter (CDOM)

CDOM is also known as gelbstoff and is composed of decaying organic marine matter and primarily contains humic and fulvic acid. There are quite high concentrations in coastal water and low concentrations in oceanic water. It mainly absorbs the blue wavelength and its absorption decreases exponentially with wavelength, as illustrated in Figure 2.5. A model to describe

this phenomena for wavelength range 350 nm < λ < 700 nm is given by the equation

$$a_{CDOM} = a_{CDOM}(\lambda_o) \exp[-0.014(\lambda - \lambda_o)] \quad (2.13)$$

Where $a_{CDOM}(\lambda)$ is the absorption due to CDOM at reference wavelength often chosen to be 440 nm [22].

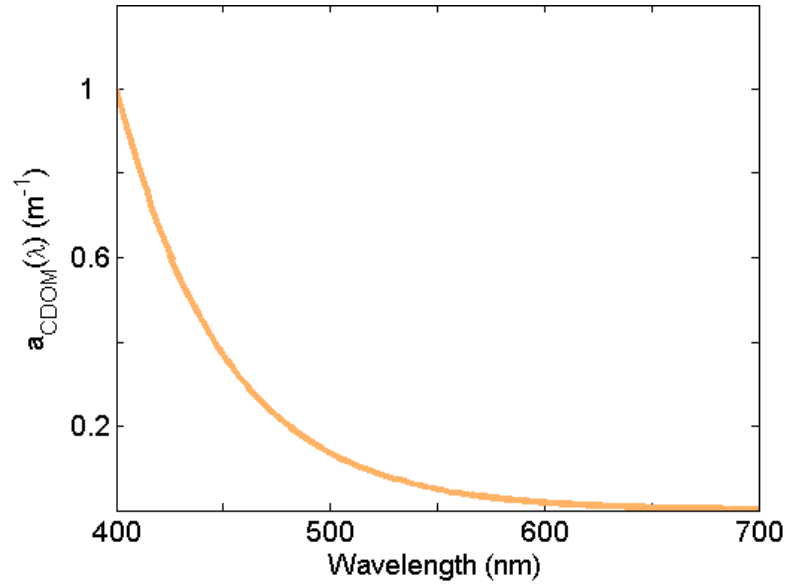


Figure 2.5: Absorption coefficient due to CDOM. Picture taken from [71].

2.4.4 Absorption by organic detritus

Detritus is organic waste produced by dead plants and animals and has a peak absorption in the blue region of the visible spectrum. Similar to absorption by CDOM, the model to describe absorption by detritus is given as

$$a_{\text{det}} = a_{\text{det}}(\lambda_o) \exp[-0.011(\lambda - \lambda_o)] \quad (2.14)$$

Where $a_{\text{det}}(\lambda)$ is the absorption due to detritus at reference wavelength, λ_o in this case is chosen to be 400 nm [22].

In general, the total absorption coefficient is high in the blue wavelength due to absorption by phytoplankton pigments and high in the red wavelength because of absorption by the water.

2.5 Scattering

Scattering happens when a photon's path is deviated due to interaction with particulate matter in water. There is no change in energy but there is a change in the direction of propagation. Scattering in ocean water is peaked in the forward direction and can also have significant back scattering. Mobley divides the scattering in natural waters into three categories; molecular scattering, scattering by large particles and turbulent scattering [22].

The scattering coefficient $b(\lambda)$ is defined as the fraction of energy dispersed from a light beam per unit of distance travelled in a scattering medium. The scattering coefficient of seawater $b(\lambda)$ is calculated as the sum of the scattering coefficient due to pure water, small particles and large particles.

$$b(\lambda) = b_w(\lambda) + C_s b_s(\lambda) + C_l b_l(\lambda) \quad (2.15)$$

Where $b_w(\lambda)$ is the scattering coefficient of pure water , $b_s(\lambda)$ is the scattering coefficient of small particles , $b_l(\lambda)$ is the scattering coefficient of large particles, C_s and C_l are the total concentrations of small and large particles.

2.5.1 Molecular scattering in pure seawater

Scattering in pure seawater is caused by the random nature of the molecular motion, such as due to varying local concentrations of sea salts in pure seawater. Figure 2.6 shows the scattering coefficient of pure water and pure seawater. The slightly larger value in scattering coefficient of pure seawater is due to the scattering of light with salt ions. From Figure 2.6, it can be concluded that scattering in pure seawater has insignificant effect to the total attenuation [11].

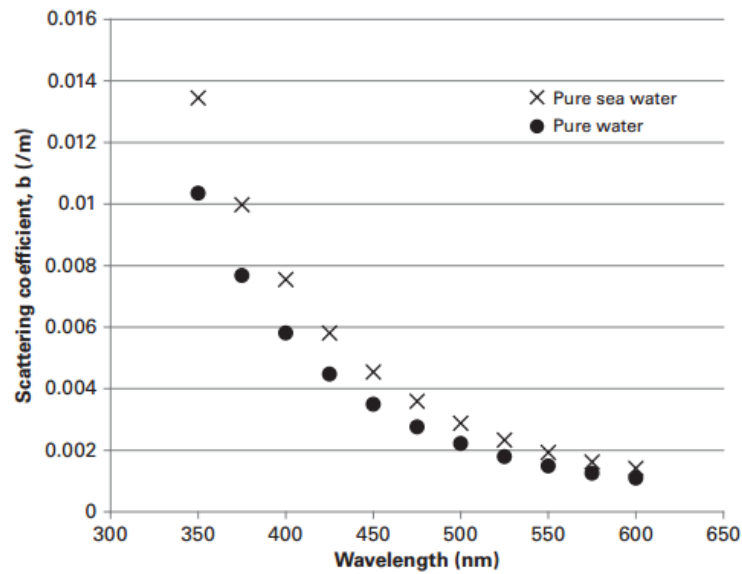


Figure 2.6: The scattering coefficient for pure water and pure seawater. Picture taken from [11].

2.5.2 Scattering by large particles ($> \lambda$)

Generally, the scattering in seawater is dominated by the scattering caused by organic and inorganic particles. These particles are typically 10 times larger than the wavelength of the light [22].

2.5.3 Turbulence scattering

Turbulence scattering is caused by the random change in refractive index, n of seawater which depends on temperature, salinity, pressure and wavelength [72]. This causes the the light beam to fluctuates temporally and spatially; a condition which is usually known as scintillations [73].

Unlike the effect of turbulence in atmospheric environment which has been studied extensively, the investigation on the effect of turbulence on the optical beams in underwater environment is still at its infancy. In [74] it is found that the refractive index in seawater does not fluctuate much especially in very short range (~ 10 m) links; thus turbulence can be neglected in such links. However, for longer ranges, the effect of turbulence has shown to be significant as reported in [74, 75]. A more detailed study on turbulence in underwater environment can be found in [76-78].

2.5.4 Single scattering albedo, ω_o

It is defined as the ratio of the scattering coefficient to the attenuation coefficient as

$$\omega_o = \frac{b(\lambda)}{c(\lambda)} \quad (2.16)$$

In water where scattering dominates, the value of albedo, ω_o will be near one and when absorption dominates, the value will be near 0. It can also be understood as the probability of the photon to be scattered rather than absorbed.

2.5.5 The effect of scattering on underwater communication

The impact of scattering on UOWC links can be explained by three mechanisms namely spatial, temporal and angular dispersions [80].

- Spatial dispersion is caused by the spreading of the beam due to the multiple scattering process. This causes the photon density to decrease at the receiver position. For a diffuse beam, photons that arrive at the receiver are spatially dispersed due to its initial distribution and also due to the underwater environment [30, 80].

- Temporal dispersion is caused when the light beam reaches the receiver at different times. Due to this, there will be a path difference and time delay which can limit the bandwidth [30, 80 and 81].
- Angular dispersion is the spread of the angle of arrival of the photons due to scattering underwater. In seawater, scattering normally occurs at small forward angles which results in small angular dispersion as will be shown in the next section. However, in turbid water where scattering dominates, angular dispersion will show significant effects [83].

2.6 *Volume scattering function*

As presented in section 2.3.1, VSF is an important parameter that determines scattering in seawater. Several researchers have conducted measurements of VSF. The next section describes the VSF measured by Petzold and two analytical equations to model VSF.

2.6.1 Petzold scattering function

Petzold phase function is the most cited and frequently used in modelling scattering underwater. In [70], it is regarded as a representation of typical ocean water. It is based on measurements conducted in the early 1970s for three types of water; namely turbid water, coastal water and clear water [84]. The turbid water measurement was conducted at San Diego Harbour, California, the coastal water measurement was obtained from the coastal water

in San Pedro Channel, California and the clear water from the Tongue of the Ocean, Bahamas Islands. Figure 2.7 depicts the VSFs for the three types of water along with the VSFs for pure sea water and Maalox antacid which is used as the scattering agent in laboratory experiment. It can be seen clearly that the VSFs are peaked in the forward direction indicating that most of the light will scatter at small forward angles.

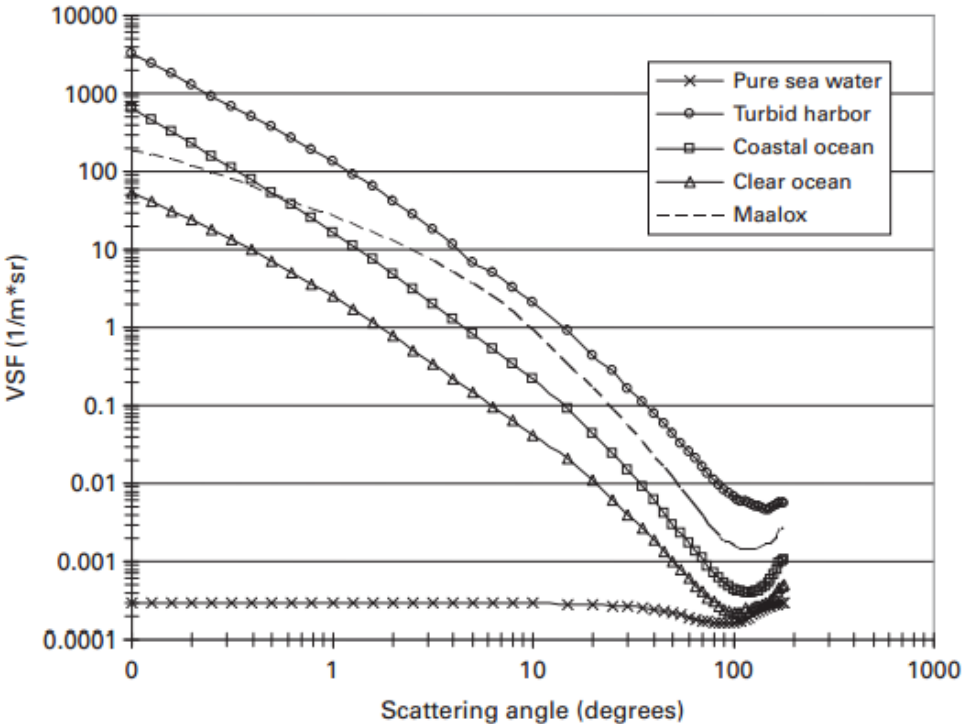


Figure 2.7: The VSFs of various types of water measured by Petzold. Picture taken from [11].

2.6.2 Analytical phase functions

Several analytical phase functions have also been proposed with two of them are discussed in the next section.

- **Henyeey-Greenstein (HG) function**

Historically, this function was proposed in 1941 to be used in describing the scattering angles caused by interstellar dust clouds in astrophysics [85]. Due to its simplicity, it is also used widely in approximating angular scattering in biological tissues [86]. Some researchers also use it in underwater environments but highlighted the fact that it is not accurate at small angles less than 20° and large angles larger than 130° [39, 86].

The HG phase function is given by the equation

$$p_{HG}(\psi, g) = \frac{1}{4\pi} \frac{1 - g^2}{(1 + g^2 - 2g \cos \psi)^{3/2}} \quad (2.17)$$

Where ψ is the scattering angle, g is the HG assymetry parameter that depends on the characteristics of the medium and is equal to the average cosine of the scattering angle ψ over all scattering directions. The value of g can be understood as the amount of light that is scattered in the forward direction [88]. If $g=0$, it indicates scattering is isotropic and if $g=1$, it indicates very forward scattering [89]. The effect of different g is illustrated in Figure 2.8.

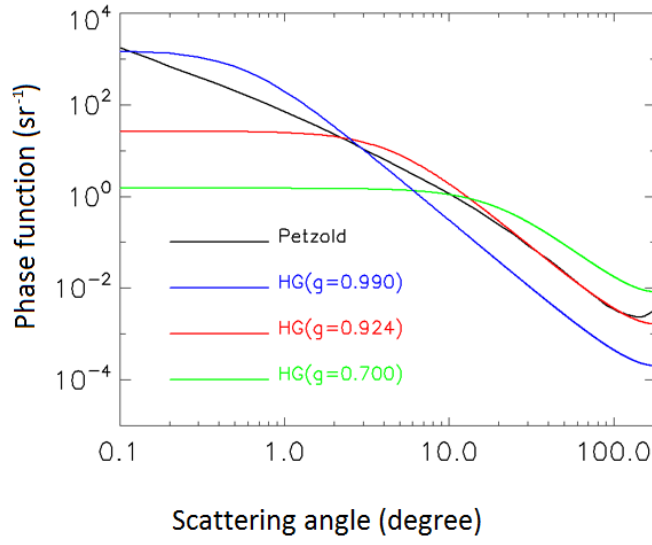


Figure 2.8: Comparison of Petzold phase function with HG phase function for various g values. Picture taken from [71].

- **Two-Term Henyey-Greenstein (TTHG) phase function**

This phase function is modified from the original HG function by Haltrin [90]. It is more accurate than the original HG model but it is not as accurate as the phase function that is measured by experiment which is conducted by Petzold. The TTHG function is given by

$$p_{TTHG}(\psi, \alpha, g_{FWD}, g_{BKWD}) = \alpha p_{HG}(\psi, g_{FWD}) + (1 - \alpha) p_{HG}(\psi, -g_{BKWD}) \quad (2.18)$$

Where α is the weight of the forward-directed HG phase function, g_{FWD} and g_{BKWD} are the asymmetry factors for the forward and backward-directed HG phase function respectively.

2.7 Attenuation length

The product of attenuation coefficient, c and transmission distance, z is called attenuation length (AL) and it is a unitless term . Note that AL is the argument of the exponential component in BL law . At 1 AL the received power would be decreased by a factor of $1/e$, or 63%. Several publications use this term in order to compare different system performance especially at various water turbidities and transmission distance [91] .

2.8 Channel model

2.8.1 Radiative Transfer Equation (RTE)

Radiative Transfer equation is used to describe the energy conservation of light that is propagating through inhomogeneous media. In this theory, radiance is treated as a ray of light where the wave properties of light are not considered . In general RTE relates the IOPs to the radiance distribution and is given in equation 2.19 [11].

$$\left[\frac{1}{v} \frac{\partial}{\partial t} + \mathbf{n} \cdot \nabla \right] I(t, \mathbf{r}, \mathbf{n}) = -c I(t, \mathbf{r}, \mathbf{n}) + \int_{4\pi} \beta(\mathbf{r}, \mathbf{n}, \mathbf{n}') I(t, \mathbf{r}, \mathbf{n}') d\mathbf{n}' + E(t, \mathbf{r}, \mathbf{n}) \quad (2.19)$$

Where v is the speed of light, c is the beam attenuation coefficient , t is time, \mathbf{n} is the direction vector, \mathbf{r} is the position vector, and ∇ is the divergence operator with respect to position \mathbf{r} , I is the radiance, β is the VSF and E is the

source radiance. In general the left hand side (l.h.s) of the equation describes the change of intensity over a differential length. The first term on the right-hand side (r.h.s) describes the losses due to absorption and scattering over a path. The second term on the (r.h.s) is the gain due to the contribution of any scattered intensity from other directions [92].

Technically, the RTE is linear integrodifferential equation because it involves both an integral and derivative of the unknown radiance. Besides that, the nonlinear scattering phase function adds the complexity in solving this equation. Due to this fact, it is quite difficult to solve the equation analytically without making several approximations and simplification [93].

Several researchers use various methods in solving the RTE such as using small angle approximation (SSA) or even neglecting scattering totally. However the assumption made will limit its applicability to a certain simple condition [94]. Due to this, numerical techniques such as MC simulation is a preferred choice in solving RTE for realistic situations. Compared to solving the RTE analytically, less simplifying approximations are required using MC simulations. The details of the MC method used to solve RTE is discussed in Chapter 3.

2.8.2 Beers-Lambert (BL) law

Most of the works on underwater wireless optical communication (UOWC) use a simple model for beam propagation where the effect of scattering and temporal dispersion are ignored. In this simple model light is attenuated by water where its intensity decreases due to absorption and scattering caused by water molecules and dissolved particles. The power received can be calculated by using Beer-Lambert (BL) law as [11]

$$P = P_o \exp(-c(\lambda)z) \quad (2.20)$$

where P_o is transmitted power, z is the path length and $c(\lambda)$ is the beam attenuation coefficient.

The beam attenuation coefficient, $c(\lambda)$ is the ratio of energy absorbed or scattered from an incident power per unit distance as described in section 2.3 . It is the measure of the light loss from the combined effects of scattering and absorption in an attenuating medium. The beam attenuation coefficient $c(\lambda)$ is calculated as the sum of the absorption coefficient $a(\lambda)$ and scattering coefficient $b(\lambda)$ as shown in equation (2.5).

2.8.3 Limitations of BL law

1. It only considers the effect of absorption and single scattering. It assumes that photons that undergo scattering are lost and not counted in the received energy. In other words, multiple scattering is ignored [80, 90].
2. It is only valid for collimated LOS links when the transmitter and receiver are perfectly aligned so it cannot be used for misalignment conditions or any other geometry [30].

2.9 Water types

There are several standards on how to classify water. In this thesis, the water types used are the ones reported by Petzold in [84]. Table 2.7 shows the various water types with its coefficients.

Table 2.7: Various water types with the coefficients. Table is reproduced from [22] .

Water type	$a(\text{m}^{-1})$	$b(\text{m}^{-1})$	$c(\text{m}^{-1})$	<i>Albedo</i>
Pure sea water	0.0405	0.0025	0.043	0.058
Clear ocean	0.114	0.037	0.151	0.25
Coastal ocean	0.179	0.219	0.398	0.55
Turbid harbour	0.366	1.824	2.190	0.83

2.10 System configurations

Generally UOWC links can be classified as line-of-sight (LOS) or non-line-of-sight (NLOS) which are based on the existence of a direct path between the transmitter and the receiver. In addition to that, the transmitter and receiver can be arranged in several other topologies depending on the requirement of the systems. The next section will describe these configurations.

2.10.1 Line-of-sight (LOS) links

For UOWC links the point-to-point collimated LOS link is the most energy efficient because the power is concentrated in a narrow beam as shown in Figure 2.9(a). Due to the nature of the source, laser is normally used in LOS links where a very high bandwidth can be achieved. However the flexibility of the LOS system is restricted because accurate alignment of the transmitter and receiver are required which complicate the implementation. In clear water accurate pointing and tracking is very crucial for LOS links as misalignment can cause a huge loss in the communication link [95]. However, the LOS links in turbid water are less prone to misalignment as the multiple scattering in turbid water will cause the collimated beam to be broadened and communication links can still be established. Recently several experimental works have demonstrated bit rates in the Gbps range using laser beams [50, 51]. However, the range is limited to less than 10 m due to the limitation in the experimental setup.

2.10.2 Non-line-of-sight (NLOS) links

NLOS links can be achieved by intentionally diverging the transmit beam or by using arrays of high divergence sources like LED as depicted in Figure 2.9(b). The advantage of the NLOS system is in the increase of link robustness because the need for aiming and tracking mechanisms is reduced. Several works on using omnidirectional transmitters and receivers have been produced. The longest distance of 200 m at 5 Mbps was reported by Pontbriand in very clear water ($c=0.025$) and in turbid water ($c=1.25$) they managed to transmit at 1Mbps at 30 m [62]. A spherical transmitter built using 100s of LEDs with 120° FOV was developed by Baiden which is able to transmit video data at 1.5 Mbps at 15 m in a turbid lake. However the exact turbidity level is not reported [96]. A comparison between diffuse NLOS and collimated LOS link were investigated experimentally in [5]. It is demonstrated that a diffuse NLOS link requires more than 30 dB of optical power than collimated LOS links to achieve a similar signal level at the receiver. An interesting finding was observed when the transmitted power is the same for both collimated and diffused channel for AL greater than 15. In [97], the power distribution and frequency response of both types of links are discussed.

2.10.3 Retro-reflector links

Retroreflector links are suitable for small devices or sensors where power is limited. In modulating retroreflective links, the interrogating system provides

the optical source and associated pointing hardware. It will target small devices such as a small passive optical retro-reflector which will modulate the reflected light back to the receiver. The geometry of this link is shown in Figure 2.9(c). This type of link is prone to the unwanted backscattered light that will increase the noise level at the receiver [98]. In [99] a polarisation discrimination technique is used to solve the interference problem in retro-reflecting geometry. In [100] a performance analysis of different link types was conducted and they observed that the modulating retroreflector is the most affected by the turbidity of the water .

2.10.4 Reflective NLOS links

A unique method of NLOS communication has been proposed by Arnon in [101] for situations where there are an obstacle blocking the path between the transmitter and the receiver. The geometry of this link is shown in Figure 2.9(d). They found out that the number of photons received in a reflective NLOS links is too low compared to LOS links for a depth of 20 m. However, a reasonable BER of 10^{-4} can be obtained for NLOS links when the node is separated by 40 m. In [40], the path loss of reflective NLOS links is investigated by considering the effects of a random sea surface in clear water and coastal water. It is found that the path loss performance degraded severely as the speed of the wind increased. In clean ocean, the path loss in reflective NLOS links is approximately -40 dB and dramatically reduced to -70 dB when considering wind blown surface waves of 3 m/s. In [41], the 3 dB channel

bandwidth is estimated to be at approximately 20 MHz in clear water for 20 m communication range.

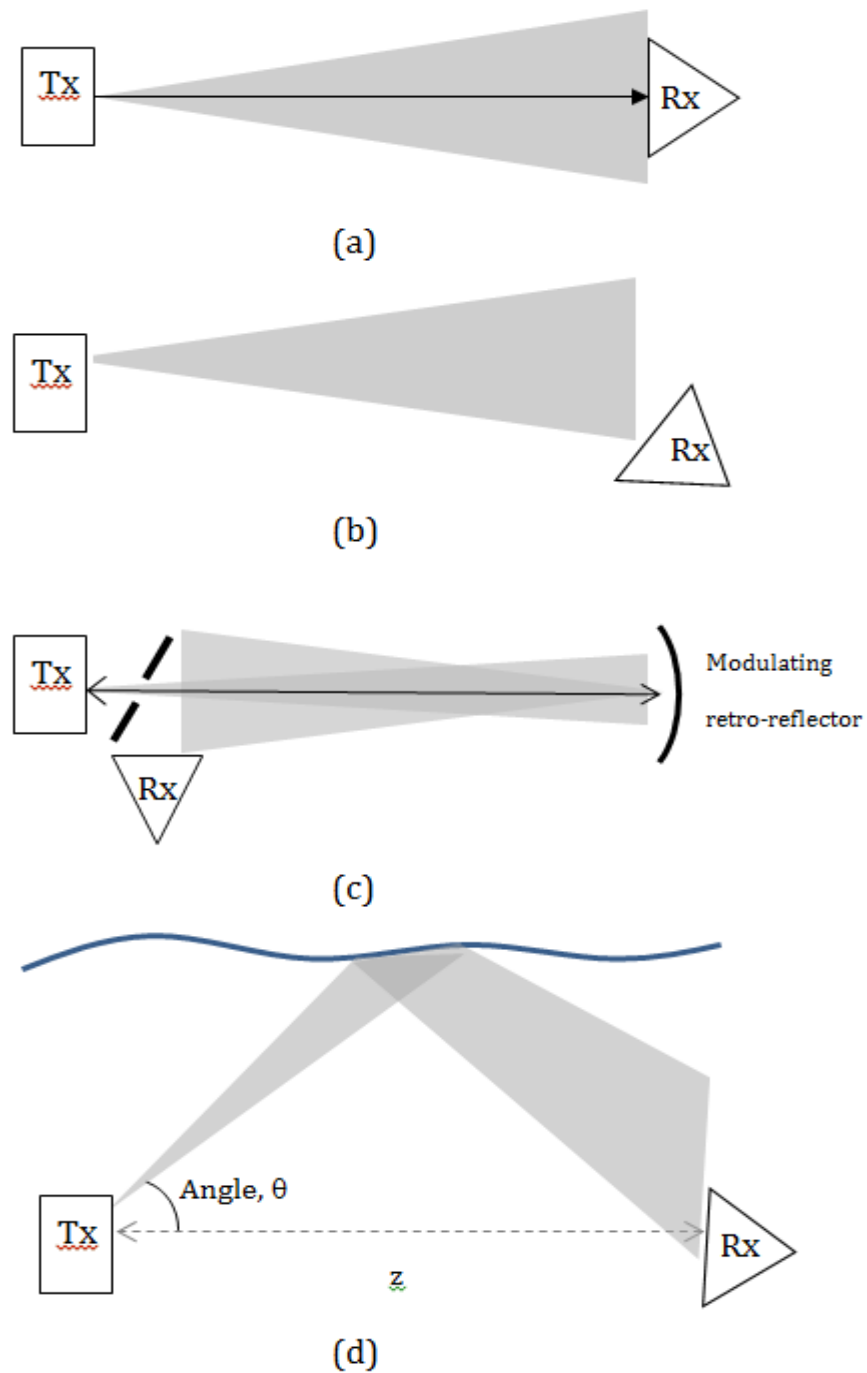


Figure 2.9: Types of link configuration.

2.11 Conclusion

This chapter started with a brief introduction on various technologies that can be used in UWC, highlighting their advantages and disadvantages. Then, a literature review of the research in UOWC was presented with emphasis on the latest advancements and achievements. The background theory and principles of light propagation underwater was discussed in detail as this will be the underlying concept for the channel modelling and characterisation. The existing channel model for UOWC was presented and its applicability and limitations were highlighted. The different system configurations that can be implemented in UOWC were also presented.

CHAPTER 3

Modelling of the Underwater Optical Wireless Communications Channels

This chapter discusses MC method in modelling light transport in underwater environment. Firstly an introduction to the concept, advantages and applications of MC method are highlighted. Then the principles, theories and mechanics of the MC simulation are presented along with the mathematical equation and probability theory that are used in modelling the underwater channel. Then, the simulation parameters and simulation geometries used in this thesis is presented.

3.1 Overview of Monte Carlo numerical simulation

Historically MC method was first reported in 1949 by a group of researchers from Los Amos laboratories [102]. Interestingly there is no exact definition of MC simulation that is well established [89]. In general, this technique uses statistical modelling where random sampling and probability theory are used to estimate mathematical equations. In other words, MC simulation uses the

known probability of an individual event to predict the probability of the entire event. Since then, it has been widely used in solving various problems in mathematics, physics, engineering, biological science, finance, economics and computer graphics.

In the field of OWC, MC methods are used extensively in solving RTE. Most of the MC simulations in communication are adapted from the MC simulation in biomedical applications. Several researchers use MC simulation in modelling outdoor channels in various types of environments [103], in indoor infrared (IR) communication channels [104] and also in ultra-violet (UV) NLOS communications [105]. In UOWC, MC method is used to simulate the interactions of photons with the sea water and the random sea surface to determine the exact photon trajectories and distribution. The first use of MC method in UOWC was presented by Hanson et.al [35].

In general MC simulation is known for its simplicity and versatility in implementation using a computer either in two dimensions (2D) or three dimensions (3D) scenario. This is especially beneficial in simulating scattering underwater which is a complex process. It also does not require complex mathematical knowledge. Most importantly, it is the best choice when experimental method is too expensive, time consuming and difficult to handle [31]. Moreover, the parameters can be varied easily according to real configurations. Specifically in UOWC, it can be used to estimate the temporal effect and impulse response which is difficult to measure. The time delay for

short ranges is normally less than 1 ns and the sensitivity of PMT is slightly larger than 1 ns [33]. Compared to analytical method which is more complex in solving RTE, MC is a preferred choice as it is the most intuitive to understand. In the field of light transport in turbid media, MC method is considered the gold standard model which has the capability to provide exact solutions to the RTE [106].

Despite the advantages described above, MC simulation also has some drawbacks. Firstly, it is a very rigorous technique where a large number of samples must be generated as the accuracy is proportional to $1/\sqrt{N}$ where N is the number of samples [88]. Since it has to trace millions individual photons for a better accuracy, it is quite slow and computationally inefficient. Moreover, the probability that the generated photons will reach the receiver is quite low causing a lot of photons that are being traced did not reach the receiver [107]. It is also not suitable for very small detector area as very few photons will reach the receiver. In terms of solving RTE, it does not provide the physical meaning relating to the RTE and there are no output equations from the simulations. In some cases, MC is not suitable where the wave nature (i.e. coherence or interference) of light is investigated [33].

3.2 *Assumptions in simulations*

Several assumptions have been made in implementing MC simulations.

- Monochromatic light source - the light is assumed to be single wavelength.
- Random scattering events - a pseudo random number generator generates random numbers which in turn generate random and independent scattering events.
- Homogeneous medium - the scattering and absorption are uniform throughout the medium that results a constant attenuation coefficient.
- Uniform index of refraction - the effect of turbulence that is caused by different index of refraction is ignored.

3.3 *Monte Carlo algorithm*

In MC simulation, light is modelled as the propagation of large group of virtual photons or photon packets. However for simplicity, the term photons instead of photon packets is used in this thesis. Each photon will be identified by its position, weight and direction. Once the photon is emitted, the photon will repeatedly move until it is lost or reach the receiver. This process will be repeated until sufficient photons are received at the receiver. The history of each photon will be recorded to be used in calculating the received power, impulse response and other parameters. It is interesting to note that this MC

simulation is not a simulation of real physical particles, as it is just a mathematical way to solve RTE [106]. Figure 3.1 shows the flowchart of the MC algorithm whose details are summarized in the following section [108].

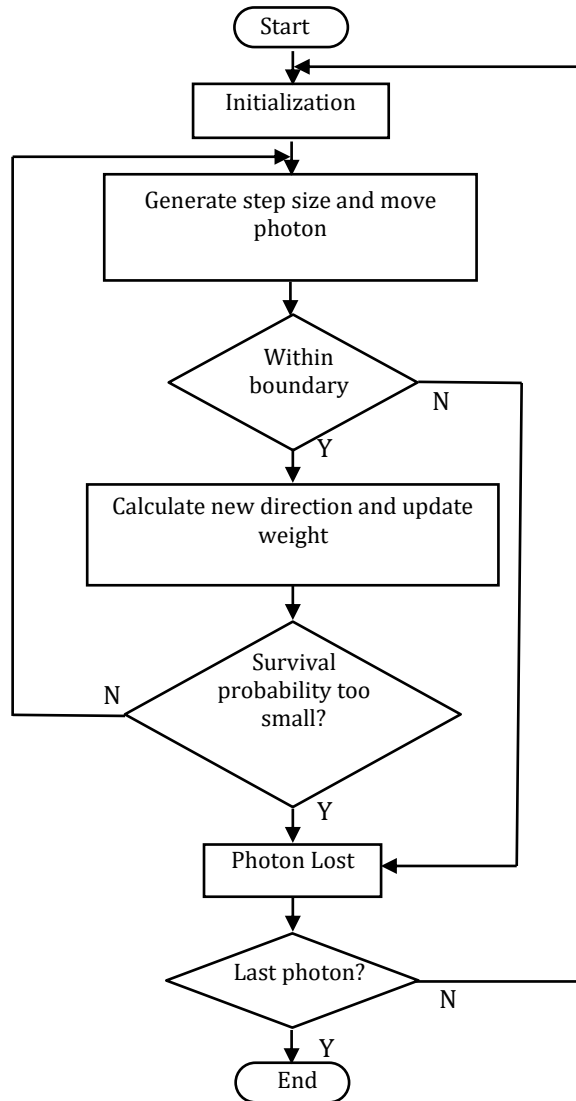


Figure 3.1: Flowchart of the MC simulation algorithm

Firstly the simulation starts by initializing all the parameters to the required value. Then the photon is launched according to the source distribution profile where the photon emission angle is generated by using probability distribution

function (pdf) of the radiation pattern of the source. The initial position of the photon is defined by its coordinate, x , y and z and the direction vector μ_x , μ_y and μ_z . Then it will move by a step size, s where it may be absorbed or scattered. The distance the photon travel between successive events, s is determined based on the attenuation coefficient of the water. If the photon travelled outside the boundary, it is considered lost. When the photon interacts with other particle, some of the energy is absorbed and some is scattered into different direction. This is determined by the albedo ω of the water that can be viewed as the probability of the photon being scattered. The new direction of the photon after scattering can be calculated using the scattering phase function. If the photon reaches the receiver, its location, weight and total distance travelled are recorded. The process is repeated until all the photons have been launched.

3.3.1 Coordinate system

In this simulation, Cartesian coordinate (xyz) system is used. The transmitter and receiver are located at the xy plane, and the direction of propagation is in the z -axis. At the same time, spherical coordinate system is also used especially in modelling the source polar angles and scattering angles θ and ϕ . For each photon propagation, the position and direction of the photon will be first defined locally and then transformed to the global coordinate system. Figure 3.2 shows the trajectory of the photon propagation path in underwater environment. Any representation of direction must be made with respect to

this coordinate system where it is referred as absolute coordinate system or global coordinate system.

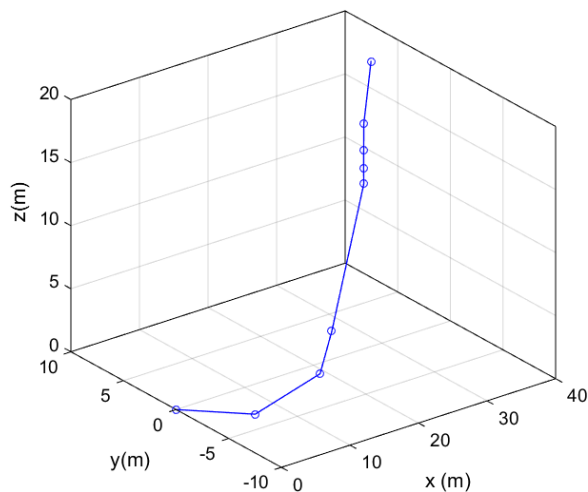


Figure 3.2: Illustrations of a photon propagation path in an underwater environment.

3.3.2 Spherical coordinate system

A moving spherical coordinate system is also used since it is easy to describe the scattering directions of photons in terms of polar and azimuthal angle. The z-axis is dynamically aligned with the direction of photon propagation.

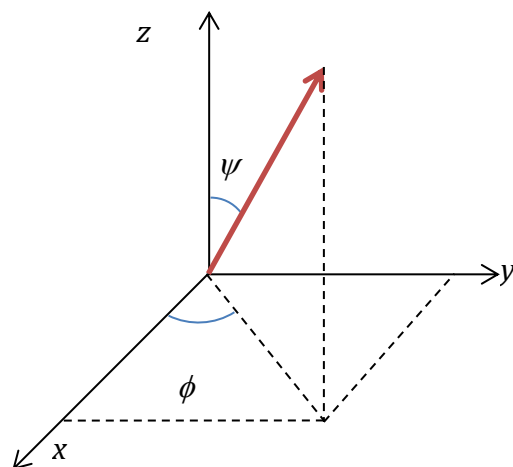


Figure 3.3: Spherical coordinate system.

3.3.3 Initial photon position

A photon is represented by its x , y and z coordinates and also the directions cosines. Figure 3.4 shows the photon direction vector which is projected onto the x , y and z axis. The direction cosines are specified as

$$\mu_x = \cos \theta_x \quad (3.1)$$

$$\mu_y = \cos \theta_y \quad (3.2)$$

$$\mu_z = \cos \theta_z \quad (3.3)$$

Where θ_x , θ_y and θ_z are the angles between the direction vector and the x , y and z axis respectively. The direction cosines must satisfy

$$\mu_x^2 + \mu_y^2 + \mu_z^2 = 1 \quad (3.4)$$

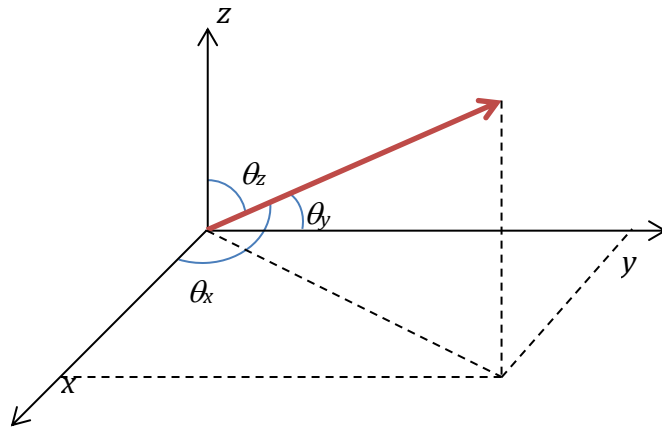


Figure 3.4: Photon direction vector shown in Cartesian coordinate system.

3.4 Source modelling

Modelling different types of sources involves modelling the polar angle and azimuthal angle of the source. Both angles are independent of each other and can be modelled separately. The azimuthal angle can be easily found as it is uniformly distributed on $[0, 2\pi]$ whereas the polar angle must be generated according to the pdf that follows specific distribution. In this thesis, Gaussian and Lambertian source distributions are used as the source emission pattern. The sampling rules for different beam profiles will be presented in the following sections.

3.4.1 Gaussian source

The intensity of Gaussian beam at the origin as a function of r is given as [109].

$$I(r) = I_o \exp\left(-\frac{r^2}{b^2}\right) \quad (3.5)$$

Where I_o is Gaussian beam optical intensity at the beam center, b is the waist radius (1/e radius) of the Gaussian beam and r is the radial distance from the beam centre. By normalizing the intensity profile,

$$\bar{I}(r) = \frac{1}{\pi b} \exp\left(-\frac{r^2}{b^2}\right) \quad (3.6)$$

The pdf describing the Gaussian beam profile as a function of r is given in equation 3.7

$$p(r) = \frac{\exp(\frac{-r^2}{b^2})}{b^2} 2r \quad (3.7)$$

The cumulative density function (cdf), $P(r)$ is obtained by integrating $p(r)$ as follows

$$P(r) = \int_0^r p(r)dr = 1 - e^{-r^2/b^2} \quad (3.8)$$

In order to find the radial distance, r of the beam, the cdf is evaluated to R where R is a random number that is uniformly distributed on the interval $[0,1]$

$$P(r) = R \quad (3.9)$$

Rearranging the equation to solve for r as a function of R yields

$$r = b\sqrt{-\ln(1-R)} \quad (3.10)$$

Since the laser beam is modelled to have a very narrow divergence, a diverging lens is used to diverge the beam [38]. Thus the focal length f_1 of the lens that is used to diverge the light is calculated based on the equation

$$f_1 = -\frac{b}{\phi_{div}} \quad (3.11)$$

Where b is the beam waist radius, and ϕ_{div} is the divergence half angle.

The polar angle of the generated photon can be defined as

$$\theta_0 = -\frac{r}{f_1} \quad (3.12)$$

The azimuth ϕ_0 is randomly chosen based on the uniform distribution $[0, 2\pi]$

The starting point of the photon is

$$x_0 = r_0 \cos \phi_0 \quad (3.13)$$

$$y_0 = r_0 \sin \phi_0 \quad (3.14)$$

The starting direction cosines

$$\mu_{x0} = \sin \theta_0 \cos \phi_0 \quad (3.15)$$

$$\mu_{y0} = \sin \theta_0 \sin \phi_0 \quad (3.16)$$

$$\mu_{z0} = \cos \theta_0 \quad (3.17)$$

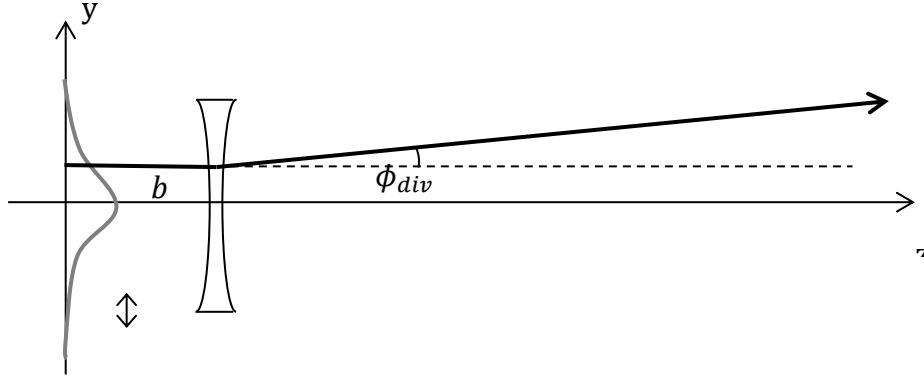


Figure 3.5: Diagram showing the generation of Gaussian beam with a divergence.

3.4.2 Lambertian source

The radiation pattern of an LED can be generally modelled using the Lambertian pattern or also known as power cosine distribution where the light intensity of the LED has a cosine dependence on the angle of emission from the surface normal. The intensity of Lambertian source is given as

$$I(\theta) = I_0 \cos^m \theta \quad (3.18)$$

Where θ is the angle of irradiance from the normal of transmitter surface, I_0 is the intensity at the centre and m is the order of Lambertian emission that is defined as

$$m = \frac{\ln(2)}{\ln(\cos \phi_{1/2})} \quad (3.19)$$

Where $\phi_{1/2}$ is the semi angle at half illuminance of an LED and m can be interpreted as the directivity of the beam pattern.

Each ray has a polar angle generated with the pdf that follows Lambertian emission pattern of a source [109,110].

The pdf of the polar angle is given as

$$p(\theta) = (\cos\theta)^m \sin\theta \quad (3.20)$$

And the cdf is calculated as

$$P(\theta) = 1 - (\cos\theta)^{m+1} \quad (3.21)$$

And by using inversion method , the polar angle can be calculated using the equation

$$\theta = \cos^{-1}(\sqrt[m+1]{R}) \quad (3.22)$$

Similar to Gaussian source, the azimuth angle is chosen randomly from a uniform distribution $[0, 2\pi]$.

From the azimuthal angle, the starting coordinates for the photons can be calculated as (3.16) and (3.17).

3.4.3 Modelling elevated source : coordinate transformations

In order to model a source whose z-axis is not aligned to Earth frame of reference, some transformations are needed in representing the direction cosines of the source with respect to the absolute coordinate system. It is easy if the source y-axis is aligned along the Earth's x-y plane so that the initial direction cosines of the photon are related to the direction cosines of the source z-axis. First, the direction angles of the source z-axis are defined as θ_{xs} , θ_{ys} and θ_{zs} and the corresponding directions cosines are μ_{xs} , μ_{ys} and μ_{zs} . The polar angle of the photons with respect to the source z-axis is defined as Θ and the corresponding azimuthal angle is Φ . Note that these two angles are calculated from the source distribution described in section 3.4. Thus the direction cosines of the photon, μ_x , μ_y and μ_z with respect to the Earth frame of reference can be calculated as [70].

$$\begin{bmatrix} \mu_x \\ \mu_y \\ \mu_z \end{bmatrix} = \begin{bmatrix} \mu_{xs}\mu_{zs}/\sqrt{1-\mu_{zs}^2} & -\mu_{ys}/\sqrt{1-\mu_{zs}^2} & \mu_{xs} \\ \mu_{ys}\mu_{zs}/\sqrt{1-\mu_{zs}^2} & \mu_{xs}/\sqrt{1-\mu_{zs}^2} & \mu_{ys} \\ -\sqrt{1-\mu_{zs}^2} & 0 & \mu_{zs} \end{bmatrix} \begin{bmatrix} \sin \Theta \cos \Phi \\ \sin \Theta \sin \Phi \\ \cos \Theta \end{bmatrix} \quad (3.23)$$

The equation can be simplified as shown below when μ_{zs} is very close to 1

$$\begin{bmatrix} \mu_x \\ \mu_y \\ \mu_z \end{bmatrix} = \text{sign}(\mu_{zs}) \begin{bmatrix} \sin \Theta \cos \Phi \\ \sin \Theta \sin \Phi \\ \cos \Theta \end{bmatrix} \quad \mu_{zs}^2 \approx 1 \quad (3.24)$$

3.5 *Photon propagation*

After the photon is generated, the photon is moved by a distance defined by its step size and then scattered according to the VSF.

3.5.1 **Photon step size**

The photon step size is calculated by sampling the probability of the photon's free path [89]. The photon step size is determined by the attenuation coefficient, c . The pdf for the attenuation of light with respect to the optical distance travelled is given by

$$p(l) = e^{-l}, \quad l > 0 \quad (3.25)$$

The cdf is given by

$$P(l) = \int_0^l e^{-l'} dl' = 1 - e^{-l} \quad (3.26)$$

By using inversion sampling to sample the path length l , let $P(l) = R$ where R is a random number from the uniform distribution over $[0,1]$. Solving for l , this becomes

$$l = -\ln(1 - R) = -\ln R \quad (3.27)$$

The photon path length is defined as $l=cs$, where c is the attenuation coefficient and s is the geometric distance between optical events, which can be calculated as

$$s = -\frac{1}{c} \ln R \quad (3.28)$$

3.5.2 Photon weight

A weight of 1 is assigned to each photon as it enters a medium. After each propagation step, the photon packet is split into two parts: a fraction is absorbed and the rest is scattered [112]. Thus the weight of the photon will change based on the percentage of energy being absorbed. By using albedo which is explained in Section 2.5.4, the fraction of the packet that is absorbed is $1 - \omega$. The new photon weight w is given by $w' = \omega w$ which represents the fraction of the packet that is scattered.

3.5.3 Terminating photons

The energy of the photon will decrease to a very small value after going through absorption and scattering. Sometimes, in simulation the energy is too low to be calculated at the receiver. To speed up the simulation time, a minimum energy is set as a threshold value to determine whether the photon should be terminated or not. The photon is considered lost when the weight of the photon is below a certain threshold level. The value of the threshold level

must be chosen carefully because the simulation time will be too long if the value of threshold is too small and the accuracy will be low if the value is big. Different researchers chose different value of the threshold level. In [33], the threshold level is set to 10^{-10} , in both [38,42] it is set to 10^{-6} and in [39] the threshold is set to 10^{-4} .

However the photon cannot be terminated just like that because it will violate the conservation of energy. Thus a method called Roulette is used to ensure that conservation of energy is obeyed and also to reduce the simulation time [38]. A parameter called roulette threshold, α is defined to be any integer (i.e. 10). Then the photon is given one chance in α of surviving with a weight of αw by using a random number R . If the random number is greater than the inverse of the rouletting threshold, the photon will be terminated. Otherwise, the photon will continue to move with a weight define by αw .

$$w' = \begin{cases} 0 & \text{if } R > \frac{1}{\alpha} \\ \alpha w & \text{if } R \leq \frac{1}{\alpha} \end{cases} \quad (3.29)$$

3.5.4 Scattering directions

The scattering angle is chosen from the VSF. There are several VSFs that are widely used as discussed in Section 2.6. In this thesis the VSF used is

determined experimentally by Petzold. In this method, the polar scattering angle is obtained from the interpolation of the tabulated values in [84]. Since the scattering process is symmetry, the radial or azimuthal scattering angle ϕ' is chosen from the equation

$$\phi' = 2\pi R \quad (3.30)$$

Where R is a random number chosen on the interval [0,1]. The random number used in finding θ' is be different from the random number used to find ϕ' to make sure that they both are independent random variables.

3.5.5 Updating the direction cosines

The new direction cosines must be updated with the chosen polar, θ' and azimuth ϕ' scattering angles. This process is transforming the local direction of scattering to global direction of scattering. The new direction cosines when rotated by ϕ' and θ' are defined as [70]

$$\begin{bmatrix} \mu'_x \\ \mu'_y \\ \mu'_z \end{bmatrix} = \begin{bmatrix} \mu_x \mu_z / \sqrt{1 - \mu_z^2} & -\mu_{xy} / \sqrt{1 - \mu_z^2} & \mu_x \\ \mu_y \mu_z / \sqrt{1 - \mu_z^2} & \mu_x / \sqrt{1 - \mu_z^2} & \mu_y \\ -\sqrt{1 - \mu_z^2} & 0 & \mu_z \end{bmatrix} \begin{bmatrix} \sqrt{1 - \mu_s^2} \cos \phi' \\ \sqrt{1 - \mu_s^2} \sin \phi' \\ \mu_s \end{bmatrix} \quad (3.31)$$

Where $\mu_s = \cos \theta'$ and when μ_z is very close to 1, the equaton reduces to

$$\begin{bmatrix} \mu'_x \\ \mu'_y \\ \mu'_z \end{bmatrix} = \begin{bmatrix} \sin \theta' \cos \phi' \\ \sin \theta' \sin \phi' \\ \frac{\cos \theta}{|\cos \theta|} \cos \theta' \end{bmatrix} = \text{sign}(\mu_z) \begin{bmatrix} \sqrt{1 - \mu_s^2} \cos \phi' \\ \sqrt{1 - \mu_s^2} \sin \phi' \\ \mu_s \end{bmatrix} \quad \mu_z^2 \approx 1 \quad (3.32)$$

3.5.6 Updating the photon propagation

After scattering process, the position and the direction cosines of the photon must be updated. The new position of the photon is defined as

$$x' = x_0 + \mu'_x s \quad (3.33)$$

$$y' = y_0 + \mu'_y s \quad (3.34)$$

$$z' = z_0 + \mu'_z s \quad (3.35)$$

Where μ'_x , μ'_y and μ'_z are the current direction cosines and s is step size.

3.6 Photon reception

Once the photon reaches the receiver, it will be selected based on the receiver characteristics i.e. its aperture and FOV. Photon which is received outside the aperture and has angle of arrival greater than FOV is considered lost. The important parameters of received photon such as xyz coordinate of the final positions, direction cosines, weight and distance travelled are recorded for

further analysis. In this simulations, the receiver noise is ignored as the focus is to investigate the channel characteristics.

3.6.1 Power loss calculation

The power received is obtained through summing the weight of all arrived photons and then normalised by the total transmitted weight as shown by

$$P_r = \frac{N_R}{N_T} \quad (3.36)$$

Where N_R is the numbers of the received photons and N_T are the number of photons transmitted.

3.7 *Calculation of impulse response*

Figure 3.6 illustrates the effect of multiple scattering on the light pulses in underwater environment. As can be seen, the propagation path of photons will change due to multiple scattering and this cause it to be longer than the distance between the transmitter and the receiver. These photons will arrive at a certain time delay after the first received photons. In MC simulation, the total distance of propagation of individual photon can be measured thus enabling the calculation of the total transit time of each photon. The maximum data rate can be estimated from the impulse response and the rms delay spread. The

details of the calculation of impulse response and frequency response are explained next.

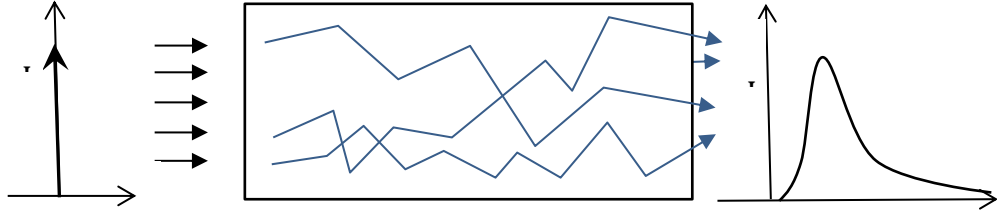


Figure 3.6: Diagram showing multiple scattering effects to the impulse response.

Firstly, the difference in path length is calculated as

$$\Delta d = d_{\text{photon}} - d \quad (3.37)$$

Where d is the distance from transmitter to receiver, d_{photon} is the distance travelled by the photon.

The time delay can be calculated by using the speed of light in water.

$$\Delta t = \frac{\Delta d}{v_{\text{water}}} \quad (3.38)$$

Where v_{water} is the speed of light in water and can be calculated as $v_{\text{water}} = \frac{c}{n_{\text{water}}}$

From this information, the histogram of the time delay, Δt is plotted. The normalised histogram is calculated by dividing the total histogram with the

weight of the photons received . The normalised histogram can be regarded as the pdf of the discrete impulse response [38,107]. The frequency response can be calculated by taking the Fourier transform of the impulse response. From the frequency response the channel capacity can be estimated as the frequency at which it drops to half or 3 dB. It is important to note that the size of the measurement bin in plotting the histogram will determine the frequency response that can be estimated. The maximum frequency that can be estimated is related to the bin size as shown in equation 3.39 [38].

$$f_{\max} = \frac{1}{2T_{bin}} \quad (3.39)$$

Where T_{bin} is the bin size in seconds. In this case the bin is the time resolution is set to 1×10^{-10} s in order to have a maximum bandwidth estimation around 5 GHz.

3.8 *Simulation setup*

This section presents the simulation setup used in this thesis to model the short-range diffuse non-line-of-sight (NLOS) link. Figure 3.7 shows the configuration where the receiver is located z m away from the transmitter. At the receiver plane, the zone of communication is defined to be a square area of $10 \text{ m} \times 10 \text{ m}$ centred at the coordinate (0,0). The interest in this configuration is mainly to investigate the range of power that is received and channel

bandwidth supported over the area defined as the desire to find the limitations imposed by the system and environmental parameters. Even though the main aim is to study diffuse links, simulations for collimated links are conducted in addition for comparison purposes.

The collimated beam is modelled to have full angle divergence of 1.5 mrad. Two sizes of diffuse beams are used, namely 15° and 30° full angle and these are modelled using Gaussian distributions for their beam shapes. Additionally three sizes of Lambertian sources are also included in the simulation with the purpose of investigating any significant impact by using the two different distributions. Two of the Lambertian sources are chosen with divergences that are of approximately size to the diffuse Gaussian beams; sources with semi-angles of 7.5° ($m=81$) and 15° ($m=21$). A third Lambertian source with a semi-angle of 60° ($m=1$) is also included as it provides wider divergence.

The receiver size is modelled to have lense aperture diameter of 10 cm (4 inch) which is considered as common lens sizes [38]. This value is then reduced to 5 cm in order to study its effect. Initially the receiver FOV is set to have a maximum full angle value of 180° and later this receiver FOV is made smaller to study the effects. In this case the FOV is defined as the maximum angle at which the incoming light can be accepted by the receiver. It should be noted that the maximum FOV (i.e. 180) is used to collect all the received photons in order to investigate the channel characteristics. Table 3.1 summarizes the simulation parameters used in this section.

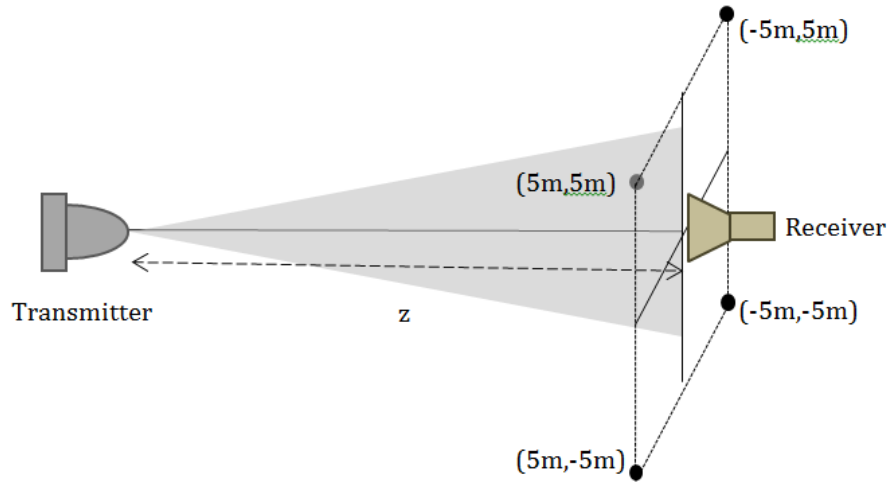


Figure 3.7: Link Geometry.

Table 3.1: Simulation parameters.

Parameter	Values
Wavelength	514 nm
Beam width	3 mm
Collimated source beam divergence	1.5 mrad
Diffuse source beam divergence (full-angle)	15°, 30°
Lambertian source (semi angle)	7.5, 15°, 60°
Receiver lense aperture diameter	10 cm and 5 cm,
Receiver FOV	10°, 20°, 40°, 120°, 180°

3.8.1 Simulation parameters

Table 3.2 shows the summary of input and output parameters that are used in the simulation, Table 3.3 shows the absorption, scattering and attenuation coefficients of three types of water and Table 3.4 presents the published simulation parameter values by other researchers for comparison.

Table 3.2: Input and output parameters used in simulations.

Input parameters	Channel	Output parameters
<ul style="list-style-type: none"> • Beam width, b • Beam divergence, ϕ_{div} • Receiver FOV • Receiver aperture size (lense diameter) 	Types of Water <ul style="list-style-type: none"> • Clear water • Coastal water • Harbour water 	<ul style="list-style-type: none"> • Path loss • Scattering order • Impulse response • Frequency response • Angle of arrival

Table 3.3: Coefficients for three types of water. Table taken from [38].

Water type	$a(m^{-1})$	$b(m^{-1})$	$c(m^{-1})$	$Albedo, \omega$
Clear ocean	0.114	0.037	0.151	0.25
Coastal ocean	0.179	0.219	0.398	0.55
Turbid harbour	0.366	1.824	2.190	0.83

Table 3.4: Published simulation parameters used in MC simulation.

Author	Beam divergence	Beam width	Aperture size	Receiver FOV	Phase Function	Water types	Links	Distance	Threshold
Li [33]	0° 0.01°	unknown	50 mm	10 mrad 8 °	HG (g=0.9)	Clear Coastal Harbour	LOS	103m, 39m, 7m (cz=15.4)	10 ⁻¹⁰ ,10 ⁻⁴
Cox [38]	0.0015 mrad	1 mm	8 mm, 1 inch, 2 inch 3 inch 4inch	1°, 2°, 4°, 8°,16°,45°, 90°,180°	Petzold	Clear Coastal Harbour	LOS	5-120 m	10 ⁻⁶
Gabriel [39]	0 20°, 45°	0.3 cm, 3 cm, 30 cm	5 mm, 20 cm, 50 cm	180°	TTHG	Pure, Clear, Coastal	LOS	10 m, 20 m, 50 m	10 ⁻⁴
Tang [42]	10°	unknown	50 cm	20° 40° 180°	Petzold HG	Coastal Harbour	LOS	10 m, 30m	10 ⁻⁶
Dong [44]	10°	unknown	50 cm	20° 40° 180°	HG	Coastal Harbour	MIMO LOS	12-30 (coastal) 5-12m (turbid water)	~

3.9 *Simulation of diffuse sources*

In this section, the effect of the beam divergence modelled using both Gaussian source distribution and Lambertian source radiation pattern is studied in three types of water. In previous simulations by other researcher as summarized in Table 3.3, different sizes of beam divergences are used. A collimated laser beam with Gaussian distribution was employed by [38]. However, many other papers did not explicitly describe the radiation pattern of the source.

3.9.1 Power distribution

In this section, the received power distribution is obtained by placing the receiver at different positions as shown in Figure 3.7. The distance between the transmitter and receiver is set to be 15 m. Figures 3.8 (a) to (c) show the cross sectional view of the power distribution at the receiver plane in three types of water for different size of beam divergence. The x -axis is the radial distance centred at (0,0) at the receiver plane and the y -axis represents the normalised received power.

Using this configuration , the maximum lateral distance to be measured is 5 m corresponding to a maximum of angular offset of 18.43° . In clear water and coastal water, a collimated beam shows a sharp reduction in the power received as the receiver is moved away from the centre so that 5 m away from the centre (off-axis) there is approximately more than 50 dB loss of power in clear water and more than 30 dB of loss in coastal water. However for all

diffuse sources in both types of water, there is relatively little loss of power as the receiver is moved away from the beam centre. The variations of power received by using diffuse sources are quite small with maximum dynamic range of 20 dB if a source of 15° is used. For the Lambertian source with semi-angle of 60° ($m=1$), it is observed that the power is almost uniformly distributed over the area with a value of approximately -60 dB. It is also apparent from Figure 3.8 that the choice of source distribution profile between Gaussian or Lambertian for the same beam divergence has little effect on the power distribution. Thus, it is reasonable to say that a Gaussian distribution can be used to approximate the radiation patterns of the diffuse sources which are commonly provided by using an LED.

Now, by comparing two diffuse sources, namely 15° and 30° for the entire radial distance in clear water, it is possible to say that the latter has a slightly more uniform power distribution compared to the former, where the dynamic range for diffuse source of 30° over the specified area is less than 10 dB. This can be seen in Figure 3.8(a) where at a distance of 5 m from the centre, the power that is recorded using diffuse source of 30° is almost 10 dB higher than the sources with a smaller divergence. However, in coastal water as shown in Figure 3.8(b), there is little distinguishable effect between all the diffuse sources as the dynamic range is less than 10 dB for all of them.

Figure 3.8(c) shows the power distribution in turbid water. An interesting behaviour is observed in this case where it can be seen that the power received

by using collimated source is almost equal to the power received by other diffuse sources except the Lambertian source of mode number 1 ($m=1$). This signifies that the collimated nature of the beam was lost due to high multiple scattering in turbid water. So in highly turbid water, the choice of source is a less significant in determining the amount of power received.

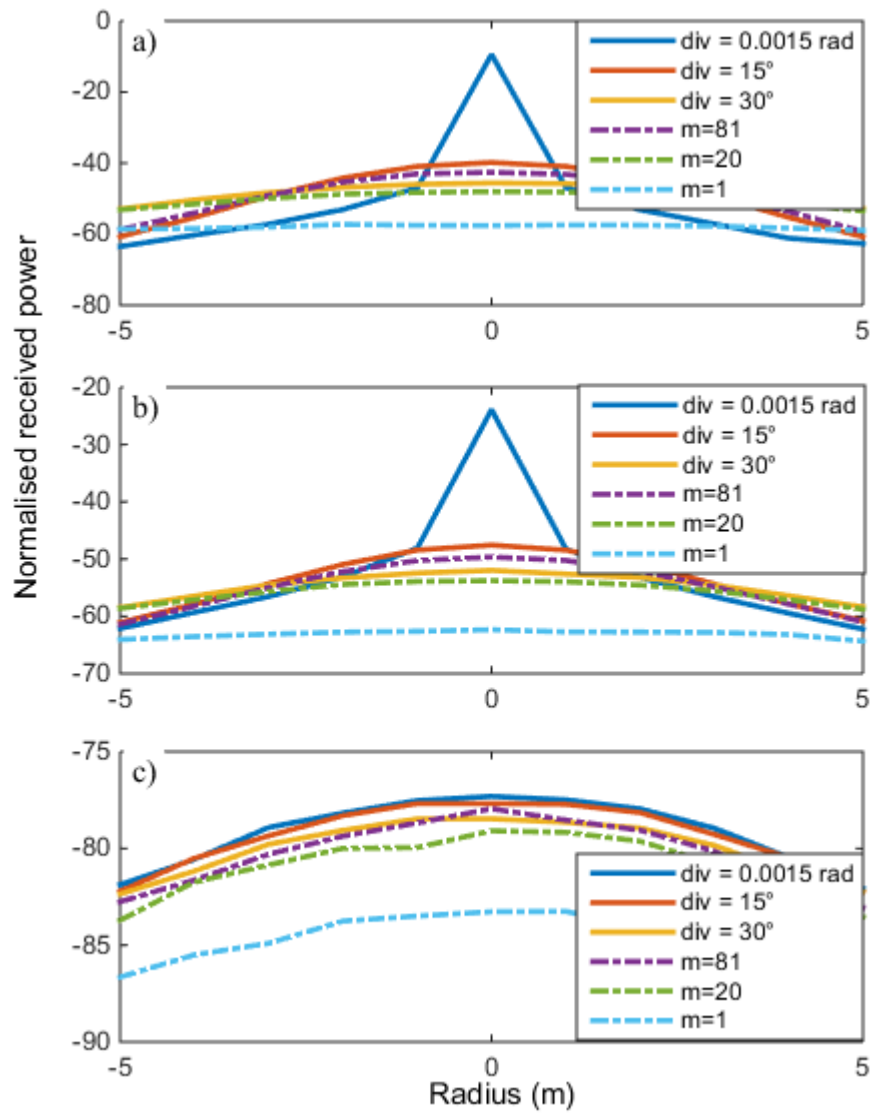


Figure 3.8: Power distribution for various beam divergences in (a) clear water, (b) coastal water and (c) turbid water.

3.9.2 Frequency Response

In this section, an example of a frequency response plot is presented to illustrate the effect of bin sizes and the number of samples on the accuracy and smoothness of the curve. For this purpose, a diffuse source of 15° is used at the transmitter and a receiver with aperture size of 10 cm and FOV of 180° is placed 30 m from the transmitter. A relatively high scattering environment (coastal water) is chosen in this case.

3.9.3 The effect of bin sizes to the frequency response

Figure 3.9 depicts the frequency responses that is plotted by using three different bin sizes, namely 1×10^{-8} s, 1×10^{-9} s and 1×10^{-10} s. It is apparent that the larger bin sizes (i.e. 1×10^{-8} s) is unable to predict the 3 dB frequency in the GHz range as described by equation 3.39. Thus, the bin size is chosen to be 1×10^{-10} s in all the simulations. This also means that a large number of samples are required in order to plot a high resolution frequency response.

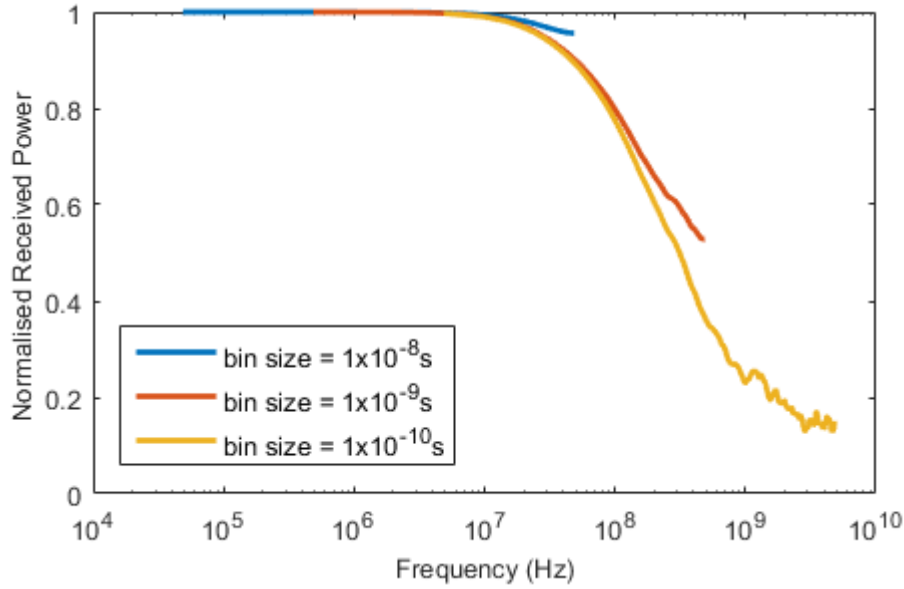


Figure 3.9: Frequency response for diffuse beam of 15° in coastal water ($c=0.4$) at 30 m for various bin sizes.

3.9.4 The effect of number of samples on the frequency response

In one simulation trials, the number of photons transmitted are 1×10^6 photons. This amount is sufficient to generate a smooth frequency response in cases when there are less scattering or shorter distance as the attenuation is less. However, when the attenuation increases either due to longer distance or higher scattering environments, the number of photons collected at the receiver reduces significantly. This causes the number of photons collected for each bin to be too small which eventually causes the frequency response curves to be noisy. Thus, more trials are needed to increase the number of photons to obtain a smoother curve. For example, Figure 3.10 shows the frequency response for diffuse beam of 15° at 30 m in coastal water for various samples sizes. It is evident that the frequency response curve generated using

large samples shows a smoother curve. However, larger samples will increase the simulation time. Thus, in such cases, it is decided that the simulations will be repeated until at least 100 photons are collected. This technique is also used when a smaller receiver FOV or aperture is used as the number of photons collected is too small for one trial. A similar observations is also reported in [33, 92].

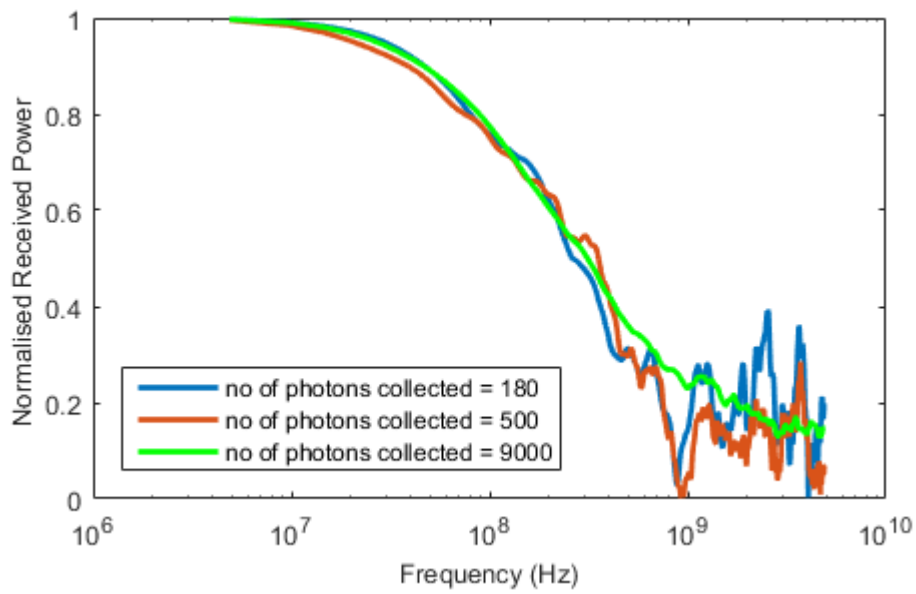


Figure 3.10: Frequency response for diffuse beam of 15° in coastal water ($c=0.4$) at 30 m for various samples sizes.

3.10 Conclusion

In this chapter, the principles of MC modelling for the simulation of UOWC were presented. It can be said that MC is a powerful tool in solving problems and equations that are difficult to solve analytically due to many variables. The advantages and disadvantages of MC simulation were also highlighted. Then

the details of the sampling method for different types of sources, step size and scattering angles were discussed. The technique to calculate the received power and impulse response from MC simulation was also presented. Next, the summary of the published values of the simulation parameters was highlighted for comparison. Finally, the simulation to compare two techniques of generating diffuse sources distributions was presented along with the discussion on factors that affect the frequency response smoothness and accuracy.

CHAPTER 4

Path Loss: Performance Analysis

This chapter introduces the important components within link budget calculation. This includes the channel path loss which is normally estimated using BL law. Due to several limitations of BL law in predicting path loss, MC simulation is used to simulate the channel with greater accuracy. Thus, the path loss performance analysis for various source divergences in various types of water along with the discussion on impact of scattering are presented. A detailed analysis on attenuation of the unscattered and scattered component of the received light are also highlighted leading to a method to characterise the transition between minimally scattered and multiply scattered regimes for diffuse beams. Then the study is extended to explore the spatial spreading effect as distance is increased which will be useful for system designers to estimate the region where uniform received power can be achieved or to estimate pointing accuracy required. The contribution of unscattered light to the total power received in off-axis locations is also presented to gain insights on how scattering impacted the spatial spreading.

4.1 *Link budget*

Before designing and building a system to operate underwater, a detailed investigation must be made to understand and predict the link performance and limitations depending on the channel environment. In link budget calculation, output power is represented as a function of the input power with the incorporation of various types of losses and gains. These include system loss, geometric loss, misalignment loss, attenuation loss due to water channel and ambient noise. However the largest losses are contributed by the geometric loss and exponential path loss due to the underwater channel [114]. The received power is given by

$$P_R = P_T G_T L_W L_{Geo} L_{pointing} G_R \quad (4.1)$$

where P_T is the transmitted optical signal, G_T is the transmitter gain that includes the beam aperture and divergence, L_W is the loss due to absorption and scattering, L_{Geo} is the geometric loss, $L_{pointing}$ is the loss due to angular and spatial mismatch and G_R is the receiver gain that includes the receiver aperture and FOV. The transmitter and receiver gain can be obtained from the device characterisation of both transmitter and receiver. In this chapter, the focus is on the investigation of channel path loss particularly for diffuse links along with collimated links for comparison purposes.

4.2 *Path loss modelling*

Channel path loss is one of the important parameter in link budget analysis where it directly affects the bit-error-rate (BER) of the links as the signal-to-noise ratio (SNR) in optical links are proportional to the square of the average received optical power [2]. Generally, BL law is used in the prediction of path loss performance as presented in Chapter 2. For convenience, the BL law is given again as

$$P = P_o \exp(-cz) \quad (4.2)$$

where P_o is the transmitted power, z is the path length and c is the beam attenuation coefficient.

However, it is understood that BL law is only applicable to a very limited situation where it is only valid for on-axis path loss using collimated beam in low turbidity environment. Additionally, it only considers unscattered light and ignores any contribution from the scattered light. Due to this, it significantly underestimates the link range in highly scattering environment such as coastal and turbid water or at high attenuation length where scattering is significant [11].

Considerable amount of work has been reported on the path loss modelling of UOWC by experimental, analytical and numerical investigations. The most

extensive numerical investigation was conducted by [38] where the effect of receiver aperture and FOV on the path loss performance were thoroughly investigated using MC simulation. In their work, a collimated source of 1.5 mrad is used. An experimental investigation on path loss for different turbidity of water has been conducted by [14] by using a 7.66 m water tank. In his work, he observed two distinct regions in the path loss performance where the behaviour of path loss match BL law or deviated from it. Since the attenuation coefficient, c is varied for a fixed distance, it can be said that the results presented are limited by the physical distance and are not accurate for longer distances.

In another earlier study in [18], the spatial spreading of a collimated beam in a highly scattering environment is also studied and an equation to represent the spatial spreading attenuation was proposed. BL law is modified to incorporate the effect of scattering by introducing a new term; system attenuation coefficient k_{sys} and is defined as

$$k_{sys} = a + (1 - \eta)b \quad (4.3)$$

where η is scattering factor ($0 \leq \eta \leq 1$) to account for the collection of multiply scattered light, a is the absorption coefficient and b is the scattering coefficient.

Thus the received power can be expressed as

$$P(z) = P_o \exp(-k_{sys} z) \quad (4.4)$$

The value of k_{sys} is obtained from the simulation results specifically from the slope of the attenuation plot where it can be used to calculate the percentage of scattered light, η . It is assumed in this equation that the scattering factor is constant for a range of propagation distances which may not be accurate as the amount of scattered light varies with distance.

In [45], a generic model to predict the signal strength in underwater links was proposed which is then compared with experimental results. This model includes the components in the systems such as light sources, detectors, amplifier and detector circuitry. While this model is comprehensive, it is limited only to clear water where scattering is not significant. The signal strength model is given as

$$P(\theta, \phi, d) = I(\theta) \frac{\exp(-cz)}{z^2} S(\phi) A_d \cos(\phi) \quad (\text{W}) \quad (4.5)$$

where $I(\theta)$ is the source radiant intensity function, $S(\phi)$ is the detector relative angular sensitivity function, d is the distance, θ is the transmission angle relative to the optical axis, ϕ is the incident signal relative to the detectors optical axis, A_d is the detector area and z is the distance.

From the discussions above, it can be seen that numerous attempts in mathematically modelling the UOWC channel have been conducted. However, it is apparent that a universal model valid for all situations is difficult to achieve due to the complexity of the underwater channel. Since most of the

works focus on collimated beams, it is believed that this work will fill the gap by presenting the simulations of the path loss for diffuse beams in various type of water. While it is understood that the amount of received power is much smaller by using diffuse source, the extent at which this affect the communication links has not been quantified. Thus, this chapter will address this issue.

4.2.1 Diffusion length, L_D

Diffusion length, L_D is defined as the distance from the source at which the light beam is propagating forward; it also can be understood as the distance where the average number of photons have lost their initial forward directionality due to multiple scattering [14, 38]. It can be used to estimate the transition between unscattered and multiply scattered dominated region in underwater environment for collimated links that are perfectly aligned and is given by.

$$L_D = \frac{1}{b(1 - \langle \cos \psi \rangle)} \quad (4.6)$$

where b is the scattering coefficient and $\langle \cos \psi \rangle$ is the average cosine of the scattering angle where it is given by

$$\langle \cos \psi \rangle = g = 2\pi \int_0^\pi \tilde{\beta}(\psi) \cos \psi \sin \psi d\psi \quad (4.7)$$

where $\tilde{\beta}$ is the scattering phase function. It was previously shown that the average cosine of the scattering angle is close to one (≈ 1), showing that photons are mostly scattered to small angles in forward direction as have been presented in Section 2.6.

From equation 4.6, the diffusion length, L_D for each types of water is calculated as shown in Table 4.1. The longest diffusion length is 205 m for clear water, followed by 75 m for coastal water and 6.8 m for turbid water. When the propagation distance is less than the diffusion length L_D , unscattered light and minimally scattered light dominate whereas when the distance is more than L_D , multiply scattered light dominate. In [115], it is highlighted that most of the photons still have forward propagation at one diffusion length while in [116], it is stated that the beam will become completely diffuse after two or three diffusion length, L_D . From this prediction, it can be seen that collimated beams will maintain their collimated nature for a long range before it starts to diffuse completely which is an advantage for light propagation in several hundreds of meters.

Besides the study on diffusion length, L_D , a slightly earlier study in [117] has proposed a categorisation of the energy transport region for blue-green pulsed laser through fog in the atmosphere. Mooradian proposed that the variation of average received energy with respect to AL can be divided into three regions as presented in Table 4.2.

Table 4.1: Optical properties of the ocean water types with the corresponding diffusion length.

	a	b	c	ω	g	L_D	C^*L_D
Clear	0.114	0.037	0.151	0.247	0.87	205	31
Coastal	0.179	0.219	0.398	0.551	0.94	75	30.24
Turbid	0.355	1.824	2.19	0.833	0.92	6.8	14.89

Table 4.2: The three regions of energy transport [117] .

Region	Range	Description
Region 1	$0 < AL < 13$	The unscattered beam dominates with exponential path loss decay of -4.34 dB/cz
Region II	$13 < AL < 32$	The region is dominated by the multiply forward scattered component. This component exhibits an exponential decay less severe than the unscattered beam but does possess slightly larger spatial, angular and temporal spreading.
Region III	$AL > 32$	This region is characterized by diffusion type multiple scattering. It is non exponential in decay and exhibits large angular, spatial and temporal spreading.

Corresponding to that, experimental work in [14] has verified the relationship between Moiradian regions and the attenuation length (AL) at which the transition between minimally scattered region and multiply scattered region occurs. From the experimental results obtained, the transition points between these two regions tallies with the Moiradian regions which is approximately 13 AL in turbid water ($c=1.7$). However, this is only valid for collimated links where the transmitter and the receiver are perfectly aligned. Thus it is believed that further work on parameterizing the transition points for the diffuse links

is needed and the diffusion length L_D values can be used as the baseline for comparison.

4.3 *Spatial distribution effects*

One of the main effects of scattering is that it will cause a highly collimated light source to spread laterally. The discussion in Section 2.5 has presented that the scattering in ocean waters is highly peaked in small forward angles. However, due to multiple small angle scattering events which increases with propagation distance, a collimated beam will be spatially broadened beyond the predicted amount by divergence alone [37]. For diffuse sources, an additional spread is also observed due to its wide divergence angles. In order to understand this effect, a beam spread function (BSF) is derived from RTE that is introduced in Section 2.8. BSF is defined as the lateral irradiance distribution of a uni-directional source on a plane that is located at r distance away from the source [118]. It can also be understood as the total scattering profile of a collimated laser beam as a function of range and water turbidity [18].

Several works studying the BSF have been reported, where historically the BSF is obtained through experiments and empirical models which in some cases have limitations in providing an understanding of the physical meaning of the situation [118, 119]. Several works have attempted to solve BSF analytically by making several approximations such as small angle approximation (SAA). In

this technique, any scattered light with large angles is ignored which makes $\cos(\theta)=1$ and $\sin(\theta)=\tan(\theta)=\theta$, where θ is the scattering angle [121]. As the result, the time dispersion effect is omitted from the calculation. Additionally, any light that has travel beyond the receiver locations is not considered. Besides that, it is also assumed that the irradiance distribution is symmetric about the beam axis. Since SAA only considers scatterings which occur at small angles, it is good approximation for collimated source in low turbidity environment and in locations with small pointing accuracies [122].

In [18], a mathematical model for BSF was derived from RTE based on SAA as

$$BSF(r, z_{rec}) = E_{NS}(r, z_{rec}) + E_S(r, z_{rec}) \quad (4.8)$$

where $E_{NS}(r, z_{rec})$ is the unscattered component given as

$$E_{NS}(r, z_{rec}) = E_0(r, z_{rec}) \exp(-cz) \quad (4.9)$$

and $E_S(r, z_{rec})$ is the scattered component of light given as

$$E_S(r, z_{rec}) = \frac{1}{2\pi} \int_0^\infty E_0(\nu, z_{rec}) \exp(-c\nu z) \times \left\{ \exp \left[\int_{z_{src}}^{z_{rec}} b(z) p(\nu(z_{rec} - z)) dz \right] - 1 \right\} J_0(\nu r) \nu d\nu \quad (4.10)$$

where $E_0(r, z_{rec})$ and $E_0(\nu, z_{rec})$ is the initial irradiance of the laser source in spatial coordinate system and spatial frequency domain, respectively. b and c are the scattering and attenuation coefficient, $p(\nu)$ is the scattering phase function and $J_0(\nu)$ is the Bessel function. It is highlighted that the equation is only valid for maximum receiver FOV (180°) and it requires a complex integration to consider finite FOV, detector area and angular orientation between receiver and transmitter.

From equation 4.8 it can be seen that both unscattered and scattered components of light are considered in the BSF calculations. From equations 4.7 and 4.8, it is observed that the unscattered light decays exponentially according to the beam attenuation coefficient, c while the scattered light attenuates as a function of beam attenuation coefficient, c and also the phase function of the scattered light which cannot be solved explicitly [122]. The proposed BSF equations displayed a good agreement with the experimental results conducted in [18].

Due to the SAA approximation, equations 4.9 and 4.10 cannot be used to model the spatial spreading effect of diffuse beam accurately. Moreover, the maximum offset distance to be studied is 4 m which will defy the SAA assumption. Thus the most suitable method to investigate the spatial spreading effect of a diffuse source at large offset distance is by using MC simulation.

4.4 Path loss performance analysis

In this section, the path loss performance for the various source divergences are investigated as the distance is varied from 5 m to 50 m for clear and coastal water and from 1 m to 20 m for turbid water. As shown previously by other works, the propagation of light in turbid water is limited to several tenths of meters only. As described in Chapter 3, three different sources are used with full angle divergence of 0.0015 rad, 15° and 30°. The receiver is set to have 180° full angle FOV and 10 cm aperture diameter.

Figures 4.1(a) and (b) depict the path loss performance in clear, coastal and turbid water. A separate plot is obtained for turbid water because the range is shorter compared to the former where the maximum distance studied for turbid water is up to 20 m only. Firstly it is illustrated that the collimated beam path loss performance is accurately predicted by BL law as expected especially for clear water, as shown in Figure 4.1(a). In coastal water, the power received is slightly higher than the prediction by BL law as in simulation, multiply scattered light is collected. This observation will be verified in the next section.

By using wider source divergences, namely 15° and 30°, the power received in clear water is less compared to collimated beam by approximately 20-45 dB as the distance is increased. A similar observation can be seen in coastal water where around 10-25 dB of power is lost compared to collimated beam. The huge loss of power is mainly due to the lower power density and geometric

loss where a lot of photons were not captured by the receiver. This shows that, in clear and coastal water, the size of the transmitter beam divergence significantly affects the power received. In [5] the power needed for 20° source divergence to be able to produce the same received power as collimated beam in clear water is found to be more than 30 dB.

However, a different behaviour is observed for turbid water, as shown in Figure 4.1(b). It can be seen clearly that both curves predicted a larger received power compared to the BL law. Besides that, the simulated received power shows a similar performance when the distance is more than 10 m. This is because, in turbid water where scattering is more significant, more photons begin to scatter out of the main path and the collimated nature of the beam is lost. Thus it can be said that in high turbidity water, the type of source does not significantly affect the power received at greater distances. An experimental measurement made by Cochenour in [14] shows a similar results at the same AL with different propagation distance.

In order to compare the path loss performance with the same reference parameter, the path loss is plotted as a function of AL as shown in Figure 4.2. From this plot the behaviour of how the path loss for various beam divergences varies can be compared. It can be seen that different source divergences have a different path loss performance albeit the same AL, which signifies that a careful interpretation of the plot must be made to avoid wrong analysis. For example, by referring to Figure 4.2, the path loss performance in

turbid water is better compared to the path loss performance in other types of water for all ranges of AL. This is completely misleading if one just make such comparison without considering the types of water and distance. In other words, it can be said that AL cannot be used as the only parameter in determining the path loss performance. This is because, even though the AL is common for three types of water, the distance is totally different due to different attenuation coefficients, c values.

This fact has been raised by Cochenour in his experimental studies where in his experiments, the results were obtained at a fixed propagation distance with various attenuation coefficients, c . It was highlighted that the path loss performance of a link in clear or coastal water may not be the same as the performance of the link in turbid water even at the same AL [14]. Thus, the results presented by simulations in this section confirmed this fact.

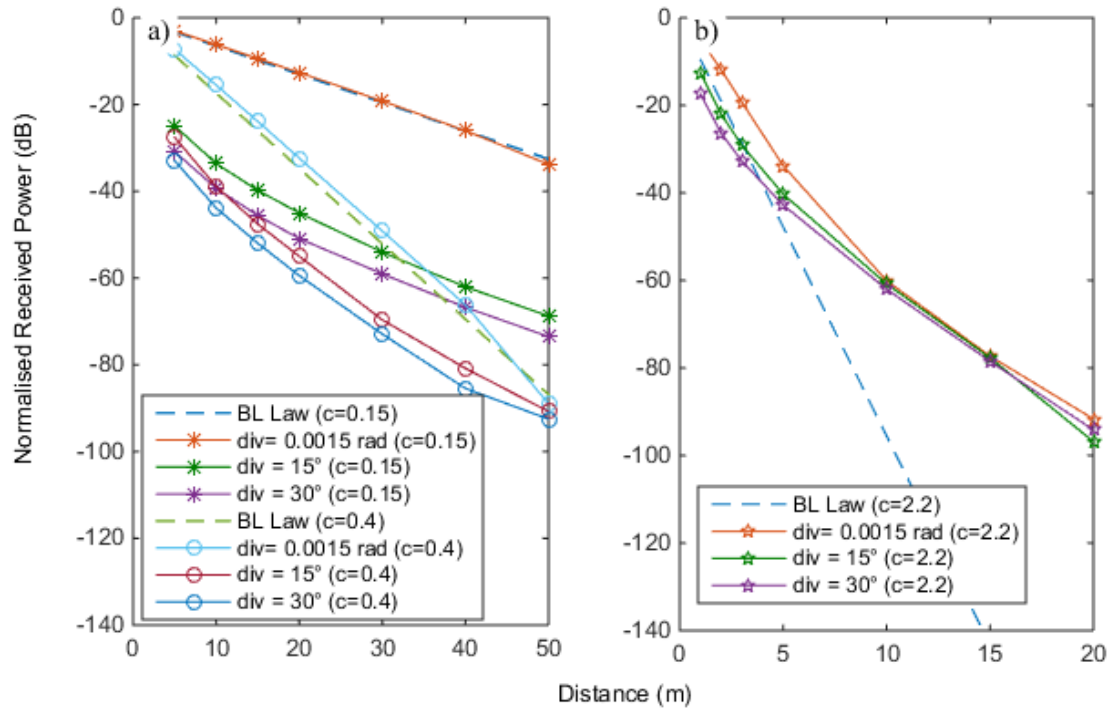


Figure 4.1: Normalised received power versus distance in (a) clear and coastal water and (b) turbid water

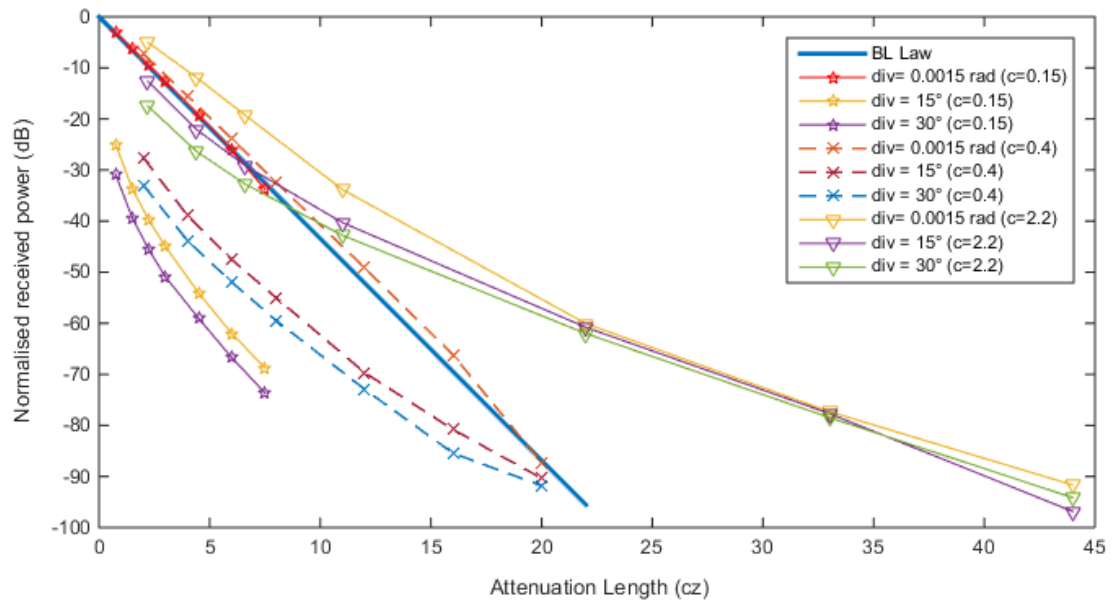


Figure 4.2: Normalised received power versus attenuation length in clear, coastal and turbid water.

4.4.1 Percentage of unscattered light

Further investigations are conducted to study the contributions of unscattered and scattered light on the total received power. Figure 4.3 shows the percentage of the unscattered light that contributed to the total power reception as the distance is varied. It is understood that the percentage of the scattered light will be the remaining percentage of the unscattered light. For collimated light in clear water, almost 100% of the light collected at the receiver consist of unscattered light which signifies that the amount of scattered light is negligible ($<1\%$). For both diffuse sources, the percentage of unscattered light dropped gradually as the distance is increased where at 50 m only 50-70% of the light collected is the unscattered component of light.

For collimated beam in coastal water, there is still significant amount of unscattered light that is collected up to a distance of 40 m where, beyond that, the percentage of unscattered light dramatically reduced to zero. For both diffuse beams in coastal water, the percentage of unscattered light collected is less than 50% even for short distance (10 m). As the distance is increased beyond 30 m all the light collected at the receiver consists of scattered lights only. In turbid water, the percentage of unscattered light that contributes to the total received power is very small for all source divergences, where less than 40% of unscattered light is collected for distance up to 1 m and there is no unscattered light collected for ranges more than 10 m. This is obviously due to high scattering environment as expected.

From this observation, it can be seen how the sizes of the source divergences influence the percentage of unscattered light that contributed to the received power. In general, by using diffuse source, most of the light collected by the receiver consists of scattered light especially in coastal and turbid water.

Additional useful information can be gained from Figure 4.3 where it can be used to predict the transition point between minimally scattered region and multiply scattered region especially for diffused beams as the previous two methods discussed in section 4.2.1 were shown to be valid for collimated beam. From this plot the distance at which the unscattered light ceased to be collected is proposed to be used as the transition point between the minimally scattered and the multiply scattered region.

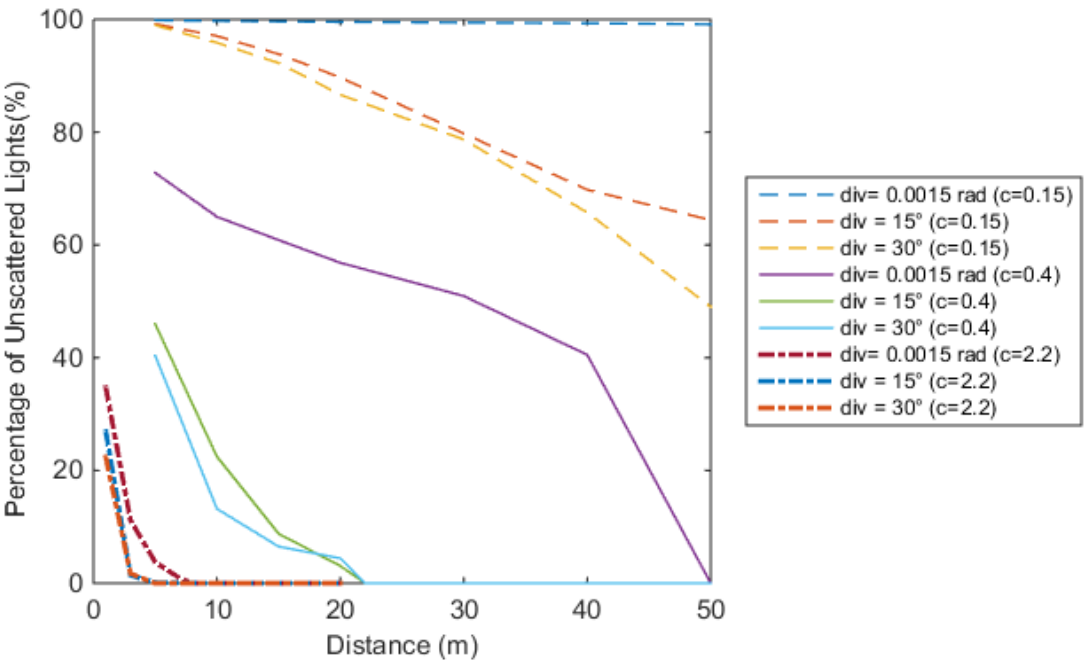


Figure 4.3: The percentage of the unscattered light that contributes to the total power reception

Since the simulation is conducted up to 50 m only, the transition point for minimally scattered and multiply scattered region for clear water cannot be obtained as it is predicted that the transition point will occur at a distance greater than 100 m. At this range the received power is expected to be attenuated by more than 150 dB which means that very large numbers of photons ($\approx 10^{15}$) need to be simulated and it is not practical in this case. Thus, this section will only discuss the proposed transition point for coastal and turbid water.

In coastal water, the distance where the percentage of unscattered light is reduced to zero is estimated to be around 50 m. This is shorter compared to the theoretical calculation where the L_D is predicted to be 75 m. For both diffuse beams, the transition point is much shorter, where the percentage of unscattered light drops to zero at approximately 22 m.

In turbid water it is found that the distance where the percentage of unscattered light is reduced to zero occurs at 7 m for collimated beam. This result matched the diffusion length, L_D predicted in section 4.2.1 where the transition point is predicted to be 6.8 m. For both diffuse beams, no unscattered light is collected beyond 3 m indicating that most of the light collected are multiply scattered light. The summary of this transition points is summarised in Table 4.3 for convenience.

Table 4.3: The proposed transition point between minimally scattered region and multiple scattering region.

	c=0.15	C=0.4	C=2.2
Div 0.0015 rad	-	50 m	7 m
Div=15°	-	22 m	3 m
Div=30°	-	22 m	3 m

4.4.2 Path loss of unscattered and scattered light

This section analyses the path loss performance of the unscattered and scattered component of the light that contributed to the total power received. The aim is to investigate how the unscattered and scattered component for various beam divergences is attenuated with propagation distance. This will provide a better understanding on the nature of unscattered and scattered component of the light and how it contributed to the total received power.

Figures 4.4(a) and (b) show the plot of the normalised power of the unscattered component for various beam divergences and water types. Firstly, it should be noted that the power received by the unscattered component from the collimated beam accurately match BL law for all types of water. This observation is predicted by equation 4.9 as presented in Section 4.3. However for larger source divergences, the power received by the unscattered component is much lower due to geometrical loss. Similar to the previous section, the power received by the unscattered light in all types of water are

plotted against the same axis as a function of AL as depicted in Figure 4.5 for comparison purposes. In general, it can be seen that the attenuation rates of unscattered components for the larger source divergences are similar to BL law with several magnitude lower due to geometrical loss. The following section will present mathematical equation that describe geometrical loss which fairly matches the results of the unscattered light attenuation.

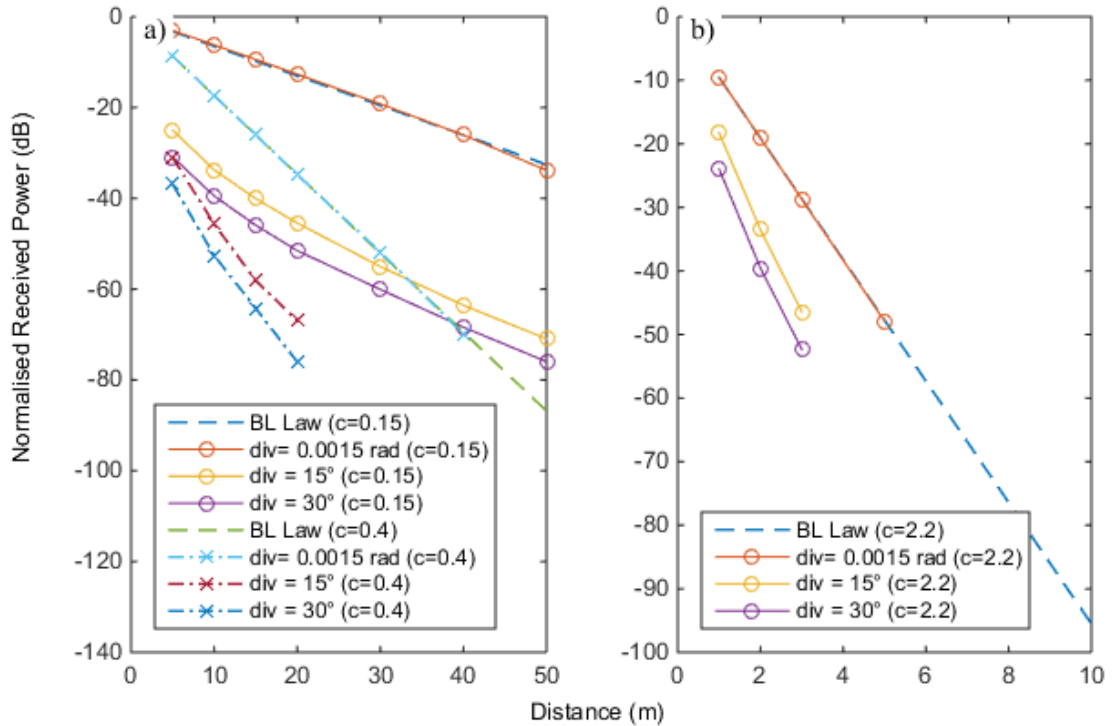


Figure 4.4: Normalised received power for (unscattered component) versus distance in (a) clear and coastal water and (b) turbid water

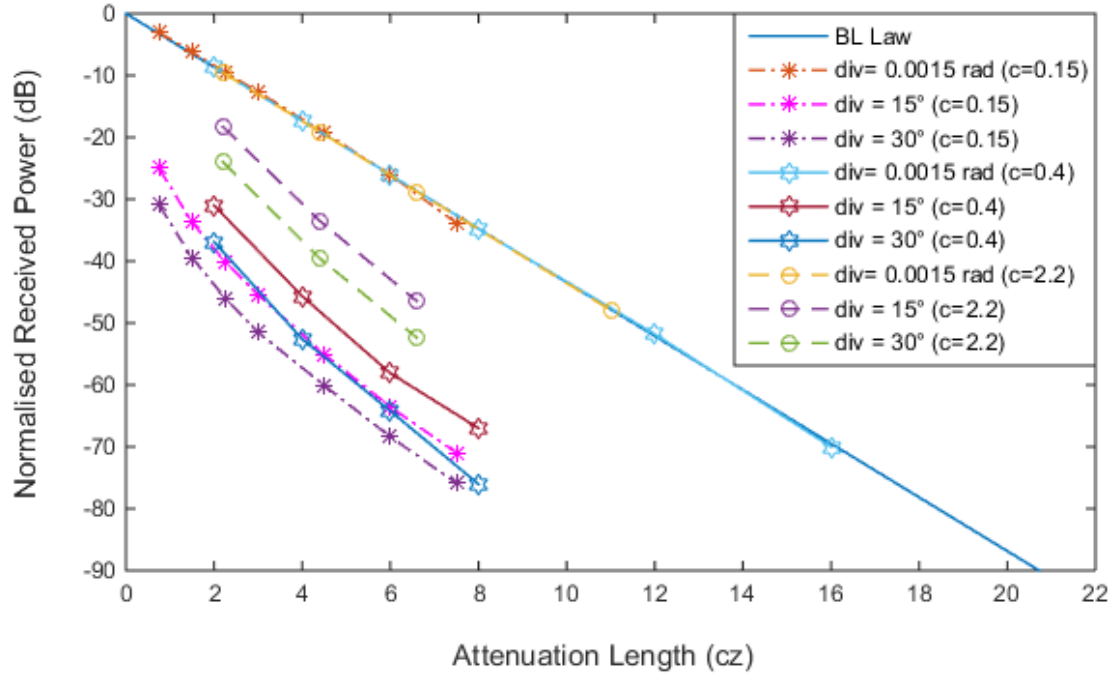


Figure 4.5: Normalised received power (unscattered component) versus attenuation length (AL) in clear, coastal and turbid water.

Figures 4.6(a) and (b) show the path loss performances for the scattered components of the light in three types of water. As discussed previously, the contribution of scattered light to the total received power is less significant as unscattered light dominates in clear water. This is illustrated in Figure 4.6(a), where the power received due to scattered light which uses collimated beam that contributed to the total received power is smaller by 20 dB compared to the total received power.

However in coastal water, the power received by the scattered component from collimated beam is relatively the same and as predicted by BL law indicating that more scattered light is collected. The power received due to

scattered light collected in turbid water for collimated beam is slightly high compared to BL law. One observation to be highlighted is that the collection of scattered light significantly impacts the received power in turbid water and causes a longer range of operation by more than 15 m at -70 dB compared to the prediction by BL law.

In order to compare how the scattered light from different sources attenuates, the path loss curves of the scattered components are plotted with respect to the AL as shown in Figure 4.7. In general, it can be seen that the attenuation rate of the scattered light can be classified into two regions based on Mooradian classification which is presented in Section 4.2.1. The first region is the minimally scattered region where the scattered light attenuates at the same rate as BL law.

The second region is the multiply scattered region where the scattered light attenuates at a slower rate compared to BL law. For example, the transition point for diffuse beam in coastal water is predicted to be 22 m as presented in Table 4.3. This value corresponds to AL of 8.8. By referring to Figure 4.7, at lower AL ($AL < 8.8$), it can be seen that the scattered light in coastal water attenuates at the same rate as BL law and at higher AL ($AL > 8.8$), the scattered light in coastal water attenuates with slightly slower rate compared to BL law. A relatively similar behaviour is also observed in the attenuation rate of scattered light in turbid water as shown in Figure 4.7.

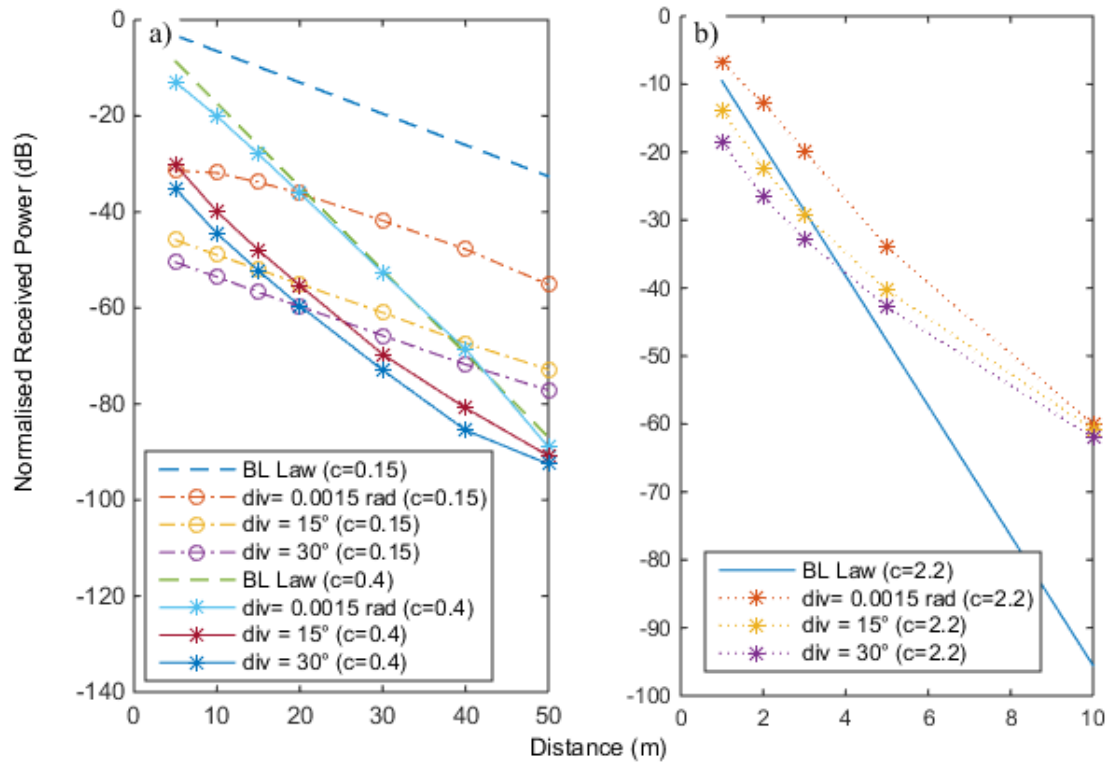


Figure 4.6: Normalised received power (scattered component) versus distance in (a) clear and coastal water and in (b) turbid water.

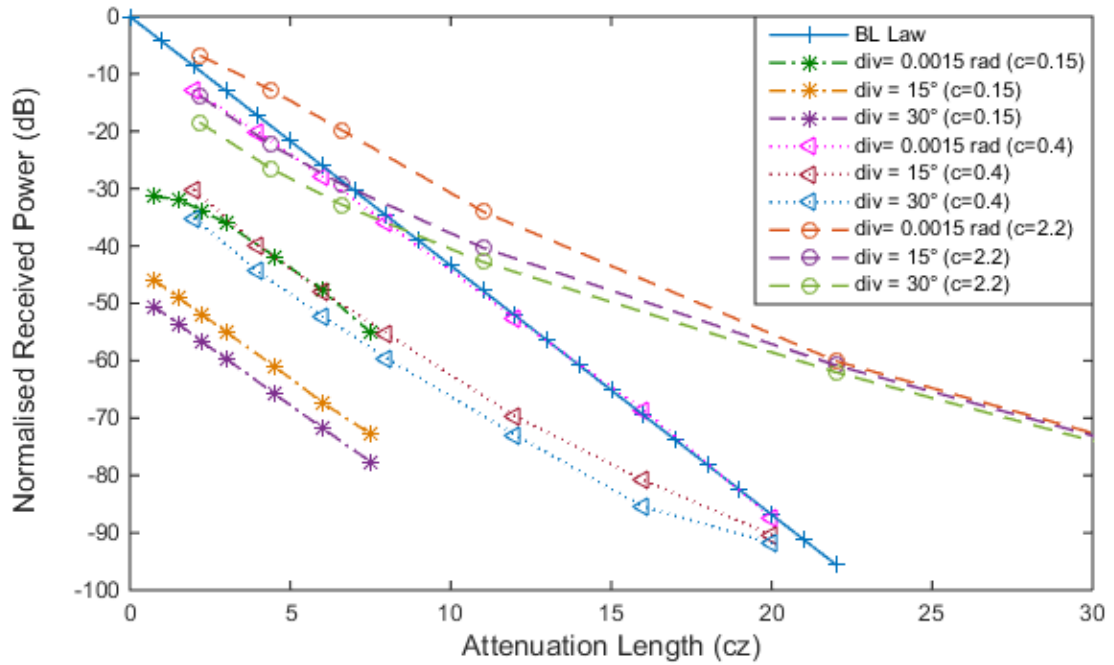


Figure 4.7: Normalised received power (scattered component) versus attenuation length (AL) in clear, coastal and turbid water.

4.5 Geometric loss

It should be noted that the simulations result for the path loss performance in the previous sections have included both loss due to the channel and also geometrical loss. The geometrical loss for a diffuse beam is much greater than the loss due to collimated beam as the beam spot size due to diffuse source is much greater than the aperture of the receiver. This fact has been demonstrated by the simulation of the diffuse beam in the previous section. Thus, in this section, the interest is to compare the results obtained by simulation and the mathematical equations used to calculate geometrical loss.

For a well aligned point to point link, the geometric loss is calculated as the ratio of receiver area to the transmitter beam spot area at the receiver [59]. The area of the beam spot size at the receiver location can be calculated as

$$A_{TX} = \pi(z \cdot \tan(\frac{\theta_{div}}{2}))^2 \quad (4.11)$$

where θ_{div} is the full angle beam divergence, z is the perpendicular distance between the transmitter and receiver. The area of a receiver with aperture diameter D_{RX} is

$$A_{RX} = \pi(\frac{D_{RX}}{2})^2 \quad (4.12)$$

Thus the geometrical loss can be calculated as

$$Loss_{geo} = \frac{A_{RX}}{A_{TX}} = \frac{D_{RX}^2}{4 \left(z \tan(\theta_{div}/2) \right)^2} \quad (4.13)$$

Combining the BL law path loss and geometrical loss equation results in the received optical power as

$$P_{RX} = P_T \frac{D_{RX}^2 \exp(-cz)}{4 \left(z \tan(\theta_{div}/2) \right)^2} \quad (4.14)$$

Next, equation 4.14 is used to plot the path loss performance to be compared with the simulations results for diffuse beams as illustrated in Figure 4.8. Notably, the path loss predicted by simulation fairly matches the path loss predicted by the equation 4.14 in clear water. However, in coastal and turbid water, the mathematical equation fails to predict the attenuation of the diffuse beams for longer ranges. For example in Figure 4.8(b), the equation accurately predicts the path loss for both diffuse beams up to distance 10 m. This is mainly because the effect of multiple scattering is not considered in the equation resulting inaccuracy in path loss calculation in high scattering environment and long distance. Thus, it is concluded that the incorporation of the geometrical loss to calculate the path loss performance of diffuse links in the widely use link equation is only able to predict the path loss in clear and coastal water where scattering is not significant.

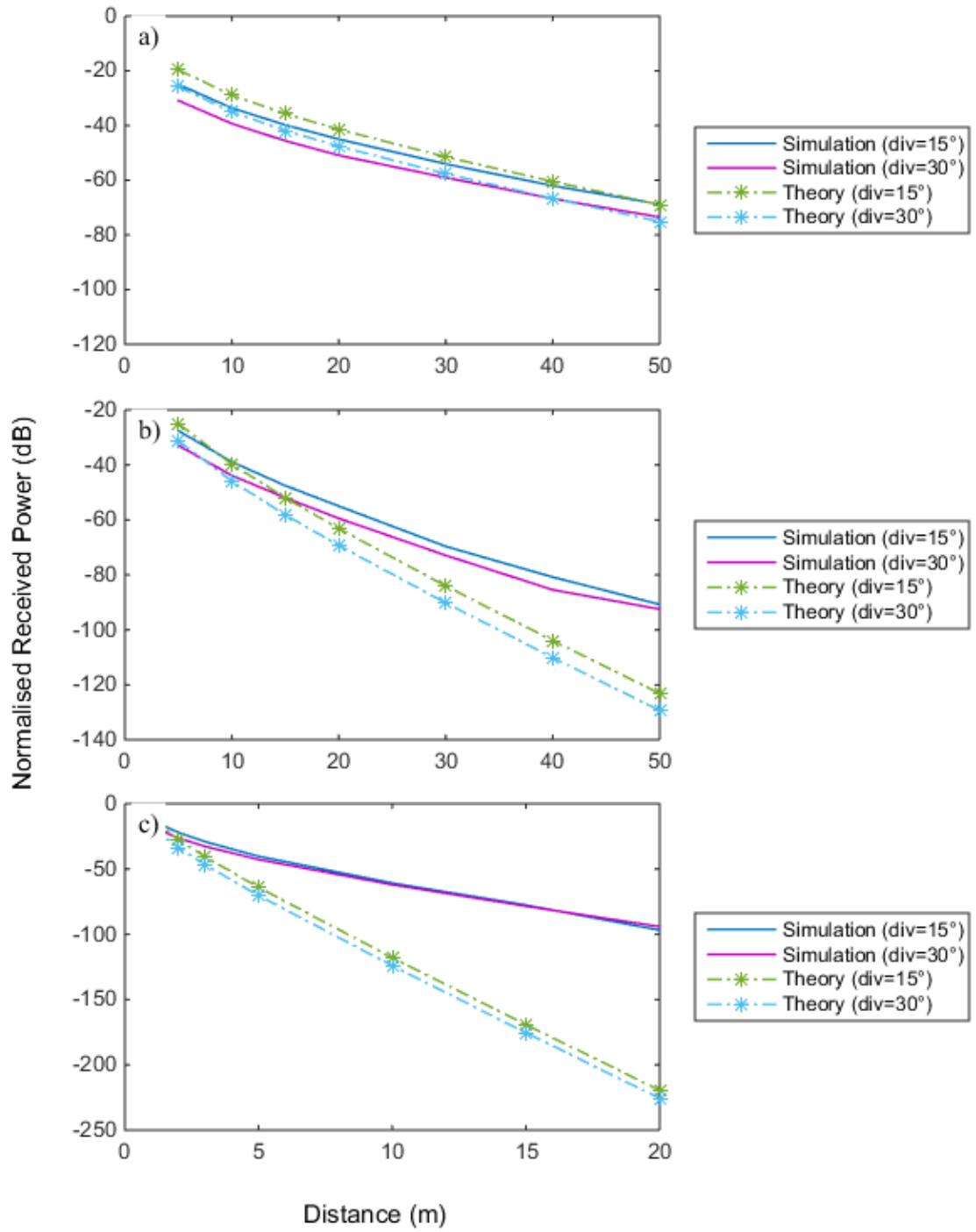


Figure 4.8: Path loss performance for diffuse beam along with theory incorporating geometrical loss in (a) clear water, (b) coastal water and (c) turbid water.

4.6 *Spatial dispersion versus distance*

The previous section presented the path loss performance for a perfectly aligned transmitter and receiver. In order to accurately describe the attenuation of light, the spatial dispersion effect due to beam spreading must also be considered. Thus, in this section the analysis is extended to study the attenuation rate of the spatial dispersion effect as the distance is increased.

Figures 4.9 to 4.11 show the normalised received power as a function of distance for various lateral positions (off-axis) in clear, coastal and turbid water. First of all, one common behaviour of the extreme off-axis ($r = 4\text{m}$) power reception is that there is a slight increase in the power received when the distance is varied from 5 m to 15 m in all types of water. This is due to the fact that at relatively short distance, less power is received at the off-axis ($r = 4\text{ m}$) location due to less spreading of the light beam. As the distance is increased, the beam spreading becomes more significant and causes an increase in off-axis power reception and subsequently decreases due to attenuation.

The information presented in this section is useful for link designers in two ways. First, it provides some insight into the effect of misalignment on the power reception specifically for collimated beams. Secondly, it can be used to predict the region where a uniform power distribution can be achieved. This is

especially useful for broadcast type links using diffuse beam where a zone of communication or a certain coverage area is to be established.

For example, it is shown in Figure 4.9(a) that the effect of misalignment for collimated beam in clear water is quite severe as a 1 m misalignment cause a reduction of power at approximately more than 30 dB depending on distance. In coastal and turbid water as shown in Figure 4.10(a) and 4.11(a), the misalignment effect for collimated beam is smaller as more light is scattered into the off-axis locations, thus increasing the power received. As the distance increases, the effect of misalignment is reduced to a point where there is no power penalty for any pointing mismatch. In coastal water, this point is approximately 50 m and in turbid water it occurs much earlier at approximately 15 m.

A similar observation in [123] where there is no region of uniform power distribution observed from 5 m till 50 m. This result can be explained by the fact that the onset of multiply scattered region occurs at 50 m as predicted by the simulation in Section 4.4.1. Thus it can be said that transmitter and receiver alignment is less critical at high scattering environment or large propagation distance. A similar result is obtained in [32] where the received irradiance is less sensitive to misalignment in highly turbid water ($c=2$) in the experimental measurement using a 12.48 m test tank.

As illustrated in Figures 4.9(b) and (c) to 4.11(b) and (c) , the impact of misalignment on diffuse beam is less significant than the collimated beam due to the higher spatial spreading caused by its wide beam divergence. The initial wider beam divergence has caused more light to be scattered to off-axis locations. The effect of misalignment is only significant for short ranges due to less beam spreading. In clear water, a uniform power distribution is reached when the distance is approximately 40 m and 30 m for 15° and 30° diffuse beam respectively. In coastal water, the distance is even shorter and found to be approximately 30 m and 20 m for 15° and 30° diffuse beam respectively.

It is also interesting to highlight that in turbid water, the same behaviour is observed irrespective of the size of beam divergence used as illustrated in Figure 4.11. This shows that in turbid water, the choice of beam divergence has little effect to the power received for the entire distance indicating that the multiple scattering is severe.

In short, it can be said that diffuse sources can be used to alleviate the pointing and tracking requirement at the expense of lower received power. For example, in clear water almost 40 dB is lost for transmission range up to 50 m if 15° diffuse source is used. In addition to that, the link designer can use this information to predict the sensitivity and the dynamic range required in the design of the UOWC system.

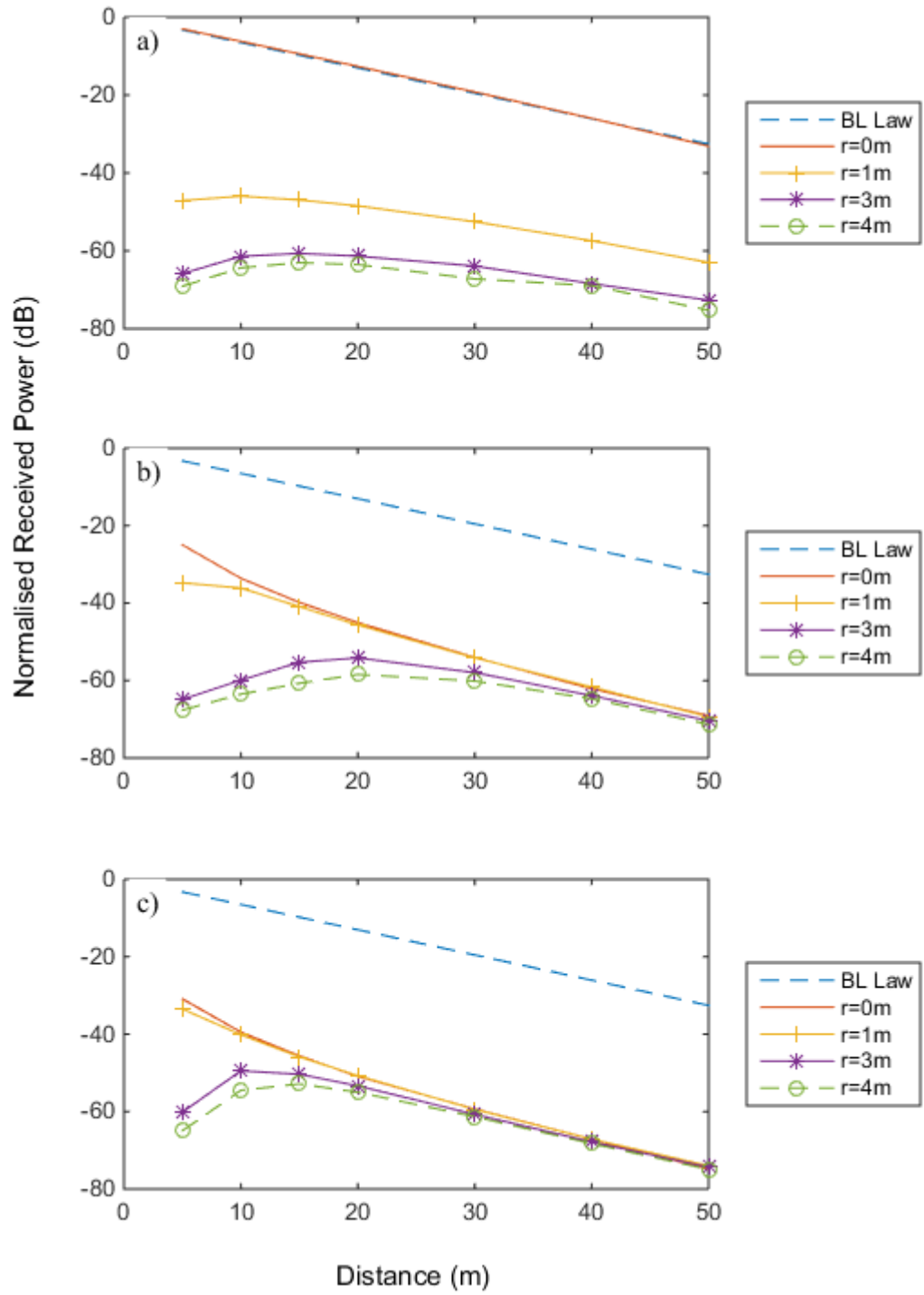


Figure 4.9: Normalised received power as a function of distance for various lateral positions in clear water for (a) collimated beam, (b) 15° diffuse beam and (c) 30° diffuse beam.

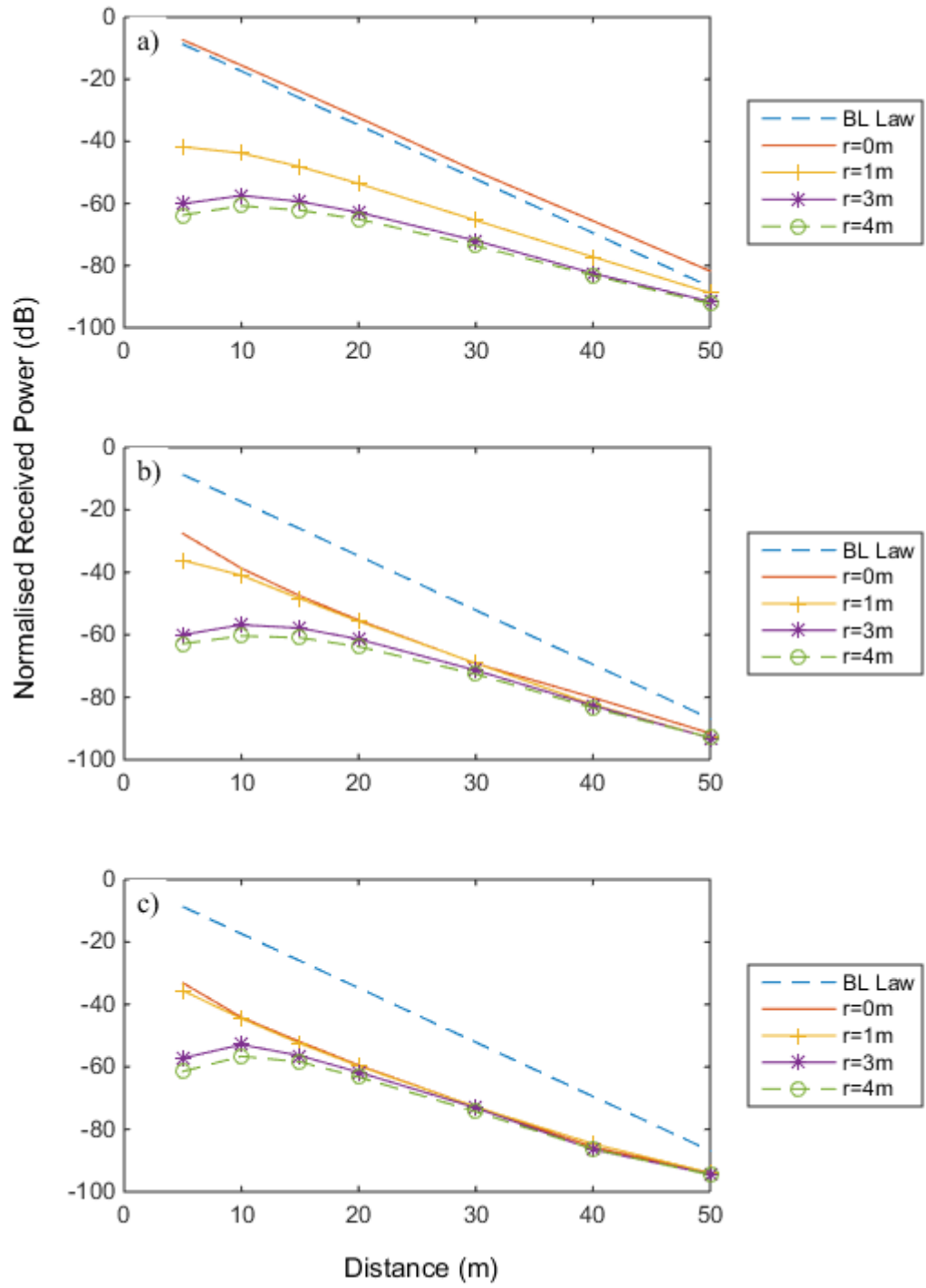


Figure 4.10: Normalised received power as a function of distance for various lateral positions in coastal water for (a) collimated beam, (b) 15° diffuse beam and (c) 30° diffuse beam.

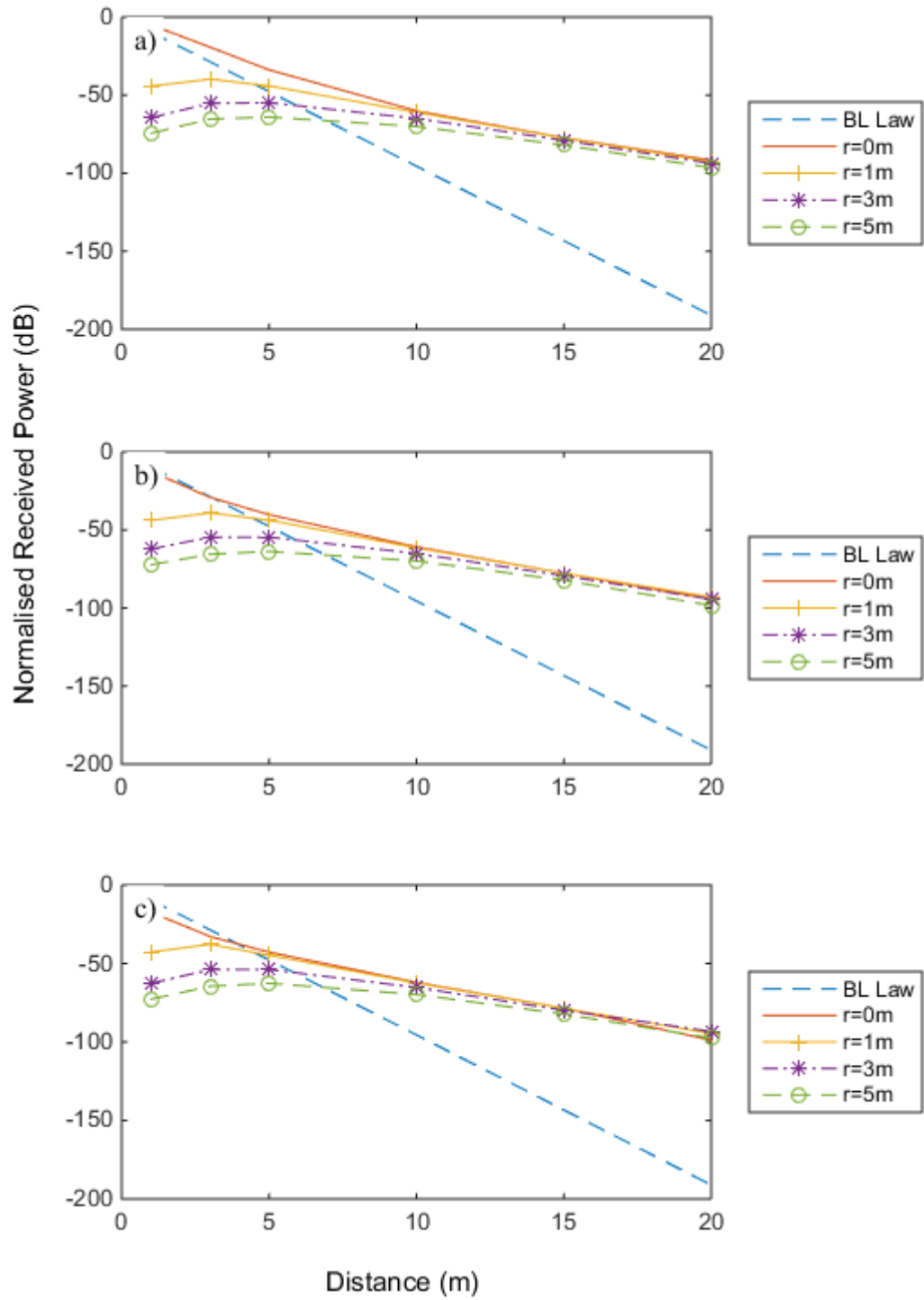


Figure 4.11: Normalised received power as a function of distance for various lateral positions in turbid water for (a) collimated beam, (b) 15° diffuse beam and (c) 30° diffuse beam.

4.6.1 Percentage of unscattered light: off-axis

This section provides further analysis of the contribution of unscattered light to the off-axis power reception. Figures 4.12 to 4.14 show the percentage of unscattered light collected at the receiver for various beam divergences at different lateral positions (off-axis) in clear water, coastal water and turbid water. In general, it can be seen that the percentage of unscattered light collected in clear water is still significant for the distance specified. One important observation to highlight is the percentage of unscattered light for all off-axis locations for 30° diffuse beam is higher compared to both smaller source divergences. This is intuitive as it is understood that more unscattered light can reach the off-axis locations due to the wider beam divergence.

In coastal water, it is clear from Figure 4.13(a) that, when collimated beam is used, unscattered light is collected for on-axis case only. This shows that the power received by all off-axis locations in this case is contributed by scattered light. For both wider source divergences, there is small amount of unscattered light collected at off-axis locations as shown in Figure 4.13 (b) and (c). For turbid water, no unscattered light is collected at off-axis locations for all beam divergences due to very high scattering environment as illustrated in Figure 4.14.

In short, the plot provides some insights in understanding how unscattered and scattered light contributes to the off-axis power reception. It can be said

that scattered light plays a major role as the vehicle that enables the communication at long range and at off-axis locations.

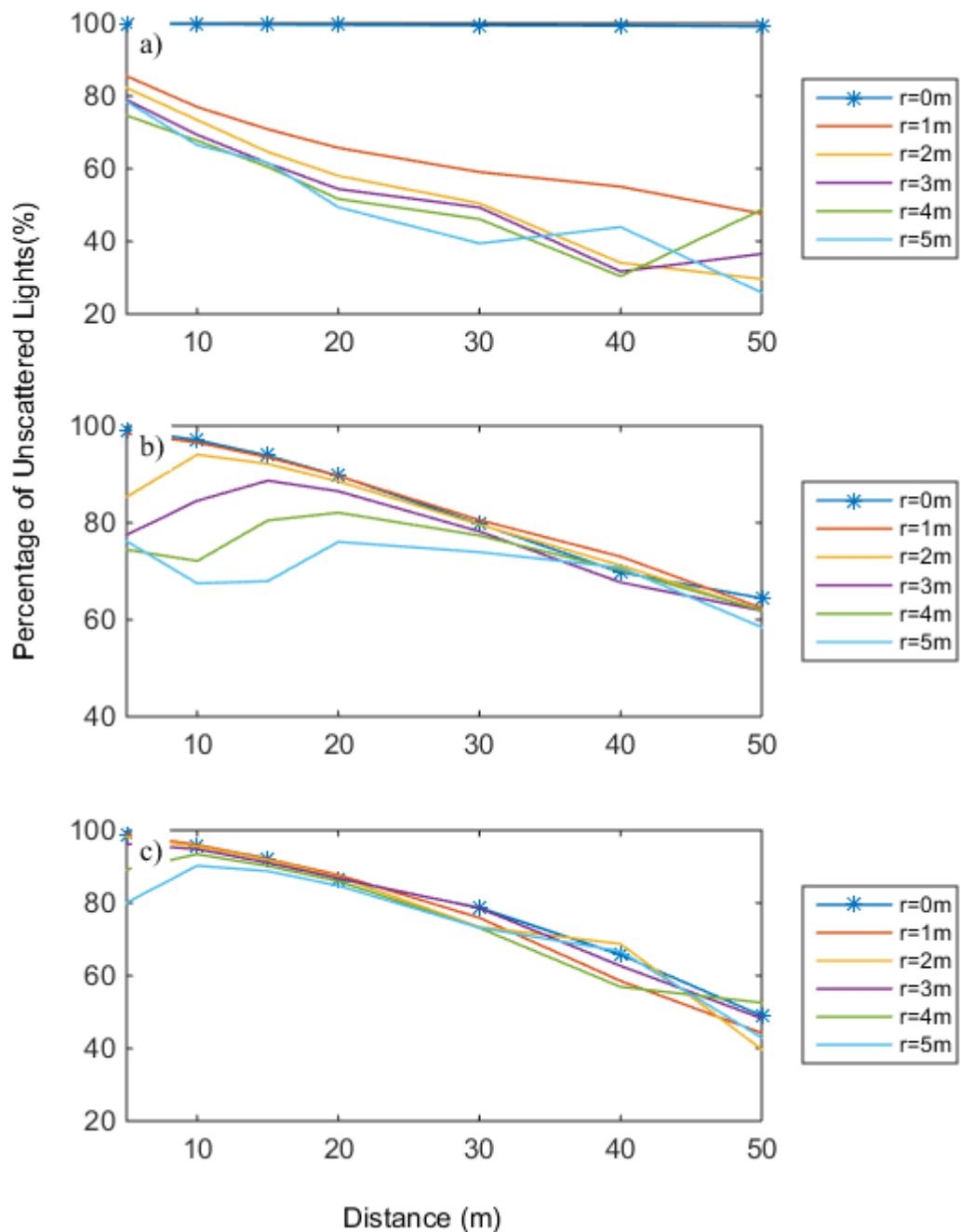


Figure 4.12: The percentage of the unscattered light that contributes to the total power reception for various lateral positions in clear water for (a) collimated beam (b) 15° diffuse beam and (c) 30° diffuse beam.

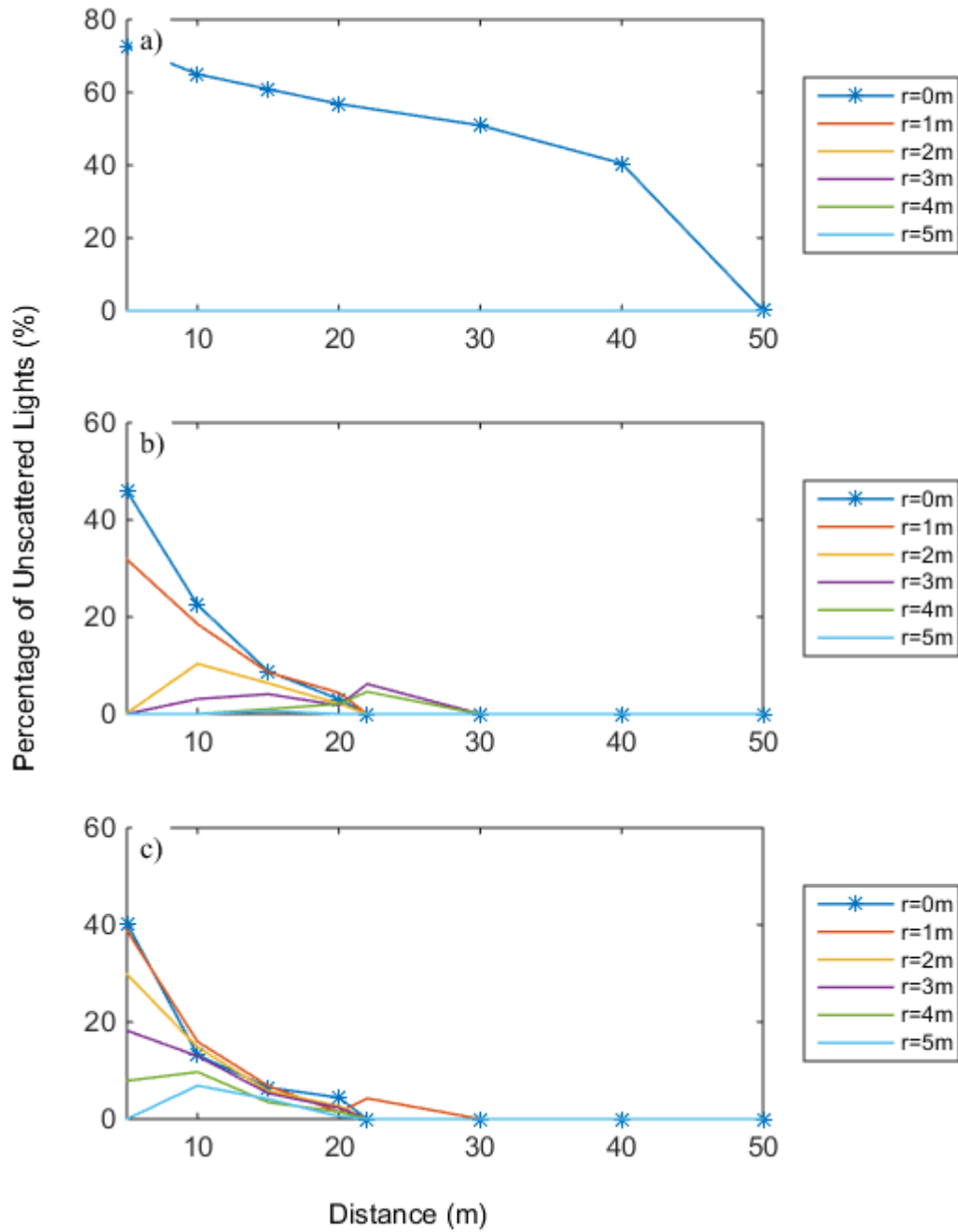


Figure 4.13: The percentage of the unscattered light that contributes to the total power reception for various lateral positions in coastal water for (a) collimated beam (b) 15° diffuse beam and (c) 30° diffuse beam.

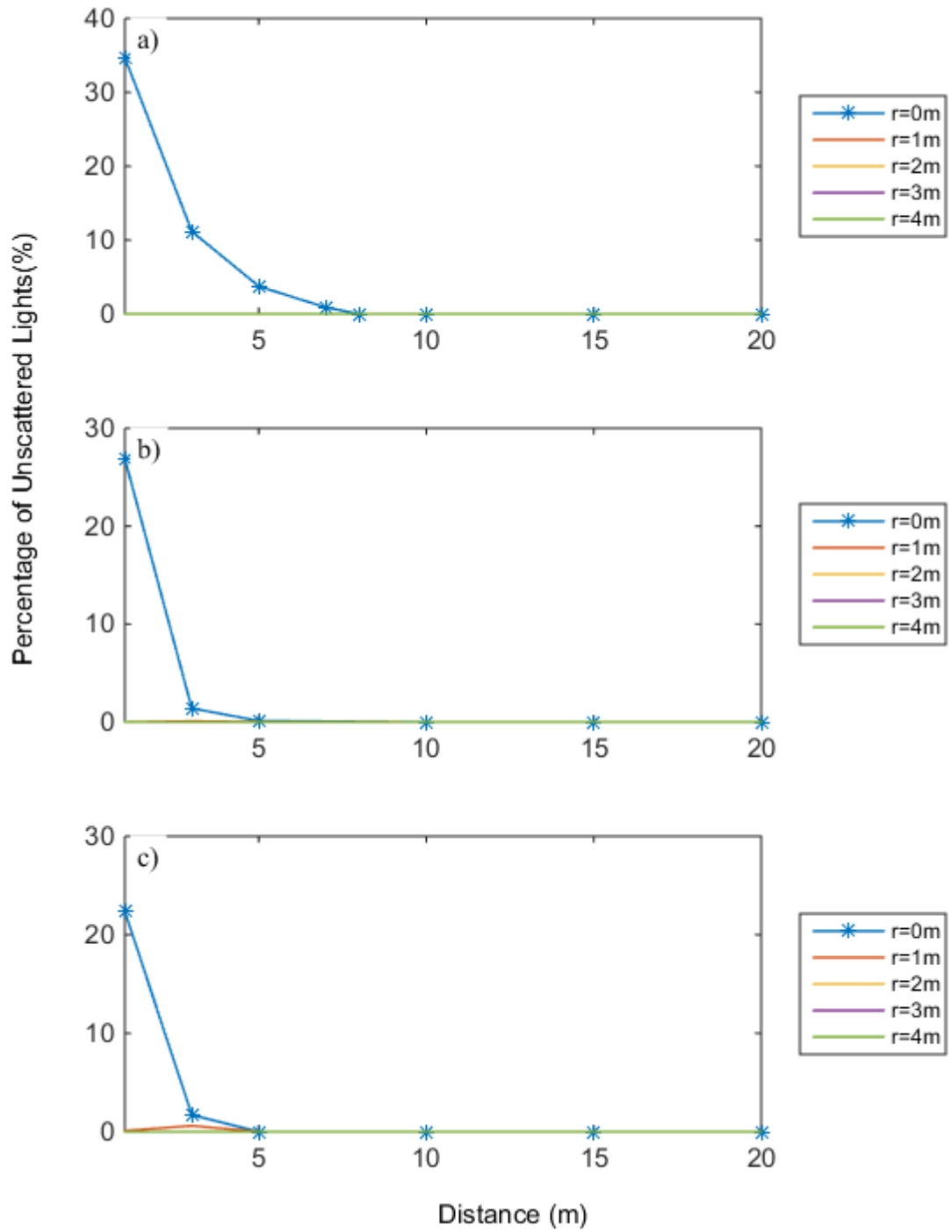


Figure 4.14: The percentage of the unscattered light that contributes to the total power reception for various lateral positions in turbid water for (a) collimated beam (b) 15° diffuse beam and (c) 30° diffuse beam.

4.7 Conclusion

This chapter presents the important components in link budget calculations; path loss modelling and characterisation. It has been shown that BL law has limited applicability as it is not accurate for all water environments. Few other analytical equations that have been proposed by other researchers are highlighted as well and have shown to be valid for a certain range due to the complexity of the signal propagation in underwater channel. Therefore, path loss modelling using MC simulation is considered as the best method to aid in link budget calculations as they provide more accurate description of the influence of scattering and other system parameters on the UOWC link performances.

Firstly, it has been demonstrated that path loss performance for diffuse beam can be predicted numerically since an exact mathematical equation is quite complicated to solve. From the simulations results presented, it is highlighted that there is an inaccuracy of characterising the path loss performance, if one just makes decisions based on AL as the determining parameter, without considering the propagation distance and attenuation coefficient, c of the water environment. Thus a plot of path loss as a function of distance will provide an accurate prediction compared to path loss as a function of AL only.

Several interesting observations have been made for the first time through simulations where a quantitative analysis of contributions from unscattered

and scattered component of light is demonstrated. This information is used to propose the transition point between minimally scattered and multiply scattered region for diffuse beam by plotting the fraction of the unscattered light collected by the receiver. At the same time, the transition point for collimated light in turbid water has been proven to match the prediction of diffusion length, L_D equation.

Further investigations on the attenuation of unscattered light and scattered light show the different behaviour between them where the former attenuate according to BL law as predicted and the latter attenuate at a slower rate as distance is increased. By incorporating the geometrical loss to BL law, it is shown that the mathematical equation is only valid to be applied to minimal scattering region where unscattered light dominates.

Next the spatial distribution attenuation is presented to highlight how the beam spreading attenuates with distance. It is shown that for diffuse beam, a zone of uniform power distribution can be achieved at a much shorter distance compared to collimated beam, except in turbid water where the distance is found to be the same. It is also discussed that, even though scattering seems to cause higher attenuation, it has some benefit by providing some range of flexibility as the signal still can be recovered when misalignments happen. The simulation results can also be used to understand the range of pointing accuracy that can be tolerated in establishing a robust communication link. Finally the impact of scattering to spatial spreading is clearly seen by plotting

the percentage of unscattered light that contributed to the light reception in off-axis locations. It is concluded that, while scattering causes adverse effects to the underwater links, it is also seen as the vehicle that enables a more flexible communication links.

CHAPTER 5

Temporal and Angular Dispersions: Performance Analysis

5.1 *Introduction*

In the previous chapter, the path loss modelling and characterisation for various source divergences in different types of water were presented. Discussion on how unscattered and scattered components of light impact the path loss and spatial dispersion were also analysed. It was also shown that despite the fact that scattering contributed to the loss of power; it also provides some flexibility in pointing and tracking where a link can still be maintained at a lower received power. However, no information about temporal dispersion was investigated in the previous chapter. Thus this chapter will analyse the effect of scattering on the temporal dispersion and angular dispersion by first introducing the concept of scattering order probability. Then, a method used to characterise the scattering regimes in turbid media is introduced to be applied in UOWC. Based on the scattering regimes, the impulse response of the link is presented along with frequency

response which is used to predict the bandwidth that the channel may support. Then, further investigations into the angular dispersion are studied by exploring the angle of arrival (AOA) distributions. The AOA distributions will be shown as one of the important tool in receiver FOV design for optimising the performance.

5.2 *Scattering order*

This section investigates the nature of scattering behaviour of the photons that are collected at the receiver for various types of water. Specifically, the focus is on scattering order which is defined as the number of times the received photons have been scattered along their propagation path. This is one of the unique features of MC simulation which can provide the statistical information regarding the individual scattering order. The investigations on scattering order for collimated links have been reported in [31, 38]. It is shown that the number of scattering events increases gradually with attenuation length and rapidly after $AL = 15$. Thus, it is interesting to explore the scattering order behaviour of diffuse beams and study how it differs from collimated beam in various water turbidity levels. The number of scattering order can be calculated by using the weight of each photon as

$$\text{Scattering order, } n = \frac{\log(w_R)}{\log(\omega)} \quad (5.1)$$

Where w_R is the weight of the received photon and ω is the albedo of the water type. The probability of occurrence can be obtained by dividing the normalised received power for each scattering order with the total power of the received photons.

5.2.1 Scattering regimes

In the study of light scattering in turbid media; particularly within inhomogeneous polydisperse turbid media such as spray systems, the scattering order information is used in classifying the scattering environment into 3 regimes as shown in Table 5.1 [124]. Based on this concept, the same technique is proposed to be applied to UOWC channel as scattering order probability can be obtained from MC simulation.

Table 5.1: Classification of scattering regimes as a function of scattering order

Regimes	Scattering order, n	Description
I Single scattering regime	$n \leq 1$	This region is dominated by unscattered and single scattering photons.
II Intermediate scattering regime	$n=2-9$	Average number of scattering events is between 2 and 9. One dominant scattering order is clearly defined.
III Multiple scattering regime	$n > 9$	In this region, the average number of scattering events is greater than 9. The amount of each scattering order is relatively the same.

Now, in order to evaluate the scattering order probability of various beam divergences in each type of water, four different distances are chosen as shown in Table 5.2 . The information on the transition point proposed in Chapter 4 where the percentage of unscattered photons drop to zero is considered in the distance selection. In order to capture all the photons that reach the receiver, the receiver FOV is set to 180° with 10 cm aperture diameter. A similar simulation parameters as Chapter 4 are used in this section.

Table 5.2: Select distance in various types of water.

Types of water	Distance
Clear water	15 m, 30 m, 50 m and 70 m
Coastal water	15 m, 22 m, 50 m and 70 m
Turbid water	1 m, 3 m, 7 m and 15 m

Figure 5.1 to 5.2 show the scattering order histogram for the three types of water as discussed in Chapter 4. For each distance, the scattering order histogram is plotted for three beam divergence sizes showing both the scattering order at on-axis and off-axis (4 m offset) locations.

- **On-axis**

It can be seen from Figures 5.1 to 5.4 that in clear water, collimated beam shows high probability of unscattered photons for the entire range up to 70 m. In contrast, both diffuse beams show a slightly lower probability of unscattered photons with small probability of higher scattering orders up to distance of 70 m. In coastal water, there is still high probability of receiving unscattered

photons when collimated beam is used up to distance 50 m where at that distance no more unscattered photons are received. On the other hand, both diffuse beams show higher contributions from the multiple scattered photons ($n>1$) compared to the unscattered photons where at 22 m, the probability of unscattered photons is reduced to less than 5%. At 50m, both diffuse beams are dominated by multiple scattered photons (i.e; $n=5-20$). Thus, it can be deduced that this distance corresponds to the intermediate scattering regime for both diffuse beams.

An interesting observation can be noticed at 70 m, where a relatively similar scattering order probability is shown irrespective of the sizes of beam divergences. It is illustrated that most photons have been scattered at least 12 times indicating that this region can be classified as multiple scattering regimes. It should be noted that this distance matched the prediction of the diffusion length, L_D for collimated beam in coastal water which is estimated to be at 76 m as presented in Section 4.2.

In turbid water, more scattering occurs which is illustrated by high probability of multiple scattering events even at short distance. For both diffuse beams, the percentage of unscattered and single scattered photons is less than 10% at 3 m. As the distance is increased to 7 m, all the photons have been scattered at least 5 times. A consistent behaviour as Figure 5.8 is observed at 15 m where the scattering behaviour for all beam divergences are relatively the same. It can be seen that all of the photons that reach the receiver have been scattered

at least 12 times. Thus it can be said that this distance can be classified as multiple scattering region for turbid water.

- Off-axis

For collimated beam in clear and coastal water, most light that reaches off-axis locations consist of the scattered components as shown in Figures 5.1(a) to 5.8(a). On the other hand, for both diffuse beams in clear and coastal water, there are high probabilities of receiving unscattered photons at the off-axis locations. This is evidently due to the wide divergence beam that causes large spread in the distribution of light that reach the off-axis locations which cause the scattering order probability to be relatively the same with on-axis locations as expected. In turbid water, at distances 1 m and 3 m a distinct behaviour of the scattering order can be seen where the off-axis locations show higher order scattering events. This is apparently due to the fact that the off-axis locations are not situated within the area where the light beam illuminates.

Briefly, this section illustrates the comparison of scattering behaviour in collimated and diffuse links in various types of water for both on-axis and off-axis locations. It can be said that both diffuse beams exhibit more scattering at a certain distance compared to collimated beam which is expected to cause more temporal dispersions and angular dispersions. This will be discussed in the next section.

From the analysis of the scattering order probability in this section, the parameterisation of the scattering regime for diffuse beam based on distance is proposed in Table 5.4. However, several modifications were made to the description of the scattering regime. Instead of classifying the scattering regime based on the average number of scattering events, a more suitable description for UOWC is to use the minimum scattering events as the determining factor. This means that if the minimum scattering exhibited by the link is less than 1, the link can be classified as minimal scattering regime and if the minimum scattering is between 2 to 9, the link can be classified as intermediate scattering and so forth.

However, the transition point for off-axis scattering regime cannot be obtained since the scattering at off-axis locations also depends on the offset distance from the beam center. Besides that, it should be noted that the scattering regimes for clear water cannot be identified as the transition point is predicted to be more than 70 m which is beyond the maximum distance simulated in this thesis. The next section will investigate temporal dispersions and angular dispersion based on the scattering regimes proposed.

5.2.2 Scattering order histogram : Clear water

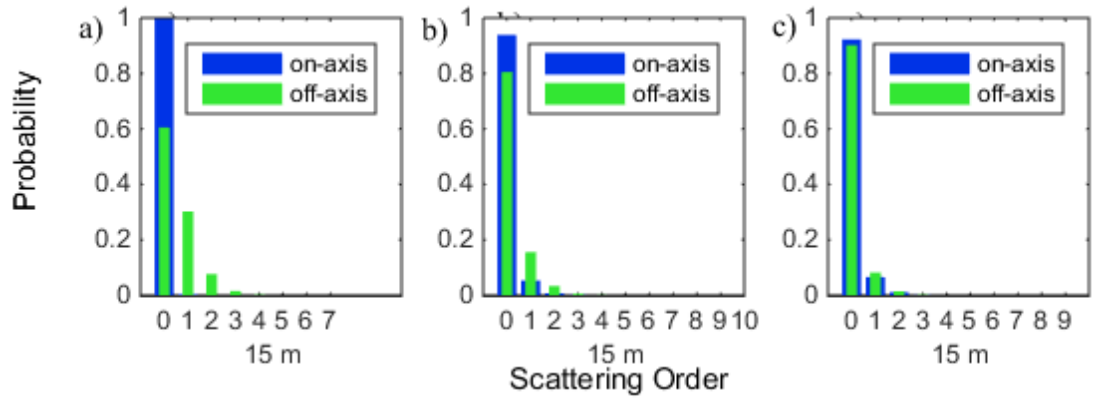


Figure 5.1: Scattering order histogram in clear water at 15 m for (a) collimated beam (b) 15° diffuse beam and (c) 30° diffuse beam.

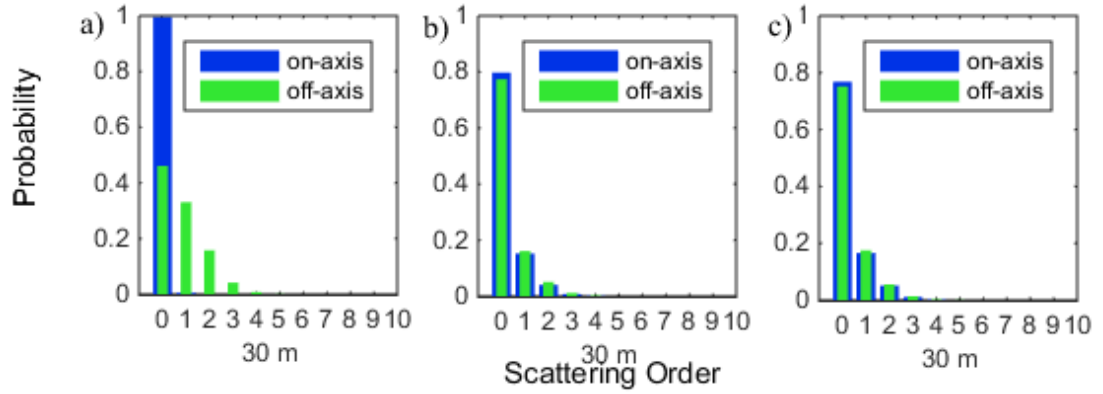


Figure 5.2: Scattering order histogram in clear water at 30 m for (a) collimated beam (b) 15° diffuse beam and (c) 30° diffuse beam.

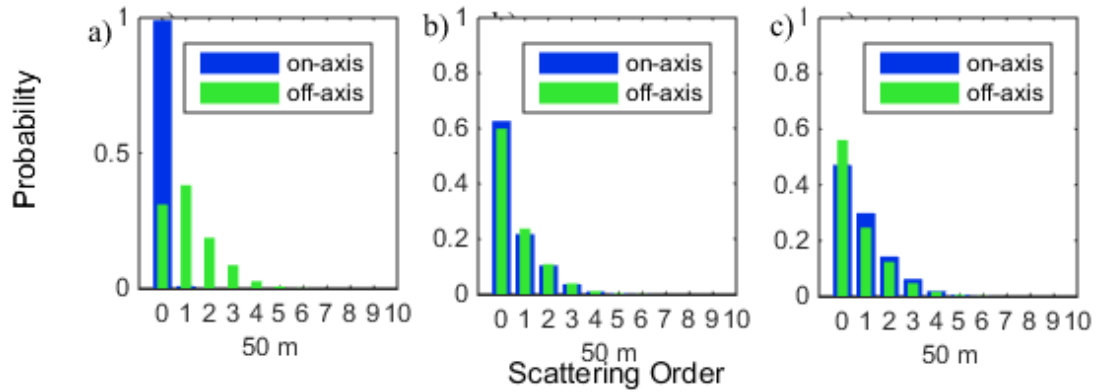


Figure 5.3: Scattering order histogram in clear water at 50 m for (a) collimated beam (b) 15° diffuse beam and (c) 30° diffuse beam.

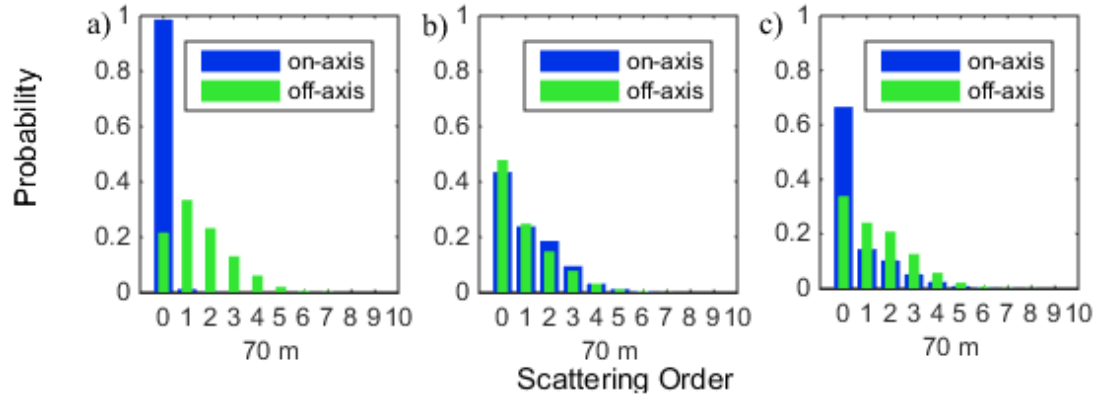


Figure 5.4: Scattering order histogram in clear water at 70 m for (a) collimated beam (b) 15° diffuse beam and (c) 30° diffuse beam.

5.2.3 Scattering order histogram : Coastal water

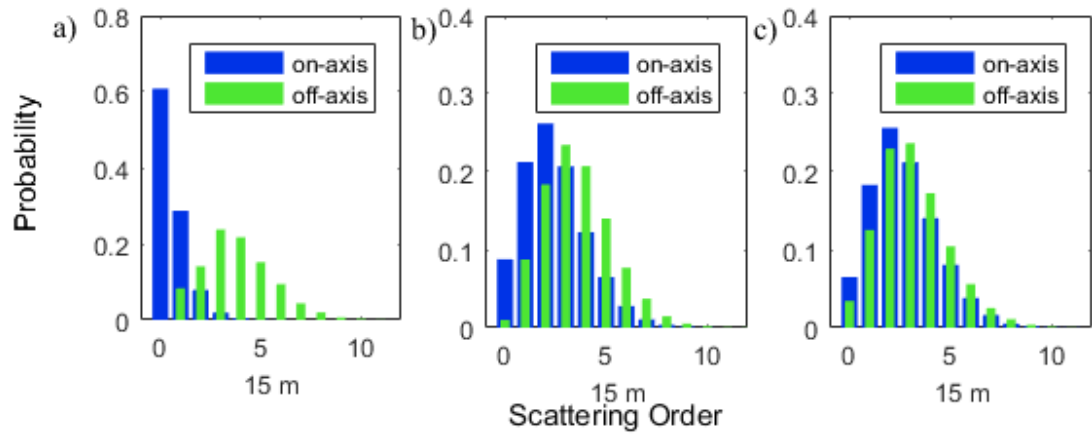


Figure 5.5: Scattering order histogram in coastal water at 15m for (a) collimated beam (b) 15° diffuse beam and (c) 30° diffuse beam.

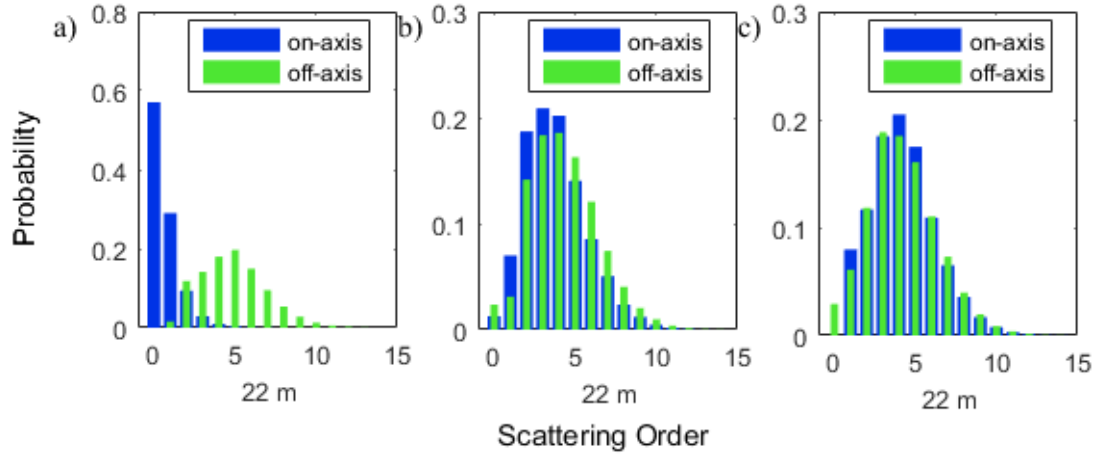


Figure 5.6: Scattering order histogram in coastal water at 22 m for (a) collimated beam (b) 15° diffuse beam and (c) 30° diffuse beam.

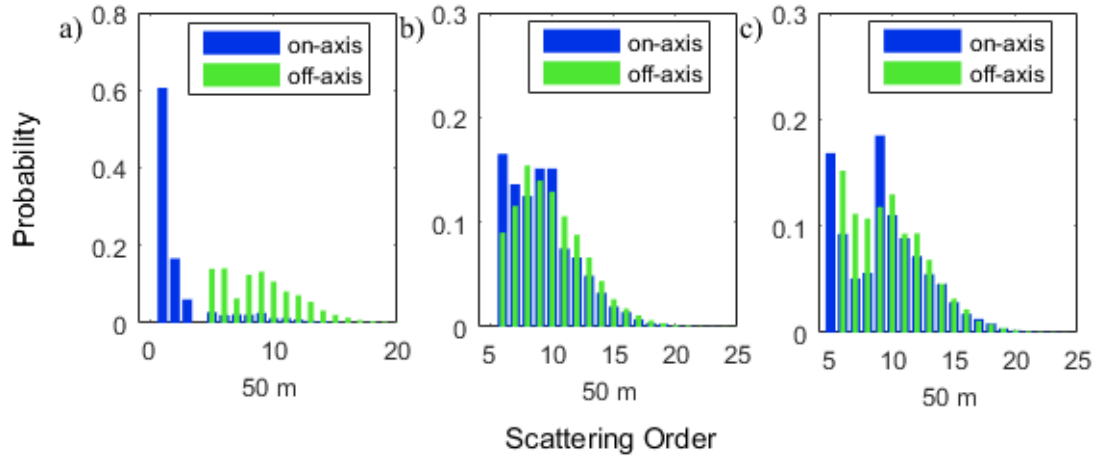


Figure 5.7: Scattering order histogram in coastal water at 50 m for (a) collimated beam (b) 15° diffuse beam and (c) 30° diffuse beam.

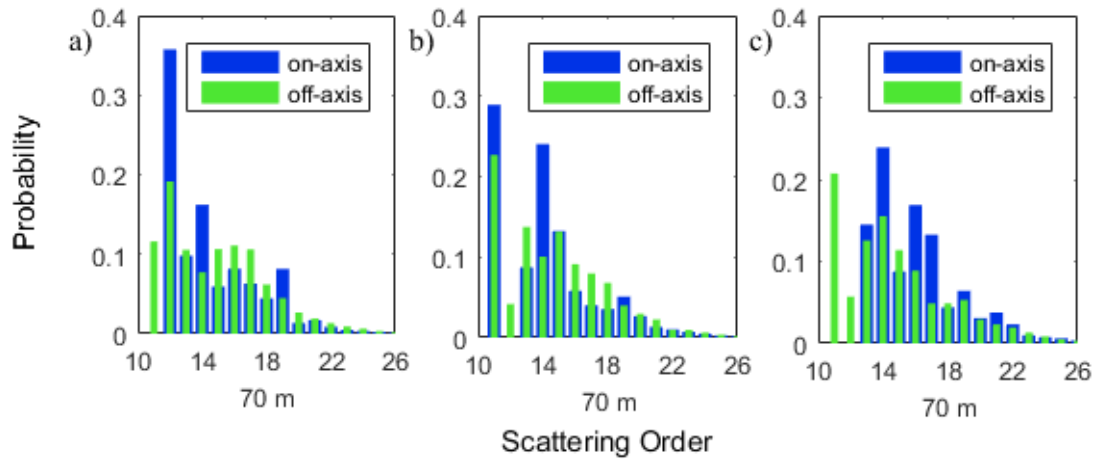


Figure 5.8: Scattering order histogram in coastal water at 70 m for (a) collimated beam (b) 15° diffuse beam and (c) 30° diffuse beam.

5.2.4 Scattering order histogram : Turbid water

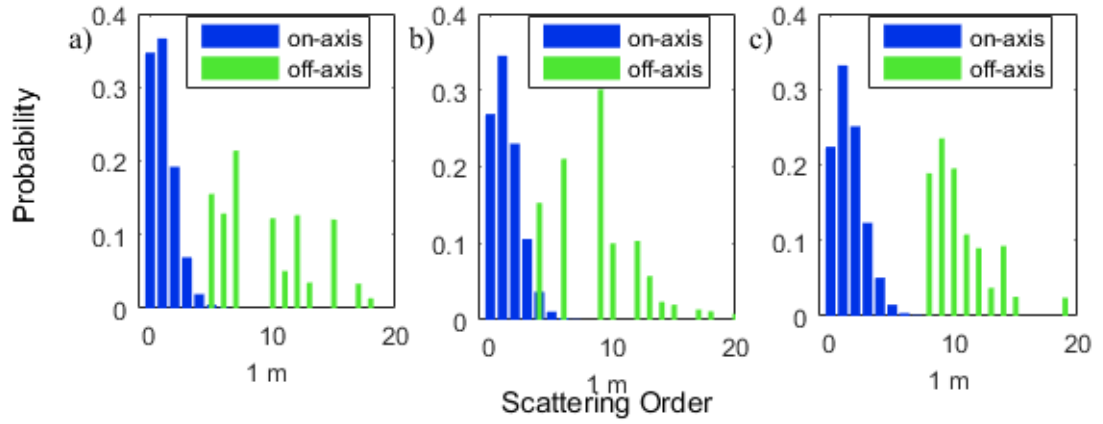


Figure 5.9: Scattering order histogram in turbid water at 1 m for (a) collimated beam (b) 15° diffuse beam and (c) 30° diffuse beam.

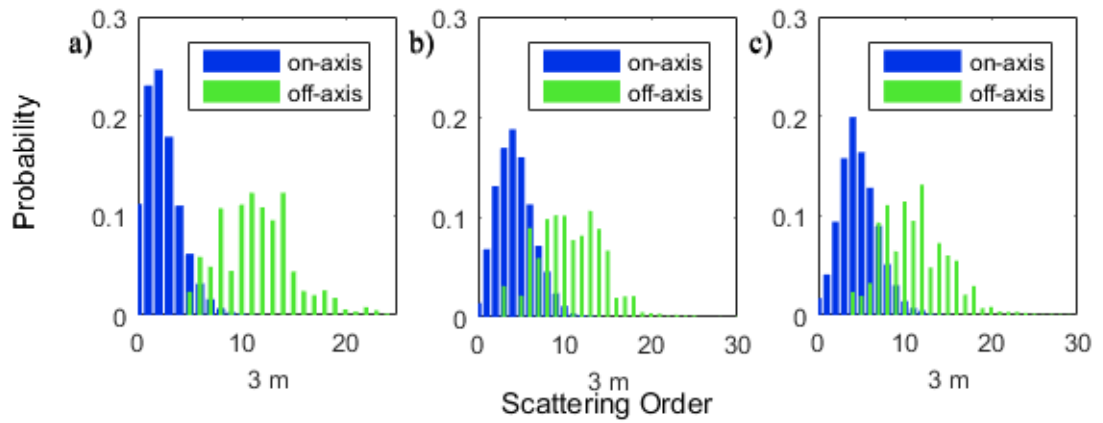


Figure 5.10: Scattering order histogram in turbid water at 3 m for (a) collimated beam (b) 15° diffuse beam and (c) 30° diffuse beam.

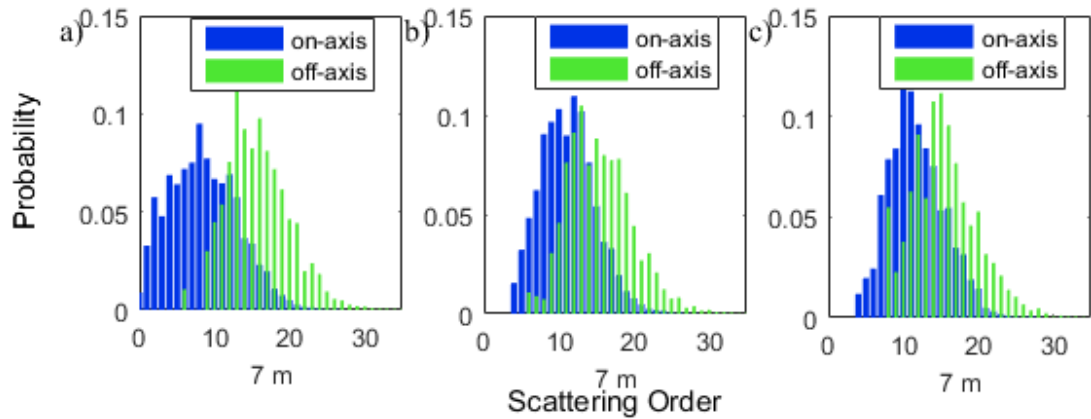


Figure 5.11: Scattering order histogram in turbid water at 7 m for (a) collimated beam (b) 15° diffuse beam and (c) 30° diffuse beam.

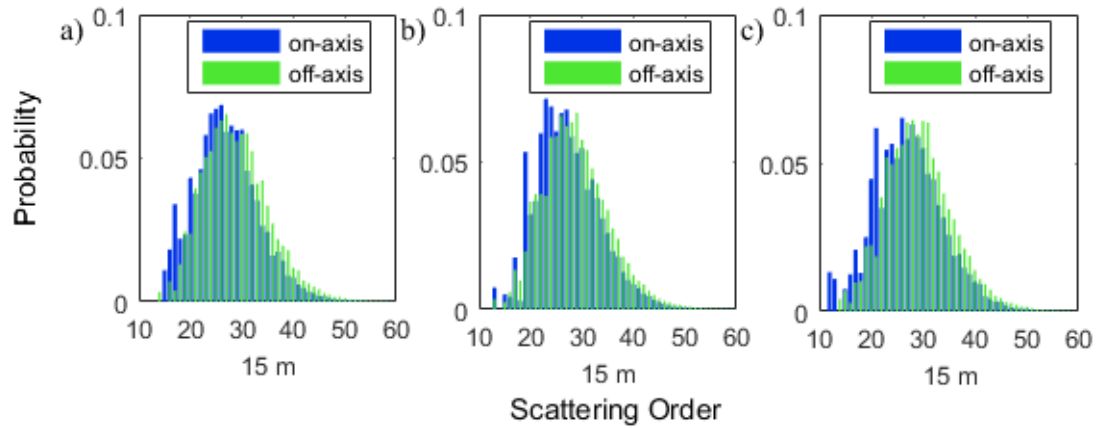


Figure 5.12: Scattering order histogram in turbid water at 15 m for (a) collimated beam (b) 15° diffuse beam and (c) 30° diffuse beam.

Table 5.3: Modified scattering regime description.

Regimes	Scattering order, n	Description
I Minimal scattering regime	$n \leq 1$	The minimum scattering events is less than or equal to 1.
II Intermediate scattering regime	$n=2-9$	The minimum number of scattering events is between 2 and 9.
III Multiple scattering regime	$n>9$	The minimum number of scattering events is greater than 9.

Table 5.4: Proposed transition points.

Types of water	Beam divergence	Scattering Regimes		
		I Minimal Scattering Regime	II Intermediate Scattering Regime	III Multiple Scattering Regime
Clear water ($c=0.15$)	0.0015 rad	~	~	~
	15°	~	~	~
	30°	~	~	~
Coastal water ($c=0.4$)	0.0015 rad	≤ 50 m	~	~
	15°	≤ 22 m	$22 \text{ m} < z < 70 \text{ m}$	$z \geq 70 \text{ m}$
	30°	≤ 22 m	$22 \text{ m} < z < 70 \text{ m}$	$z \geq 70 \text{ m}$
Turbid water ($c=2.2$)	0.0015 rad	≤ 7 m	$7 \text{ m} < z < 15 \text{ m}$	$z \geq 15 \text{ m}$
	15°	≤ 3 m	$3 \text{ m} < z < 15 \text{ m}$	$z \geq 15 \text{ m}$
	30°	≤ 3 m	$3 \text{ m} < z < 15 \text{ m}$	$z \geq 15 \text{ m}$

5.3 *Impulse response*

The channel impulse response is one of the key parameters that is necessary in understanding the channel performance and has been studied by several researchers to characterise UOWC links. Due to the complex nature of solving RTE analytically, MC numerical simulation is widely used to model the channel impulse response. One main advantage of using MC simulation is it can be used to predict the temporal dispersion effects at a very high resolution in which is difficult to measure experimentally due to the limitation of the receiver

sensitivity [35]. In [39], by using a diffused beam of 20° , it is found that in clear water, the channel can still be considered as frequency nonselective for distances up to 50 m. In [31], an experiment is conducted to measure the impulse response of collimated beam in a water tank of length 12.48 m which is then used to validate the simulation results.

Apart from using MC simulation and experimental work, an effort to develop a closed form expressions using double Gamma functions to model the impulse response has been conducted in [42]. They concluded that the double Gamma functions model is valid for wide configuration systems, defined as systems with a large beam divergence and a large receiver FOV. However, for narrow communication system which consist of narrow source divergence and narrow FOV, the impulse response can be approximately modelled by ideal delta function. It is also highlighted that the exact region where the double Gamma is valid is unknown.

Thus, it is believed that the transition regimes proposed in this thesis will provide some insights on how to classify the region where the model can be applied. In [42], the double Gamma function is evaluated for coastal link ($c=0.4$) at 30 m and 40 m and in turbid water ($c=2.2$) at 10 m and 12 m respectively which matches the intermediate scattering regimes proposed in this thesis for diffuse beam.

5.3.1 Impulse response: Analysis

This section discusses the impulse response for each case corresponds to the distance chosen in the previous section where scattering order probability is presented. The largest receiver FOV, i.e. 180° is considered because the aim is to investigate the temporal dispersion that is caused by all the photons that reach the receiver. Figures 5.13 to 5.15 depict the impulse responses for both on-axis and off-axis locations using different beam divergences in the three types of water. The vertical coordinate represents the normalized received power and the horizontal coordinate represents the time delay relative to the time of arrival of the first photon (i.e. the time at which the first photon reaches the receiver is set as the origin).

5.3.2 On-axis

By comparing the scattering order histogram in Section 5.1 and the impulse response in Figures 5.13 to 5.15, the correlations between them can be understood clearly. Thus it is helpful to discuss the impulse response behaviour based on the three scattering regimes proposed in Section 5.2. Firstly, in minimal scattering regimes, the impulse response shows a dominant peak implying higher percentage of unscattered photons. As the number of unscattered photons reduce, the impulse response peak decreases and shows larger spread primarily due to collection of high delays photons which undergoes multiple scattering. This can be seen in Figure 5.14(c) that depicts

the impulse response at 22 m in coastal water. It should be noted that at this distance, the contributions of unscattered component to the power received is less than 5% for both diffuse beams. In intermediate scattering regime (Regime II), such as at 50 m in coastal water and 7 m in turbid water, the impulse response still shows a dominant peak but at a smaller magnitude due to the high probability of multiple scattering events. In the third regime (Regime III), where multiple scattering dominates, the impulse response shows longer 'tail' signifying the collection of high delay multiple scattered photons. For example, by referring to Figure 5.14(g) and Figure 5.15(g) which illustrates the impulse response at 70 m in coastal water and 15 m in turbid water, the impulse responses show large spread due to the fact that all of the photons have been scattered by at least 12 times in coastal water and 13 times in turbid water. It is also apparent from those figures that the behaviour of the impulse responses for different beam divergences are not very distinguishable from each other.

5.3.3 Off-axis

At off-axis locations in clear water, the high contribution of scattered photons results in a very large spread impulse response for collimated beam. As expected, the impulse response due to both diffuse beam show high peak indicating the high contributions from unscattered photons. A similar behaviour is also observed in coastal water up to distances of 22 m where beyond that, the peak diminishes and the impulse response shows larger

spread. In turbid water, the impulse response shows no dominant peak due to the fact that most photons have undergone at least 5 scatterings events.

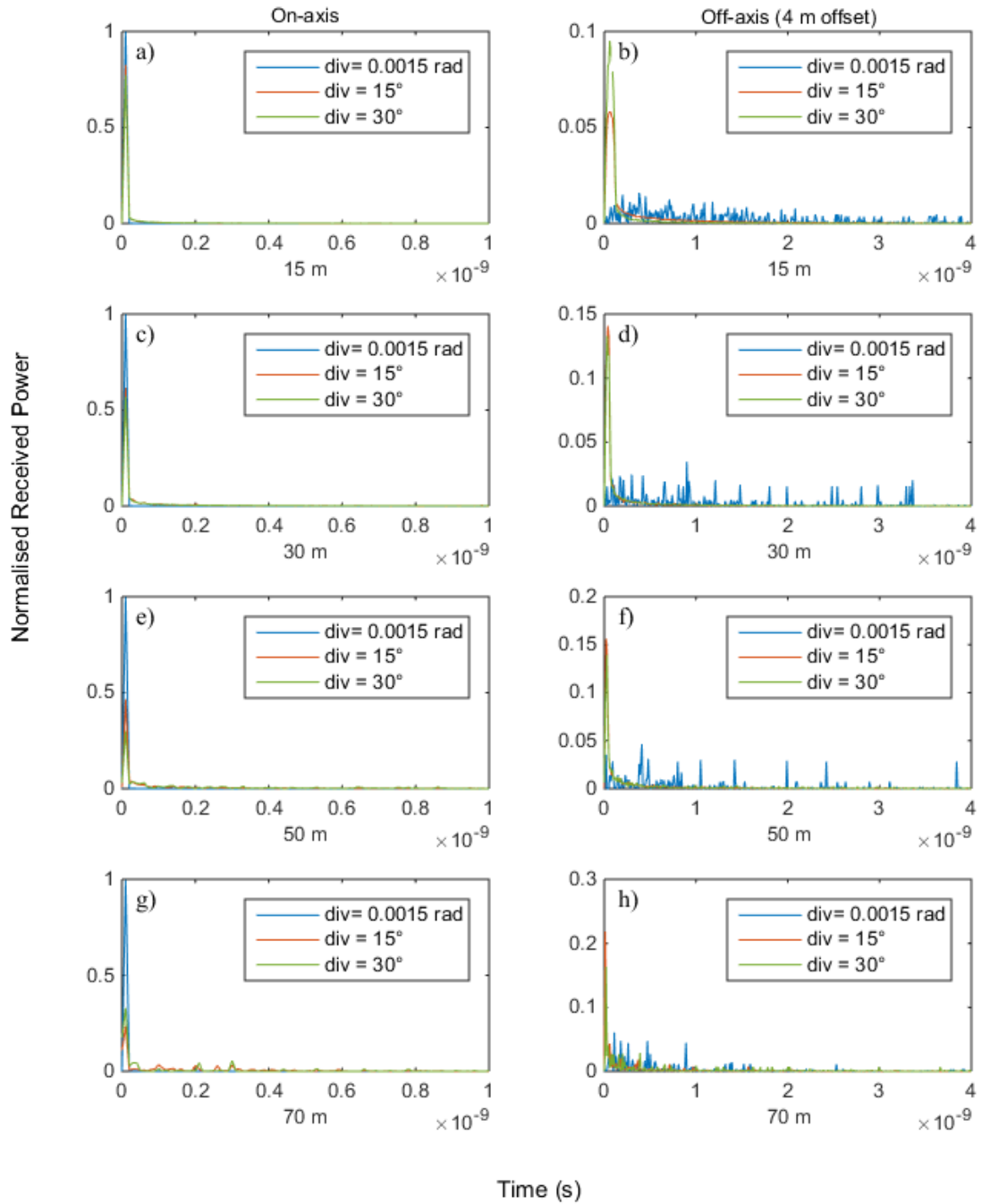


Figure 5.13: Channel impulse response in clear water for on-axis(left column) and off-axis(right column), with increasing distance . (a) and (b) 15 m, (c) and (d) 30 m, (e) and (f) 50 m, (g) and (h) 70 m.

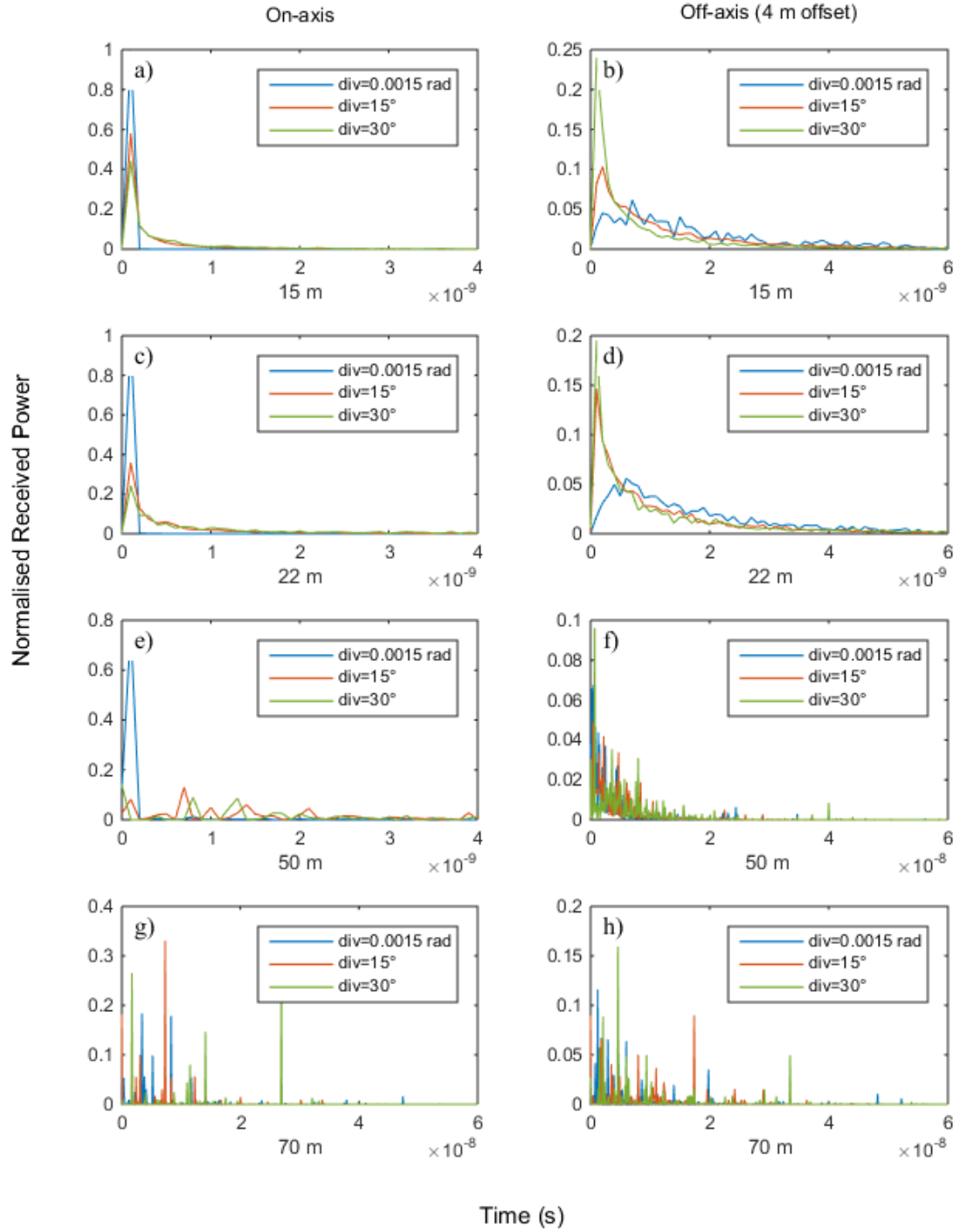


Figure 5.14: Channel impulse response in coastal water for on-axis (left column) and off-axis (right column), with increasing distance . (a) and (b) 15 m, (c) and (d) 22 m, (e) and (f) 50 m, (g) and (h) 70 m.

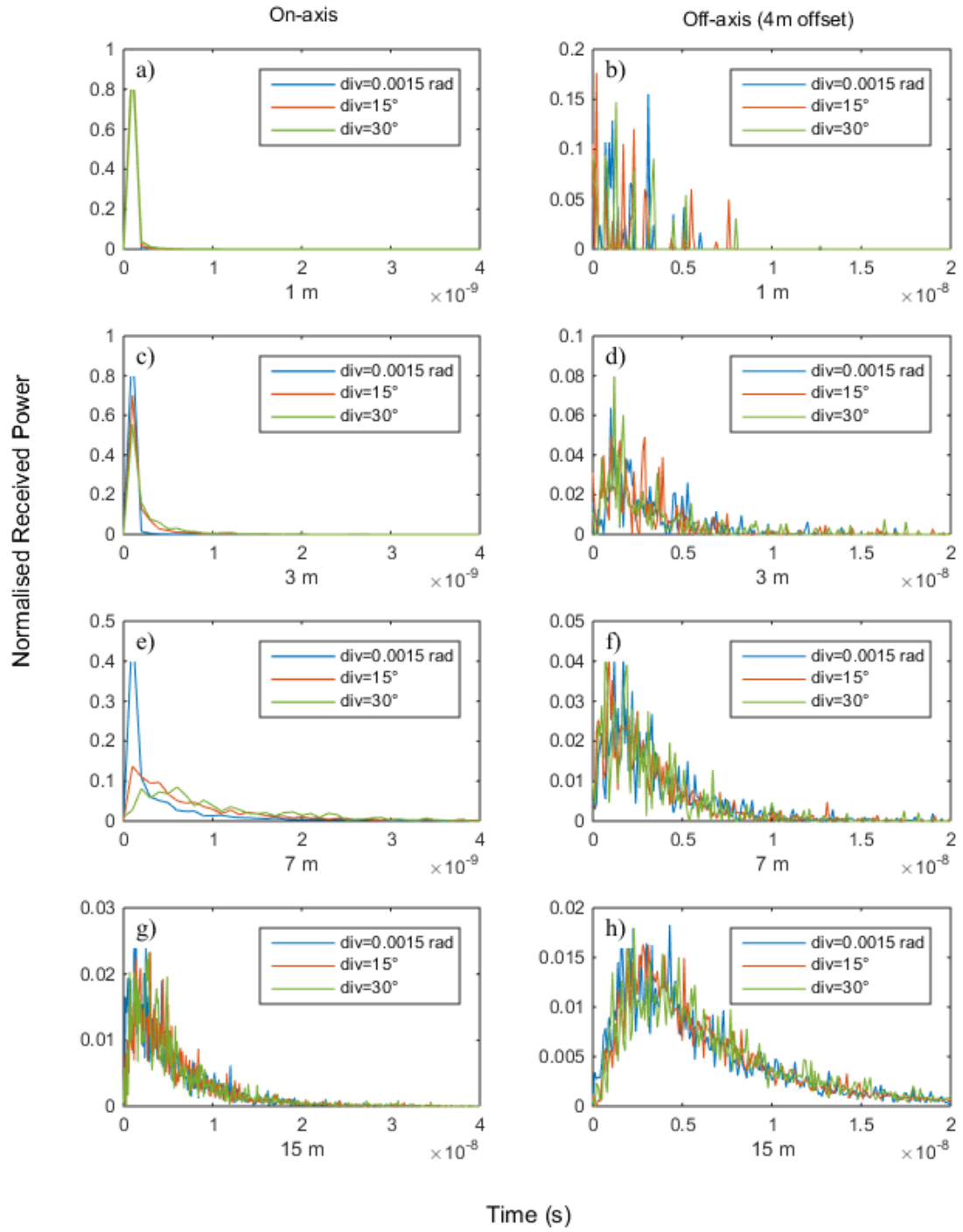


Figure 5.15: Channel impulse response in turbid water for on-axis (left column) and off-axis (right column), with increasing distance: (a) and (b) 1 m, (c) and (d) 3 m, (e) and (f) 7 m, (g) and (h) 15 m.

5.4 *Frequency response*

From the impulse response generated in section 5.3, the frequency response is calculated to estimate the channel bandwidth supported by the links. This is achieved by estimating the frequency at which the signal drops to half in the plot (i.e. drops by 3 dB). It should be noted that the bandwidth calculated in this section will be the minimum bandwidth that can be supported by the channel since the impulse response is calculated by setting the receiver FOV as 180°.

5.4.1 On-axis and off-axis

Figures 5.16 to 5.18 show the frequency responses that correspond to the impulse responses calculated in the previous section for various types of water. In clear water, irrespective of the size of beam divergence, more than 1 GHz bandwidth can be supported by the links except at off-axis locations for collimated beam. The fact that more than 1 GHz bandwidth can be supported by all source divergences in clear water is apparent from the scattering order histogram (Figure 5.1 to 5.4) where it can be seen that the links are dominated by the unscattered photons. Additionally this can be related to the impulse response shown in Figure 5.13 where the impulse response exhibit a dominant peak signifying small delays photons are received .

On the contrary, at all off-axis locations for collimated beam, the bandwidth is limited to several hundreds of MHz (i.e. : 170-415 MHz). This is quite small compared to the bandwidth that can be supported by both diffuse beams at off-axis locations. This is because, for collimated beam, most of the light received at off-axis locations consist of scattered light with high delays as shown by the scattering order and impulse response in Figure 5.1 and 5.13 whereas for both diffuse beam, there is high probability of unscattered photons that contributes to the power received.

In coastal water, collimated beam can still supports high bandwidth (>1 GHz) up to distances 50 m where at 70 m the bandwidth is reduced to 44 MHz. However for larger beam divergences, the channel bandwidth is slightly smaller at approximately several hundreds of MHz (360 MHz-730 MHz) up to distances 22 m. As the distance is increased to 50 m and beyond, the bandwidth supported by both diffuse beams is reduced to less than 100 MHz.

Due to the high scattering environment in turbid water, collimated beam can only support more than 1 GHz up to distance 7m. One interesting observation that can be seen in turbid water is that at all off-axis locations, the frequency response is the same irrespective of the beam divergence sizes which results the same 3 dB bandwidth. Another observation to highlight is that at 15 m, the on-axis bandwidth performance is degraded significantly until it matches the performance at off-axis locations at approximately 55 MHz . This indicates that the scattering is so severe that the scattering behaviour is relatively the same

at on-axis and off-axis. Table 5.5 summarizes the 3 dB bandwidth supported by various links in the three types of water.

To conclude, this section analyses the bandwidth supported by various source divergences at on-axis and off-axis locations at the specified distance. It can be concluded that more than 1 GHz can be supported in clear water by all source divergences at on-axis locations. However for off-axis locations, the bandwidth supported by the collimated links is limited to several hundreds of MHz. On the other hand, in higher scattering environments such as coastal and turbid water, the bandwidth is limited to several tens to hundreds of MHz depending on distance.

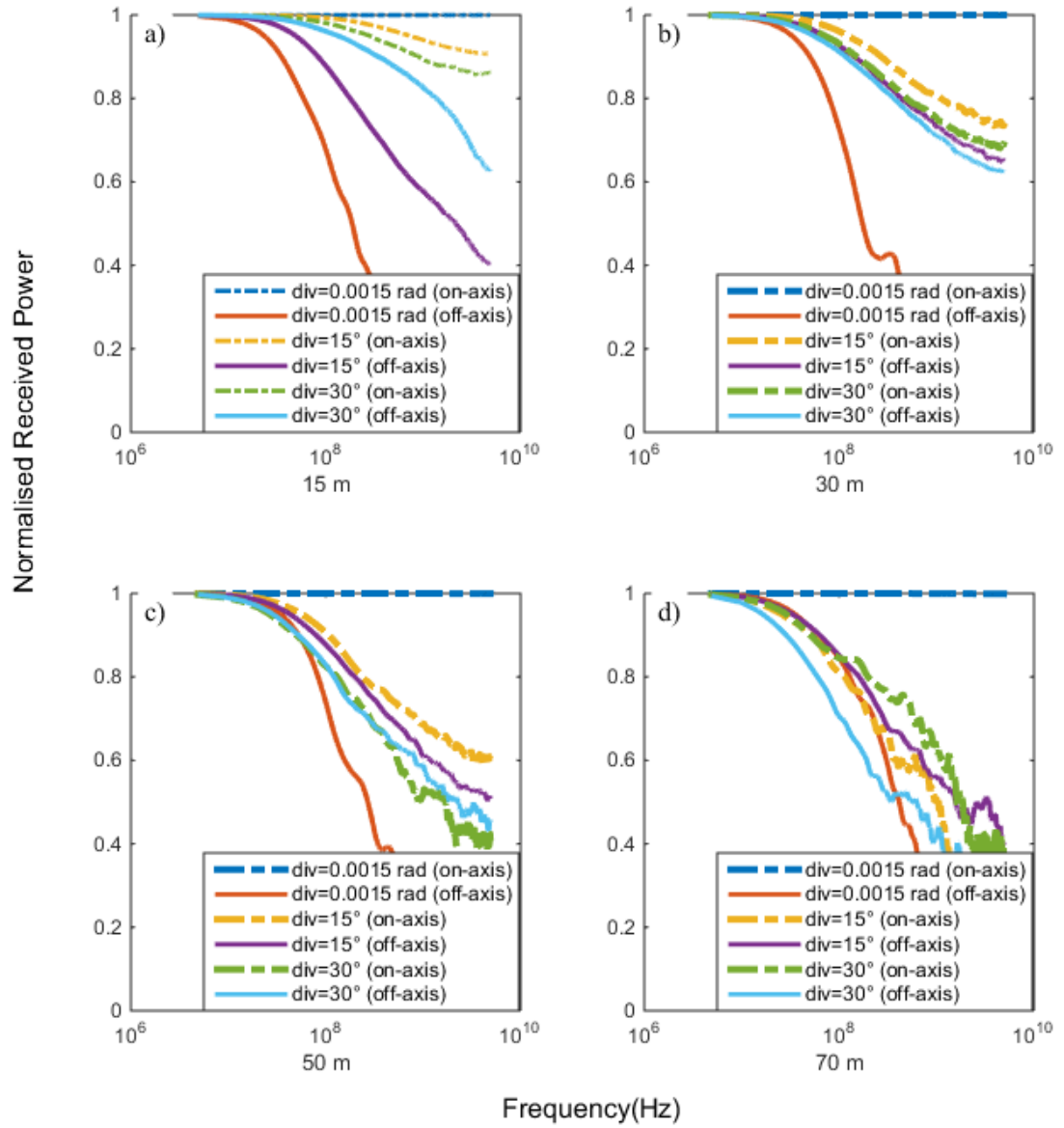


Figure 5.16: Frequency response in clear water ($c=0.15$) for on-axis and off-axis (4 m offset) locations using various source distributions at (a) 15m (b) 30 m (c) 50 m and (d) 70m.

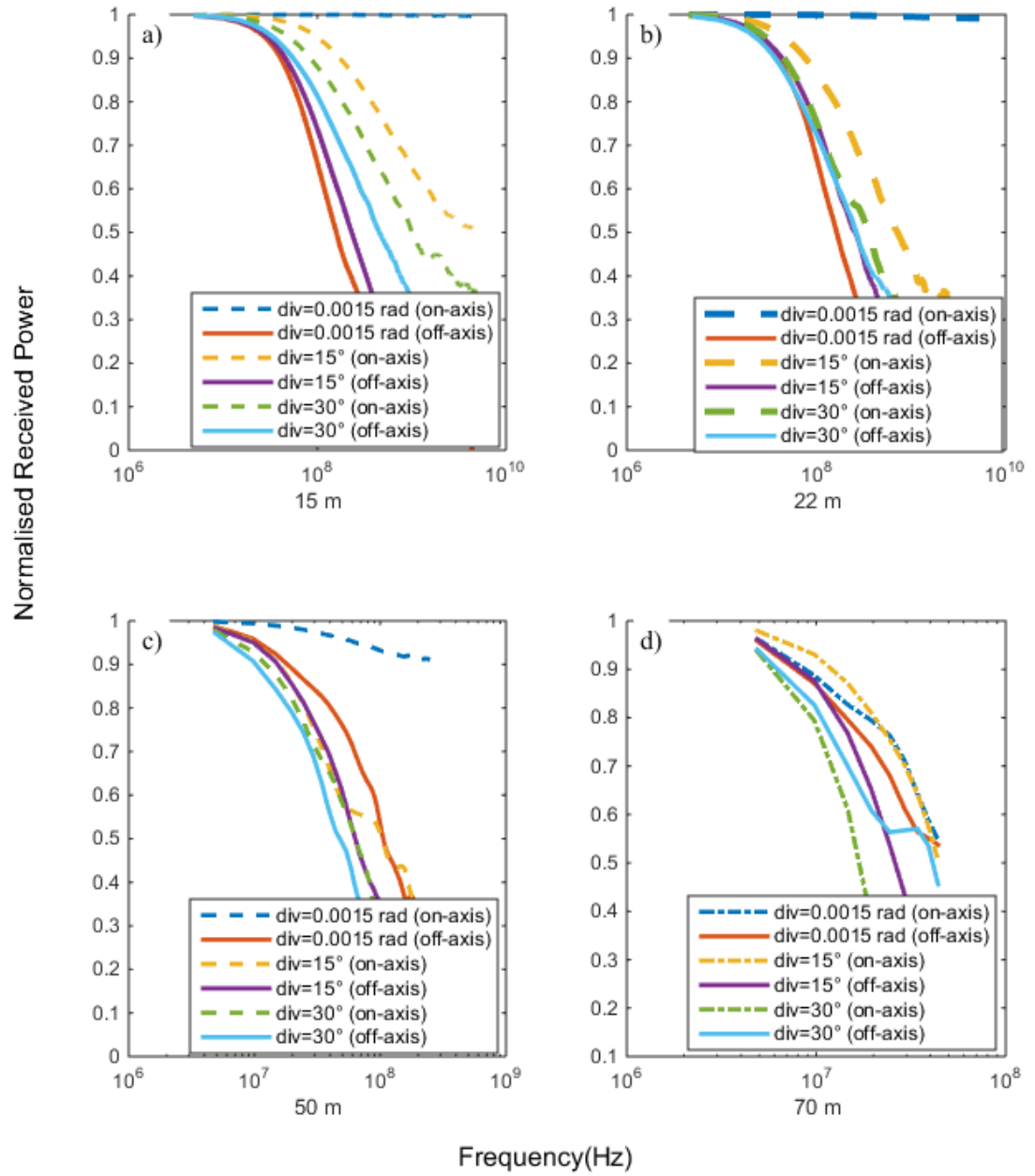


Figure 5.17: Frequency response in coastal water ($c=0.4$) for on-axis and off-axis (4 m offset) locations using various source distributions at (a) 15 m (b) 22 m (c) 50 m and (d) 70m..

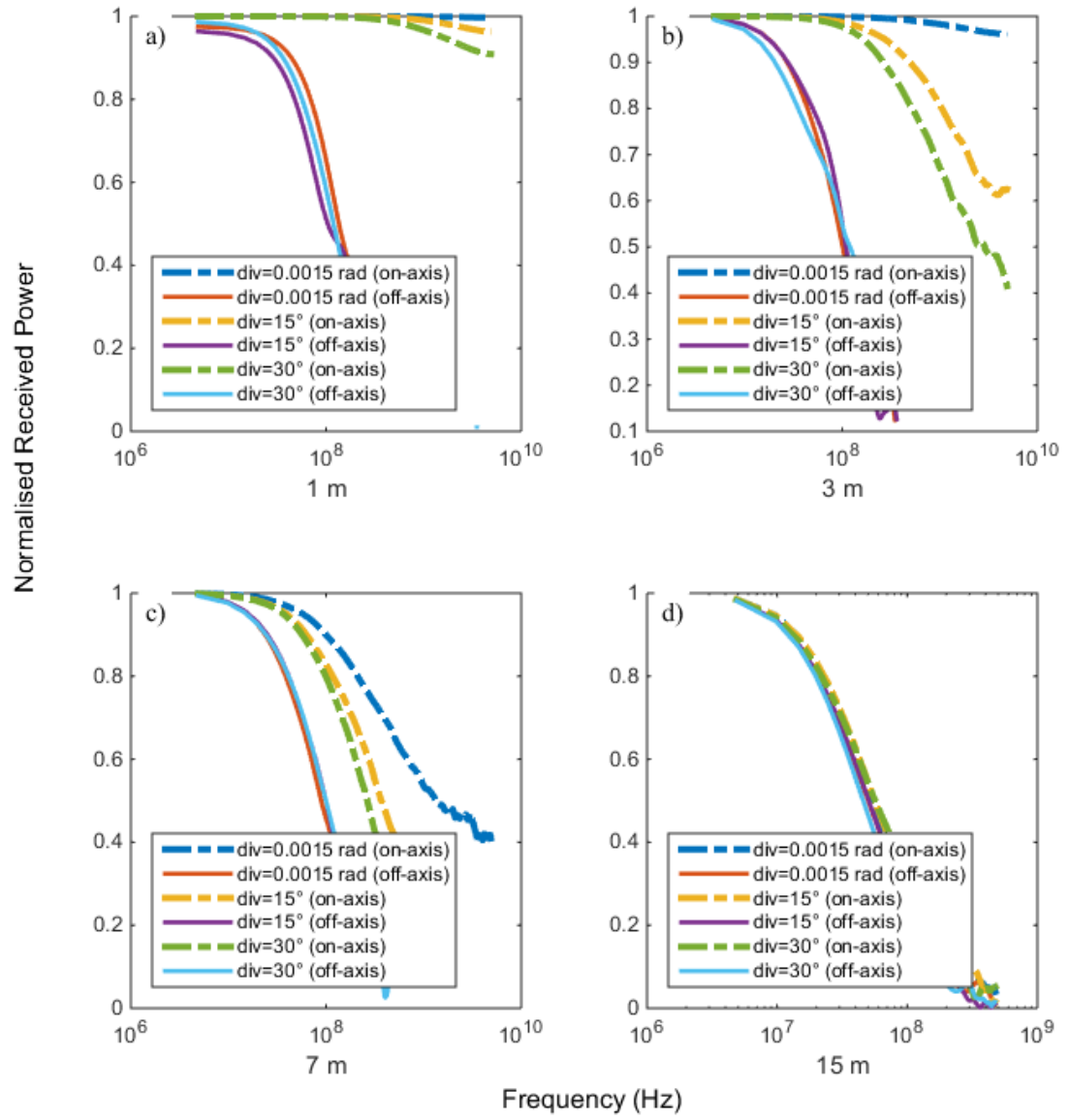


Figure 5.18: Frequency response in turbid water ($c=2.2$) for on-axis and off-axis (4 m offset) locations using various source distributions at (a) 1 m (b) 3 m (c) 7 m and (d) 15 m .

Table 5.5: 3 dB bandwidth for various select distances in (a) Clear water (b) Coastal water and (c) Turbid water for three sizes of beam divergences.

(a) Clear water ($c=0.15$)

	Div=0.0015 rad		Div= 15°		Div=30°	
Distance	On-axis	Off-axis	On-axis	Off_axis	On-axis	Off-axis
15 m	> 1GHz	190 MHz	> 1GHz	> 1GHz	> 1GHz	> 1GHz
30 m	> 1GHz	170 MHz	> 1GHz	> 1GHz	> 1GHz	> 1GHz
50 m	> 1GHz	270 MHz	> 1GHz	> 1GHz	> 1GHz	> 1GHz
70 m	> 1GHz	415 MHz	> 1GHz	> 1GHz	> 1GHz	> 1GHz

(b) Coastal water ($c=0.4$)

	Div=0.0015 rad		Div= 15°		Div=30°	
	On-axis	Off-axis	On-axis	Off_axis	On-axis	Off-axis
15 m	> 1GHz	150 MHz	> 1GHz	230 MHz	> 1GHz	450 MHz
22 m	> 1GHz	170 MHz	730 MHz	260 MHz	360 MHz	260 MHz
50 m	> 1GHz	93 MHz	100 MHz	64 MHz	64 MHz	50 MHz
70 m	50 MHz	50 MHz	50 MHz	25 MHz	16 MHz	25 MHz

(c) Turbid Water ($c=2.2$)

	Div=0.0015 rad		Div=15°		Div=30°	
	On-axis	Off-axis	On-axis	Off_axis	On-axis	Off-axis
1 m	> 1GHz	110 MHz	> 1GHz	110 MHz	> 1GHz	110 MHz
3 m	> 1GHz	120 MHz	> 1GHz	120 MHz	> 1GHz	120 MHz
7 m	> 1GHz	98 MHz	366 MHz	98 MHz	264 MHz	98 MHz
15 m	55 MHz	55 MHz	55 MHz	55 MHz	55 MHz	55 MHz

5.5 *Angle of arrival (AOA) distribution*

The need to investigate the angle of arrival (AOA) distribution was motivated by several observations in previous works when the receiver FOV is varied to optimise the performance of the link [14, 38]. There is a very limited range of work that studying the AOA distribution in UOWC, where only quite recently, a closed form expression for AOA distribution was proposed in [83]. A good agreement is observed between the proposed expression and the MC simulation for collimated links with no misalignment. It should be noted that this expression is not valid for intermediate and multiple scattering regimes since their model only considers ballistic and single scattering components of the received photons. Thus, this section will address this issue.

In most of the analytical studies on light underwater, SAA approximation is used to model light scattering as light underwater undergoes small angle scattering in forward directions as described by the phase scattering functions discussed in Section 2.6. However, as distance increases, more scattering occurs causing the AOA to spread to larger angles. This is particularly obvious if wide beam divergence is used where light is spread into a larger initial angles.

Thus in this thesis, the AOA distribution is explored for various sizes of the beam divergences in different types of water. To do this, the FOV of the receiver is maximized to 180° to collect all the photons that reach the receiver.

The rest of the simulations parameters are the same as previous section. Figures 5.19 to 5.21 shows the AOA distribution in various types of water.

5.5.1 On-axis

In regime I where unscattered and single scattered photons dominate, the AOA distributions are confined to small angles. However, the AOA for diffuse beams show larger angle spread with strong peak at smaller angles. In regime II, where there are moderate scattering events, the peak at smaller angles vanishes but the AOA is still distributed at small moderate angles. In regime III, where there are high number of multiple scattering, the AOA distribution shows significant spread at larger angles as shown in Figure 5.21(g).

5.5.2 Off-axis

It can be seen that at off-axis locations, the peak of the AOA distribution is displaced by a certain angle with respect to the origin. This angle is equal to the misalignment angle, θ that can be calculated as $\theta = \tan^{-1}(d_{\text{offset}}/z)$ where z is the distance between the transmitter and receiver. As the distance is increased, this angle become smaller. This is why the peak of the AOA distribution shifts to smaller angles as the distance is increased.

One important observation to highlight in clear water; the AOA for collimated beam is spread at larger angles compared to diffuse beam due to the fact that most of the light that reaches off-axis locations are contributed by the

scattered photons as shown in the scattering order histogram in Figures 5.1 to 5.4. The AOA distribution for both diffuse beams show a high peak with smaller spread as a result of high unscattered photons received. Similar to on-axis locations, the AOA distribution shows larger spread when it is dominated by multiple scattered photons.

To summarise, this section presents the AOA distribution for both collimated beam and diffuse beam. Several important observations that can be highlighted are; diffuse beam shows larger AOA distribution compared to collimated beam even they are operating in regime I. It is also observed that the AOA distribution is significantly affected by the geometry or the locations of the receiver with respect to the transmitter. This is shown by the AOA at off-axis locations where the AOA are significantly displaced depending on the locations. Thus, it can be said that this kind of information is useful in optimising the receiver design.

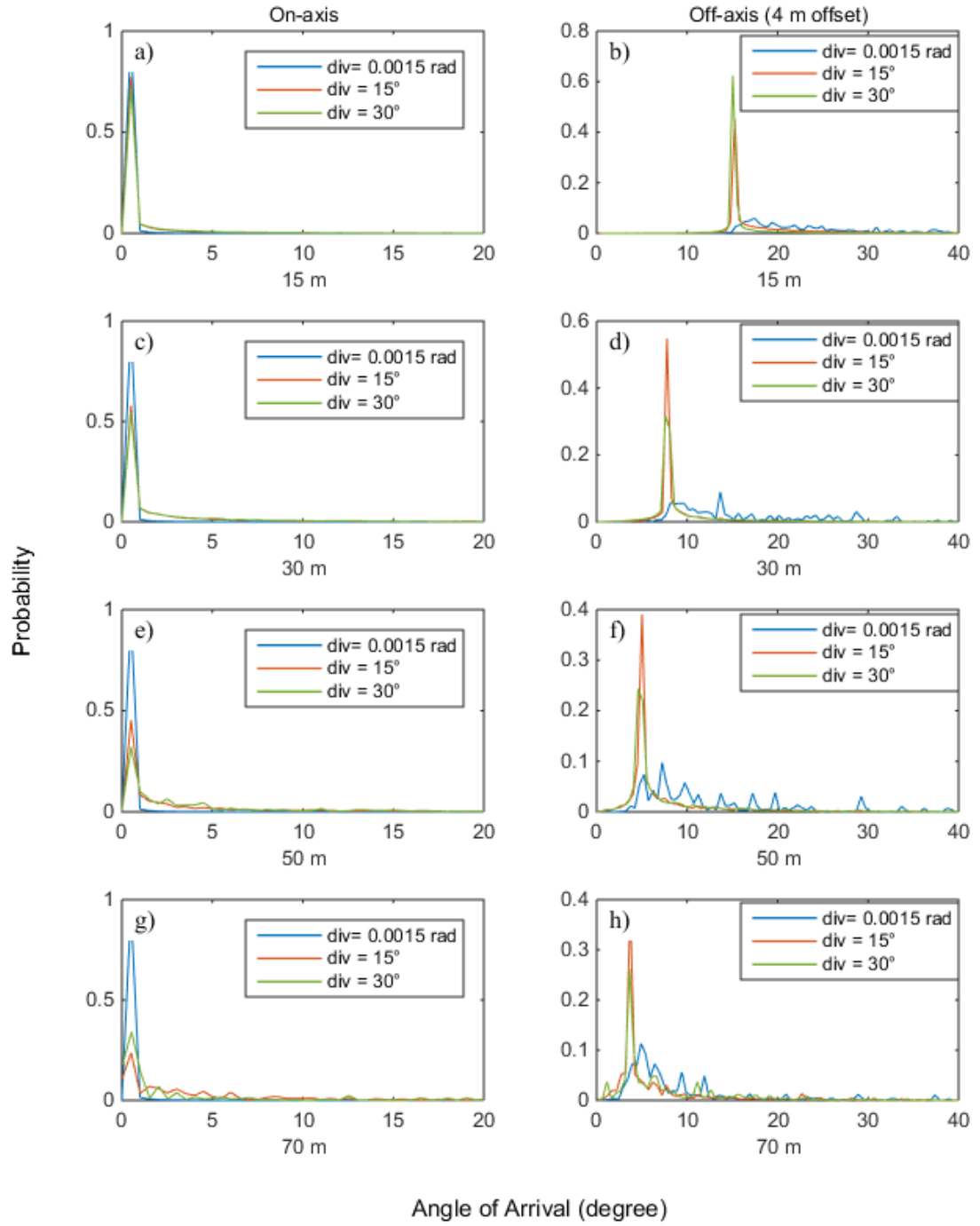


Figure 5.19: AOA distribution in clear water for on-axis (left column) and off-axis (right column), with increasing distance: (a) and (b) 15 m, (c) and (d) 30 m, (e) and (f) 50 m, (g) and (h) 70 m.

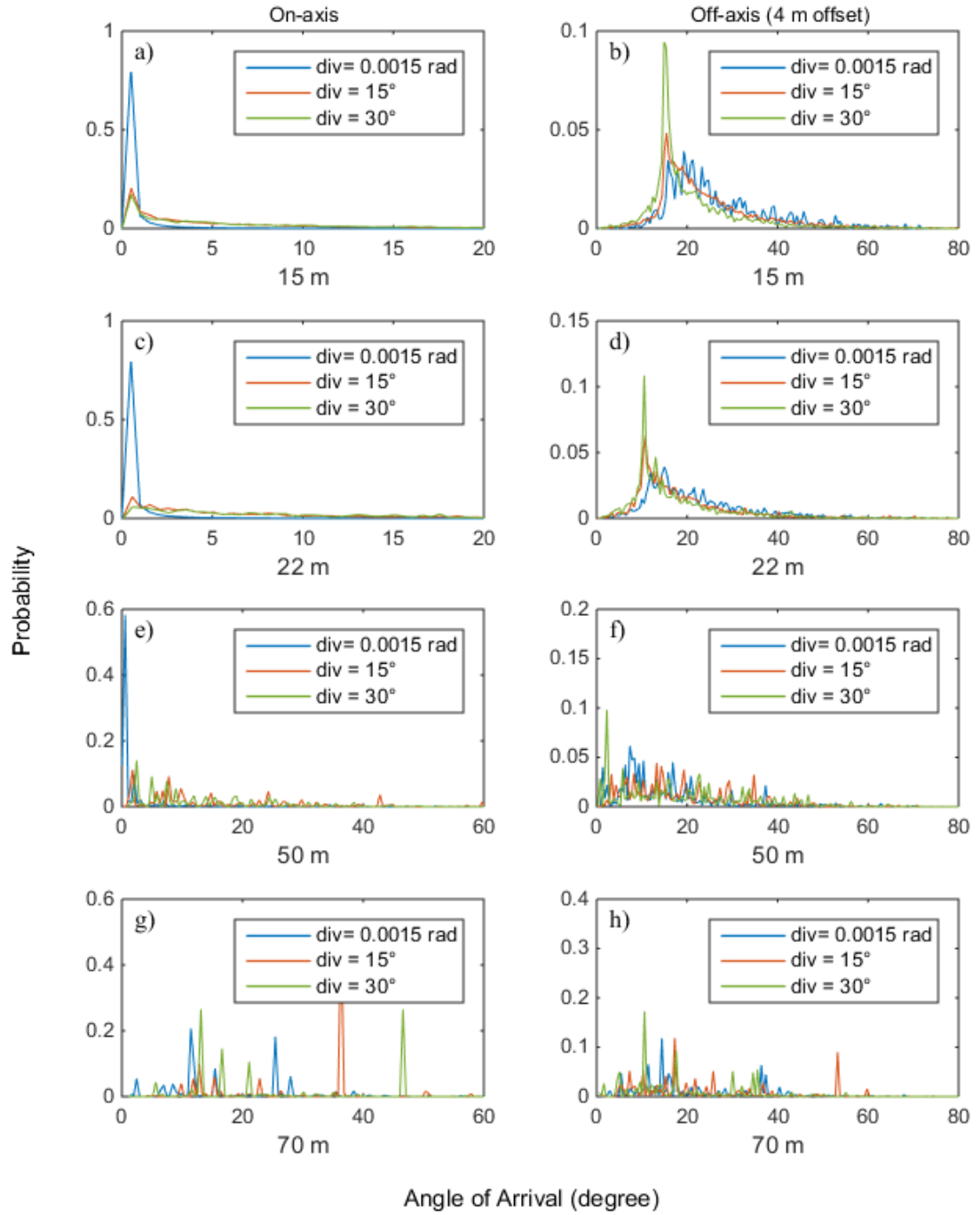


Figure 5.20: AOA distribution in coastal water for on-axis (left column) and off-axis(right column), with increasing distance : (a) and (b) 15 m, (c) and (d) 22 m, (e) and (f) 50 m, (g) and (h) 70 m.

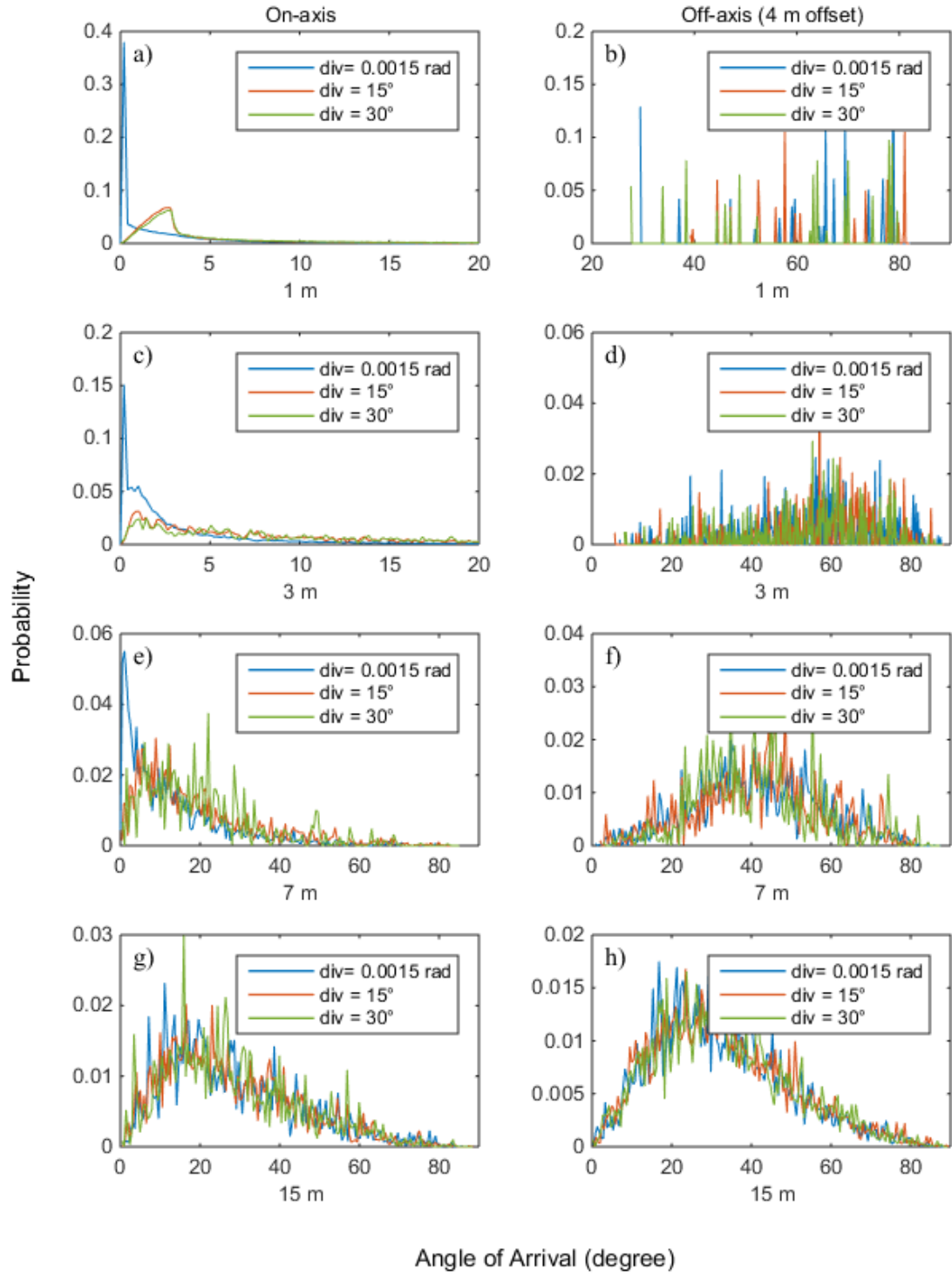


Figure 5.21: AOA distribution in turbid water for on-axis (left column) and off-axis(right column), with increasing distance : (a) and (b) 1 m, (c) and (d) 3 m, (e) and (f) 7 m, (g) and (h) 15 m.

5.6 *Effect of receiver FOV*

There are several previous studies on the impact of receiver FOV on the UOWC as an effort to understand how to optimize the receiver design for optimum performance. In [38], the impact of varying the receiver FOV from 1° to 180° on the power received and the frequency response for collimated beam was presented. It is observed that the receiver FOV has significant impact on the received power and bandwidth. Experimental work using collimated beam in [14] also studied how varying the FOV from 1° and 7° affects the UOWC performance. It is concluded that by varying the FOV, two situations can occur. Firstly, by using a wider receiver FOV the amount of light collected by the receiver can increase. Secondly, a wider FOV may also result in more multiple scattered light being collected which can affect temporal dispersion. It is also observed that receiver FOV has significant impact to the temporal dispersion near the beam axis but not off-axis locations. Additionally it is also observed that receiver FOV has little effect on the temporal dispersion at longer distance.

However the impact of receiver FOV on the performance of diffuse beam for both on-axis and off-axis locations has not previously been investigated. Thus, in this section further investigations into the effect of FOV on the bandwidth performance will be conducted specifically for diffuse beams at on-axis and off-axis locations.

5.6.1 Effect of receiver FOV on bandwidth : On-axis

Based on the Table 5.5 that summarised the 3 dB bandwidth supported by various links in clear water, it is observed that more than 1 GHz can be achieved in the worst case scenario as the receiver FOV is set to be 180° . Thus the effect of FOV is not going to be investigated for clear water. The focus is on improving the bandwidth in coastal and turbid water by reducing the receiver FOV to 40° and 20° . This receiver FOV is chosen based on the AOA distribution presented in Section 5.5 where the most of the AOA distribution in coastal water is found to be within this range ($AOA < 20^\circ$).

- Coastal water

In coastal water, the effect of FOV is investigated at 22 m, 50 m and 70 m as at this distance the bandwidth is less than 1 GHz for diffuse beam. Figure 5.22 shows the frequency response of all source divergences in coastal water at the select locations. At 22 m, by reducing the receiver FOV to 20° , a bandwidth of more than 1 GHz can be achieved for both diffuse beams. However at 50 m and 70 m, the bandwidths supported by diffuse beams are limited to several tens to hundreds of MHz only when the receiver FOV is reduced to 20° .

- Turbid water

Similarly, the effect of receiver FOV is studied in turbid water for distance 7m and 15 m as more than 1 GHz can be supported by diffuse links up to 3 m. At 7 m, by reducing the receiver FOV to 20°, more than 1 GHz bandwidth can be achieved for 15 ° diffuse beam but not 30° diffuse beam. However, at 15 m, the receiver FOV has minimal effect to the bandwidth performance as there is relatively little increase of bandwidth from 55 MHz to 100 MHz as the receiver FOV is decreased from 180° to 20°. Table 5.6 and 5.7 summarises the finding obtained in this section.

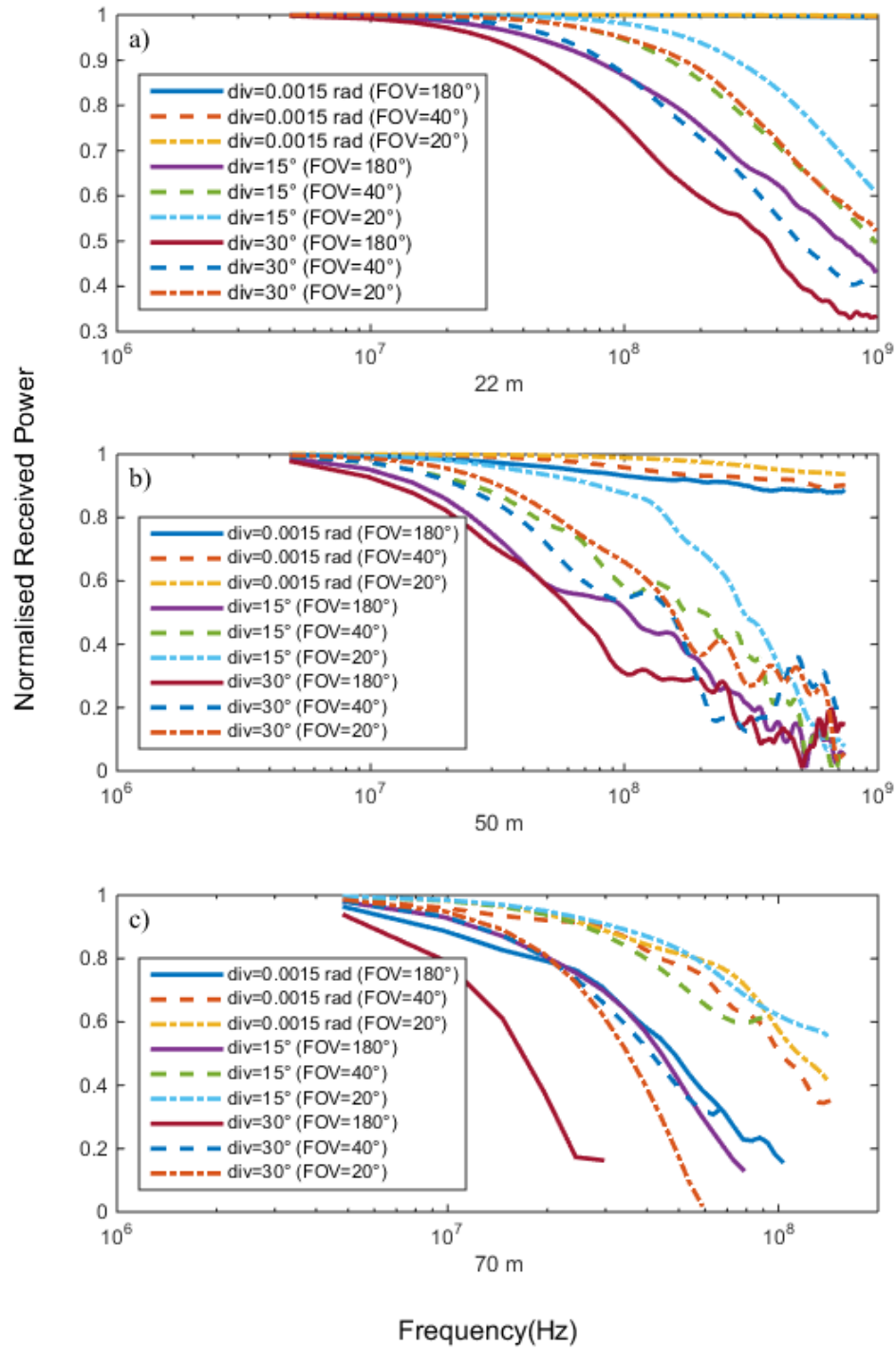


Figure 5.22: Frequency response in coastal water at (a) 22 m, (b) 50 m and (c) 70 m.

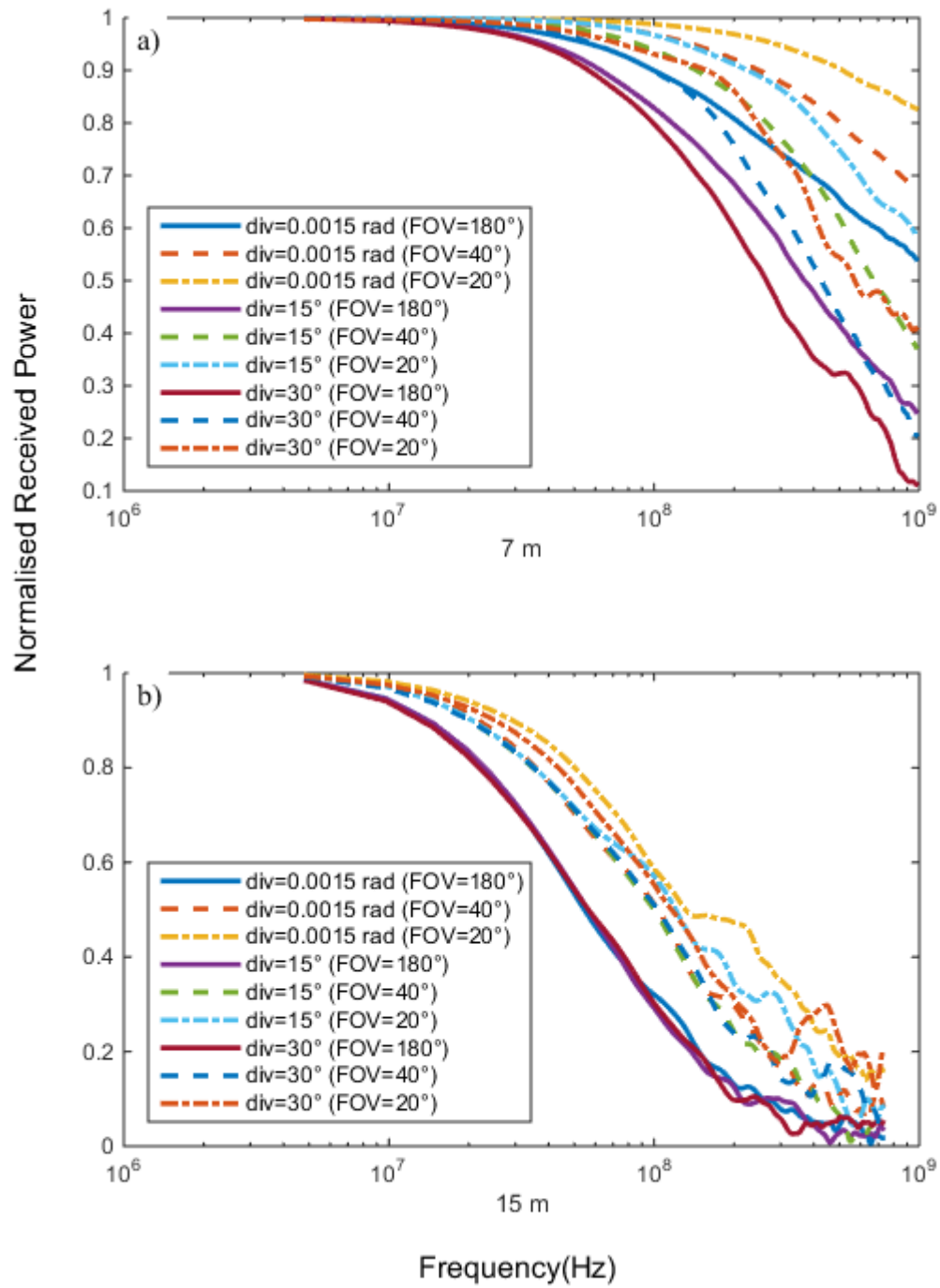


Figure 5.23: Frequency response in turbid water at (a) 7 m and (b) 15 m.

Table 5.6: 3 dB bandwidth for various receiver FOVs at (a) 22 m (b) 50 m and (c) 70 m for three sizes of beam divergences in coastal water.

Beam divergence	FOV =180°	FOV =40°	FOV =20°
Div=0.0015 rad	> 1GHz	> 1GHz	> 1GHz
Div= 15°	730 MHz	> 1GHz	> 1GHz
Div=30°	360 MHz	480 MHz	> 1 GHz

(a) 22 m

Beam divergence	FOV =180°	FOV =40°	FOV =20°
Div=0.0015 rad	> 1GHz	> 1GHz	> 1 GHz
Div= 15°	100 MHz	200 MHz	290 MHz
Div=30°	60 MHz	150 MHz	150 MHz

(b) 50 m

Beam divergence	FOV =180°	FOV =40°	FOV =20°
Div=0.0015 rad	50 MHz	100 MHz	150 MHz
Div= 15°	50 MHz	100 MHz	150 MHz
Div=30°	16 MHz	40 MHz	45 MHz

(c) 70 m

Table 5.7: 3 dB bandwidth for various receiver FOVs at (a) 7 m and (b) 15 m for three sizes of beam divergences in turbid water.

Beam divergence	FOV =180°	FOV =40°	FOV =20°
Div=0.0015 rad	> 1GHz	> 1GHz	> 1GHz
Div= 15°	370 MHz	670 MHz	> 1GHz
Div=30°	260 MHz	400 MHz	570 MHz

(a) 7 m

Beam divergence	FOV =180°	FOV =40°	FOV =20°
Div=0.0015 rad	55 MHz	100 MHz	100 MHz
Div= 15°	55 MHz	100 MHz	100 MHz
Div=30°	55 MHz	100 MHz	100 MHz

(b) 15 m

5.6.2 Effect of receiver FOV on bandwidth : Off-axis

Similarly, this section investigates the effect of receiver FOV on the bandwidth at off-axis locations in all types of water with the main aim in optimising the bandwidth.

- **Clear water**

Figure 5.24 shows the frequency response for various receiver FOV for collimated beam in clear water. It can be seen that there is increase in the 3 dB bandwidth as the receiver FOV is reduced. However, this is contrary to the results obtained in [14], where it is concluded that the FOV has minimal effect to the temporal dispersions at off-axis locations. It is believed that such observations are obtained due to the fact that the size of receiver FOV used in their experimental work is limited to 1° and 7° . It is predicted that a wider range of FOV (more than 7°) will show significant effects to the temporal dispersions.

- **Coastal water**

Figures 5.25 and 5.26 show the effect of reducing the receiver FOV in coastal water for all beam divergences. An interesting observation can be seen at 15 m where the bandwidth achieved by reducing the receiver FOV to 40° is higher compared to the bandwidth achieved by reducing the receiver FOV to 20°

irrespective of the beam divergence size. This is contrary to the conventional understanding that bandwidth will be maximum at a smaller FOV due to collection of less scattered light. By referring to the AOA distribution illustrated in Fig 5.20(b) previously, this can be explained by the fact that smaller receiver FOV than 40° cannot capture enough of the small delay photons as the peak of the AOA distribution occurs at 15° as shown in Figure 5.20(b). It should be recalled that a receiver FOV of 40° implies that the receiver is able to capture photons with maximum AOA of 20° , as 40° is the FOV full angle value. At 22 m and 50 m, the bandwidth can be increased by reducing the FOV to 20° as expected. However, at 70 m there is only little increase when the FOV is reduced.

- **Turbid water**

Figures 5.27 and 5.28 show the frequency response for various receiver FOVs in turbid water. For short distance ($z=1$ m and 3 m), a larger receiver FOVs is chosen (120°) since the AOA distribution in Figure 5.21 (b) and (d) show large spread compared to the longer distance ($z=7$ m and 15 m). It can be said that the receiver FOV has little impact to the bandwidth performance at off-axis locations. Thus it can be said that at off-axis location, the bandwidth is limited to several tens of MHz irrespective of receiver FOV sizes.

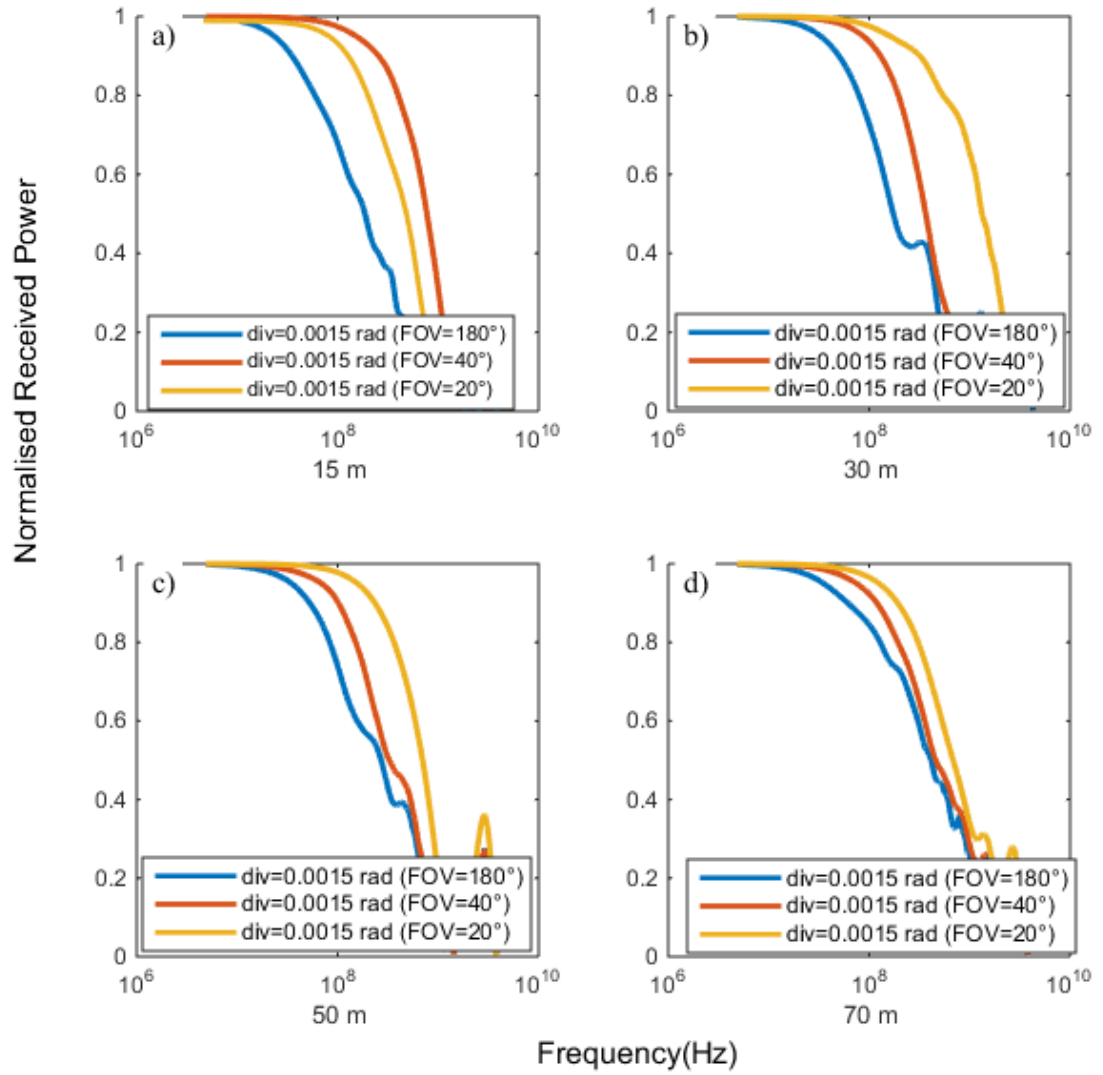


Figure 5.24: Frequency response in clear water at off-axis (4 m offset) locations : (a) 22 m, (b) 50 m and (c) 70 m.

Table 5.8: 3 dB bandwidth for various receiver FOVs in clear water for collimated beam at off-axis locations.

Distance	FOV =180°	FOV =40°	FOV =20°
15 m	185 MHz	760 MHz	460 MHz
30 m	170 MHz	350 MHz	1 GHz
50 m	270 MHz	320 MHz	700 MHz
70 m	410 MHz	430 MHz	680 MHz

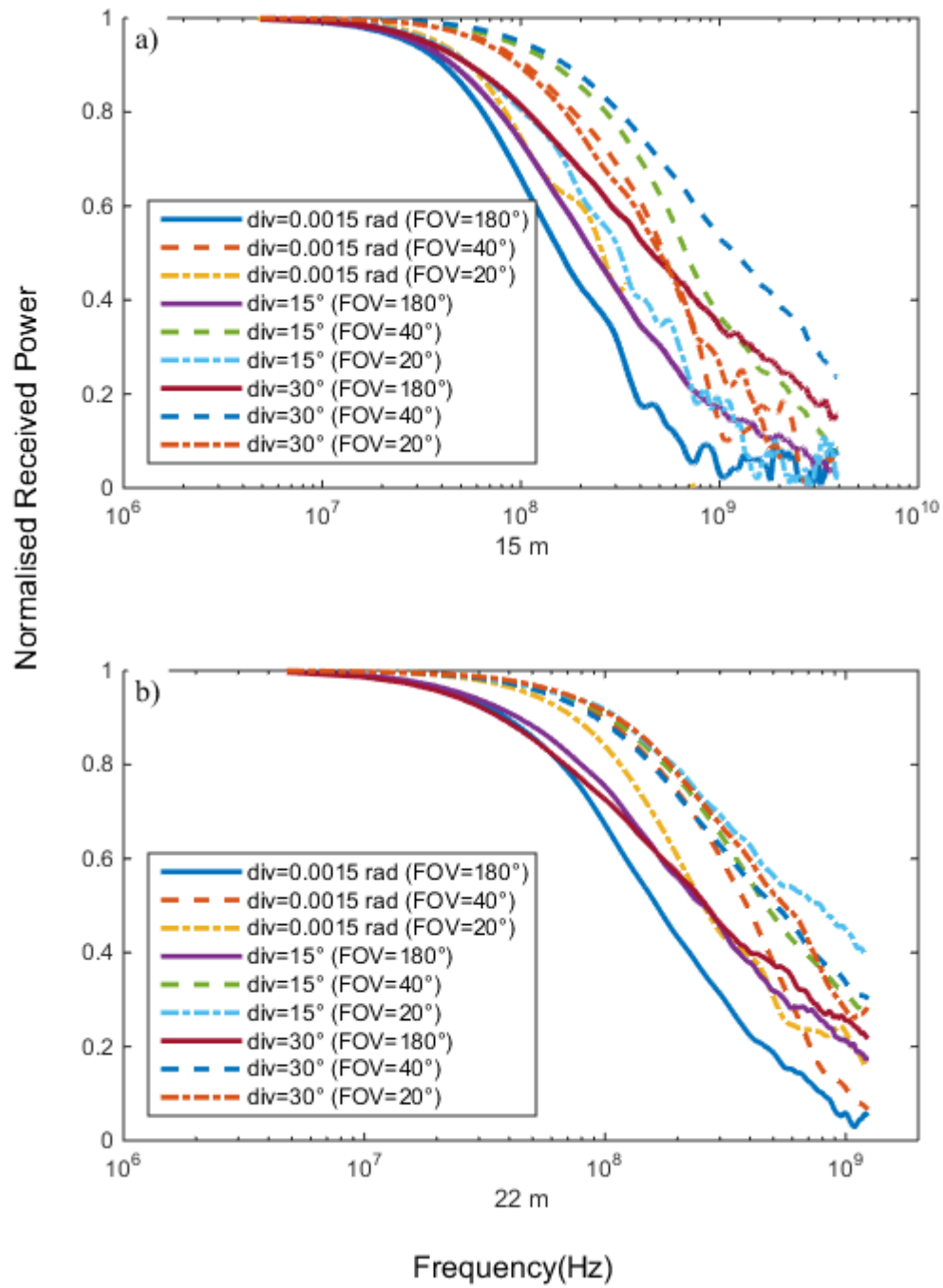


Figure 5.25: Frequency response in coastal water at off-axis (4 m offset) locations: (a) 15 m and (b) 22 m.

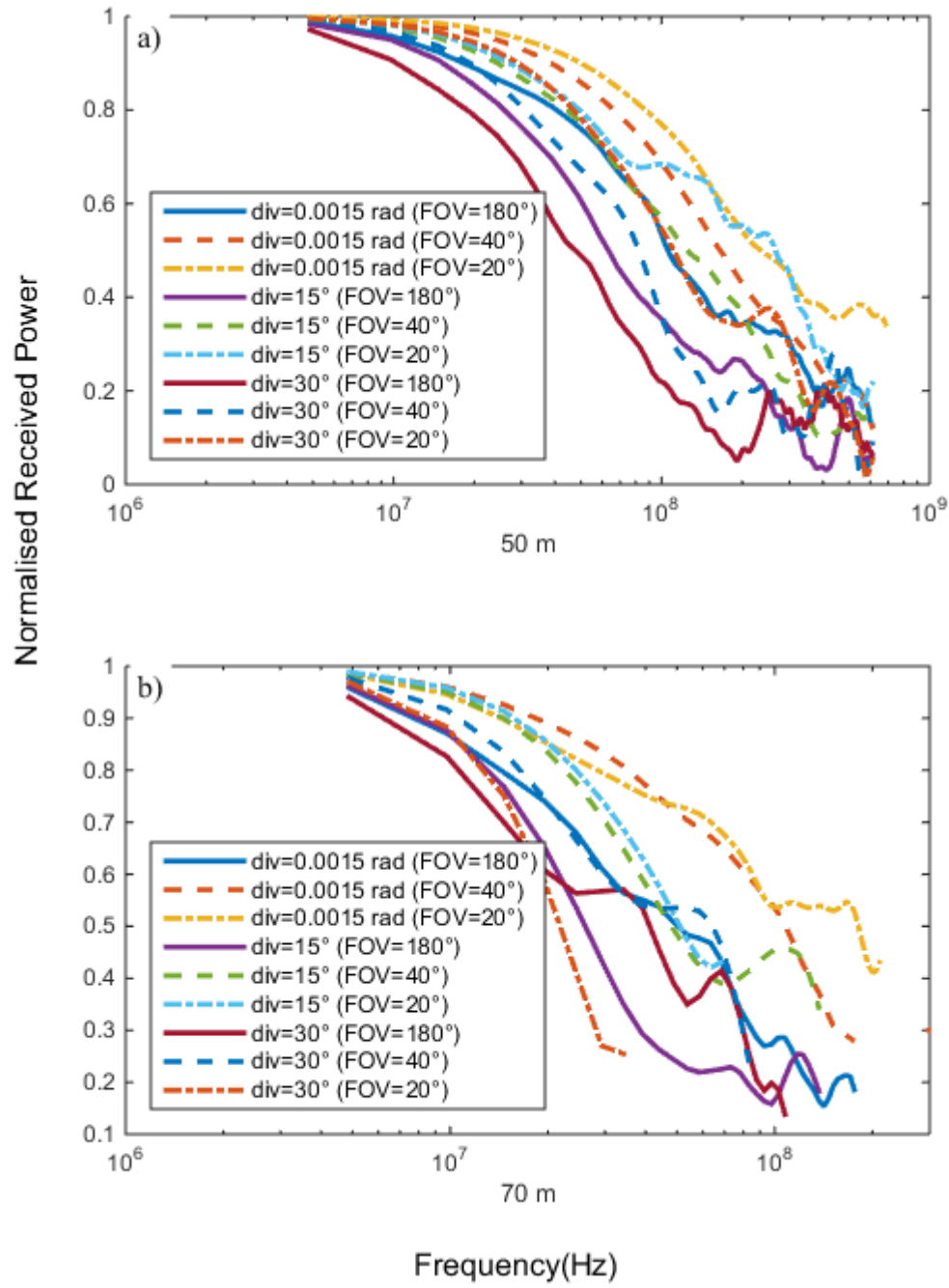


Figure 5.26: Frequency response in coastal water at off-axis (4 m offset) locations : (a) 50m and (b) 70 m.

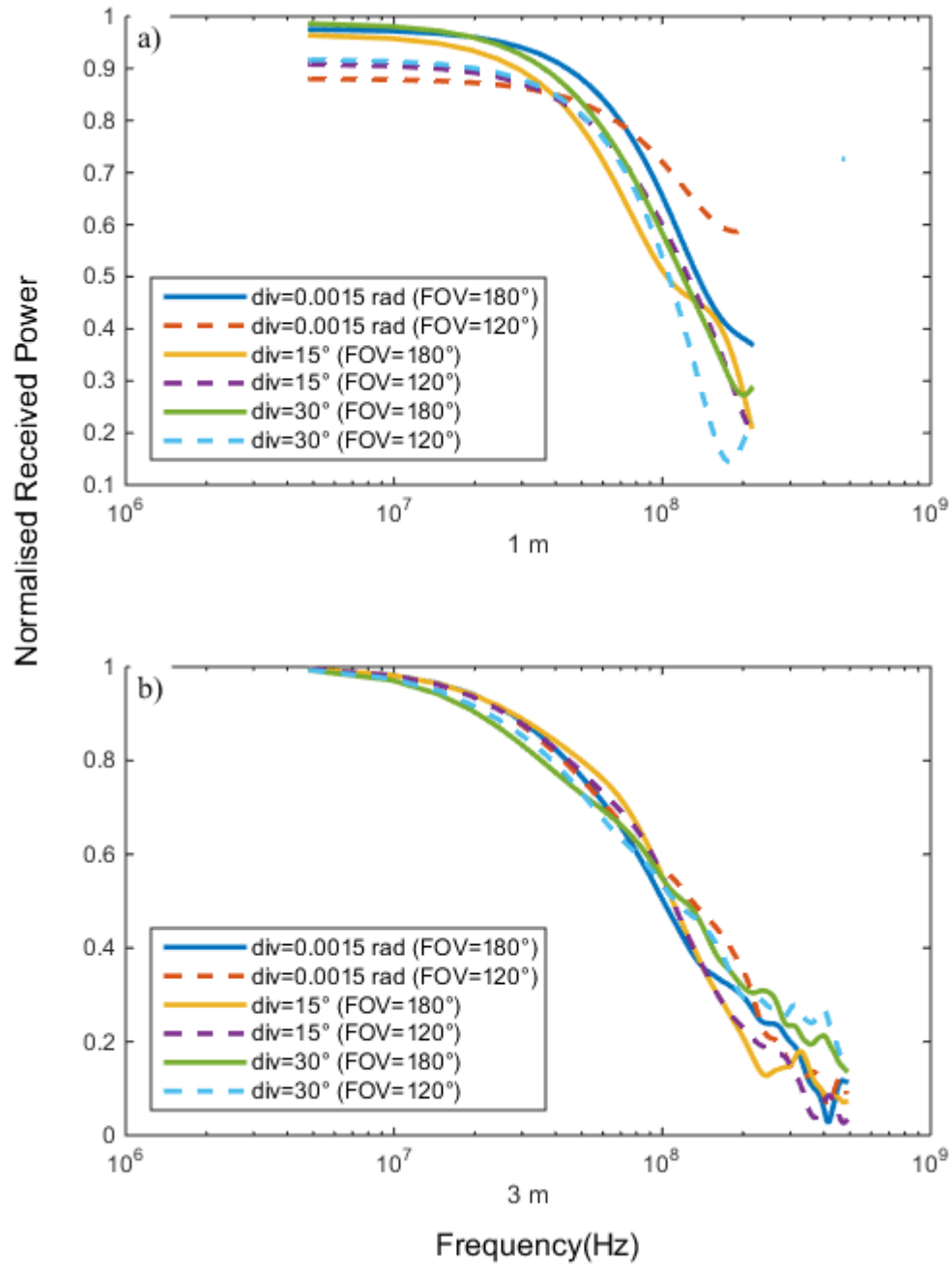


Figure 5.27: Frequency response in turbid water at off-axis (4 m offset) locations : (a) 1 m and (b) 3 m.

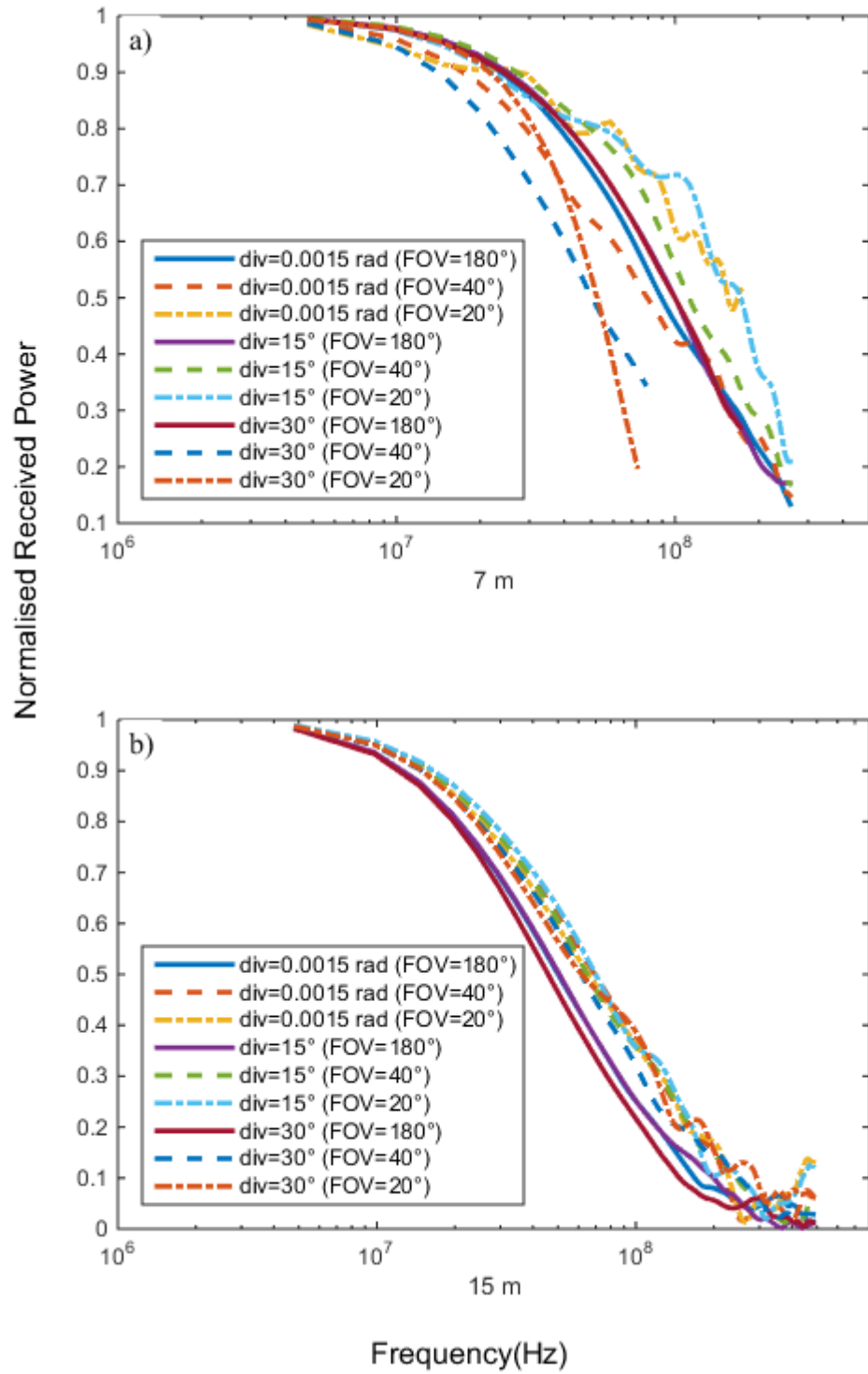


Figure 5.28: Frequency response in turbid water at off-axis (4 m offset) locations : (a) 7 m and (b) 15 m.

Table 5.9: 3 dB bandwidth for various receiver FOVs in coastal water for off-axis (4 m offset) locations at (a)15 m, (b) 22 m, (c) 50 m and (d)70 m.

Beam divergence	FOV =180°	FOV =40°	FOV =20°
Div=0.0015 rad	150 MHz	510 MHz	250 MHz
Div= 15°	230 MHz	670 MHz	310 MHz
Div=30°	450 MHz	1 GHz	500 MHz

(a) 15 m

Beam divergence	FOV =180°	FOV =40°	FOV =20°
Div=0.0015 rad	170 MHz	380 Hz	250 MHz
Div= 15°	260 MHz	460 MHz	760 MHz
Div=30°	260 MHz	500 MHz	500 MHz

(b) 22 m

Beam divergence	FOV =180°	FOV =40°	FOV =20°
Div=0.0015 rad	93 MHz	160 MHz	230 MHz
Div= 15°	64 MHz	120 MHz	260 MHz
Div=30°	50 MHz	83 MHz	100 MHz

(c) 50 m

Beam divergence	FOV =180°	FOV =40°	FOV =20°
Div=0.0015 rad	50 MHz	100 MHz	100 MHz
Div= 15°	25 MHz	50 MHz	50 MHz
Div=30°	25 MHz	63 MHz	25 MHz

(d)70 m

Table 5.10: 3 dB bandwidth for various receiver FOVs in turbid water for off-axis (4 m offset) locations at (a) 1 m, (b) 3 m, (c) 7 m and (d) 15 m.

Beam divergence	FOV =180°	FOV =120°
Div=0.0015 rad	110 MHz	100 MHz
Div= 15°	110 MHz	100 MHz
Div=30°	110 MHz	100 GHz

(a) 1 m

Beam divergence	FOV =180°	FOV =120°
Div=0.0015 rad	120 MHz	100 MHz
Div= 15°	120 MHz	100 MHz
Div=30°	120 MHz	100 MHz

(b) 3 m

Beam divergence	FOV =180°	FOV =40°	FOV =20°
Div=0.0015 rad	98 MHz	78 MHz	150 MHz
Div= 15°	98 MHz	110 MHz	170 MHz
Div=30°	98 MHz	50 MHz	50 MHz

(c) 7 m

Beam divergence	FOV =180°	FOV =40°	FOV =20°
Div=0.0015 rad	55 MHz	60 MHz	60 MHz
Div= 15°	55 MHz	60 MHz	60 MHz
Div=30°	55 MHz	60 MHz	60 MHz

(d) 15 m

5.7 *Effect of receiver FOV on the scattering order histogram*

The results in previous section show that reducing the receiver FOV has different effects in different situations. Thus, it is interesting to investigate the effect of reducing the receiver FOV on the scattering order histogram. Similar to section 5.6, the receiver FOV is reduced to 20° . In order to show this clearly, a histogram of the ratio of the received power by the smaller FOV, i.e. 20° to the power received by the larger FOV, i.e. 180° is calculated instead of the absolute probability. This histogram is plotted in the same axis with the absolute probability histogram of the scattering order of 180° . By doing this, a better picture on how the individual scattering order changes can be compared. Since the interest is to investigate how this relates to the improvement in bandwidth, only coastal and turbid water are considered.

Figures 5.29 to 5.36 show the effect of reducing the receiver FOV from 180° to 20° in coastal water. By examining all the plots, it is observed that in the minimal and intermediate scattering regime; (coastal water : 15 m, 22 m and 50 m) and turbid water (1 m, 3 m and 7 m) the magnitude of the higher order scattering is reduced when the receiver FOV is reduced. This implies that less multiple scattered photons are collected which results in a higher bandwidth. However in the multiple scattering regime, (coastal water : 70 m) and (turbid water : 15 m) , the reduction of receiver FOV does not specifically reduce the magnitude of the higher order scattering but reduce all the scattering order

randomly. Thus, this explains why there is no change in bandwidth as the receiver FOV is reduced. This shows that in the multiple scattering regime, most photons that have been multiple scattered have a wide range of AOA.

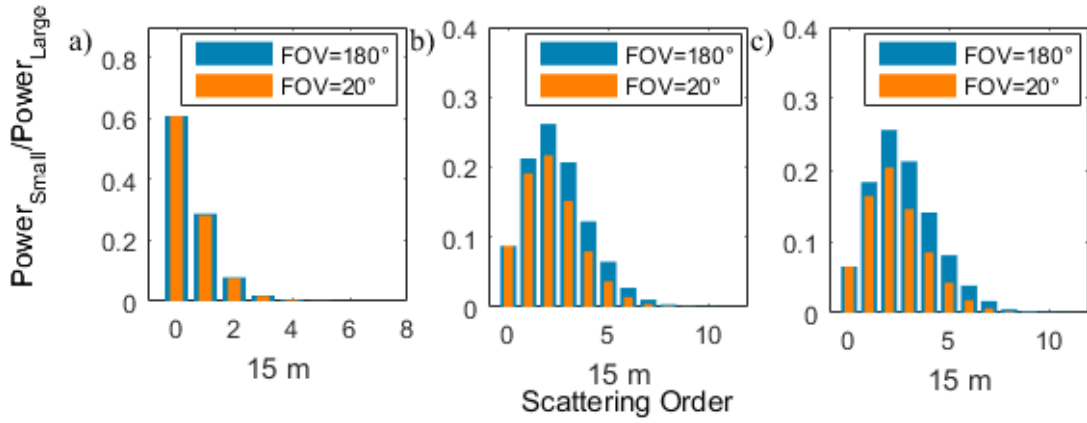


Figure 5.29: Scattering order histogram in coastal water at 15 m for (a) collimated beam (b) 15° diffuse beam and (c) 30° diffuse beam.

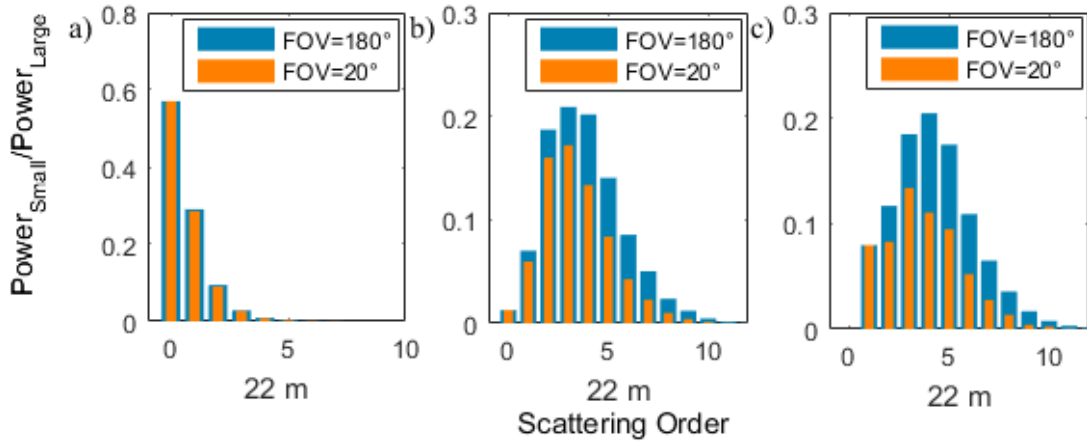


Figure 5.30: Scattering order histogram in coastal water at 22 m for (a) collimated beam (b) 15° diffuse beam and (c) 30° diffuse beam.

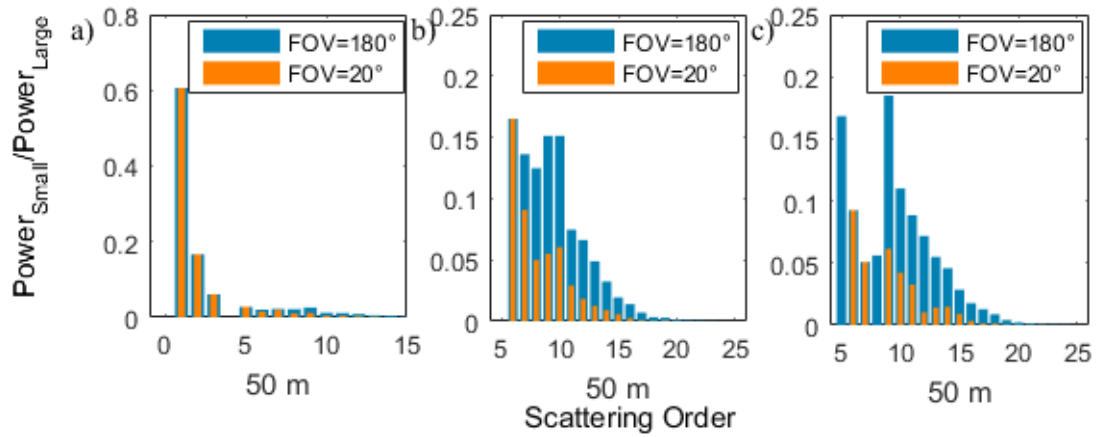


Figure 5.31: Scattering order histogram in coastal water at 50 m for (a) collimated beam (b) 15° diffuse beam and (c) 30° diffuse beam.

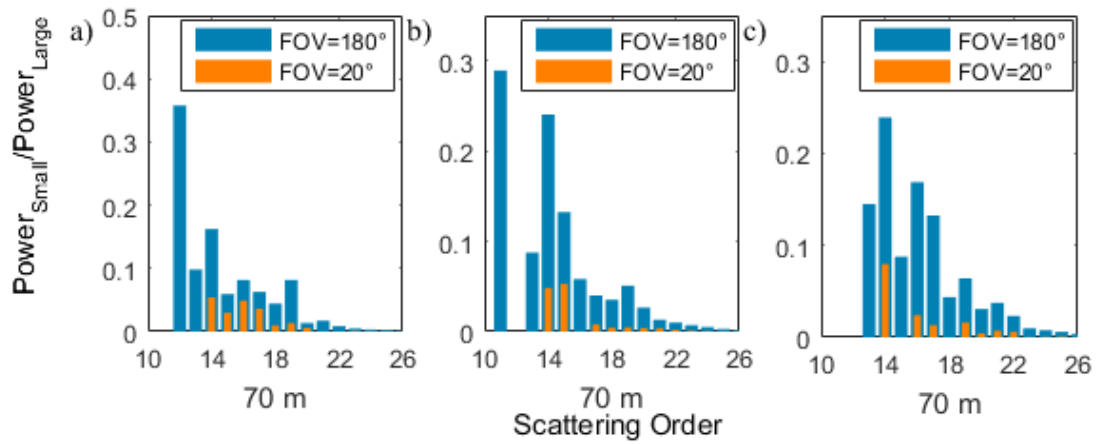


Figure 5.32: Scattering order histogram in coastal water at 70 m for (a) collimated beam (b) 15° diffuse beam and (c) 30° diffuse beam.

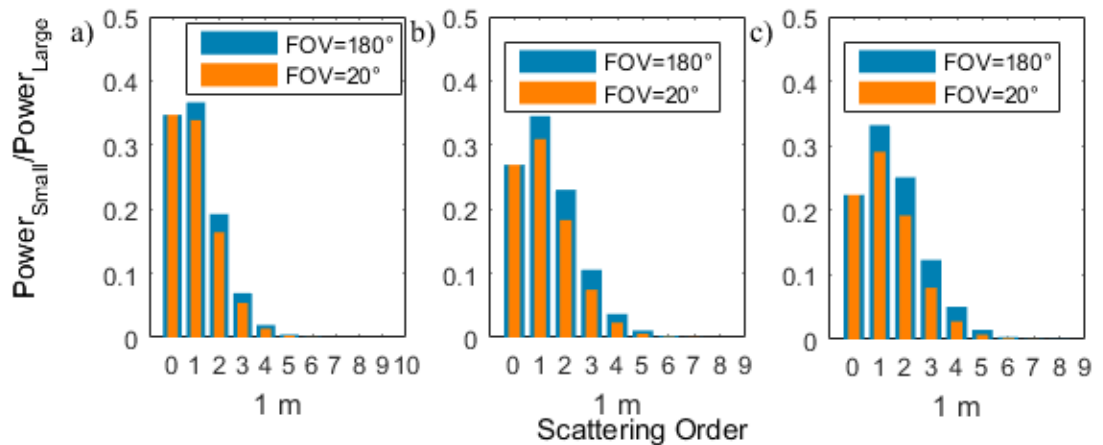


Figure 5.33: Scattering order histogram in turbid water at 1m for (a) collimated beam (b) 15° diffuse beam and (c) 30° diffuse beam.

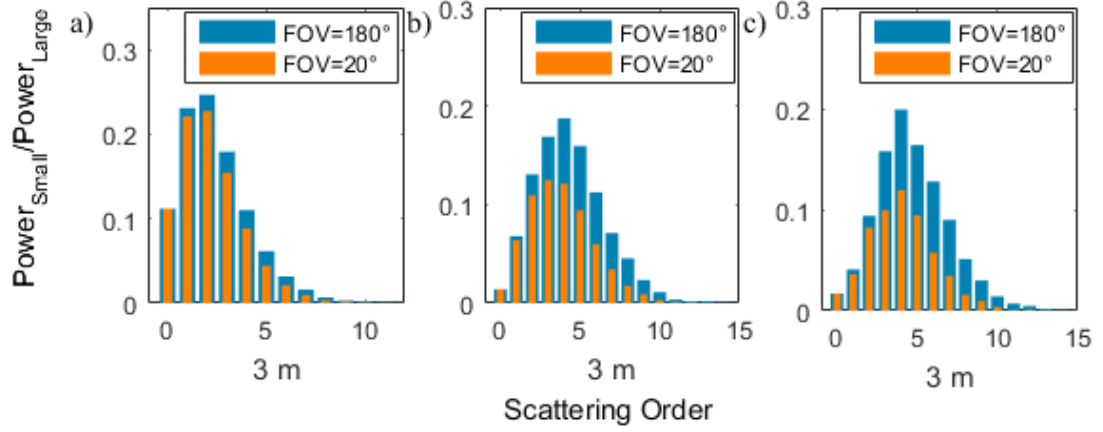


Figure 5.34: Scattering order histogram in turbid water at 3 m for (a) collimated beam (b) 15° diffuse beam and (c) 30° diffuse beam.

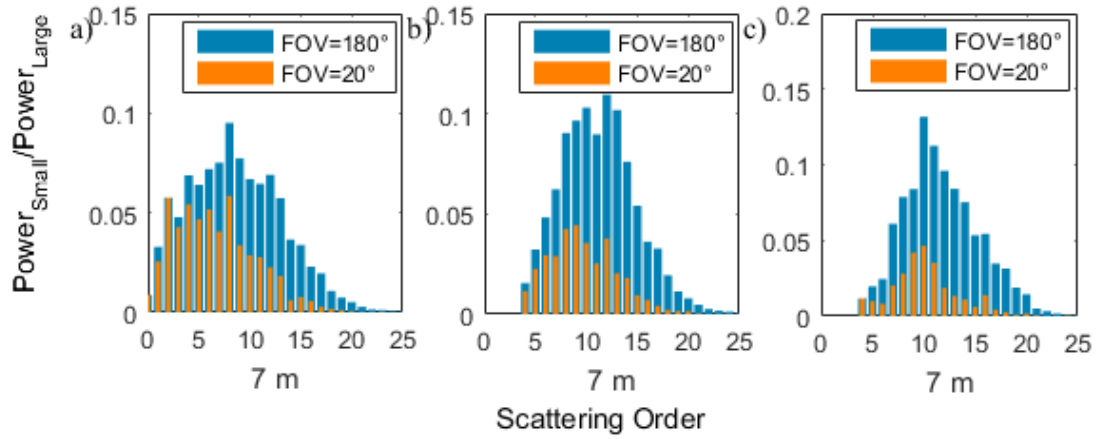


Figure 5.35: Scattering order histogram in turbid water at 7 m for (a) collimated beam (b) 15° diffuse beam and (c) 30° diffuse beam.

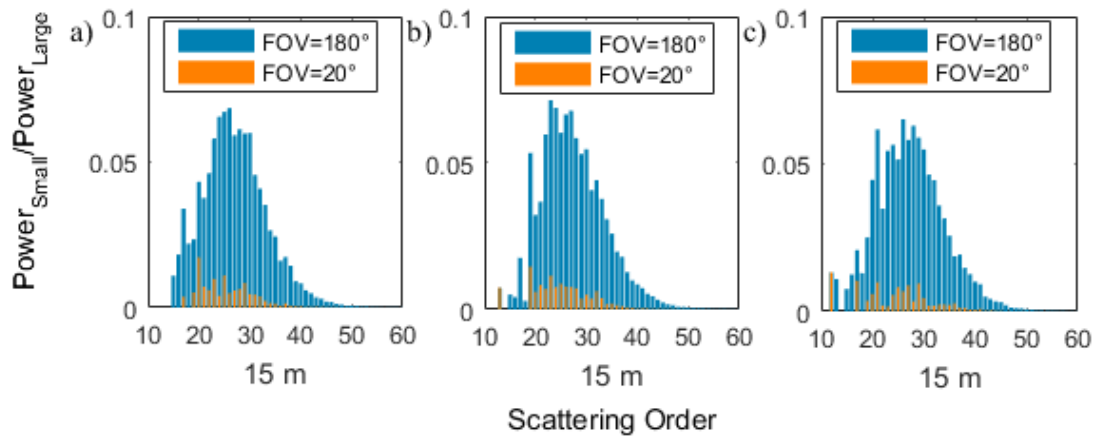


Figure 5.36: Scattering order histogram in turbid water at 15m for (a) collimated beam (b) 15° diffuse beam and (c) 30° diffuse beam.

5.8 Conclusion

In this chapter, the concept of scattering order probability was introduced to understand the scattering behaviour of diffuse beams in three types of water. This kind of information is only achievable through MC simulation which provides valuable insights on how photons from different beam divergences scatter. This concept was further used in the characterisation of the scattering regime for diffuse links. From the simulations results, the transition point for each scattering regime was proposed for coastal water and turbid water.

Based on this scattering regime classifications, the temporal dispersion effect was evaluated by investigating the impulse response and frequency response to determine the supported channel bandwidth. Besides that, the angular dispersion that results from scattering was also demonstrated by exploring the AOA distribution which is beneficial in studying the effect of FOV on the bandwidth performance. Thus, it is believed that the AOA distribution will be one of the tools in understanding the angular behaviour of the received photons and aid system designers in optimizing the receiver FOV performance. To conclude the findings obtained in this chapter, it is useful to present the summary based on the three scattering regimes as presented next.

- **Regime I : Minimal scattering regime**

It is observed that for diffuse beams, apart from the unscattered and single scattered components that exist, higher order multiple scattering also present at a higher probability due to the wider nature of the beam divergence. Thus in this regime, it can be concluded that as long as the unscattered component and single scattering exist, the link can be considered less affected to temporal dispersions as bandwidth more than 1 GHz is possible to be supported. The AOA distribution of the diffuse beam in this region shows that the AOA is distributed at a small angular dispersion. From this information, it can be said that a smaller receiver FOV ($<30^\circ$) can be used to capture all the photons which is also preferred as narrow FOV receiver will limit the amount of ambient light that enters the receiver.

- **Regime II : Intermediate scattering regime**

It is found that due to the absence of unscattered and single scattering photons, the bandwidth of the links is limited to several hundreds of MHz. However, the bandwidth can be increased by reducing the receiver FOV as discussed previously. The AOA distribution shows slightly larger spread at larger angles ($\sim 40^\circ$ - 80°) as now, more photons have been multiple scattered indicating a large receiver FOV is needed.

- **Regime III : Multiple scattering regime**

In this regime, the scattering is so severe that it cause very large delays that limit the bandwidth to several tenth of MHz. The AOA distributions shows angular dispersion that spread to very large angles ($\sim 60^\circ$ - 90°) signifying a very large receiver FOV is needed to collect most of the photons. Reducing the receiver FOV has little effect to the bandwidth as all the photons exhibit higher number of scatterings ($n > 9$). It is also observed that the source distribution size has indistinguishable effect on the scattering order, impulse response and bandwidth. Another interesting observation to highlight is the bandwidth performance for on-axis and off-axis performance is relatively the same . This shows that this region can be characterised by diffusion type multiple scattering [117]. The summary of this analysis is shown in Table 5.11.

On the other hand, the temporal and angular dispersions performance for off-axis locations are quite complex to be quatified in terms of scattering regimes as geometrical factors (i.e. offset distance) do influence their behaviour. Suffice to say that, at off-axis locations, high bandwidth significantly depends on the collection of unscattered and single sacttered photons. In cases where only multiple scattered photons are collected, very limited bandwidth is supported even by reducing the receiver FOV.

Finally, it was also believed that the proposed transition point in this chapter can be useful in determining the regime where the analytical model developed

in [42] can be used. In their work, two types of impulse response model namely ideal delta function and double Gamma function was proposed to represent the system studied. However, the exact region as to where the model is valid is unknown. Thus, the information on the transition points and scattering regimes in this chapter will provide some insight into the issue.

Table 5.11: Summary of the characteristics of the scattering regime for diffuse beam (on-axis).

Parameters	Regime I	Regime II	Regime III
Types of water and the corresponding transition points	Coastal water : $z \leq 22$ m Turbid water : $z \leq 3$ m	Coastal water : $22 \text{ m} < z < 70 \text{ m}$ Turbid water : $3 \text{ m} < z < 15 \text{ m}$	Coastal water : $z \geq 70$ m Turbid water : $z \geq 15$ m
Scattering order (minimum n)	$n \leq 1$	$1 < n \leq 9$	$n > 9$
Impulse response	Strong peak	Moderate peak with large spread	Large spread
Bandwidth and Impact of FOV on bandwidth	Can support high bandwidth. Bandwidth can be improved to more than 1 GHz by reducing the receiver FOV.	The bandwidth is limited to several hundreds of MHz, but can be increased by reducing the receiver FOV.	The bandwidth is limited to several tens of MHz. The reduction of FOV has minimal effect on the bandwidth as a small increase is observed.
AOA distribution and receiver FOV requirement	Small range of AOA. Small receiver FOV is needed to capture most of the photons i.e. (FOV: 20° - 40°) depending on water types.	Medium range of AOA. Medium receiver FOV is needed to capture most of the photons. i.e. (FOV: 40° - 60°) depending on water types.	Large range of AOA. Wide receiver FOV is needed to capture most the photons i.e. (FOV : 80° - 90°) depending on water types.

CHAPTER 6

Impact of Receiver Aperture and Performance Trade-Off

6.1 *Introduction*

In this chapter, the impact of receiver aperture size on the scattering order will be analysed to assess how this change will influence scattering order histogram behaviour. In addition to that, the investigation on the impact of receiver FOV and aperture on the received power is also presented. Subsequent section discusses the performance trade-off between the power and bandwidth by utilising the scattering regime proposed in Chapter 5.

6.2 *Impact of receiver aperture size*

The investigation on the effect of receiver aperture size has been conducted by several authors . In [125], the effect of aperture to the impulse response was investigated by increasing the aperture from 5 mm to 50 cm. It was shown that there is an increase in the peak of the impulse response signifying higher

power received. Besides that the impulse response became more spread which cause an increase in delay spread but still negligible for 1 GHz transmissions for 50 m distance in clear water. A similar observation is also reported by Cox, where it is found that the size of aperture has significant effect on the received power but little effect on the bandwidth of the system. It was also shown that at lower AL, the aperture has little effect on the received power due to the small beam spreading which cause the beam to be restricted to small area at the centre of the receiver aperture [38]. Thus in this section, the effect of receiver aperture on the scattering order histogram and received power will be presented.

6.2.1 Impact of receiver aperture size on scattering order histogram

It should be recalled that the scattering order probability introduced in Chapter 5 was calculated by using the largest receiver FOV, i.e. 180° to consider all the photons that reach the receiver while the receiver aperture is set to be 10 cm. Thus in this section the impact of reducing the receiver aperture size on the scattering order histogram is investigated.

Figures 6.1 to 6.11 show the scattering order histogram when the receiver aperture diameter is reduced to 5 cm. Similar to Section 5.7, instead of calculating the absolute probability of the scattering order for smaller aperture, the ratio of the power received by smaller aperture to the power

received by larger aperture is calculated. Then the histogram of this ratio is plotted on the same axis as the original histogram obtained in section 5.2.

By observing all the plots, it can be seen clearly that the reduction of aperture size significantly reduces the magnitude of the individual scattering order but maintains the same behaviour of the scattering order. This signifies that, by reducing the aperture, the amount of photons collected is decreased due to a smaller collection area. However the distribution of the scattering order behaviour is not affected implying that, the particular scattering order histogram can still be classified to the same scattering regime. From this observation, it can be said that the scattering order histogram is a valid indicator to be used in the classification of the scattering regime.

- **Clear water**

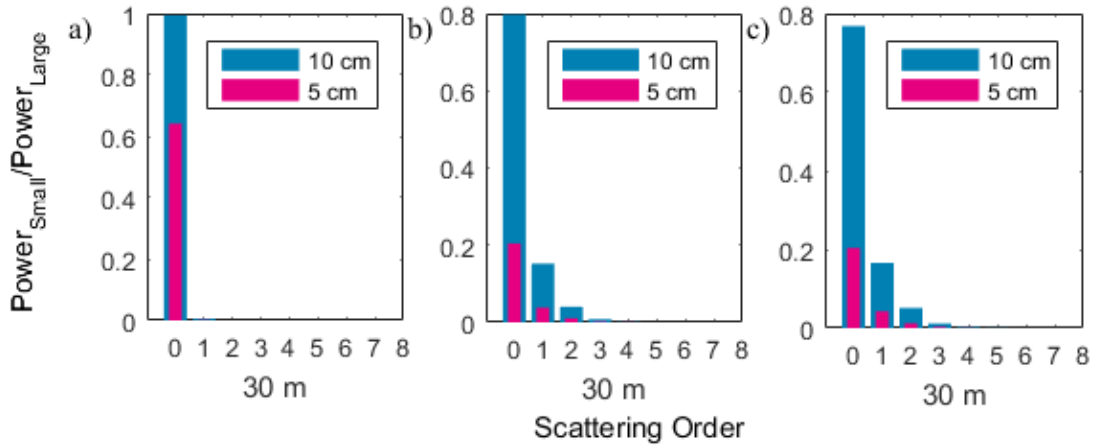


Figure 6.1: Scattering order histogram in clear water at 30 m for (a) collimated beam (b) 15° diffuse beam and (c) 30° diffuse beam.

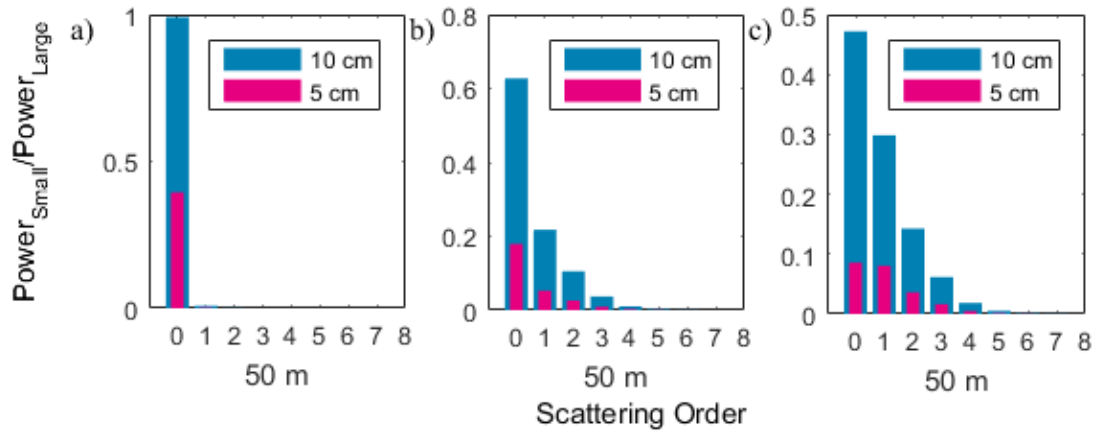


Figure 6.2: Scattering order histogram in clear water at 50 m for (a) collimated beam (b) 15° diffuse beam and (c) 30° diffuse beam.

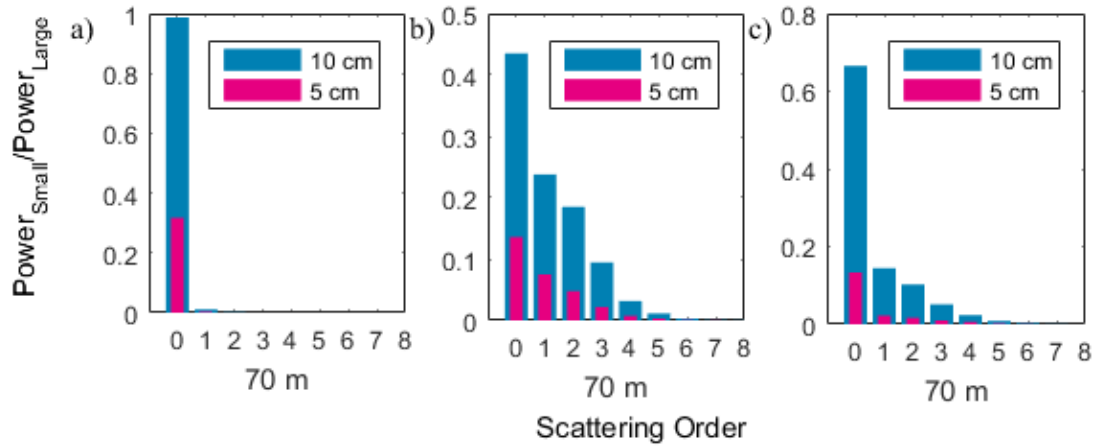


Figure 6.3: Scattering order histogram in clear water at 70 m for (a) collimated beam (b) 15° diffuse beam and (c) 30° diffuse beam.

- **Coastal water**

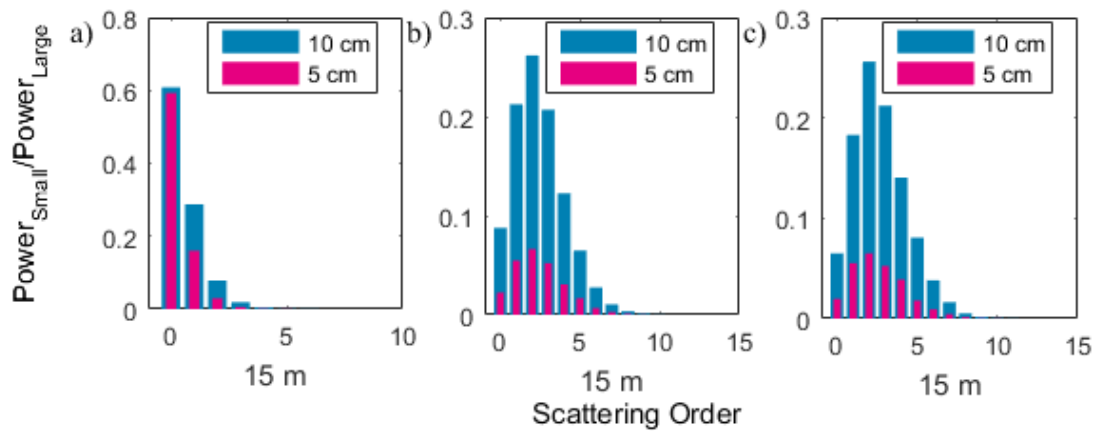


Figure 6.4: Scattering order histogram in coastal water at 15m for (a) collimated beam (b) 15° diffuse beam and (c) 30° diffuse beam.

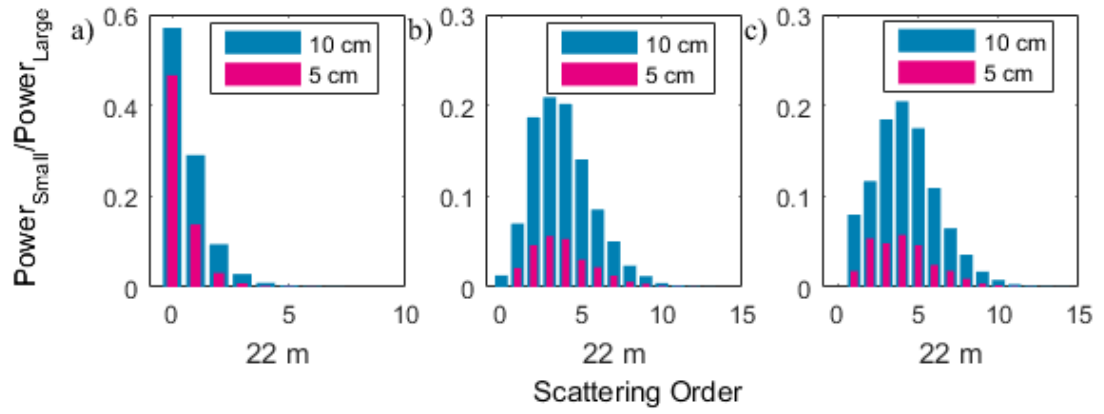


Figure 6.5: Scattering order histogram in coastal water at 22 m for (a) collimated beam (b) 15° diffuse beam and (c) 30° diffuse beam.

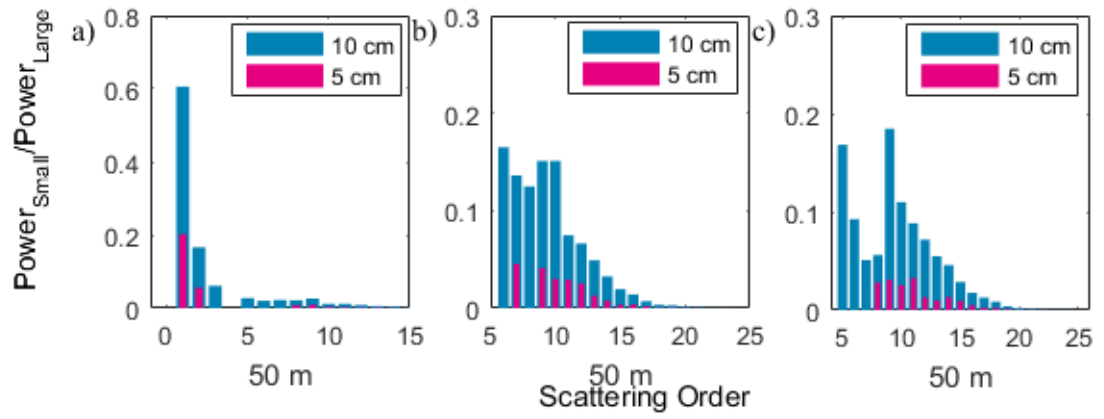


Figure 6.6: Scattering order histogram in coastal water at 50 m for (a) collimated beam (b) 15° diffuse beam and (c) 30° diffuse beam.

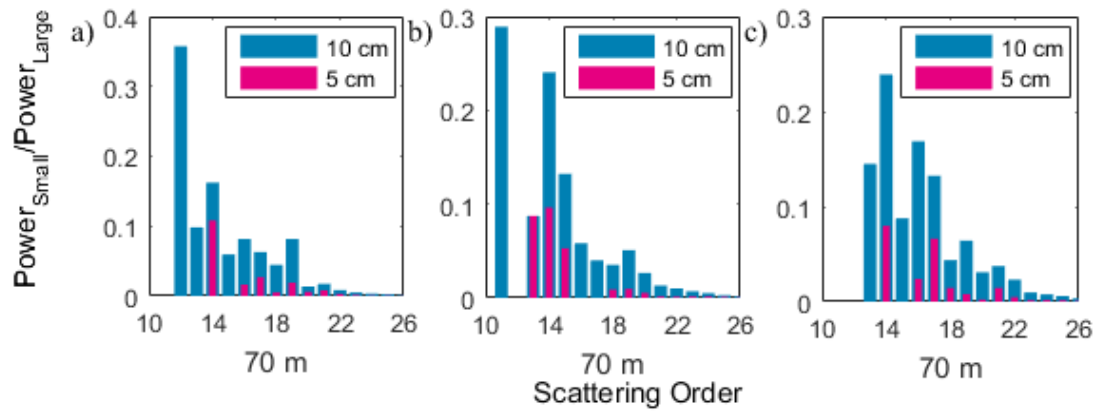


Figure 6.7: Scattering order histogram in coastal water at 70 m for (a) collimated beam (b) 15° diffuse beam and (c) 30° diffuse beam.

- **Turbid water**

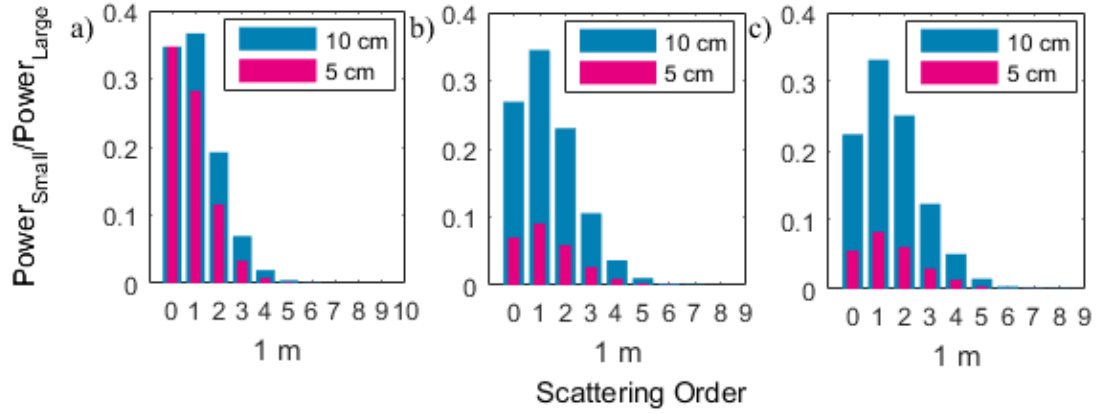


Figure 6.8: Scattering order histogram in turbid water at 1 m for (a) collimated beam (b) 15° diffuse beam and (c) 30° diffuse beam.

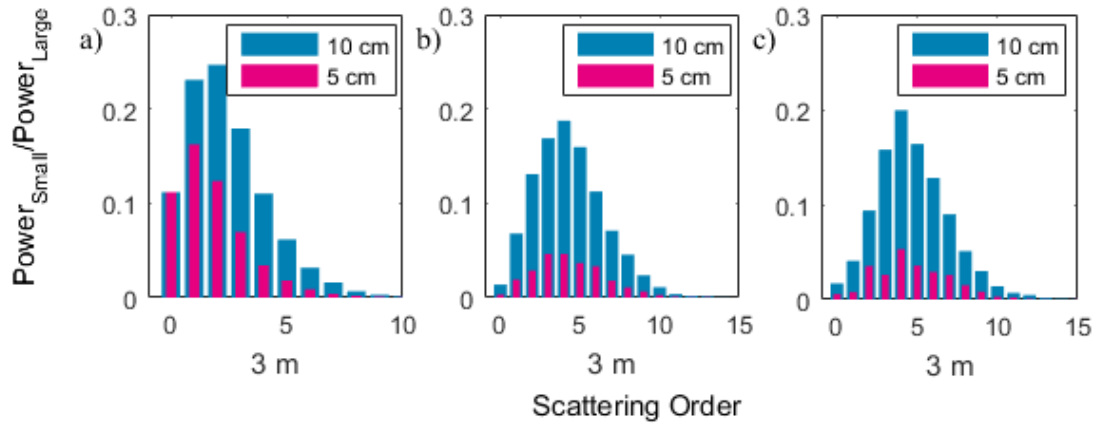


Figure 6.9: Scattering order histogram in turbid water at 3 m for (a) collimated beam (b) 15° diffuse beam and (c) 30° diffuse beam.

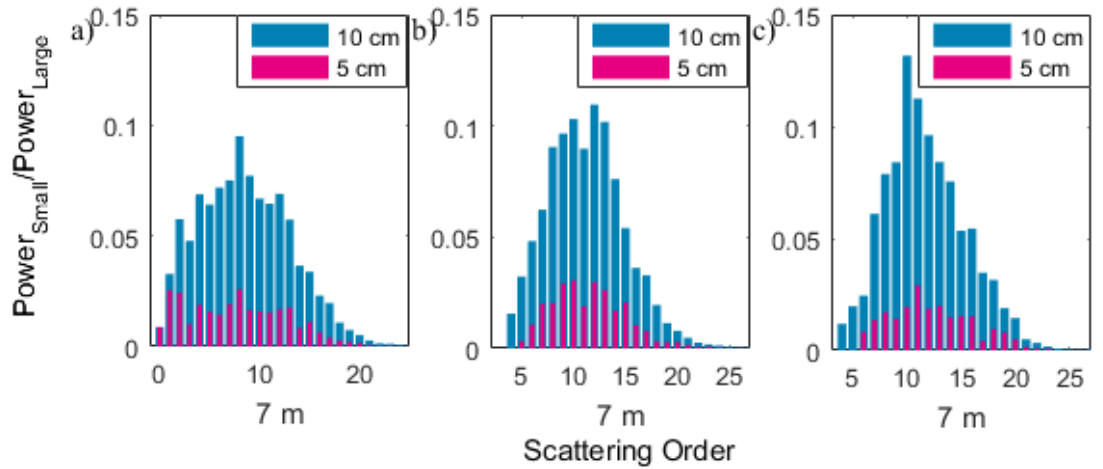


Figure 6.10: Scattering order histogram in turbid water at 7 m for (a) collimated beam (b) 15° diffuse beam and (c) 30° diffuse beam.

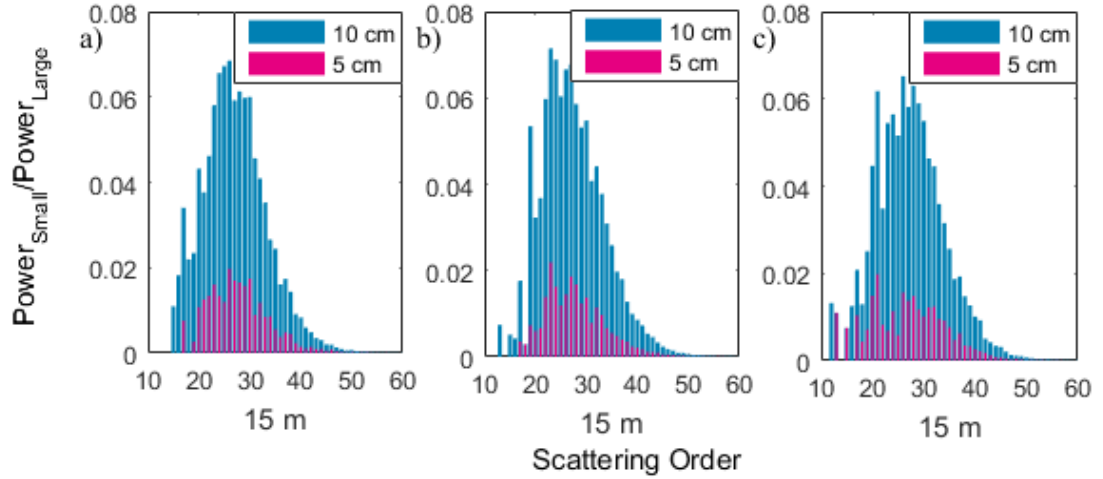


Figure 6.11: Scattering order histogram in turbid water at 15 m for (a) collimated beam (b) 15° diffuse beam and (c) 30° diffuse beam.

6.2.2 Impact of receiver aperture size on the received power

Having seen how the scattering order histogram is impacted by the reduction of aperture, it is interesting to see how the reduction of the receiver aperture affects the received power. In this section, the receiver aperture is reduced from 10 cm to 5 cm and 2.5 cm to investigate its effect on the received power.

Figures 6.12(a) to (c) show the percentage of the received power when the receiver aperture is decreased to 5 cm and 2.5 cm in three types of water. The percentage of the received power is calculated by taking the ratio of the received power of the smaller aperture to the received power when the 10 cm aperture is used. Overall, it can be seen that a distinct behaviour is observed for collimated beam and both diffuse beams in all types of water. From Figure 6.12(a), it can be seen that the reduction of receiver aperture size has little effect on the received power for collimated beam at short distance. This can be explained by the fact that at short distance, most of the light from collimated

beam is concentrated at the centre of the beam axis; a similar scenario is also observed in [38].

However, in contrast to collimated beam, both diffuse beams show a similar reduction of received power irrespective of the distance and turbidity level. This is due to the large beam spreading that cause a large beam spot to be formed at the receiver location. As a results, the percentage of the received power can be calculated as proportional to the area of receiver. This is shown by the constant percentage of received power for both diffuse beam; the power is reduced to 25 % and 6% when the receiver aperture diameter is reduced to 5 cm and 2.5 cm respectively.

Another interesting observation to highlight is the point at which the reduction of power for collimated beam in turbid water becomes insensitive to the distance can be related to the diffusion length of the collimated beam. This is shown clearly in turbid water where at 7 m, the power received when using collimated beam is reduced to the same percentage as both diffuse beams indicating that at this distance, the beam has been spread at a larger area due to multiple scattering.

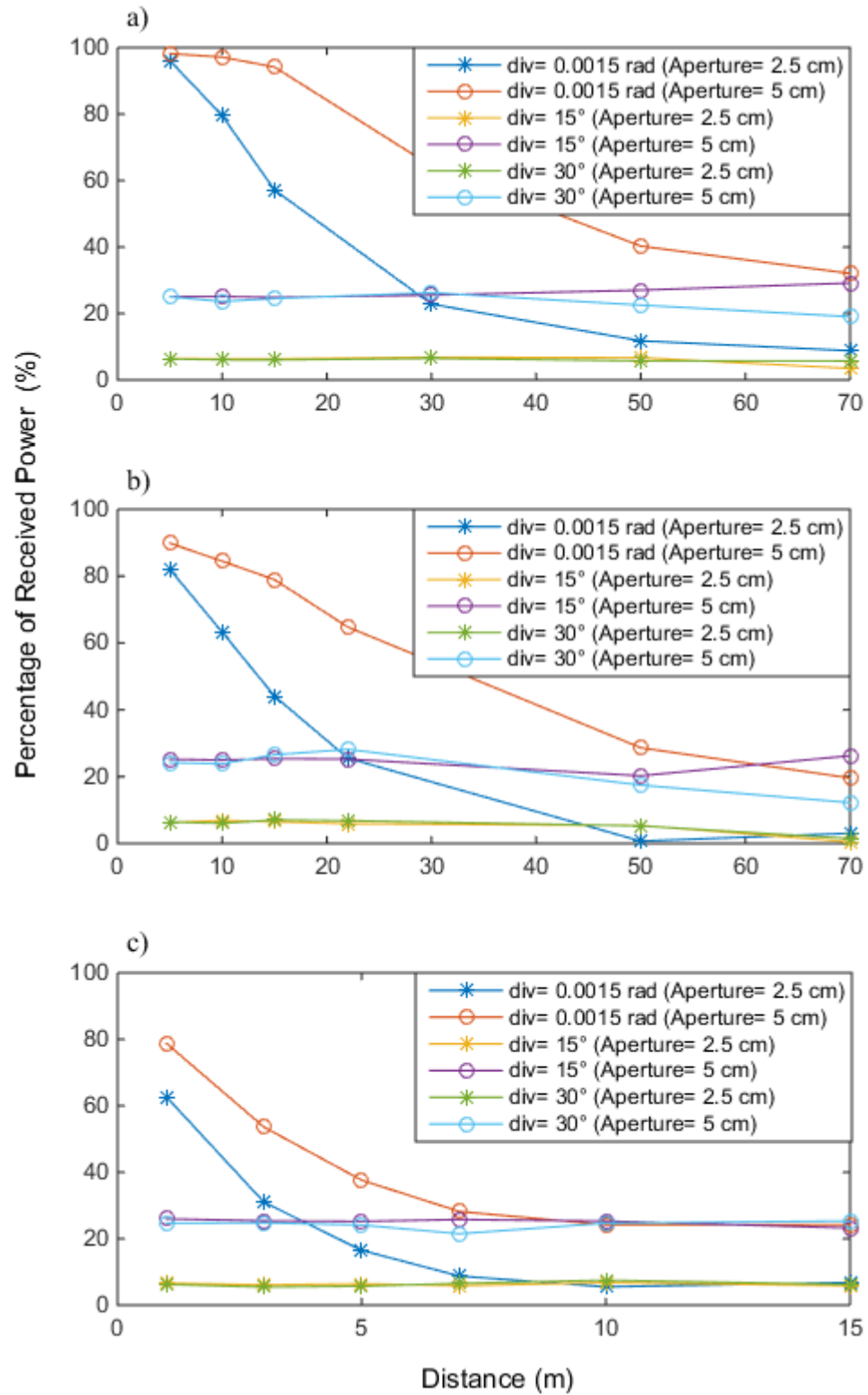


Figure 6.12: Percentage of received power for various receiver aperture in (a) clear water (b)coastal water and (c) turbid water.

6.3 *Impact of receiver FOV on the received power*

Based on the AOA distribution presented in Section 5.5, it can be seen that a smaller receiver FOV than 180° can be used to collect all the photons in most of the cases. Thus, in this section, the size of the receiver FOV is varied to investigate the impact of FOV on the received power for both on-axis and off-axis positions by calculating the percentage of the received power. This is done by taking the ratio of the received power at the smaller receiver FOV to the received power when receiver FOV is 180° .

Figures 6.13 to 6.15 show the percentage of the received power in various types of water for various beam divergences at on-axis locations. For collimated links in clear water, it can be said that a receiver FOV of 1° is sufficient to collect 95% of the photons. For both diffuse beams, a larger receiver FOV at approximately 30° is needed to collect 90% the photons.

In coastal water, for collimated beam, it is apparent that except at 70 m, a smaller receiver FOV (i.e. 10°) is needed to collect 90% of the photons. At 70 m where multiple scattering dominates, it can be seen that more than 90% of power is lost if receiver FOV of 10° is used. In contrast, for both diffuse beams, it can be seen that larger receiver FOV are needed as shown in Figure 6.14.

In turbid water, at shorter range ($<5\text{m}$), a larger receiver FOV of 40° is needed by both diffuse beams to capture more than 70% of the photons, compared to

collimated beam that only requires FOV of 20° . On the other hand, at 10 m and beyond, a larger receiver FOV of approximately 80° is needed to collect 80% of the photons irrespective of the beam divergences sizes.

- **Off-axis**

It should be recalled that the AOA distribution for all off-axis locations depicted in Figure 5.13 to 5.17 showed an angular displacement due to the lateral position of the receiver with respect to the center of the beam. Thus, most of the peaks of the AOA distribution occur at a certain angle as discussed in Section 5.5.2. Therefore, a wider receiver FOV is needed to collect all the photons. This is particularly apparent for shorter distance where the angular displacement is larger. As a results, it can be seen from Figures 6.16 to 6.18 that reducing the receiver FOV significantly affects the received power at shorter distance. For off-axis locations in clear water, as the distance increases, a smaller FOV is sufficient to collect all the photons as now most of the photons have smaller AOA distribution. On the contrary, for all off-axis locations in coastal and turbid water, a larger FOV is needed as shown in Figure 6.17 and 6.18.

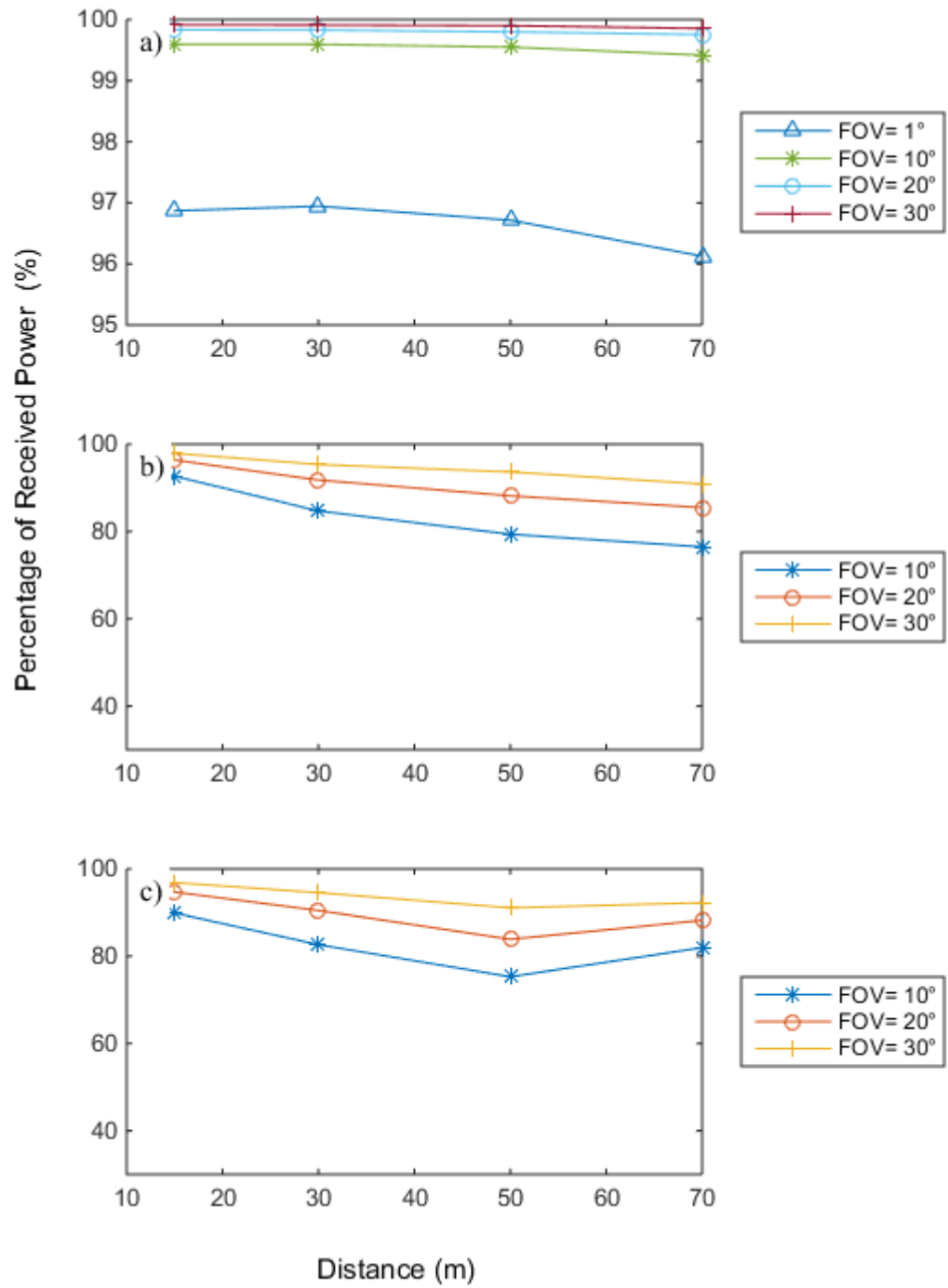


Figure 6.13: Percentage of received power for various receiver FOV in clear water at on-axis location using (a) collimated beam, (b) 15° diffuse beam and (c) 30° diffuse beam.

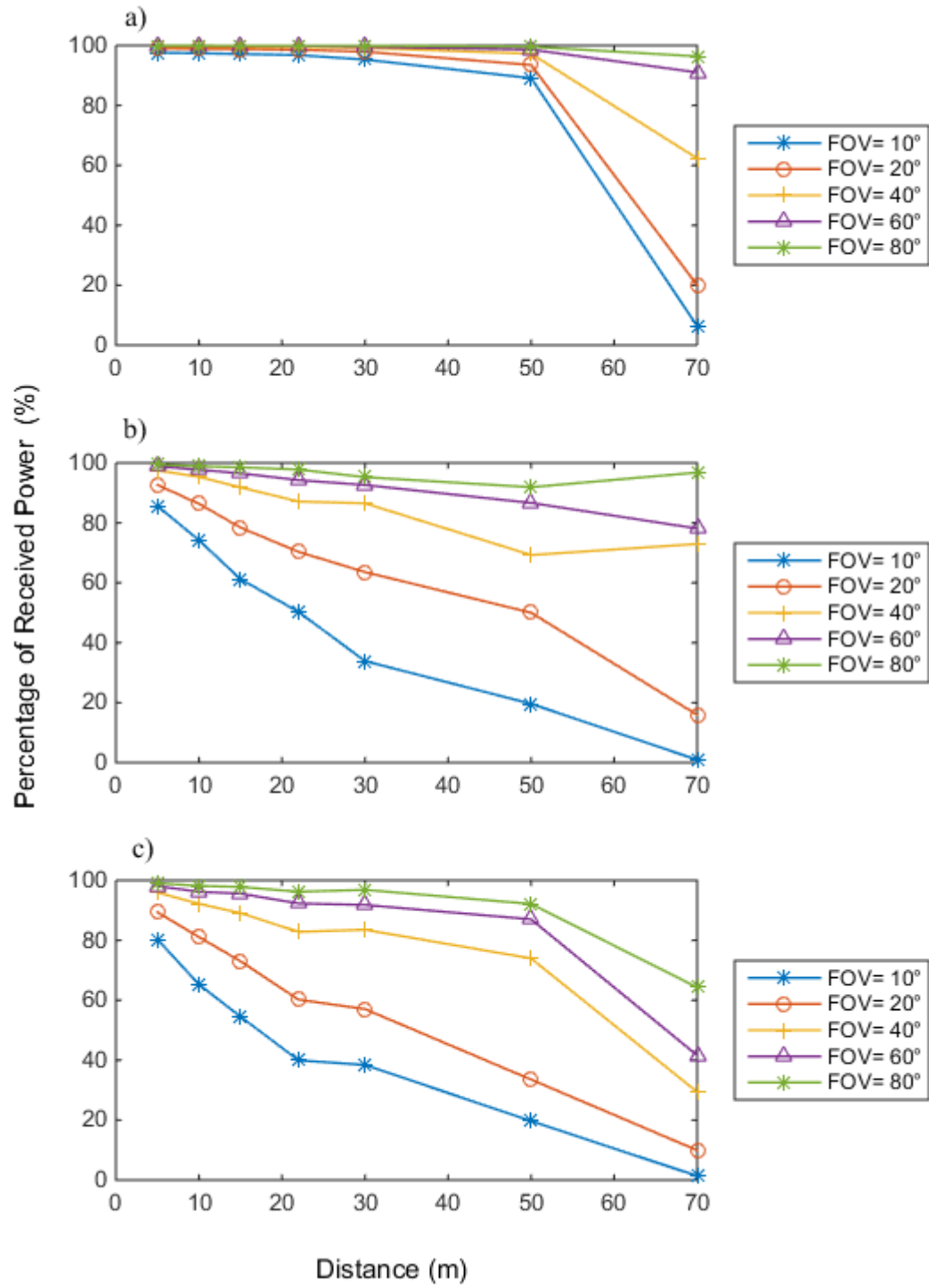


Figure 6.14: Percentage of received power for various receiver FOVs in coastal water at on-axis location using (a) collimated beam, (b) 15° diffuse beam and (c) 30° diffuse beam.

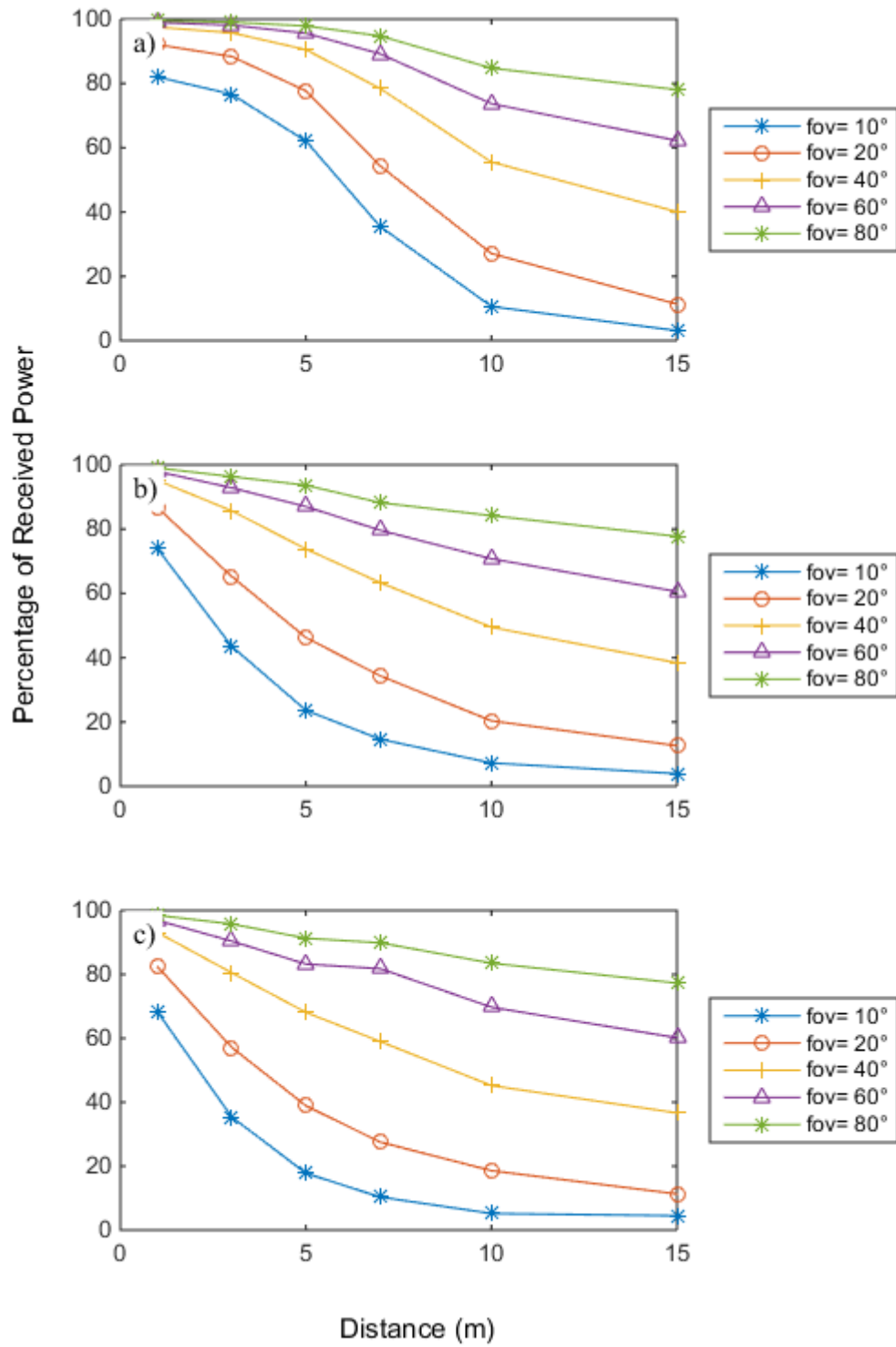


Figure 6.15: Percentage of received power for various receiver FOVs in turbid water at on-axis location using (a) collimated beam, (b) 15° diffuse beam and (c) 30° diffuse beam.

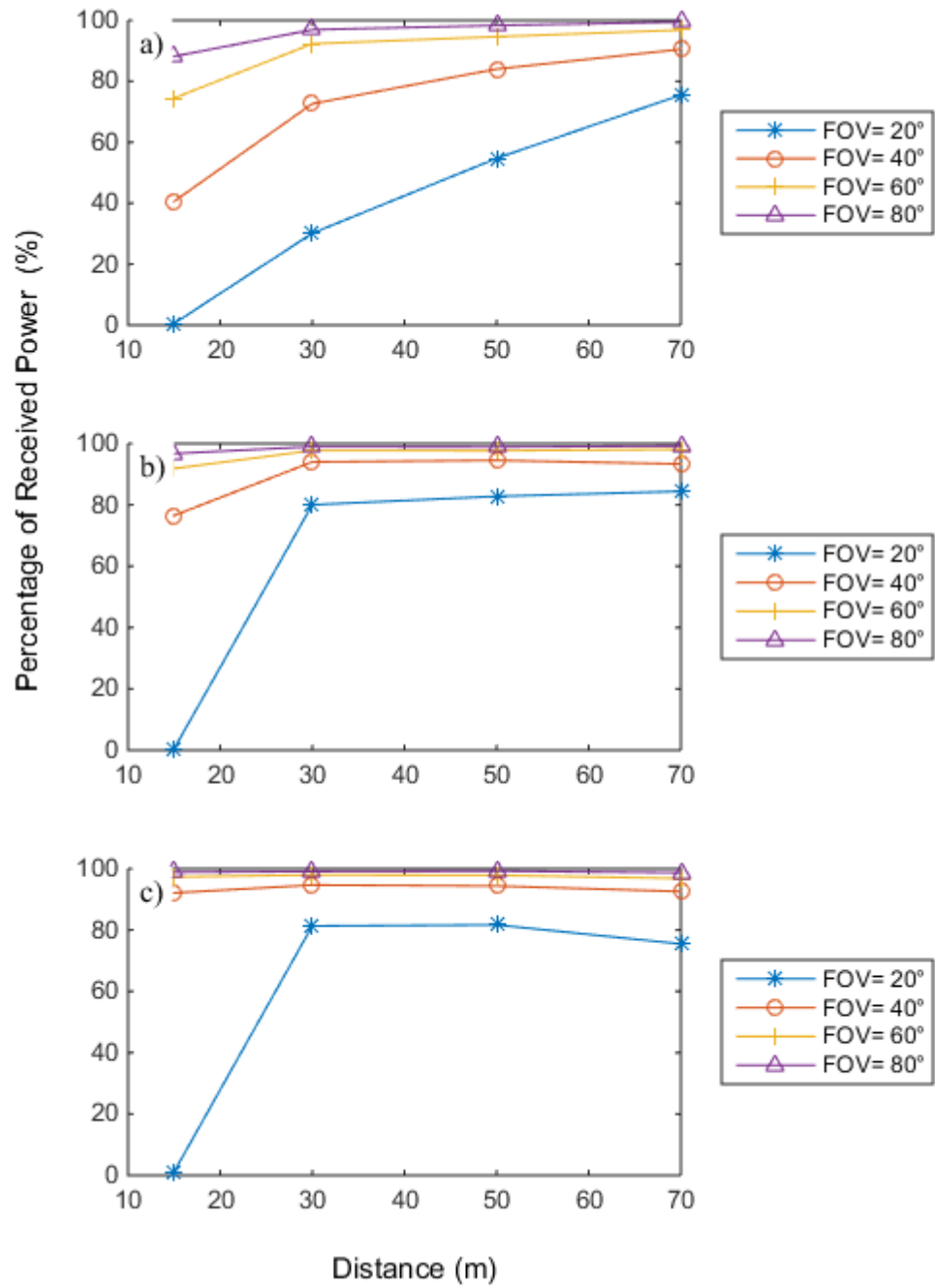


Figure 6.16: Percentage of received power for various receiver FOVs in clear water at off-axis location using (a) collimated beam, (b) 15° diffuse beam and (c) 30° diffuse beam

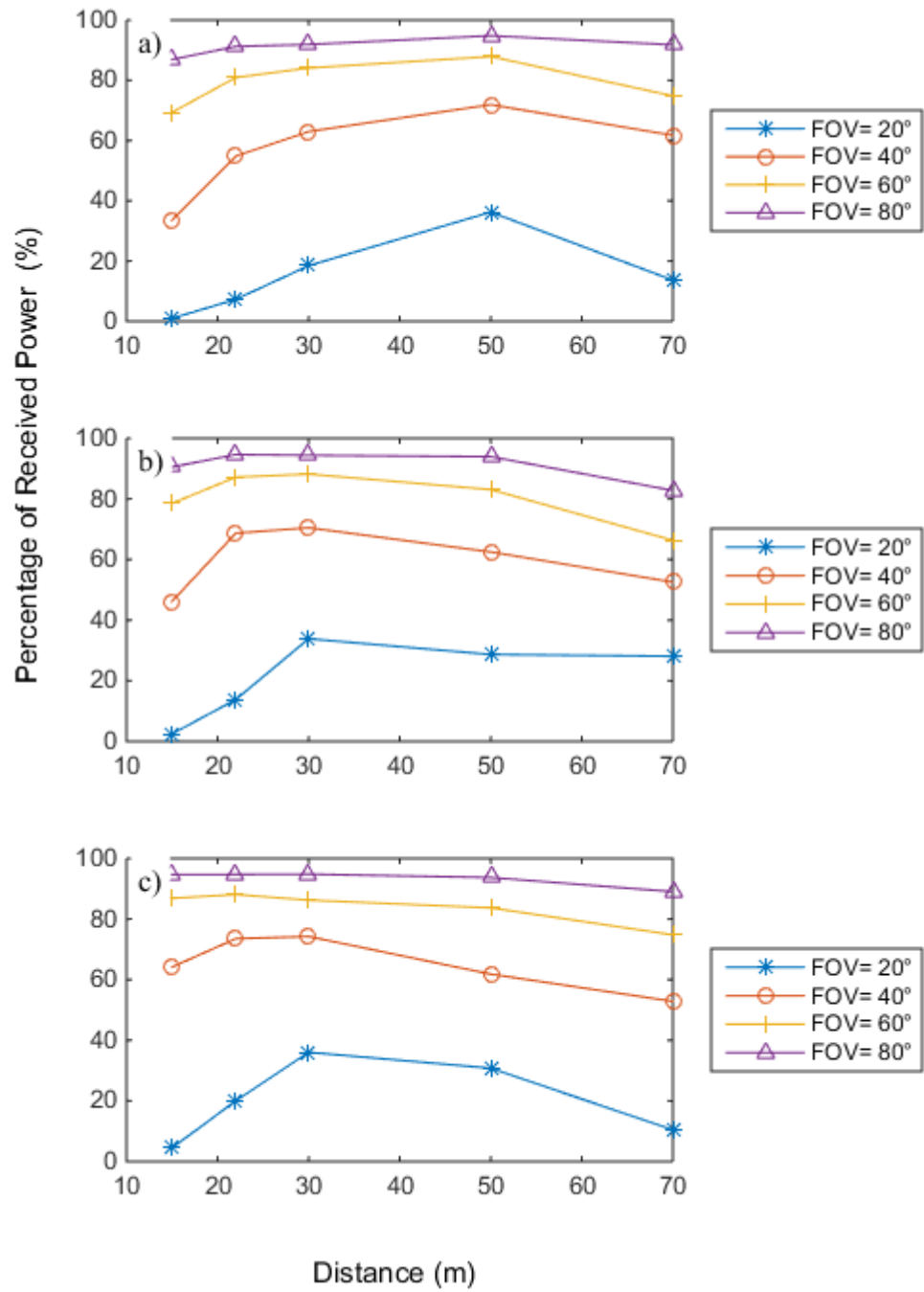


Figure 6.17: Percentage of received power for various receiver FOVs in coastal water at off-axis location using (a) collimated beam, (b) 15° diffuse beam and (c) 30° diffuse beam.

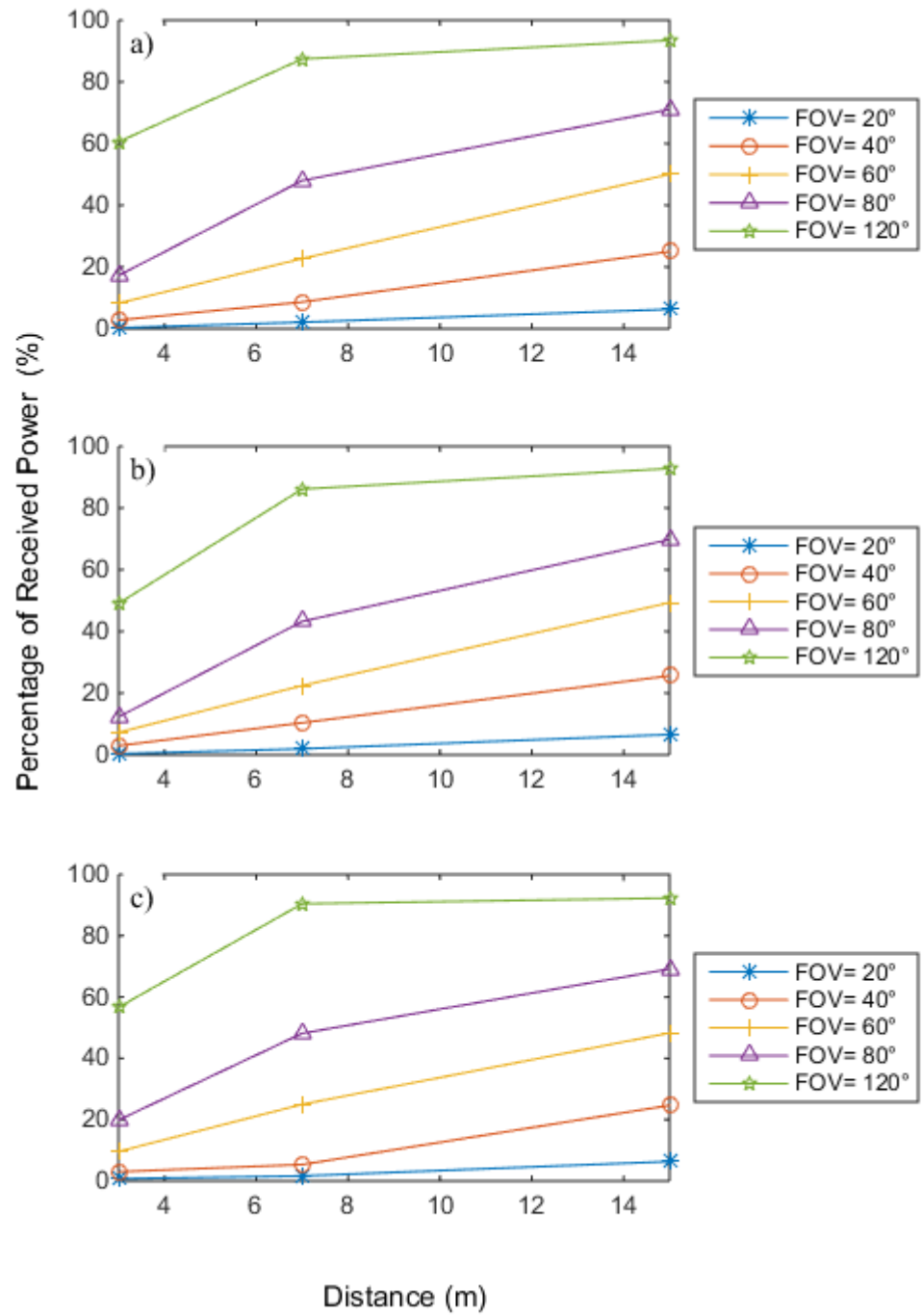


Figure 6.18: Percentage of received power for various receiver FOVs in turbid water at off-axis location using (a) collimated beam, (b) 15° diffuse beam and (c) 30° diffuse beam.

6.4 *Performance trade-off: Power and bandwidth*

In the previous section, the impact of receiver FOV on the received power performance has been evaluated for both collimated and diffuse beams, at both on-axis and off-axis locations. It should be recalled that in Section 5.6, the receiver FOV has also shown to affect the bandwidth in various ways depending on the scattering regime and geometry of the links. Thus, the aim of this section is to evaluate the performance trade-off between power and bandwidth in three types of water. It is useful to discuss this based on the scattering regime introduced in Chapter 5. Besides that, the information on the 3 dB bandwidth tabulated in Tables 5.5 to 5.10 are also referred to aid the discussion. To simplify the discussion, the diffuse beam of 15° is referred to.

6.4.1 Clear water

Diffuse links in clear water for range (5-70 m) is classified as regime I. From the bandwidth performance analysis in Section 5.4, it can be seen that diffuse links are able to support bandwidth of 1 GHz at both on-axis and off-axis locations. Thus, in clear water, the main aim is to choose the receiver FOV that can optimised the power. By referring to Figure 6.13, it can be concluded that receiver FOV of 30° can be used to collect most of the photons. At the same time a smaller FOV will reduce the amount of ambient light which ultimately reduces noise.

This is better compared to collimated beam that offers superior bandwidth performance at on-axis but not at off-axis locations. A slight bandwidth improvement can be obtained at off-axis locations for collimated links at an expense of a lower power. By referring to Table 5.8, a bandwidth of more than 500 MHz can be obtained by reducing the receiver FOV to 40° and 20° and this causes the received power to decrease by approximately 30-60% depending on distance.

Thus, diffuse links are considered as a better choice for systems that aim to provide a higher bandwidth with a wider coverage area. However, the drawback of using diffuse beam in this case is the low received power compared to collimated beam. It is shown in Figure 4.1 previously that the received power when diffuse beam is used is 30-40 dB less than the power that can be delivered by collimated beam at on-axis location.

6.4.2 Coastal water

In coastal water, diffuse links can only support high bandwidth when it is operating in regime I (5 m-22 m). For regime II (22 m-70 m), the on-axis bandwidth performance can be improved by reducing the FOV from 180° to 20° at an expense of 20% - 50% power lost. At regime III ($z=70$), the link has very limited bandwidth as a reduction of FOV from 180° to 20° results in minimal increase in bandwidth. At the same time, a significant amount of power is lost (>60%). Thus, in regime III, a wider FOV is needed to maximize

the received power. Figure 6.19 shows the trade-off between power and bandwidth as a function of FOV for three locations in coastal water.

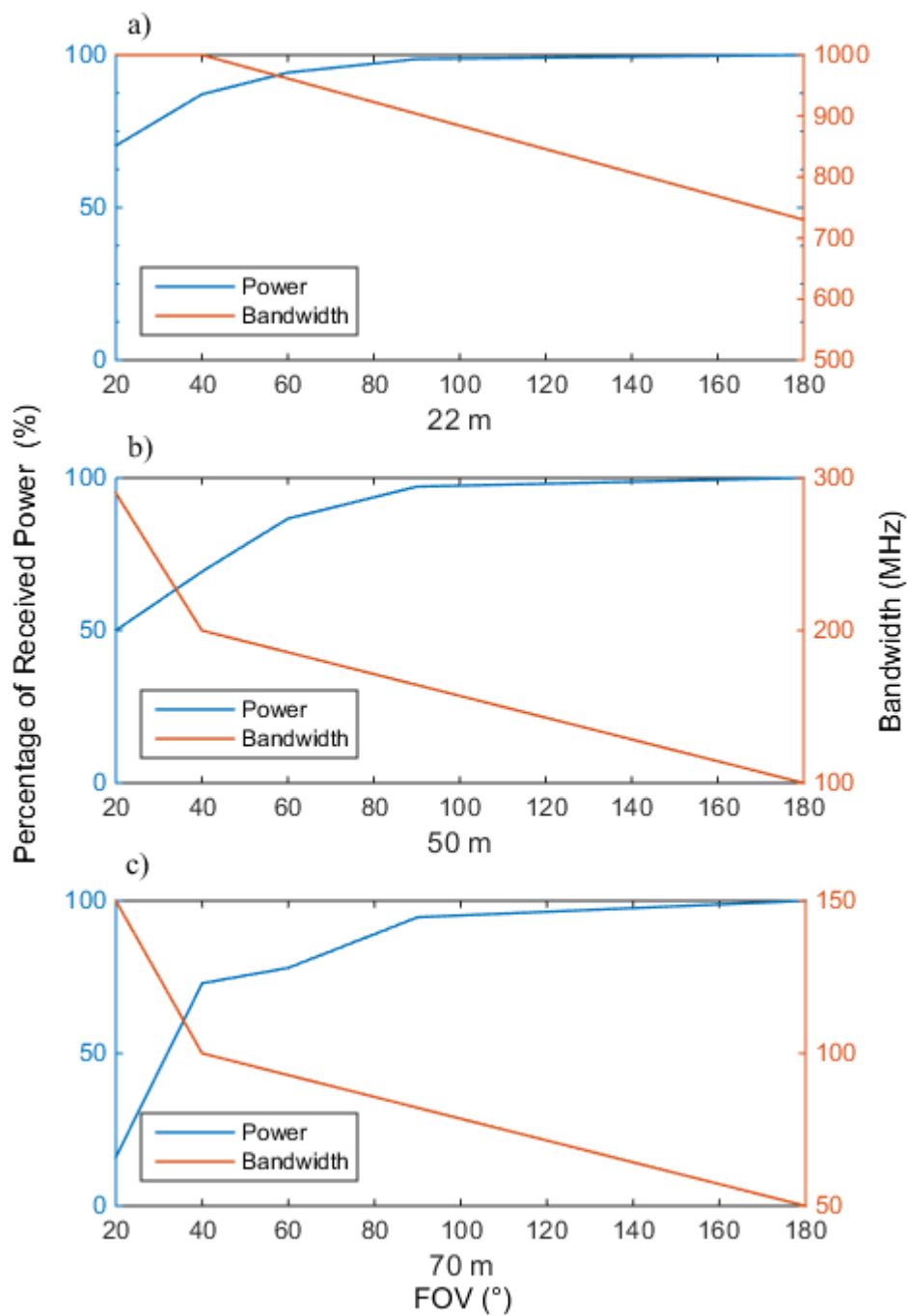


Figure 6.19: Trade-off between power and bandwidth as a function of FOV for diffuse beam of 15° in coastal water at (a) 22m (b) 50 m and (c) 70 m.

6.4.3 Turbid water

In turbid water, an interesting scenario is observed where the power performance for all source divergences are relatively the same for both on-axis and off-axis locations except for collimated beam that shows better power performance at distance less than 10 m (Figure 4.11). Not only that, the overall bandwidth performance are comparatively the same except that collimated beam is able to support more than 1 GHz up to 7 m but both diffuse beams are able to support 1 GHz only when the receiver FOV is reduced to 20°. This will reduce the received power by more than 60%.

Interestingly, for distance longer than 15 m the size of the beam divergences has negligible effect on power and bandwidth performance indicating that a cheaper diffuse source such as LED is more economical in such application. Figure 6.20 shows the trade-off between power and bandwidth as a function of FOV for two locations in turbid water.

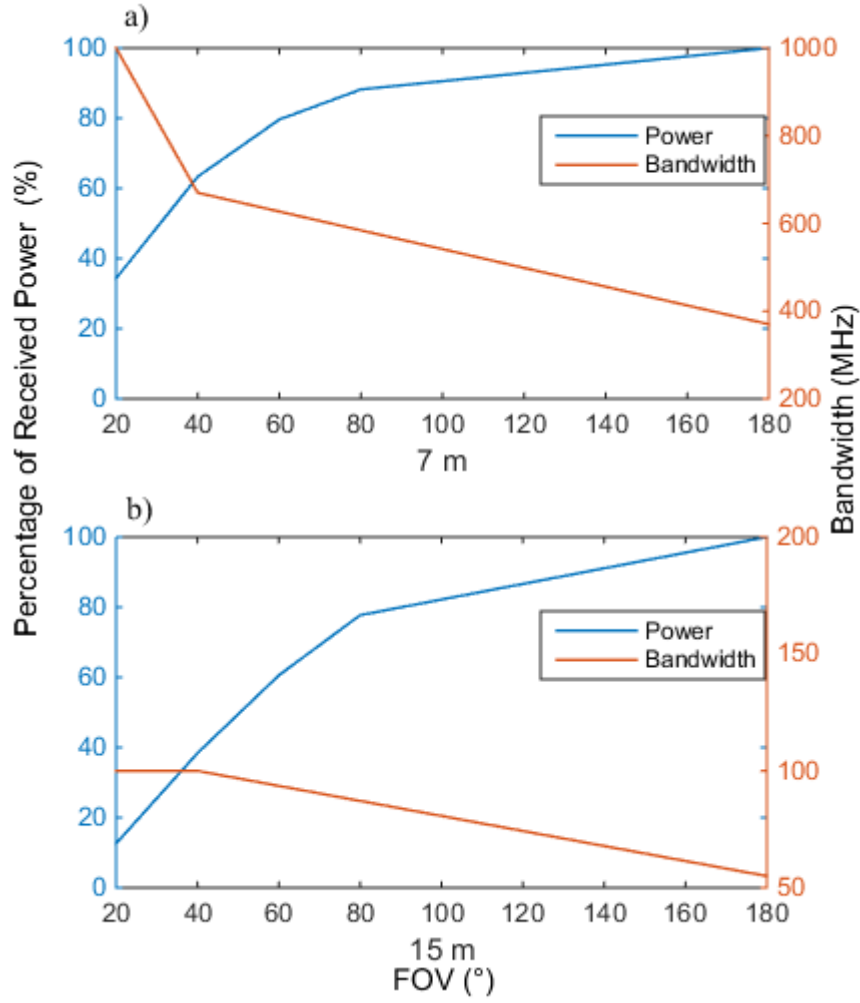


Figure 6.20: Trade-off between power and bandwidth as a function of FOV for diffuse beam of 15° in turbid water at (a) 7m and (b) 15 m.

6.5 Conclusion

This chapter investigates the effect of reducing the receiver aperture size on the scattering order histogram to evaluate any changes in the behaviour. It was shown that the behaviour of scattering order histogram remain the same signifying that, the method proposed in Section 5.2 to characterise the

scattering regimes was valid to be applied to UOWC links. In addition to that, the effect of reducing the receiver aperture and FOV on the received power were also studied.

Overall, it can be concluded that the bandwidth limitation imposed by diffuse links were only significant in coastal water and turbid water where high bandwidth (>1 GHz) can only be achieved at limited distance. In clear water, diffuse links can support high bandwidth at a wider coverage area but at a lower received power compared to collimated beam. In other words, it can be concluded that communication links using a diffuse links is more power limited rather than bandwidth limited as shown by the analysis.

CHAPTER 7

Conclusions & Future Work

7.1 *Conclusions*

There have been significant efforts in establishing a universal analytical model to predict the performance of UOWC links. However, due to the complexity and high variability of the light properties underwater, this is not possible. Thus, a more flexible method utilising MC simulation was used to model and characterise the underwater channel, as presented in this thesis. Particularly, the aim was to model and characterise the performance of diffuse links along with the use of a collimated beam, for comparison.

The thesis started with the introduction to UOWC, highlighting its importance in underwater applications. The motivation and the objectives of this thesis were presented in Chapter 1. Then, in Chapter 2, a brief introduction to various technologies used in underwater applications was presented, highlighting its advantages and disadvantages. Due to its limited operating range, UOWC was seen more as a complementary technology to acoustic technology, rather than alternative as it can support high bandwidths, but only over short ranges. The

subsequent section presented a review of the literature on channel modelling efforts and experimental works. Then, the background theory on the light properties underwater was discussed, with the main emphasis on the absorption and scattering processes. The main equation used to describe the light underwater, RTE, was introduced, highlighting its complexity, and signifying the necessity of using a numerical MC method in solving it.

Chapter 3 presented the MC simulation method in modelling light in the underwater environment. The details of the simulations, including the theory, mathematical equations and algorithm were discussed. Then, a simulation to compare two techniques in modelling diffuse beams was also presented, showing minimal differences between them. Finally, the description of the simulation setup and parameters used in this thesis, were presented.

Chapter 4 presented the path loss performance analysis, for both collimated and diffuse beams, which led to several important contributions. Firstly, by plotting the path loss performance for various types of water with respect to the same parameter, namely the AL, a more accurate picture of how different links attenuated as the AL was varied, was obtained. This observation showed that the AL cannot be used as the only parameter in characterising an underwater links, as the performance of underwater links significantly depends on water types, distance and system parameters.

Next, a detailed investigation of the individual analysis of the path loss performance of unscattered and scattered light led to a better understanding of how diffuse beam attenuate with distance. For the first time, the distance at which the unscattered component drops to zero was predicted, using MC simulation. This distance is useful, as it serves to estimate the transition point from the minimally-scattered region to the multiple-scattered region. As shown in the analysis, in the minimally scattered region, the rate of the attenuation can be approximated by the BL law, and, for the multiple-scattered region, the attenuation rate is slower.

Additionally, it was also shown that the link budget equation employing the BL law, which includes geometrical loss, can only predict the path loss performance in clear water, but not in coastal and turbid water, due to highly scattering events. Thus, the MC simulation is the best way to model accurately the path loss performance of the diffuse beam in coastal and turbid water. Further investigation of the power reception at the off-axis locations was also presented, which is believed to be useful for a link designer. The plot illustrated the range at which a uniform power could be obtained at off-axis locations.

Next, in chapter 5, the concept of scattering order probability was introduced, together with a method to classify the links into three scattering regimes. One of the contributions in this chapter was the characterisation of the diffuse links into three scattering regimes, based on their scattering probability profile. To

evaluate the characteristics of each scattering regime, the temporal and angular performances were investigated for several cases in the scattering regimes. Apart from that, the AOA distribution for a collimated beam and a diffuse beam were evaluated for the first time, for a wide range of distances, and in three types of water. It was shown that diffuse beams exhibit larger angular dispersion effects compared to collimated beams, as expected. Based on the AOA distribution, the receiver FOV was varied to investigate its effect to bandwidth performance. Several observations, particularly at off-axis locations, illustrate how AOA distributions are used to optimise the bandwidth performances.

In the subsequent chapter, the scattering order histogram was evaluated for smaller receiver apertures, so as to find the limitation of this technique. It was observed that the reduction of the size of the aperture had little effect on the scattering order histogram behaviour, as it only reduced the magnitude of the individual scattering order due to the reduction of the photons collected. Thus, it can be said that the method used in classifying diffuse links, based on scattering order information, is generally valid for various sizes of aperture. Besides that, the impact of reducing the receiver aperture and FOV on the power received were also investigated. Finally, the performance trade-off in optimising the bandwidth and power were evaluated, based on the scattering regime, providing some insights into how receiver FOV affect the bandwidth and power at different scattering regimes. On the whole, it can be concluded that the scattering regime proposed for diffuse links can be useful as a general

guide for link designers, in order to predict the power and bandwidth performance for diffuse links.

7.2 *Future research*

There are several future works that can be done as extensions to the work documented in this thesis.

- Improvement of the MC simulation efficiency.

One of the main disadvantages of the MC simulation is the long simulation time due to tracking millions of photons propagating through the channel. Typically, the simulation time can range up to several tens of hours. Thus, a method to improve the simulation time is needed to boost the performance of an MC simulation. Various techniques that have been used in accelerating MC simulation in biomedical applications. can be interesting technique to be applied in UOWC [126].

- Off-axis study : Fixed angular offset.

The off-axis locations studied in this thesis were set at a fixed distance of maximum 5 metres away from the centre of the diffuse beam. As the propagation distance increases, the angular offset decreases from the largest angular offset value, namely 79° , which corresponds to the propagation distance of 1 metre, to the smallest angular offset of 4° which corresponds to

the propagation distance of 70 metres. This implies that, as the propagation distance increases, most of the off-axis location defined in this thesis is situated within the illuminated area predicted by the divergence of the source. Thus, it is expected that the performance at off-axis locations at a fixed angular offset will show some variations.

- Using an attenuation coefficient that varies with wavelength.

In the simulations, the diffuse source was assumed to be monochromatic, which may not be very accurate, as typical diffuse sources, such as LEDs, have a very wide spectral linewidth. Due to this, the MC simulation could be modified to include this effect for more accurate results. This could be done by using the attenuation coefficient, c that is a function of for different wavelengths.

- Effect of turbulence and fading

In this thesis, the effect of turbulence and fading were not considered. It would be interesting to investigate how turbulence and fading influence the performance of the links. Recently, several research that investigate the effect of oceanic turbulence have been reported in [127,128,129].

- Evaluation of full system parameters (eg: BER)

The MC channel model obtained in this thesis specifically the impulse response can be used as the channel model to evaluate other system performance parameters such as BER. This can be done by finding a method to convolve the impulse response of the channel with an input signal to the full system. Recently, in [130] the impulse response generated by MC simulation has been used to evaluate the BER performance of MIMO UOWC links.

References

- [1] A. K. Majumdar and J. C. Ricklin, *Free-space laser communications: principles and advances*, vol. 2, Springer Science & Business Media, 2010.
- [2] Z. Ghassemlooy, W. Popoola, and S. Rajbhandari, *Optical wireless communications: system and channel modelling with Matlab®*, CRC Press, 2012.
- [3] R. J. Drost, T. J. Moore, and B. M. Sadler, "UV communications channel modeling incorporating multiple scattering interactions," *JOSA A*, vol. 28, no.4, pp. 686-695, 2011.
- [4] M. Chitre, S. Shahabudeen, and M. Stojanovic, "Underwater acoustic communications and networking: Recent advances and future challenges," *Marine Technology Society Journal*, vol. 42, no. 1, pp. 103-116, 2008.
- [5] B. Cochenour and L. Mullen, "Channel response measurements for diffuse non-line-of-sight (NLOS) optical communication links underwater," in *OCEANS*, Waikoloa, Hawaii, 19-22 Sept 2011, pp. 1-5.
- [6] H. M. Oubei, J. R. Duran, B. Janjua, H.-Y. Wang, C.-T. Tsai, Y.-C. Chi, T. K. Ng, H.-C. Kuo, J.-H. He, and M.-S. Alouini, "4.8 Gbit/s 16-QAM-OFDM transmission based on compact 450-nm laser for underwater wireless optical communication," *Opt Express*, vol. 23, no. 18, pp. 23302-23309, 2015.
- [7] D. Anguita, D. Brizzolara, and G. Parodi, "Building an Underwater Wireless Sensor Network Based on Optical: Communication: Research Challenges and Current Results," in *3rd Int. Conf. on Sensor Technol. and Applications*, Athens, Glyfada, 18-23 June 2009, pp. 476-479.
- [8] N.Tollinsky, "Penguin unveils optical technology", [Online]. Available: <http://www.sudburyminingssolutions.com/penguin-unveils-optical-technology> [Accessed: Dec. 20, 2015].
- [9] "BlueComm Underwater Optical Modem," [Online]. Available: <http://www.sonardyne.com/products/all-products/instruments/1148-bluecomm-underwater-optical-modem.html> [Accessed: Dec. 20, 2015].

- [10] "High-Bandwidth Underwater Tranceivers," [Online]. Available: <http://www.ambalux.com/underwater-transceivers.html> [Accessed: Dec 20, 2015].
- [11] S. Arnon, J. Barry, G. Karagiannidis, R. Schober, and M. Uysal, *Advanced optical wireless communication systems*, Cambridge University Press, 2012.
- [12] I. Vasilescu, K. Kotay, D. Rus, M. Dunbabin, and P. Corke, "Data collection, storage, and retrieval with an underwater sensor network," in *Proc. of the 3rd Int. Conf. on Embedded Networked Sensor Systems*, San Diego, Ca, USA, 2-4 Nov 2005, pp. 154-165.
- [13] N. Farr, A. Chave, L. Freitag, J. Preisig, S. White, D. Yoerger, and F. Sonnichsen, "Optical modem technology for seafloor observatories," in *OCEANS*, Boston, MA, 18-21 Sept, 2006, pp. 1-6.
- [14] B. Cochenour, "Experimental Measurements of Temporal Dispersion for Underwater Laser Communications and Imaging," Ph.D. thesis, Dept. Elect. and Comp. Eng, North Carolina State Univ, NC, USA, 2012.
- [15] A. Shaw, A. Al-Shamma'a, S. Wylie, and D. Toal, "Experimental investigations of electromagnetic wave propagation in sea water," in *European Microwave Conf*, Manchester, 10-15 Sept 2006, pp. 572-575.
- [16] I. F. Akyildiz, D. Pompili, and T. Melodia, "Challenges for efficient communication in underwater acoustic sensor networks," *ACM Sigbed Review*, vol. 1, no. 2, pp. 3-8, 2004.
- [17] J. Partan, J. Kurose, and B. N. Levine, "A survey of practical issues in underwater networks," *ACM Sigmoblie Mobile Computing and Communications Review*, vol. 11, no. 4, pp. 23-33, 2007.
- [18] B. M. Cochenour, L. J. Mullen, and A. E. Laux, "Characterization of the Beam-Spread Function for Underwater Wireless Optical Communications Links," *IEEE J. of Ocean. Eng.*, vol. 33, no. 4, pp. 513-521, Oct 2008.
- [19] F. Schill, U. R. Zimmer, and J. Trump, "Visible spectrum optical communication and distance sensing for underwater applications," in *Proc. of ACRA*, Canberra, Australia, 6-8 Dec, 2004, pp. 1-8.
- [20] J. Lloret, S. Sendra, M. Ardid, and J. J. Rodrigues, "Underwater wireless sensor communications in the 2.4 GHz ISM frequency band," *Sensors*, vol. 12, no. 4, pp. 4237-4264, 2012.

- [21] X. Che, I. Wells, G. Dickers, P. Kear, and X. Gong, "Re-evaluation of RF electromagnetic communication in underwater sensor networks," *IEEE Commun. Mag*, vol. 48, no. 12, pp. 143-151, 2010.
- [22] C. D. Mobley, *Light and Water: Radiative Transfer in Natural Waters*, Academic Press, 1994.
- [23] M.Chaplin, "Water Structure and Science". [Online]. Available: http://www1.lsbu.ac.uk/water/water_structure_science.html, [Accessed: Jan. 19 2014].
- [24] S. Karp, "Optical communications between underwater and above surface (satellite) terminals," *IEEE Trans. Commun.*, vol. 24, no. 1, pp. 66-81, 1976.
- [25] T. Wiener and S. Karp, "The role of blue/green laser systems in strategic submarine communications," *IEEE Trans. Commun.*, vol. 28, no. 9, pp. 1602-1607, 1980.
- [26] L. Chien-Lan, C. Yung-Fu, H. Chong-Lung, W. Meng-Chyi, L. Chien-Yu, H. Mau-Phon, H. Yuan-Tai, and Y. Cheng-Fu, "Light-emitting diodes for visible light communication," in *Int. Wireless Communications and Mobile Computing Conf. (IWCMC)*, Dubrovnik, 24-28 Aug, 2015, pp. 665-667.
- [27] J. R. Longacre, D. E. Freeman, and J. B. Snow, "High-data-rate underwater laser communications," in *Int. Society for Optics and Photonics*, Orlando, 16-20 April, 1990, pp. 433-439.
- [28] J. B. Snow, J. P. Flatley, D. E. Freeman, M. A. Landry, C. E. Lindstrom, J. R. Longacre, and J. A. Schwartz, "Underwater propagation of high data rate laser communications pulses," in *Int. Society for Optics and Photonics*, San Diego, 1992, pp. 419-427.
- [29] B. Cochenour, L. Mullen, A. Laux, and T. Curran, "Effects of multiple scattering on the implementation of an underwater wireless optical communications link," in *OCEANS*, Boston, MA, 18-21 Sept 2006, pp. 1-6.
- [30] B. Cochenour, L. Mullen, and A. Laux, "Spatial and temporal dispersion in high bandwidth underwater laser communication links," in *IEEE Military Commun. Conf., MILCOM*, San Diego, CA, 16-19 Nov, 2008, pp. 1-7.
- [31] F. R. Dalglish, J. J. Shirron, D. Rashkin, T. E. Giddings, A. K. V. Dalglish, I. Cardei, B. Ouyang, F. M. Caimi, and M. Cardei, "Physical layer

- simulator for undersea free-space laser communications," *Optical Engineering*, vol. 53, no. 5, pp. 051410-051410, 2014.
- [32] F. R. Dalgleish, F. M. Caimi, A. K. Vuorenkoski, W. B. Britton, B. Ramos, T. E. Giddings, J. J. Shirron, and C. H. Mazel, "Efficient laser pulse dispersion codes for turbid undersea imaging and communications applications," in *SPIE Defense, Security, and Sensing*, pp. 76780I-76780I-12, 2010.
 - [33] J. Li, Y. Ma, Q. Q. Zhou, B. Zhou, and H. Y. Wang, "Monte Carlo study on pulse response of underwater optical channel," *Optical Engineering*, vol. 51, no. 6, pp. 066001-1, Jun 2012.
 - [34] S. Jaruwatanadilok, "Underwater Wireless Optical Communication Channel Modeling and Performance Evaluation using Vector Radiative Transfer Theory," *IEEE J. Sel. Areas Commun.*, vol. 26, no. 9, pp. 1620-1627, 2008.
 - [35] F. Hanson and S. Radic, "High bandwidth underwater optical communication," *Appl Opt*, vol. 47, no. 2, pp. 277-283, 2008.
 - [36] J. Li, Y. Ma, Q. Zhou, B. Zhou, and H. Wang, "Channel capacity study of underwater wireless optical communications links based on Monte Carlo simulation," *J. Opt.*, vol. 14, no. 1, p. 015403, 2012.
 - [37] L. Mullen, A. Laux, and B. Cochenour, "Propagation of modulated light in water: implications for imaging and communications systems," *Appl Opt*, vol. 48, no. 14, pp. 2607-2612, 2009.
 - [38] W. C. Cox Jr, "Simulation, Modeling, and Design of Underwater Optical Communication Systems," Ph.D. thesis, Dept. Elect. and Comp. Eng, North Carolina State Univ, NC, USA, 2012.
 - [39] C. Gabriel, M. Khalighi, S. Bourennane, P. Leon, and V. Rigaud, "Monte-Carlo-based channel characterization for underwater optical communication systems," *IEEE/OSA J. of Optical Communications and Networking*, vol. 5, no. 1, pp. 1-12, 2013.
 - [40] S. Tang, Y. Dong, and X. Zhang, "Impulse Response Modeling for Underwater Wireless Optical Communication Links," *IEEE Trans. Commun.*, vol. 62, no. 1, pp. 226-234, 2014.
 - [41] F. Jasman and R. J. Green, "Monte Carlo simulation for underwater optical wireless communications," in *2nd Int. Workshop on Optical Wireless Communications (IWOW)*, Newcastle, UK, 21 Oct 2013, pp. 113-117.

- [42] S. Tang, Y. Dong, and X. Zhang, "Impulse Response Modeling for Underwater Wireless Optical Communication Links," *IEEE Trans. Commun.*, vol. 62, no. 1, pp. 226-234, 2014.
- [43] H. Zhang and Y. Dong, "Impulse response modeling for general underwater wireless optical MIMO links," *IEEE Commun. Mag*, vol. 54, no. 2, pp. 56-61, 2016.
- [44] Y. Dong, H. Zhang, and X. Zhang, "On impulse response modeling for underwater wireless optical MIMO links," in *IEEE/CIC Int. Conf. on Communications (ICCC)*, Shanghai, China, 13-15 Oct, 2014, pp. 151-155.
- [45] M. Doniec, M. Angermann, and D. Rus, "An End-to-End Signal Strength Model for Underwater Optical Communications," *IEEE J. of Ocean. Eng.*, vol. 38, no. 4, pp. 743-757, 2013.
- [46] D. Rashkin, I. Cardei, M. Cardei, F. Dalglish, and T. Giddings, "Detector noise model verification for undersea free space optical data links," in *OCEANS*, Hampton Roads, VA, 14-19 Oct, 2012, pp. 1-7.
- [47] L. J. Johnson, R. J. Green, and M. S. Leeson, "Underwater optical wireless communications: depth dependent variations in attenuation," *Appl Opt*, vol. 52, no. 33, pp. 7867-7873, 2013.
- [48] H. Zhang and Y. Dong, "General Stochastic Channel Model and Performance Evaluation for Underwater Wireless Optical Links," *IEEE Trans. Wireless Commun.*, vol. 15, no. 2, pp. 1162-1173, 2016.
- [49] I. Vasilescu, "Using light underwater: devices, algorithms and systems for maritime persistent surveillance," Ph.D. thesis, Dept. Elect. Eng. and Comp. Science Massachusetts Institute of Technology, 2009.
- [50] K. Nakamura, I. Mizukoshi, and M. Hanawa, "Optical wireless transmission of 405 nm, 1.45 Gbit/s optical IM/DD-OFDM signals through a 4.8 m underwater channel," *Opt Express*, vol. 23, no. 2, pp. 1558-1566, 2015.
- [51] H. Oubei, J. Duran, B. Janjua, and H. Wang, "4.8 Gbit/s 16-QAM-OFDM transmission based on compact 450-nm laser for underwater wireless optical communication," *Optics Express*, vol.23, no. 18, pp. 23302-23309,2015.
- [52] D. Anguita, D. Brizzolara, and G. Parodi, "Optical wireless communication for underwater Wireless Sensor Networks: Hardware modules and circuits design and implementation," in *OCEANS*, Seattle, WA, 20-23 Sept, 2010, pp. 1-8.

- [53] D. Anguita, D. Brizzolara, G. Parodi, and Q. Hu, "Optical Wireless Underwater Communication for AUV: Preliminary Simulation and Experimental Results," in *OCEANS*, Santander, 6-9 June, 2011, pp.1-5.
- [54] M. Doniec, I. Vasilescu, M. Chitre, C. Detweiler, M. Hoffmann-Kuhnt, and D. Rus, "AquaOptical: A lightweight device for high-rate long-range underwater point-to-point communication," *Marin Technology Society Journal*, vol. 44, no. 4, pp. 55-65, 2010
- [55] M. Doniec, X. Anqi, and D. Rus, "Robust real-time underwater digital video streaming using optical communication," in *IEEE Int. Conf. on Robotics and Automation (ICRA)*, Karlsruhe, 6-10 May 2013, 2013, pp. 5117-5124.
- [56] M.A.Chancey,"Short Range Underwater Optical Communication links," M.S. thesis, Dept. Elect. and Comp. Eng, North Carolina State Univ, NC, USA, 2005.
- [57] W. C. Cox Jr, "A 1 Mbps Underwater Communication System Using 405 nm LASr Diodes and Photomultiplier Tube," M.S. thesis, Dept. Elect. and Comp. Eng, North Carolina State Univ, NC, USA, 2008.
- [58] J. A. Simpson, "A 1 Mbps Underwater Communication System Using 405 nm LEDs and Photodiodes with Signal Processing Capability," M.S. thesis, Dept. Elect. and Comp. Eng, North Carolina State Univ, NC, USA, 2008.
- [59] J. A. Simpson, "Underwater Free-Space Optical Communication using Smart Transmitter and Receivers," Ph.D. thesis, Dept. Elect. and Comp. Eng., North Carolina State University, NC, USA, 2012.
- [60] J. W. Bales and C. Chrissostomidis, "High-bandwidth, low-power, short-range optical communication underwater," in *Int. Symp. on Unmanned Untethered Submersible Technology*, 1995, pp. 406-415.
- [61] M. Tivey, P. Fucile, and E. Sichel, "A Low Power, Low Cost, Underwater Optical Communication System," *Ridge 2000*, vol. 1, pp. 27-29, 2000.
- [62] C. Pontbriand, N. Farr, J. Ware, J. Preisig, and H. Popenoe, "Diffuse high-bandwidth optical communications," in *OCEANS*, Quebec City, QC, 15-18 Sept 2008, pp. 1-4.
- [63] J. A. Simpson, W. C. Cox, J. R. Krier, B. Cochenour, B. L. Hughes, and J. F. Muth, "5 Mbps optical wireless communication with error correction coding for underwater sensor nodes," in *OCEANS MTS/IEEE SEATTLE*, 2010, pp. 1-4.

- [64] H. Brundage, "Designing a wireless underwater optical communication system," M.S. thesis, Dept. Mech. Eng, MIT, Cambridge, USA, 2010.
- [65] M. Doniec and D. Rus, "BiDirectional optical communication with AquaOptical II," in *IEEE Int. Conf. on Communication Systems (ICCS)*, Singapore, 17-19 Nov. 2010, pp. 390-394.
- [66] G. Baiden and Y. Bissiri, "High bandwidth spherical optical wireless communication for subsea telerobotic mining," in *OCEANS MTS/IEEE KONA*, pp. 1-4, 2011.
- [67] G. Cossu, R. Corsini, A. Khalid, S. Balestrino, A. Coppelli, A. Caiti, and E. Ciaramella, "Experimental demonstration of high speed underwater visible light communications," in *2nd Int. Workshop on Optical Wireless Communications (IWOW)*, Newcastle, UK, 21-23 Oct. 2013, pp. 11-15.
- [68] N. Farr, a. Bowen, J. Ware, C. Pontbriand, and M. Tivey, "An integrated, underwater optical /acoustic communications system," in *OCEANS IEEE - SYDNEY*, 2010, pp.1-6
- [69] V. I. Haltrin, "Absorption and scattering of light in natural waters," in *Light Scattering Reviews*, Springer, 2006, pp. 445-486.
- [70] R. A. Leathers, T. V. Downes, C. O. Davis, and C. D. Mobley, "Monte Carlo Radiative Transfer Simulations for Ocean Optics: A Practical Guide," Naval Research Lab., Washington, DC, Tech.Memo. NRL/MR/5660—04-8819, Sept 1, 2004.
- [71] Emmanuel Boss, "Ocean Optics Web Book". [Online]. Available: <http://www.oceanopticsbook.info/view/introduction/overview>. [Accessed: March 1, 2015]
- [72] L. Sun, J. Wang, K. Yang, M. Xia, and J. Han, "The Research of Optical Turbulence Model in Underwater Imaging System," *Sensors & Transducers*, vol. 163, no. 1, pp. 107-112, 2014.
- [73] D. Chada, *Terrestrial Wireless Optical Communication*. McGraw-Hill Professional, 2013.
- [74] R. W. Austin and G. Halikas, "The Index of Refraction of Sea water," Scripps Institution of Oceanography, San Diego, California, Report SIO Reference 76-1, Jan 1976.
- [75] V. V. Nikishov, "Spectrum of Turbulent Fluctuations of the Sea-Water Refraction Index," *Int. J. Fluid Mech. Res.*, vol. 27, no. 1, 2000.

- [76] N. Farwell, "Optical Beam Propagation in Oceanic Turbulence," Ph.D thesis, University of Miami, Ohio, USA, 2014.
- [77] Y. Ata and Y. Baykal, "Structure functions for optical wave propagation in underwater medium," *Waves in Random and Complex Media*, vol. 24, no. 2, pp. 164–173, 2014.
- [78] S. Tang, X. Zhang, and Y. Dong, "Temporal statistics of irradiance in moving turbulent ocean," in *OCEANS 2013 MTS/IEEE Bergen*, 2013, pp. 1-4.
- [79] Z. Xu, X. Guo, L. Shen, and D. K. P. Yue, "Radiative transfer in ocean turbulence and its effect on underwater light field," *J. Geophys. Res. Ocean.*, vol. 117, no. 3, pp. 1–14, 2012.
- [80] G. C. Mooradian and M. Geller, "Temporal and angular spreading of blue-green pulses in clouds," *Appl. Opt.*, vol. 21, no. 9, pp. 1572–1577, 1982.
- [81] B. Cochenour, L. Mullen, and J. Muth, "Temporal response of the underwater optical channel for high-bandwidth wireless laser communications," *IEEE J. Ocean. Eng.*, vol. 38, no. 4, pp. 730–742, 2013.
- [82] Y. Gawdi, "Underwater Free Space Optics," M.S. thesis, Dept. Elect. And Comp. Eng., North Carolina State University, NC, USA, 2006.
- [83] H. Zhang, I. Hui, and Y. Dong, "Angle of Arrival Analysis for Underwater Wireless Optical Links," *IEEE Commun. Lett.*, vol. 19, no. 12, pp. 2162–2165, 2015.
- [84] T. J. Petzold, "Volume scattering functions for selected ocean waters," Scripps Institute of Oceanography, San Diego, CA, Tech. Rep. Oct 1972.
- [85] L. C. Henyey and J. L. Greenstein, "Diffuse radiation in the Galaxy," *Astrophys. J.*, vol. 93, p. 70, Jan. 1941.
- [86] T. Binzoni, T. S. Leung, a H. Gandjbakhche, D. Rüfenacht, and D. T. Delpy, "The use of the Henyey-Greenstein phase function in Monte Carlo simulations in biomedical optics," *Physics in medicine and biology*, vol. 51. pp. L39–L41, 2006.
- [87] V. I. Haltrin, "Theoretical and empirical phase functions for Monte Carlo calculations of light scattering in sea water," in *4th Int. Conf. on Remote Sensing for Marine and Coastal Environments*, 1997, pp. 17- 19.

- [88] S. A. Prahl, "Light transport in tissue," Ph.D. thesis, University of Texas at Austin, USA, 1988.
- [89] L. Wang and S. L. Jacques, "Monte Carlo modeling of light transport in multi-layered tissues in standard C," *The University of Texas*, MD Anderson Cancer Center, Houston, 1992.
- [90] V. I. Haltrin, "One-parameter two-term Henyey-Greenstein phase function for light scattering in seawater.," *Appl. Opt.*, vol. 41, no. 6, pp. 1022–1028, 2002.
- [91] W. Cox and J. Muth, "Simulating channel losses in an underwater optical communication system," *JOSA A*, vol. 31, no. 5, pp. 920-934, 2014.
- [92] H. R. Gordon, "Modeling and simulating radiative transfer in the ocean," *Oxford Monographs on Geology and Geophysics*, vol. 25, no. 1, pp. 3-3, 1994.
- [93] B. M. Cochenour and A. E. Laux, "Experimental validation of a Monte Carlo model for determining the temporal response of the underwater optical communications channel," in *SPIE Defense and Security*, 2015, pp. 94590A-94590A-9.
- [94] E. Berrocal, D. L. Sedarsky, M. E. Paciaroni, I. V. Meglinski, and M. A. Linne, "Laser light scattering in turbid media Part I: Experimental and simulated results for the spatial intensity distribution," *Opt Express*, vol. 15, pp. 10649-10665, 2007.
- [95] A. S. Fletcher, S. A. Hamilton, and J. D. Moores, "Undersea laser communication with narrow beams," *IEEE Commun. Mag.*, vol. 53, no. 11, pp. 49–55, 2015.
- [96] G. Baiden, Y. Bissiri, and A. Masoti, "Paving the way for a future underwater omni-directional wireless optical communication systems," *Ocean Engineering*, vol. 36, no. 9, pp. 633-640, 2009.
- [97] F. Jasman and R. Green, "Power Distribution and Frequency Response Performance of Underwater Optical Wireless Communications.," in *IEEE 20th Int. Workshop on Computer Aided Modelling and Design of Communication Links and Networks (CAMAD)*, Surrey, UK, 7-9 Sept 2015, pp.288-292.
- [98] B. Cochenour, L. Mullen, W. Rabinovich, and R. Mahon, "Underwater optical communications with a modulating retro-reflector," *SPIE defense, Security and Sensing*, 2009, pp. 73170G.

- [99] L. Mullen, B. Cochenour, W. Rabinovich, R. Mahon, and J. Muth, "Backscatter suppression for underwater modulating retroreflector links using polarization discrimination," *Appl Opt*, vol. 48, no. 2, pp. 328-337, 2009.
- [100] S. Arnon, "Underwater optical wireless communication network," *Optical Engineering*, vol. 49, no. 1, pp. 015001-015001-6, 2010.
- [101] S. Arnon and D. Kedar, "Non-line-of-sight underwater optical wireless communication network," *JOSA A*, vol. 26, no. 3, pp. 530-539, 2009.
- [102] N. Metropolis and S. Ulam, "The Monte Carlo method," *J. of the American Statistical Association*, vol. 44, no. 247, pp. 335-341, 1949.
- [103] M. Grabner and V. Kvicera, "Multiple scattering in rain and fog on free-space optical links," *J. of Lightwave Technology*, vol. 32, no. 3, pp. 513-520, 2014.
- [104] S. Dimitrov, R. Mesleh, H. Haas, M. Cappitelli, M. Olbert, and E. Bassow, "Path Loss Simulation of an Infrared Optical Wireless System for Aircrafts," in *IEEE Glob. Telecommun. Conf. 2009 (IEEE GLOBECOM 2009)*, pp. 1-6, 2009.
- [105] H. Ding, G. Chen, Z. Xu, and B. Sadler, "Channel modelling and performance of non-line-of sight ultraviolet scattering communications," *IET Commun.*, vol. 6, no. 5, pp. 514-524, 2012.
- [106] E. Alerstam, "Optical spectroscopy of turbid media: time-domain measurements and accelerated Monte Carlo modelling," Ph.D. thesis, Lund University, Sweden, 2011.
- [107] M. Chowdhury, W. Zhang, and M. Kavehrad, "Combined deterministic and modified monte carlo method for calculating impulse responses of indoor optical wireless channels," *J. Lightw. Technol.*, vol. 32, no. 18, pp. 3132-3148, 2014.
- [108] H. Ding, "Modeling and characterization of ultraviolet scattering communication channels," Ph.D. thesis, University of California, Riverside, USA, 2011.
- [109] E. Ghargomi and I. S. Attia, "Modeling of a focused Gaussian beam into multi-layered tissue with Monte Carlo simulation," M.S. thesis, Dept. Elect. and Comp. Eng, Concordia University, Canada, 2004.

- [110] O.Ertl, "Numerical Methods for Topography Simulation," Ph.D. thesis, Institute for Microelectronics, Vienna University of Technology, Austria, 2010.
- [111] J. Greenwood, "The correct and incorrect generation of a cosine distribution of scattered particles for Monte-Carlo modelling of vacuum systems," *Vacuum*, vol. 67, no. 2, pp. 217-222, 2002.
- [112] S. Prahl, M. Keijzer, S. Jacques, and A. Welch, "A Monte Carlo model of light propagation in tissue," *Dosimetry of laser radiation in medicine and biology*, vol. 5, pp. 102-111, 1989.
- [113] W. Cox, J. Simpson, and J. F. Muth, "Monte Carlo Simulation of Turbid Water Channels and Use of Segmented Field of View Smart Transmitters and Receivers for Underwater Optical Communications," in *Underwater Optical Communications Networking, UComms*, 2012, pp.1-8.
- [114] J. A. Simpson, B. L. Hughes, and J. F. Muth, "Smart Transmitters and Receivers for Underwater Free-Space Optical Communication," *IEEE J. Sel. Areas Commun.*, vol. 30, no. 5, pp. 964-974, 2012.
- [115] R. M. Lerner and J. D. Summers, "Monte Carlo Description of Time- and Space-Resolved Multiple Forward Scatter in Natural Water," *Appl Opt*, vol. 21, no. 5, pp. 861-869, 1982.
- [116] E. A. Bucher, "Computer simulation of light pulse propagation for communication through thick clouds," *Appl Opt*, vol. 12, no. 10, pp. 2391-2400, 1973.
- [117] G. Mooradian, M. Geller, L. Stotts, D. Stephens, and R. Krautwald, "Blue-green pulsed propagation through fog," *Appl Opt*, vol. 18, no. 4, pp. 429-441, 1979.
- [118] Z. Xu and D. K. Yue, "Analytical solution of beam spread function for ocean light radiative transfer," *Opt Express*, vol. 23, no. 14, pp. 17966-17978, 2015.
- [119] K. J. Voss, "Simple empirical model of the oceanic point spread function," *Appl Opt*, vol. 30, no. 18, pp. 2647-2651, 1991.
- [120] W. Hou, D. J. Gray, A. D. Weidemann, and R. A. Arnone, "Comparison and validation of point spread models for imaging in natural waters," *Opt Express*, vol. 16, no. 13, pp. 9958-9965, 2008.

- [121] J. W. McLean, J. D. Freeman, and R. E. Walker, "Beam spread function with time dispersion," *Appl Opt*, vol. 37, no. 21, pp. 4701-4711, 1998.
- [122] W. Wei, Z. Xiao, C. Yue, and Z. Xue, "An analytical model of the power spatial distribution for underwater optical wireless communication," *Optica Applicata*, vol. 42, no. 1, pp. 157-166, 2012.
- [123] T. Shijian, D. Yuhan, and Z. Xuedan, "On Link Misalignment for Underwater Wireless Optical Communications," *IEEE Commun. Lett.*, vol. 16, no. 10, pp. 1688-1690, 2012.
- [124] E. Berrocal, "Multiple Scattering of Light in Optical Diagnostics of Dense Sprays and Other Complex Media," Ph.D thesis, Cranfield University, 2006.
- [125] C. Gabriel, M. A. Khalighi, S. Bourennane, P. Leon, and V. Rigaud, "Channel modeling for underwater optical communication," in *2011 IEEE GLOBECOM Work.*, pp. 833-837, 2011.
- [126] C. Zhu and Q. Liu, "Review of Monte Carlo modeling of light transport in tissues," *J. Biomed. Opt.*, vol. 18, no. 5, p. 050902, 2013.
- [127] F. Hanson and M. Lasher, "Effects of underwater turbulence on laser beam propagation and coupling into single-mode optical fiber.," *Appl. Opt.*, vol. 49, no. 16, pp. 3224-3230, 2010.
- [128] S. Arpali, Y. Baykal, and Ca. Arpali, "BER evaluations for multimode beams in underwater turbulence," *J. Mod. Opt.*, pp. 1-4, 2016.
- [129] H. Gerçekcioğlu, "Bit error rate of focused Gaussian beams in weak oceanic turbulence," *JOSA A*, vol. 31, no. 9, pp. 1963-1968, 2014.
- [130] M. V. Jamali and J. a. Salehi, "On the BER of Multiple-Input Multiple-Output Underwater Wireless Optical Communication Systems," in *4th Int. Workshop on Optical Wireless Communications, (IWOW)*, Istanbul, Turkey, Sept 2015, pp. 26-30.